LABEL-FREE MONITORING OF TUMOR MODELS BY SURFACE-ENHANCED RAMAN SCATTERING

PhD Thesis

Javier Plou Izquierdo

Supervised by: Professor Luis Liz-Marzán and
Professor Arkaitz Carracedo

Donostia-San Sebastián, 2022

Universidad del País Vasco
Euskal Herriko Unibertsitatea

Label-Free Monitoring of Tumor Models by Surface-Enhanced Raman Scattering

A manuscript submitted to the university of the Basque Country

For the degree of doctor in sciences

Presented by Javier Plou Izquierdo

Under the supervision of:

Luis Manuel Liz Marzán (Bionanoplasmonic Lab/ CIC Biomagune)

Arkaitz Carracedo Pérez (Cancer Cell Signaling and Metabolism Lab/ CIC Biogune)

CIC bioGUNE
MEMBER OF BASQUE RESEARCH & TECHNOLOGY ALLIANCE

CIC biomaGUNE
MEMBER OF BASQUE RESEARCH & TECHNOLOGY ALLIANCE

eman ta zabal zazu
Universidad del País Vasco
Euskal Herriko Unibertsitatea

AGRADECIMIENTOS

Aunque la realización de una tesis doctoral constituye un ejemplo más de las diferentes actividades télicas que realizamos a lo largo de nuestra vida, aquellas que tienen una meta final, y que terminan cuando se cumple dicho objetivo. Dentro de la tesis, escribir la parte de agradecimientos sirve para conectar, en cierta forma, con la importancia del proceso en sí, lo atélico, por encima de la consecución o no de los objetivos planteados inicialmente. De hecho, al igual que en una discusión científica de resultados, los agradecimientos se conjugan en pasado, pero estos adquieren una dimensión presente y futura que nos moldea de forma atélica (sin fin).

Entre los muchos aspectos positivos por los que podría dar las gracias, creo que ha sido muy importante la existencia de un ambiente, creado por todas las personas con la que he interactuado, donde he podido mostrar con sinceridad mis inseguridades y virtudes, y que, en definitiva, me han permitido perseguir la mejor versión de mi mismo. En este sentido, disfrutar de la confianza de mis directores de tesis, y en especial de Luis, en los buenos, pero sobre todo en los malos momentos (los comienzos son duros siempre) ha sido clave para encarar los proyectos con optimismo y seguridad. Ha sido todo un lujo poder observar de cerca vuestra profesionalidad y dedicación por la ciencia y el trabajo bien hecho (realmente encomiables). Me gustaría darte las gracias, Luis, por todo lo que me has enseñado, por tu tiempo y tus consejos. Por tu preocupación constante para que este proceso fuera lo mas completo para mí, tanto científica como personalmente. Pertenecer a la escuela “Liz-Marzán” nos marca a todos en futuros trabajos, y es algo que siempre voy a llevar con mucho orgullo. Además, poder contar con Arkaitz para las discusiones mas biológicas del proyecto ha sido muy enriquecedor. Gracias, Arkaitz, por mejorar este trabajo, por tu actitud siempre proactiva a pesar de que era un proyecto alejado de las cosas que normalmente trabajáis en vuestro labo. A pesar de la distancia (he pasado poco tiempo en BioGUNE) siempre me he sentido arropado por tu parte. En general, los meetings que hemos tenido los tres juntos los siento como un privilegio, y una enseñanza única.

Además de la contribución de mis directores, poder contar con Isa a lo largo de estos años ha sido esencial para el éxito final de este trabajo. Sin tu apoyo personal a lo largo de estos años, y sobre todo, en el primero año, no habría podido mantener mis ganas de seguir luchando, y fracasando (al principio fracasé mucho) en mis experimentos. Representas a la ciencia que se hace en los laboratorios, la que se realiza por personas cada una con sus propias historias. Tú éxito radica en que sabes escuchar las historias de las personas para que brillen en el pequeño ecosistema que es

Bionanoplasmonics (y eso no se mide con impact factors). En definitiva, hemos formado un pedazo de equipo, que ha sabido retroalimentarse de forma muy positiva.

Haber pertenecido durante estos años a Bionanoplasmonics ha sido una experiencia increíble, seguramente pocos grupos en el mundo combinan ciencia de tan alto nivel, con un ambiente de trabajo tan positivo para sus miembros. Para mantener este buen rollo a lo largo de los años, y con tanta gente yendo y viniendo, es esencial la labor que realizan aquellas personas que siempre están, que forman el "core" del grupo. En este sentido, tanto Ada, Malou, Dorleta y Judith sois las principales responsables de que esta cultura "Bionanoplasmonics" siga viva con el paso de los años, es de agradecer el buen recibimiento y la atención que les dais a todo aquel que llega a Bionanoplasmonics por primera vez.

Una de las cosas con la que más he disfrutado a lo largo de estos 4 años y medio, ha sido la interacción con todas las personas que han ido pasando por el grupo (más de 40 personas!!), y con las que he tenido la posibilidad de ser cercano, compartiendo opiniones y formas de ver la vida. Un punto fuerte del grupo siempre han sido sus postdocs, llenos de experiencia y dispuestos a echarte una mano en lo que sea. Así pues, los resultados de esta tesis tienen mucho de los conocimientos proporcionados por Christoph, Jesús, Guille, Jatish, Christian, Marta Q, Javi Reguera en los primeros años, y más tarde de la colaboración con Clara, Carlos, Govind, Bea, Carlos Albuquerque, Oscar, Anish, Ana H… Está claro que cuando uno juega en el mismo equipo con todos estos compañeros, los problemas son menos problemas y no hay objetivos inalcanzables.

Por otra parte, debido a que justo cuando llegué acababa de terminar la primera hornada de PhDs del grupo, me ha tocado jugar, durante una buena parte del tiempo, un rol de PhD veterano (ese que cuenta anécdotas de otras épocas y da consejos que él nunca siguió), lo cual ha sido y es muy divertido. No obstante, en los primeros momentos fueron muy importantes antiguos PhDs como María y Rafaela que me acogieron y me enseñaron los trucos para sobrevivir a un doctorado. Mi comienzo de tesis también coincidió con el de Mathi, y ese primer mail que nos mandamos con el asunto los "new PhDs", que marcó el comienzo de colaboraciones increíbles. Aunque hemos pasado muchas horas juntos en los últimos años, compañeros de piso y de labo, siempre ha sido muy fácil trabajar contigo. Viniendo de campos distintos, hemos confiado mucho el uno al otro, tanto que ahora me siento un poco con "Mathidependencia". Gracias por tu paciencia, por seguirme las bromas y todas esas explicaciones físicas en las que andaba un poco perdido.

Besides, I would like to especially thank Vished, you arrived few months later, and you came along with taki-taki and PhD nights. We influenced each other, and you were always available

when I needed, for a conversation about science or disconnecting from work. I really appreciated the effort you made to understand my sense of humor. You really rock, I think we should ask Peter (from Peter answers) when we are meeting again, I am really looking forward to this. Mas adelante (un año después) llegaron Chris Vila y Eli, y con ellos me ha unido el trabajar en el mismo proyecto, compartiendo éxitos y frustraciones. Con Eli, además, compañeros de oficina. Gracias, Eli, por aguatar mis rollos con una sonrisa y por tus consejos, siempre se ha notado tu mayor experiencia tanto en ciencia como en la vida. Al poco, se sumó Cris, y con ella aumentó un poco la locura en el lab (que no vino nada mal). Gracias Cris, por contribuir a crear buen ambiente y reírnos de nosotros mismos. Gracias también a David, supongo que el verdadero veterano del grupo, me ha molado siempre discutir contigo sobre ciencia pero también sobre aquellos aspectos menos tangibles que rodean al mundo científico. Y así poco a poco el número de PhD ha ido aumentando, Paula Vázquez, Uxue, Paula Piñeiro, Marita, Laura… creo que el buen ambiente en Bioanoplasmonics está asegurado con todos vosotros. Por último, quería dar las gracias a Pablo, seguramente el que más me ha tenido que sufrir en el último año y medio. Gracias por tus ganas de aprender, por el buen rollo que transmites todos los días y esa pasión característica, por la ciencia o cualquier plan aleatorio que surja. El poder enseñarte las cosas que yo he aprendido a lo largo de mi tesis, y ver como tú las mejoras, representa uno de los aspectos de mayor valor a lo largo de estos años en CIC BiomaGUNE.

Fuera del laboratorio, vivir en el Collective Research Association Segundo Izpizua (Crasi) hizo mi vida en Donosti mucho más entretenida. Llegar a casa, y tener como compis de piso a Stefan, Cris, Mathi, me ayudó a despreocuparme un poco cuando las cosas no salían como esperaba (y justo todo empezó a ir rodado). Darte las gracias, Stef, por proponer planes que se van superando los unos a los otros, por los primeros meses en la Talent House, y alguna fiesta que se nos fue de las manos. Y también gracias por todas esas charlitas al estilo Stefan, tranquilas pero cargadas de contenido. De mayor quiero ser como tú, Stefan. Gracias también a Cris, el Ibai Llanos de la casa, ver una peli contigo la hace mejor de lo que es, una charla consigue que cualquier tema super loco, parezca posible. Que queremos ser hoy? Cantantes de trap?. Gracias por hacerme sentir que siempre tengo algo interesante que decir. Y gracias también a la última incorporación del Crasi, Johanne, tu actitud de carpe diem, y esas ganas de vivir sin miedo a equivocarse son contagiosas (como el COVID que te acabé pasando).

En Donosti, he estado rodeado de muy buenos amigos tanto compañeros del CIC BiomaGUNE (en especial la gente de la office de estudiantes), como de fuera de la ciencia (“la Kuadrilla”). Dar las gracias a los paisanos de la Maños, (Dani, Javi, Marcos, Guille), con los que he podido compartir aficiones, no solo los colores del Real Zaragoza, y con los que siempre han surgido reflexiones profundas. También han jugado un papel importante para que me sintiera como en

casa, los compañeros del Bosteko, con los que podido seguir manteniendo mi pasión por el baloncesto y el trabajo en equipo, lástima el COVID que nos arrebató ser campeones de Gipuzkoa en 2020.

Seguir contando con mis amigos de Zaragoza ha sido muy importante en este proceso, me ha ayudado a salir de la burbuja que a veces tenía en el trabajo y a recordar batallitas de otros tiempos. Tanto "El grupo AC" (Tico, Lucas, Joako, German, Zay) como los Biotec (Belloc, Yago, Juan) os agradezco que me hayáis venido a visitar en múltiples ocasiones, con sidrerías mediante. Aunque me tocaba hacer de anfitrión y siempre acabábamos perdidos (menos mal que estaba Zay), todos los planes con vosotros han sido geniales. Gracias por dejarme seguir formando parte de vuestras vidas, siempre podréis contar con mi apoyo para futuros proyectos. En especial, quería agradecer a Joako y German, cuando todo el mundo se fue de Zaragoza, siempre habéis hecho un esfuerzo por organizar planes y poder vernos. Gracias Tico, por tu espíritu libre, representas para mi un ejemplo de capacidad de sacrificio y lucha por alcanzar los sueños. Gracias, Lucas, por transmitirme tu filosofía de vida, aquella en la que siempre luchas por tu mejor versión sin renunciar a la esencia que te caracteriza, tu compañía mejora cualquier plan. A Yago, por tu espíritu crítico y profesionalidad, gracias por tu confianza, compartiendo penas y alegrías en el mundo científico. A Belloc, por trasmitirme tu vitalidad y ganas por descubrir el mundo y ayudar a los demás. A Juan, por tu pasión hacia la ciencia y la creencia de que podemos mejorar la vida de los demás a través de ella.

En todos estos años, mi familia ha jugado un papel esencial para llegar a ser la persona en que me he convertido. Creo que venir de una familia grande ha marcado mi personalidad y me ha ayudado mucho en este trabajo. Desde luego, no hay mejor forma de pasar unas vacaciones de agosto, que en la Torre con toda la familia Plou al completo. Me gustaría agradecer a mi tío Kiko, el interés que despertó en mi por la ciencia, y sus consejos a lo largo de estos años sobre la carrera del investigador. También recordar a mi tío José Ángel, un ejemplo vital, capaz de luchar y disfrutar de la vida en todo momento. Dar las gracias a mis hermanos, seguramente, los que mas han tenido que aguantar mis malas bromas, el hermano mediano siempre ha sido el más cantoso. Darte la gracias, Carlos, por todos los momentos que hemos pasado juntos, por dejarme hacer de hermano mayor, aún siendo tú el más responsable. Compartimos forma de hablar, gestos y sentido de la ironía, pero tú siempre has sabido mejorar lo hecho por tus hermanos mayores. Darte las gracias, Sara, por enseñarme el camino, por ser el referente en el que mirarme. Siempre has tenido una actitud ante la vida de trabajo duro, pero también de disfrutar y ayudar a los demás que admiro.

Por supuesto, dar las gracias a mis padres, contar con vuestro apoyo, ha hecho que la vida parezca mucho más sencilla. Nuestra casa ha sido y sigue siendo ese sitio, casi idílico, donde se solucionan

todos los problemas. Nos habéis dado a los tres las herramientas para creer en nosotros mismos, para entender que, con trabajo y honestidad, todo es posible. Además de mantenernos siempre con los pies en el suelo, destacando la importancia de la amistad y de ayudar a las personas que nos rodean. Gracias Mamá, por tu solidaridad y amor inagotables, por anteponernos frente a todo. Gracias por tu cariño y confianza, que nos guiaba para sacar siempre lo mejor de nosotros mismos, haces del mundo un sitio mejor. Gracias Papá, por hacerme de guía en la vida, por transmitirme siempre tranquilidad y felicidad. Por inculcarnos nuestra afición por la cultura, las ciencias, el deporte, y la más importante, la pasión por vivir.

Finalmente agradecer a María, mi principal apoyo durante todos estos años. La persona que se ha recorrido más kilómetros para estar conmigo y acompañarme en los momentos en los que me sentía más solo. Contigo he compartido los mejores días en estos últimos 8 años (incluida tu visita salvadora a Canadá). Gracias por tu empatía infinita y ese sentido del humor característico para subirme y bajarme de las nubes. Gracias, porque, a pesar de lo que suponía venirme a Donosti, me apoyaste y me ayudaste en el proceso de cambio desde el primer momento. Aunque en los últimos años no ha tocado pasar por momentos complicados, sobre todo una pandemia que te pilló en primera línea y que te ha obligado a entregar la mayor parte de tu tiempo y esfuerzo, te tengo que agradecer que siempre te las has arreglado para para poder estar juntos y pensar en nuevos desafíos. Gracias por tu cariño, por tu sacrificio, por intentar entenderme, aunque a veces sea difícil, y en definitiva, por hacerme mejor persona cuando estoy contigo

CONTENTS

RESUMEN

El objetivo general de la presente tesis se ha centrado en la monitorización de modelos celulares mediante la técnica de espectroscopia de Raman aumentada en superficies (SERS). Las tecnologías desarrolladas en la tesis han perseguido, por un lado, mejorar la recreación del ambiente tumoral a escala de laboratorio, y por otra parte, su integración junto con estructuras plasmónicas para el análisis por SERS de los modelos tumorales creados artificialmente. Más en concreto, se han analizado las alteraciones en la concentración relativa de los metabolitos presentes en el medio extracelular como resultado de la reprogramación metabólica característica de los tumores, la cual permite a su vez un crecimiento descontrolado de dichas células.

La disposición conjunta de ambas tecnologías (cultivos celulares en 3D y nanoplasmónica) ofrece un marco único para la identificación de aquellos procesos celulares que se encuentran alterados durante el crecimiento de tumores. Hasta la fecha, la mayoría de las técnicas de laboratorio que se habían empleado para caracterizar ambientes celulares en el laboratorio implicaban procesos invasivos, es decir, que modifican o incluso desintegraban la muestra para poder analizarla. En contraposición, la espectroscopia Raman había permitido adquirir información sobre la composición del medio celular de una manera mínimamente invasiva. Basada en los fenómenos de dispersión inelástica, la técnica de Raman emplea luz monocromática (generalmente de un láser) para irradiar la muestra bajo análisis, de forma que la interacción entre la muestra y el láser provoca un cambio en la energía de los fotones dispersados, específico de los modos vibraciones de las moléculas irradiadas. Por lo tanto, la luz dispersada y recogida por un detector, permite caracterizar el sistema biológico que ha sido previamente iluminado, sin marcaje previo. Sin embargo, las señales detectadas por dispersión Raman son de manera general muy débiles, por lo que se requiere una intensificación de dichas señales para poder detectar la presencia de metabolitos extracelulares (a bajas concentraciones). En esta tesis se decidió implantar la modalidad conocida como SERS, que hace uso de las propiedades plasmónicas de nanopartículas metálicas (principalmente de oro), las cuales dan lugar a campos eléctricos elevados cuando se iluminan en

resonancia con los plasmones superficiales. Como resultado, la señal de Raman de las moléculas adsorbidas sobre dichas superficies metálicas se ve amplificada en varios órdenes de magnitud. Sobre esta base, se han desarrollado en la tesis diferentes plataformas destinadas a combinar sustratos plasmónicos, formados por fijación de nanopartículas de oro sobre estructuras rígidas en 2D, o bien embebidas en redes poliméricas, junto con modelos de células tumorales en crecimiento. La finalidad de la tesis ha sido pues, la monitorización de diferentes procesos celulares en dichos dispositivos mediante SERS, y su posterior interpretación biológica en el ámbito del metabolismo tumoral y la mejora del tratamiento.

En el **Capítulo 1** se recoge la fabricación de sustratos amplificadores de SERS, basada en dos estrategias que comparten la fijación de nanopartículas de oro (30 nm de diámetro) sobre un soporte de vidrio, pero se diferencian en su distribución sobre el sustrato. Mientras que aquellas estructuras plasmónicas fabricadas a través de la disposición de capas de polielectrólitos con cargas opuestas presentan una distribución desorganizada, la utilización de moldes con cavidades nanométricas guía el ensamblaje de las nanopartículas hacia el interior de dichos espacios, creando agrupaciones controladas de las nanopartículas en las posiciones previamente definidas por el molde. Además, dicho diseño en forma de superred genera, tras irradiación con un láser a la longitud de onda adecuada, un efecto de difracción sobre la luz irradiada que da lugar a un aumento de intensidad del campo eléctrico, y por tanto de la señal de SERS. Posteriormente, se evaluó la capacidad de ambos sustratos plasmónicos para amplificar la señal Raman de metabolitos con funciones inmunoreguladoras en el microambiente tumoral, como son el triptófano, la kinurenina y los derivados de purinas. Ambos sustratos plasmónicos demostraron sensibilidad en incubación con disoluciones acuosas de dichos metabolitos hasta concentraciones de 1 μM, amplificando las vibraciones características de cada molécula. Sin embargo, cuando dichos metabolitos se miden en conjunto con los medios celulares, necesarios para el crecimiento de tumores, únicamente los sustratos ordenados permiten monitorizar la presencia de dichos metabolitos en la mezcla. En consecuencia, la mayoría de los experimentos llevados a cabo en etapas posteriores se realizaron con sustratos plasmónicos organizados en superredes.

Una vez determinada la eficacia de los sustratos plasmónicos (su capacidad para detectar metabolitos en el rango micromolar en ambientes complejos), se inició la monitorización

de sobrenadantes en contacto con células tumorales. Como primer paso, se investigó la sobreexpresión de la enzima indolamina-2,3-dioxigenasa 1 (IDO-1) en la línea celular HeLa (procedente de un tumor de cuello de útero), tras su activación con la citoquina interferón-γ. Como resultado de su expresión, las células eran capaces de consumir el triptófano, y liberar al medio extracelular el producto de kinurenina generado en la reacción. Este fenómeno fue utilizado para medir por SERS (simultáneamente) las fluctuaciones de ambos metabolitos en los sobrenadantes celulares, y estimar a su vez la actividad de IDO-1 en el tumor. Además, se observaron cambios significativos en los espectros SERS (reflejados en la aparición de nuevas bandas de vibracionales) cuando el cofactor de hemina, necesario para la actividad de IDO-1, se incubaba con las células a altas concentraciones. Este evento, que ocurría en paralelo a un aumento de la muerte celular por el efecto citotóxico de la hemina, se asoció a la liberación de metabolitos derivados de purina (especialmente hipoxantina) en condiciones de estrés celular. En el siguiente paso, este proceso de estrés y muerte celular se estudió en dispositivos celulares denominados como "tumores-en-un-chip" que habían sido previamente diseñados para favorecer el crecimiento de los tumores en matrices de colágeno, permitiendo su ensamblaje con los sustratos amplificadores de SERS previamente fabricados. Como consecuencia, los metabolitos liberados por las células podían, en esta configuración, interaccionar directamente con las nanopartículas fijadas en el sustrato, sin necesidad de tomar muestras del sobrenadante en cada medida. Esta aproximación destaca por su capacidad para facilitar el seguimiento de diferentes procesos celulares de manera rápida y sencilla a diferentes tiempos.

No obstante, se observó que para mantener la precisión en los resultados a lo largo del tiempo era necesario renovar el sustrato plasmónico en cada medida. Esta situación suponía un gasto elevado de material, a la vez que añadía la desventaja de una manipulación continuada del chip celular, con riesgos asociados como pueden ser la contaminación o la perturbación de la muestra biológica. Por lo tanto, en el **Capítulo 3**, se investigó una nueva estrategia que permitió medir la señal de SERS con exactitud independientemente del momento de medida.

En una primera etapa, se identificó que la adsorción irreversible de los metabolitos sobre los sustratos plasmónicos, fenómeno denominado como efecto memoria SERS, era la principal causa de la inexactitud de los resultados obtenidos a lo largo del tiempo; los

espectros de SERS presentaban vibraciones propias de metabolitos que, aunque habían estado en contacto con el sustrato, ya no estaban presentes en el medio incubado. Además, se comprobó que este fenómeno era extrapolable a una gran variedad de condiciones, en las que se suelen analizar diferentes compuestos sobre distintos tipos de sustratos. En este contexto, la estrategia planteada en este capítulo buscaba proteger el sustrato plasmónico con una capa delgada de un polímero impermeable de PLGA (co–polímero ácido poli(láctico–co–glicólico)), para posteriormente degradar el PLGA localmente por irradiación con un haz de laser a alta potencia. Debido al efecto fototérmico originado en las nanopartículas presentes en el sustrato, el aumento local de la temperatura en el área iluminada con el láser daba lugar a una degradación del film de PLGA, creando ventanas micrométricas en las que se exponía la superficie plasmónica a la muestra. La realización de diferentes ventanas de medida a lo largo del tiempo permite medir con precisión la señal SERS en el momento deseado. Esta estrategia no sólo se utilizó para evaluar el ambiente tumoral en los chips diseñados en el capítulo 2, sino que también mostró su eficacia en combinación con dispositivos de microfuídica y en el análisis de muestras en flujo.

El **Capítulo 4** de la tesis está orientado a profundizar en el concepto de secretoma, entendido como el conjunto de metabolitos liberados por las células en los procesos de estrés y muerte celular, analizando por SERS las variaciones en el secretoma de las células en función del estímulo que ocasiona su muerte. En esta aproximación se buscó además la implementación de técnicas computacionales de aprendizaje automático no supervisado (técnicas de procesamiento multivariante) y supervisado, en concreto arquitecturas basadas en redes neuronales (CNN). Con estas estrategias se pretendía extraer la información contenida en los espectros SERS, en especial para aquellas situaciones donde la complejidad de la señal obtenida dificultaba la identificación directa de los metabolitos de forma individual, tal y como se había realizado en los capítulos anteriores. Los resultados obtenidos revelaban la existencia de secretomas específicos asociados a las condiciones en la que se había inducido la muerte celular. En una segunda aplicación, se demostró que los perfiles SERS, tras la inducción de situaciones de estrés, mostraban una evolución temporal característica. De esta manera, fue posible monitorizar el efecto de diferentes tratamientos antitumorales (quimioterapia y radioterapia) tanto a periodos de tiempo cortos (24 horas) como de larga duración (3 semanas)

Finalmente, en el **Capítulo 5,** se llevó a cabo un cambio en el diseño de los sustratos de SERS utilizados, orientado en este caso a favorecer su inserción dentro de modelos tisulares más complejos, es decir, se buscaba que existiera un contacto más estrecho entre el sensor plasmónico y el entorno de las células. Para dicho fin, se generaron por impresión 3D andamios formados por polímeros biocompatibles (alginato y gelatina) con nanopartículas distribuidas en su interior, permitiendo así la detección por SERS de compuestos con propiedades antitumorales, en particular el azul de metileno (MB), a lo largo de la estructura que sustentaba el crecimiento de las células. En este contexto, se comprobó que las cargas opuestas entre el polímero de alginato que formaba el andamio y las moléculas de MB, favorecía la penetración del fármaco a través de la red tridimensional de polímero. De esta forma, se facilitaba su posterior interacción con las nanopartículas de oro, lo cual era necesario para poder realizar la monitorización por SERS de la difusión del fármaco en tiempo real. En el siguiente paso, se puso a punto el crecimiento de tumores embebidos en una matriz extracelular generada por la polimerización de Matrigel©, dispuesta homogéneamente a lo largo de la superficie del andamio. Dicha configuración permitía estudiar de forma no invasiva los gradientes de MB generados, en función de las condiciones del ensayo; por ejemplo, la presencia o no de la matriz extracelular, o de células tumorales sembradas a altas densidades. Los resultados obtenidos proporcionaron información acerca de la distribución del fármaco en los tejidos, y cómo esto puede afectar a la eficacia del tratamiento, correlacionado los parámetros de difusión del MB con la citotoxicidad generada a lo largo del andamio.

Aunque las técnicas desarrolladas en la tesis se encuentran todavía en estadios tempranos para su integración rutinaria en la práctica clínica y de investigación, su utilidad ha sido demostrada a través de la detección de diferentes biomarcadores tumorales. La combinación de sensores plasmónicos con plataformas de cultivo celular en 3D permitió el seguimiento de procesos metabólicos característicos del microambiente tumoral, lo que aportó nueva información sobre el comportamiento de estos tejidos. En definitiva, a lo largo de esta tesis se han desarrollado nuevas herramientas que han concluido con la generación de sensores para SERS con mayor versatilidad, permitiendo encarar nuevos desafíos previos a su implantación final en el campo biomédico.

GLOSSARY

SERS	Surface-enhanced Raman scattering
ECM	Extracellular matrix
TME	Tumor microenvironment
CAFs	Cancer associated fibroblasts
MMP	Matrix metalloproteinases
IFN-γ	Interferon-gamma cytokine
TGFβ	Transforming growth factor β
IDO-1	Indoleamine-2,3-dioxygenase
Trp	Tryptophan
Kyn	Kynurenine
AhR	Aryl hydrocarbon receptor
ATP	Adenosine triphosphate
ADP	Adenosine diphosphate
AMP	Adenosine monophosphate
Ado	Adenosine
MTAP	Methylthioadenosine phosphorylase
MTA	Methylthioadenosine
PCD	Programmed cell death
LC-MS	Liquid chromatography coupled to mass spectrometry
NMR	Nuclear magnetic resonance
IR	Infrared
EM	Electro-magnetic
NP	Nanoparticle
AuNPs	Gold nanoparticles
LSPR	Localized surface plasmon resonance
AuNRs	Nanorods
UV	Ultraviolet
EF	Enhancement factor
PDMS	Poly-dimethylsiloxane
PMMA	Poly-methylmethacrylate
PBS	Phosphate-buffered saline
POC	Point of care

MIPs	Molecular imprinting polymers
PCA	Principal components analysis
LbL	Layer-by-layer
L	Lattice period
Ino	Inosine
HX	Hypoxanthine
A	Adenine
STP	Staurosporine
AI	Artifical intelligence
PLGA	Poly(lactic co-glycolic acid)
NIR	Near-infrared
4-MBA	4-Mercaptobenzoic acid
Nam	Nicotinamide
TBZ	Thiabendazole
CV	Crystal violet
MB	Methylene blue
4-NTP	4-Nitrothiophenol
ACD	Accidental cell death
DNN	Deep neuronal network
t-SNE	t-Distributed Stochastic Neighbouring Entities
HBBS	Hanks′ Balanced Salt solution
DA	Discriminant analysis
DT	Decision trees
Bag	Bootstrap aggregation
SVM	Support vector machine
DMEM	Dulbecco's Modified Eagle Medium
FBS	Fetal Bovine Serum
ROS	Reactive oxygen species
ABDA	9,10-Anthracenediyl-bis(methylene)dimalonic acid
PI	Propidium iodide
GFP	Green fluorescent protein

CHAPTER 0

"Scope and objectives"

This thesis has been performed in the context of the ERC Advanced Grant "Four-Dimensional Monitoring of Tumour Growth by Surface Enhanced Raman Scattering (4DbioSERS)", under the joint supervision of Prof. Luis M. Liz-Marzán (CIC biomaGUNE) and Prof. Arkaitz Carracedo (CIC bioGUNE). The context and co-supervision have necessarily resulted in a multidisciplinary thesis project, most importantly with components of nanomaterials science and cancer metabolism, but where a wealth of techniques and concepts were unified to advance in the understanding of cancer.

More specifically, the thesis was oriented towards the screening of tumor environments by a non-routine spectroscopic tool, namely surface-enhance Raman scattering (SERS). Therefore, the results presented in this document aim at supporting the development of cell cultures in 3D and applications of SERS toward in situ, time- and space-resolved monitoring of specific biomarkers secreted during tumor growth. In particular, we focused our attention on the secretion of metabolites that may impact the disease outcome, for instance by eliciting an immunosupressive activity. The deployed technology seeks both, a better recreation of tumor models in 3D, and the close integration of such biological systems within plasmonic nanostructures for efficient SERS monitoring of nearby cell events. We ultimately aimed at demonstrating that SERS technology can be used for fast metabolomic profiling in multiple applications, such as the preclinical evaluation of novel therapeutic systems.

A first stage in the thesis involved the fabrication of suitable plasmonic substrates for SERS spectroscopy, comprising gold nanoparticles of different sizes and shapes and with different degrees of organization, for their use as Raman signal enhancers. The confinement of light at nanoscale volumes by such plasmonic nanomaterials is the responsible for the dramatic increase in Raman scattering by adsorbed molecules. In this thesis, the nanostructured hierarchical materials were devised to be constructed on 2D rigid supports, following literature reports, but additionally within three-dimensional composite scaffolds made of biopolymer hydrogels with embedded nanoparticles. Highly sensitivity SERS sensors with multiplexing capability allowed the detection of metabolites in complex mixtures, even at low concentrations, thus rendering them excellent candidates for biological sensing applications.

The synthesis and fabrication of plasmonic substrates was carried out in CIC BiomaGUNE. The Bionanoplasmonics group has an extensive track record in the field of colloidal metal nanoparticles and SERS-based sensors. Indeed, prior work by the group showed that quorum sensing metabolites in Pseudomonas aeruginosa communication could be detected by SERS. Notwithstanding, the conditions required to sustain tumor growth are typically more complex than those found in bacteria cultures, resulting in larger interferences from the large variety of biomolecules present in the cell medium. As a consequence, the spectra acquired in cell media can largely differ from reported results in the literature of the same metabolites in pure water. This thesis thus goes beyond the state of art by addressing continuous, long-term monitoring of tumor cell metabolites in situ, which demanded the improvement of both SERS substrates and methods for SERS spectral analysis of cell milieu.

Because of the limited availability of data on the detection of cancer metabolites by SERS, potential candidates were initially identified by considering the following features.

- In the first instance, we select secreted tumor metabolites with a well-described role in the tumor environment, and which extracellular concentrations increased because of altered mechanisms sustaining tumor growth. Examples of such oncometabolites with demonstrated relevance in tumor progression include lactate, adenosine and kynurenine, which are known to impair immune system activation.

- Subsequently, their intrinsic Raman cross section (i.e. the intensity of the acquired Raman signal), as well as their affinity to metallic surfaces, which is necessary for plasmonic enhancement, were the parameters of choice among the library of metabolites with previously reported biological activity. On this account, the higher polarizability of aromatic moieties renders adenosine and kynurenine metabolites more amenable for SERS detection, and thus preferentially selected over lactate or related metabolites.

To support a complete biological analysis, part of the activity in this thesis was carried out at CIC bioGUNE, within the Cancer Cell Signaling and Metabolism group, with extensive experience in state-of-the-art techniques for characterizing metabolic alterations in cancer. The work within this group has largely contributed to describe different molecular pathways involved in metabolism reprogramming processes that catapult tumor proliferation. Such previous knowledge of tumor regulation was thus meant to guide the biological interpretation of those environmental changes sensed by SERS.

The construction of cell culture devices with a suitable design that supports the integration of plasmonic nanostructures, was additionally required in the process, towards non-invasive SERS monitoring within complex tumor models. To do so, different strategies were explored using modifications of available 3D printing technology, taking into account the optimization of the acquired SERS signal and the conditions that better mimic the cancer environment. In this respect, it was essential that the plasmonic substrates maintain their optical features and sensitivity over time, while being accessible to the biological fluid for SERS monitoring. The design of the materials used for 3D-printing was based on prior expertise in the Bionanoplasmonics group, regarding the fabrication of porous films (hydrogels) containing gold nanoparticles. Besides, the group in CIC bioGUNE has routinely worked with 3D tumor models, and related fluorescence-based tools to capture spatio-temporal tumor heterogeneity.

Finally, the major challenge was the practical demonstration of the deployed systems towards the identification of a subset of metabolites under uncontrolled environmental conditions (i.e., real world application) and upon administration of therapeutic treatments. In this scenario, the implementation of methods based on artificial intelligence was addressed to extract the information contained in SERS spectra. To better approach this task, international collaboration was established with Professor Alexandre Brolo at Victoria University (Canada), wherein different chemometrics techniques were applied for SERS data classification. Furthermore, the combination of experiments performed in CIC biomaGUNE and Victoria University, employing machine-learning architectures for analysis of SERS spectra, were evaluated in terms of their ability to assess the impact of cancer therapies.

Considering the interdisciplinary nature of the thesis, the objectives can be divided in three groups:

A. Design of plasmonic substrates and involved materials:

1. Fabrication of 2D plasmonic substrates supported on rigid materials, and design of configurable cell culture devices that can be combined with such SERS sensors.

2. Development of nanocomposite scaffolds containing SERS-active plasmonic nanoparticles, that can establish an intimate contact with the cell milieu.

B. Monitoring of metabolites by SERS and tumor growth

3. Identification of potential cancer biomarkers, based on their relevant biological activity for tumor progression and a chemical structure that favors their detection by SERS.

4. Demonstration of SERS sensing of such cancer-associated analytes in cell media using previously developed SERS substrates.

5. SERS analysis of selected metabolites when secreted by growing tumor cells, first from samples of the cell supernatant, and subsequently measured on cell culture platforms for in situ monitoring.

6. SERS monitoring of tumor-secreted events with spatial and temporal resolution, under different environmental conditions.

C. Applications aiming to explore cancer therapy impact on tumor environments

7. Analysis of the effect of cancer therapies (or other stress conditions) on registered SERS profiles, combined with the implementation of strategies based on artificial intelligence.

8. SERS monitoring of drug diffusion within 3D cell models, and correlation with cytotoxicity.

CHAPTER 1

"General Introduction"

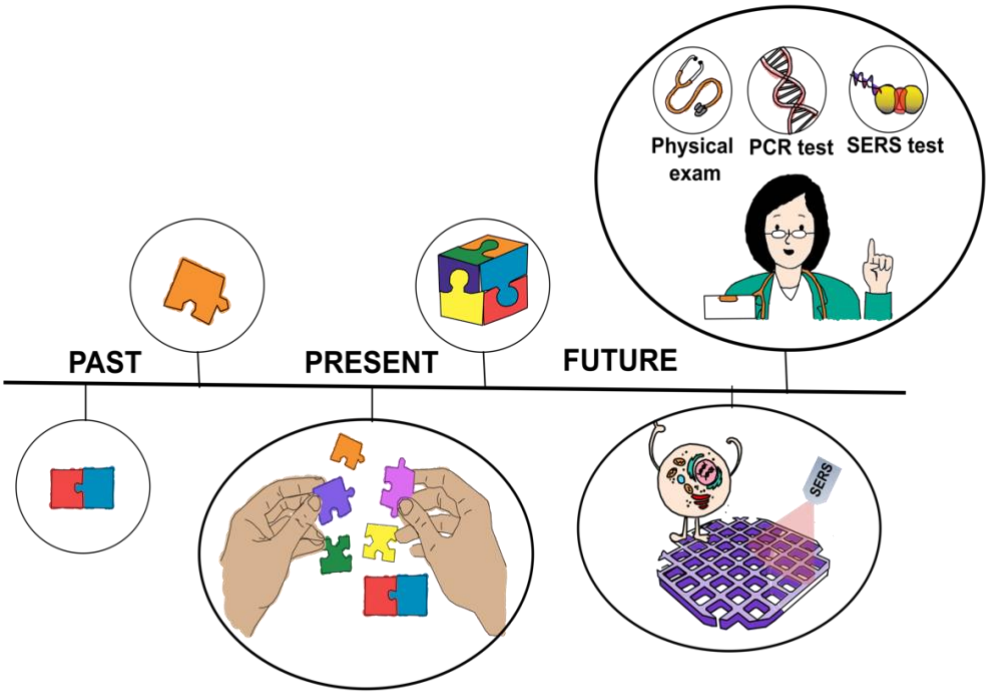

The future treatment of cancer will be undoubtedly sustained by the detection of validated biomarkers and the development of personalized in vitro models that enable a precise classification of patients, as well as understanding the basis of the disease. Up to now, genomics, transcriptomics and immunohistochemistry have been the main amenable tools at hand for identifying key processes in tumors. However, other strategies, including metabolomics or 3D cell cultures, are still in their infancy and require more progress towards their routine implementations. In this context, surface-enhanced Raman scattering (SERS) spectroscopy has been recently recognized as a promising technology for cell environment monitoring, including complex tumor models, thanks to its high sensitivity and label-free operation. SERS promises to accelerate the discovery of biomarkers and their corresponding screening in a simpler, faster, and less expensive manner, so that it may improve cancer treatment and diagnosis. In this chapter, we introduce cancer disease and the challenges that lie ahead, with special emphasis on metabolism and tumor environments. Then, we discuss strategies for 3D cancer cell models and the use of SERS (among other label-free optical techniques) to shed light on cell extracellular milieu, along with other biomedical applications.

1.1 Cancer

Our understanding of cancer disease and how we treat it, has evolved throughout history. Noteworthily, the eldest reports containing references of this pathology date back to 1600 BC in Egypt. The disease was later named by the Greek physician Hippocrates (460-370 BC) who employed the terms Karkinos and Karkinomas, accounting for their crab-like appearance, to denominate lesions ranging from benign processes to malignant tumors.[1] Nowadays, by using the word "cancer", we are including different pathologies that share the uncontrollable division of abnormal cells, originated upon certain DNA mutations that cause alterations in cell differentiation, proliferation and death.[2] Hence, cancerous cells are mainly characterized by following their own internal agenda for reproduction, accumulation and invasion of their surroundings, which cause local damage and inflammation. Particularly, they may even spread into the host body, so that other tissues and distant organs can also get affected, to an extent that most aggressive tumors can be lethal if they impair the function of organs required for survival of the whole organism.[3]

According to the World Health Organization, cancer disease represents the second cause of mortality worldwide, with an estimated of 9.6 million deaths in 2018. Indeed, these numbers are expected to rise by about 70% over the next two decades (http://www.who.int/cancer/en). On this account, the development of new therapeutic and diagnostic tools is still required towards a better understanding of the disease. Current knowledge suggests that there could be over 200 different forms of cancer; almost every tissue may develop this malignancy and what is more, some even yield several types. Moreover, cancer cells present dynamic and constantly evolving properties, therefrom originates a significant intracellular heterogeneity of the bulk tumor.[4] This intrinsic complexity dramatically hampers the eventual goal of complete cancer eradication since, despite of sharing common features, every cancer case demands different therapeutic and diagnosis strategies (**Figure 1.1a**). This displayed heterogeneity has imposed a daunting health challenge that motivated intense scientific research, not only into biomedical science, but also in traditionally non-related disciplines such as physics and engineering.

1.2 Hallmarks of cancer

Two decades ago, Hanahan and Weinberg aimed at classifying cancer´s commons capabilities,[5,6] a view that has been recently updated.[7] Owing to the problem of high cancer complexity – with a great variation of types and subtypes, they sought to unveil a logical framework that could simplify the diversity of neoplastic disease.[5,6] Their final observations identified that the vast

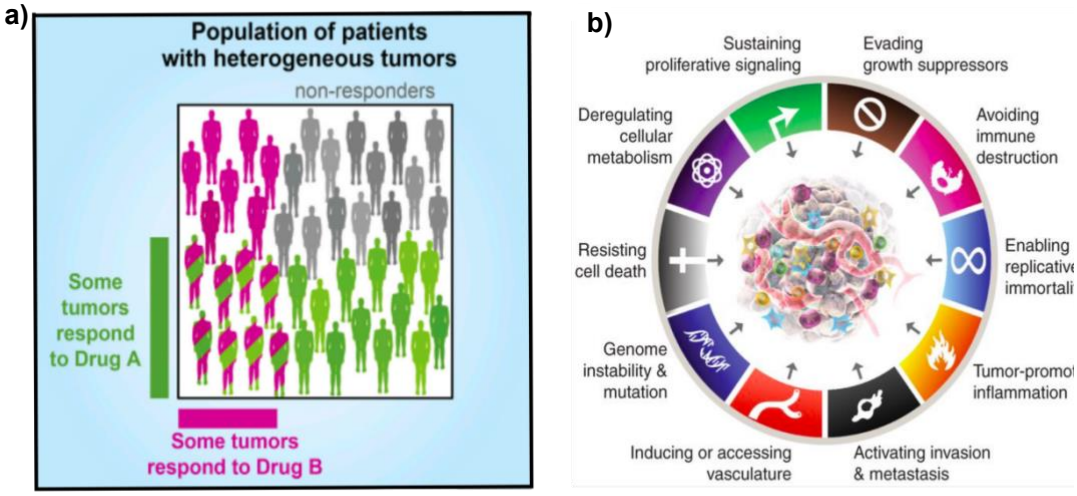

Figure 1.1. a) The high heterogeneity among different patients can only be tackled through the development of new therapeutic and diagnosis strategies, which will underpin future precision medicine in oncology. Modified from ref. 4. b) Revised hallmarks of cancer, the great diversity among cancer phenotypes is originated mainly from the acquisition of eight common alterations in functional capabilities. Two enabling capabilities are pivotal to trigger such alterations: genome instability and inflammation. Modified from ref. 7.

catalogue of phenotypes in cancer disease is primarily originated by the acquisition of six common alterations in functional capabilities, which together constitute the hallmarks of cancer. Nevertheless, these common alterations can be acquired through multiple routes, which in turn determine the distinctive and complementary traits that dictate tumor growth and cancer dissemination.

Originally, such common capabilities in cancer included: self-sufficiency in growth signals, evading growth suppressors, activating tissue invasion, limitless replicative potential, sustained angiogenesis and evasion of programmed cell death. Over the past twenty years, the initial concept of cancer hallmarks has been extended and redefined as the result of a growing knowledge in the field (see **Figure 1.1b**). Specifically, new concepts have been proposed; for example, the term "enabling characteristics" has been incorporated to define those properties that are essential for the acquisition of core hallmarks. Likewise, new emerging hallmarks have been included in agreement with their reported roles in tumorigenesis processes, such as avoiding immune destruction and the deregulation of metabolism.[6,7]

In view of their great significance and implications, much effort has been focused on describing the specific mechanisms underlying every cancer hallmark, which has also been guiding the development of more targeted treatments.[7–10] In addition, the hypothesis that considers tumors as more than insular masses of proliferating cancer is now widely endorsed. Recent studies have described tumors as complex tissues, comprising multiple cells that participate in heterotypic

interactions with each other, which were found to crucially contribute to the expression of certain hallmark capabilities. [11,12] In this context, multiple lines of evidence have revealed that the biology of tumors must be understood in tandem with the contributions of the "tumor surroundings", where stromal components may dictate the final fate of the tumor.

1.3 Tumor Microenvironment

Contrary to the initial reductionist idea of cancer, the tumor mass was found to not only present transformed cells generated by clonal division, but also a great variety of resident and infiltrating cell types, secreted factors, and the extracellular matrix (ECM). The interactions among all these components (e.g., malignant and non-transformed cells) create a unique physiology that is collectively known as the tumor microenvironment (TME). Hence, cancer cells do not act alone in disease progression; their behavior is closely influenced by their communication with the nearby environment, which ultimately determines whether the primary tumor is eradicated or, instead, proliferates and metastasizes.[13-15] Particularly, some microenvironments are favorable for progression of altered cells, whereas other restrict it. Cancer niches may otherwise display some plasticity, evolving from suppressing to pro-tumoral environments, so that cancer cells will try to functionally sculpt their microenvironment through the secretion of various cytokines and metabolites.[16–18] In this context, deciphering the environmental instructions that dictate the fate of malignancies has become crucial to the next-generation of cancer treatments.

Examples of stroma components that are widely recognized for exhibiting tumor promoting functions are fibroblasts, type I collagen, and infiltrated immune cells. Fibroblasts are mesenchymal cells localized in the stroma of most tissues, their main physiological function is the deposit and turnover of the ECM. Unlike normal fibroblasts, cancer associated fibroblasts (CAFs) are abundant in the TME; they stimulate cancer cell growth and inflammation by high overexpression of pro-tumoral factor (for example, transforming growth factor β -TGFβ) and can even promote tumor migration by remodeling the ECM.[19,20] Such alterations in ECM could include the upregulation of the ECM synthesis, which causes a stiffer fibrotic matrix, and an extensive transformation of ECM proteins by proteinases (e.g., matrix metalloproteinases (MMP)). On the other hand, modifications in the type I collagen architecture are commonly reported in the ECM. Whereas collagen fibers are normally curly and parallel-oriented to normal epithelium, they become straighter and mostly perpendicular along the tumor border; this process accelerates cell invasion and enhances tumor proliferation via integrin signaling.[21–23] Moreover, immune cells also contribute to the final ecosystem. In spite of their well-known abilities to kill tumor cells, consistent evidences confirm that innate cells (e.g., macrophages, dendritic cells,

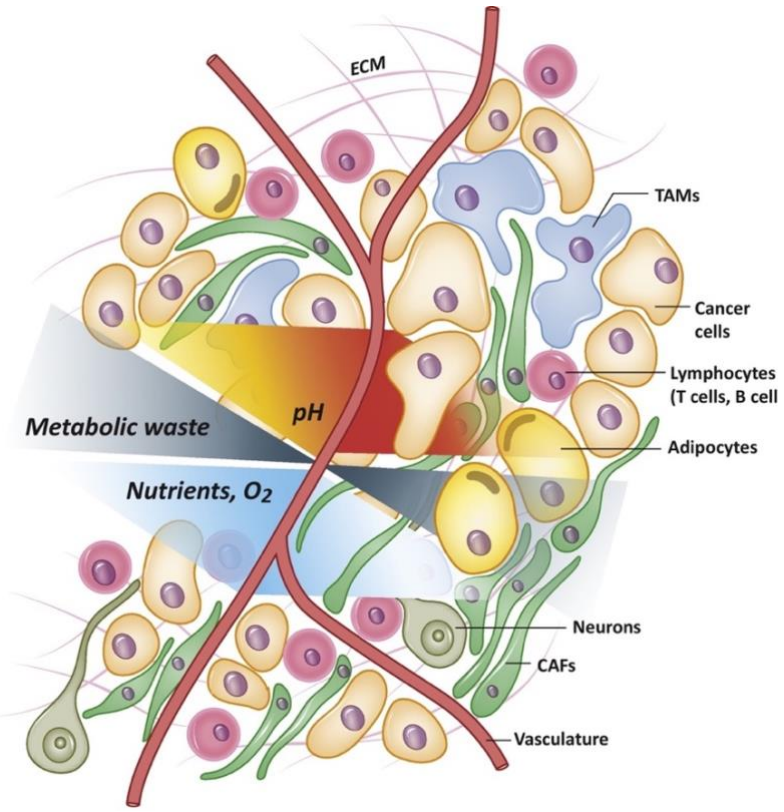

Figure 1.2. Features of tumor microenvironments, comprising tumor cells and other specific cell types. Intrinsic properties of tumor cells, such as multiple gene mutations, in combination with the extrinsic conditions of the tumor microenvironment: acid pH, low oxygen and nutrients, orchestrate an aberrant cell metabolism. The metabolites produced under such conditions play in turn a messenger role in multiple pathophysiological interactions between cancer and stroma cells. Adapted from ref. 25.

natural killer cells) as well as adaptive cells (T and B cells) can be recruited by diverse cytokines for cancer promotion within the TME (such as interferon-gamma cytokine, IFN-γ).[24]

Despite of all these induced alterations, the TME typically remains hostile for the proliferation of cancer cells, mainly due to a deficient activity of the vascular system. The uncontrolled growth of the tumor mass, along with the increased interstitial pressure, impairs bloods vessels to efficiently deliver nutrients and remove waste products. Moreover, the limitation in gas exchange creates regions of hypoxia and the accumulation of lactate, thereby acidifying the environment.[25,26] Under such extrinsic features of TME, the malignant cells must rewire their metabolic features accordingly,[27] so that reprograming will enable them to sustain growth and proliferation over time. All these mechanisms together (**Figure 1.2**) govern cross-talk communication between cancer cells and surrounding stroma, thereby contributing to more aggressive cancer states.[28]

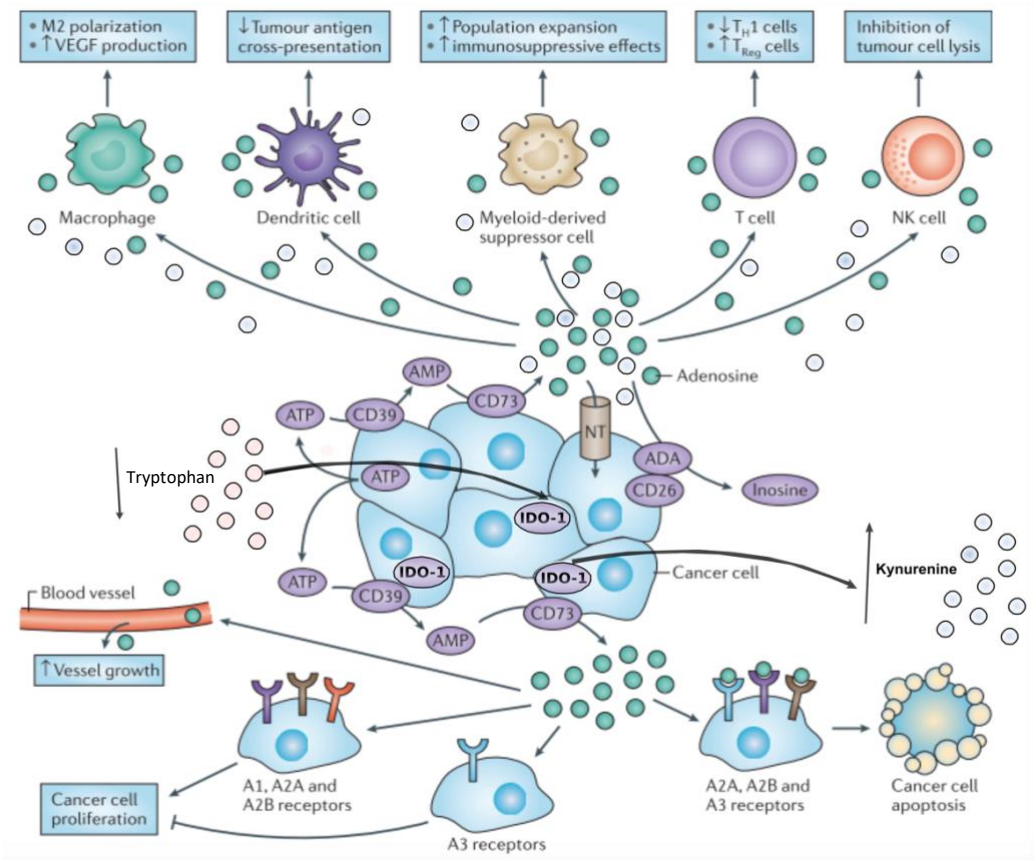

Figure 1.3. Schematic representation of different metabolic interactions within the tumor microenvironment. Purine derivatives, which are metabolically connected, play diverse functions on immune cells according to the expression of a group of ectonucleotidases and receptors on the surface of cancer cells. Modified from ref. 37. For IDO-1 expressing cells, Trp is catalytically converted into Kyn, which plays an immunomodulatory function in the tumor niche.

1.3a Metabolic interactions in the tumor microenvironment

As discussed earlier, the TME is characterized by deregulated metabolic properties. The exacerbated growth and the intrinsic deranged metabolism of cancer cells, one of their hallmarks, affect the composition of the extracellular space, while poor blood perfusion is insufficient to properly re-establish physiological levels.[29] These accumulative effects lead to considerable local variations in the concentration of metabolites, which can modulate the behavior of different cells within the TME. In this context of reshaping environments, symbiotic and competitive interactions among the components of the TME have been reported, revealing a metabolite-based communication system which fosters tumor growth and hinders antitumor immunity. The identification of these intratumoral alterations and the involved metabolites is still in its infancy.[30] Some of the already described metabolic processes (addressed in the following chapters) in the literature are included in **Figure 1.3**.

- **Tumor immune escape mediated by IDO-1:**

Numerous solid tumor types overexpress tryptophan-degrading dioxygenases (e.g., Indoleamine-2,3-dioxygenase (IDO-1)), which convert the essential amino acid, tryptophan (Trp), into kynurenine (Kyn). This phenomenon is widely considered as one the most relevant enzymatic mechanisms co-opted by malignant cells, on their way to evading the immune system. The activity of IDO-1 causes a significant tryptophan depletion and the subsequent accumulation of immunosuppressive metabolites, mostly Kyn. Therefore, Kyn is released to the extracellular media where it acts as a ligand for the aryl hydrocarbon receptor (AhR). In virtue of the AhR expression on immune cells, Kyn transduces tolerogenic immune responses imparted by IDO-1. Finally, Kyn may also potentiate autocrine signaling through the AhR on cancer cells themselves, promoting degradation of the extracellular matrix and invasion.[31–35]

- **Extracellular purines and tumor growth:**

Another significant example of metabolic reprogramming is observed with the purinergic signaling, mediated through adenosine and purine derivative nucleotides. These extracellular analytes have been revealed to have similar implications to those mentioned in Trp metabolism, such as switching the functions of immune cells. The concentration of this group of metabolites, which are metabolically connected, is physiologically low in the interstitial fluids of unstressed tissues. However, within cancer tissues, a significant increase has been reported and the expression of a family of ectonucleotidases on the outer surface of cancer cells (CD39 and CD73) is well documented to be a key determinant in the response to these extracellular metabolites. These ectonucleotidases are plasma membrane-bound enzymes that degrade purine derivative metabolites with different affinities: converting adenosine triphosphate (ATP), adenosine diphosphate (ADP) and adenosine monophosphate (AMP) into adenosine (Ado) and hypoxanthine (HX), and therefore controlling their fluctuations within the TME. The activity of these ectonucleotidases, in combination with other cell receptors, allows purine metabolites to exert either immunosuppression or immunostimulation on the host, while inducing either growth stimulation or cytotoxicity effects on tumor cells.[36–41]

Following similar mechanisms, new groups of metabolites are gaining more and more attention in the manner they can influence the fate of other cells in their vicinity. Moreover, different metabolic alterations are only observed in specific types of cancer cells. For instance, homozygous deletion of methylthioadenosine phosphorylase (MTAP) enzyme is one of the most frequent genetic alterations in glioblastoma, the most common and malignant type of brain

tumors.[42] This specific depletion causes the release of high concentrations of the metabolite methylthioadenosine (MTA) to the extracellular media, which may potentially trigger different responses in the TME.[43] In summary, all these effects reinforce the significance of metabolic interactions for tumor progression and their study is likely to fuel the discovery of novel druggable targets.

- **Tumor secretome in cell death and resistance:**

One emerging mechanism that allows tumor cells to overcome the described stressing conditions within the TME (such as chemotherapy or starvation) is the tumor cell secretome, an array of factors (including diverse metabolites) released by tumor cells. Moreover, the exposure to different stressing factors will alter the final composition and abundance of tumor secretome components, which can promote events such as tumor relapse and the formation of an immunosuppressive tumor microenvironment (TME).[44] In this direction, recent studies have demonstrated the important role of the activated cell death pathways in shaping the released secretomes and its impact on the TME.[45] Depending on the treatment variables of conventional chemo-, radio- and immunotherapy, as well as the genetic composition of the tumor cells, particular cell death pathways are activated and, therefore, an associated response in the TME.

In recent years, multiple cell death modalities have been identified and characterized concerning their corresponding stimuli, the molecular mechanisms involved, and the elicited impact on the neighboring cells. Cell death mechanisms are typically categorized into programmed cell death (PCD) or non-PCD, based on their signal dependency.[46] PCD can be further classified as apoptotic cell death or non-apoptotic cell death. In particular, multiple mechanisms and phenotypes can be defined as programmed non-apoptotic cell death, including autophagy, iron-dependent cell death (ferroptosis) or immune-reactive cell death (pyroptosis and NETosis), among many others such as necroptosis. Finally, necrosis represents a form of non-programmed cell death. In this context, much effort has been devoted toward controlling the activated mechanisms of cell death upon therapy, which can then be utilized to modulate the TME through the released secretome. By following this strategy, meaningful advances have been reported in the field of novel anti-cancer treatments that were capable, for example, of inducing an intense immune system activation.[47]

1.4 Emerging technologies to recreate and image the Tumor environment

Despite the growing knowledge on metabolism within the TME, a detailed understanding of the involved mechanisms is still required. The main complexity lies in the fact that metabolic signaling within the TME occurs in a temporally and spatially regulated manner, i.e. it is developed and sustained from one cell to its neighbors. Hence, this paracrine communication can barely be addressed experimentally. Therefore, the development of new cancer models, which more closely recreate the physiological conditions of the TME, combined with new imaging technologies appear as a key step towards expanding current knowledge on the TME and associated therapeutic vulnerabilities.

1.4a Bioengineering of 3D cancer models

The strong implications of heterocellular communication in the TME have motivated a reconsideration of the in vitro models employed so far. Conventionally, cancer models have been carried out in isolation and did not include the interactions with other cell types (stromal, immune cell types). Such models have been normally grown in "petri dish"-based cell cultures, meaning that cell-cell and cell-extracellular matrix (ECM) interactions were very limited.[48] Flat cell cultures not only compromise cell shape, motility, and polarity but also lack important secondary tissue-specific stimuli. One of the most meaningful differences is the mechanical environment: the stiffness of plastics used in 2D models is orders of magnitude higher than that sensed in soft tissues.[49] Additionally, the ECM of different tissues is capable of sequestering biomolecules, creating gradients of soluble factors, whereas in 2D models cell metabolites would diffuse freely into the culture medium.[50] Likewise, tissues present internal 3D structures that model many morphogenesis and development processes, including cancer, which cannot be mimicked in flat systems.[51,52] Arguably, the integration of a third dimension into cancer models, as depicted in **Figure 1.4a**, is crucial to bridge the gap between cell culture models and live tissues.

Novel cancer models proved essential in many cell studies, in which the generation of in vitro 3D cell cultures markedly affect cell behavior, in comparison with 2D assays.[53,54] For example, numerous studies have demonstrated the effect of matrix stiffness on metabolism regulation, by controlling the incorporation of L-arginine into either creatine or phosphocreatine, or by enhancing glycolysis.[55,56] Furthermore, based on their more physiological response against tumor treatments, sophisticated 3D models are also gaining significance as tools for anticancer drug discovery, while avoiding animal experimentation.[57-59]

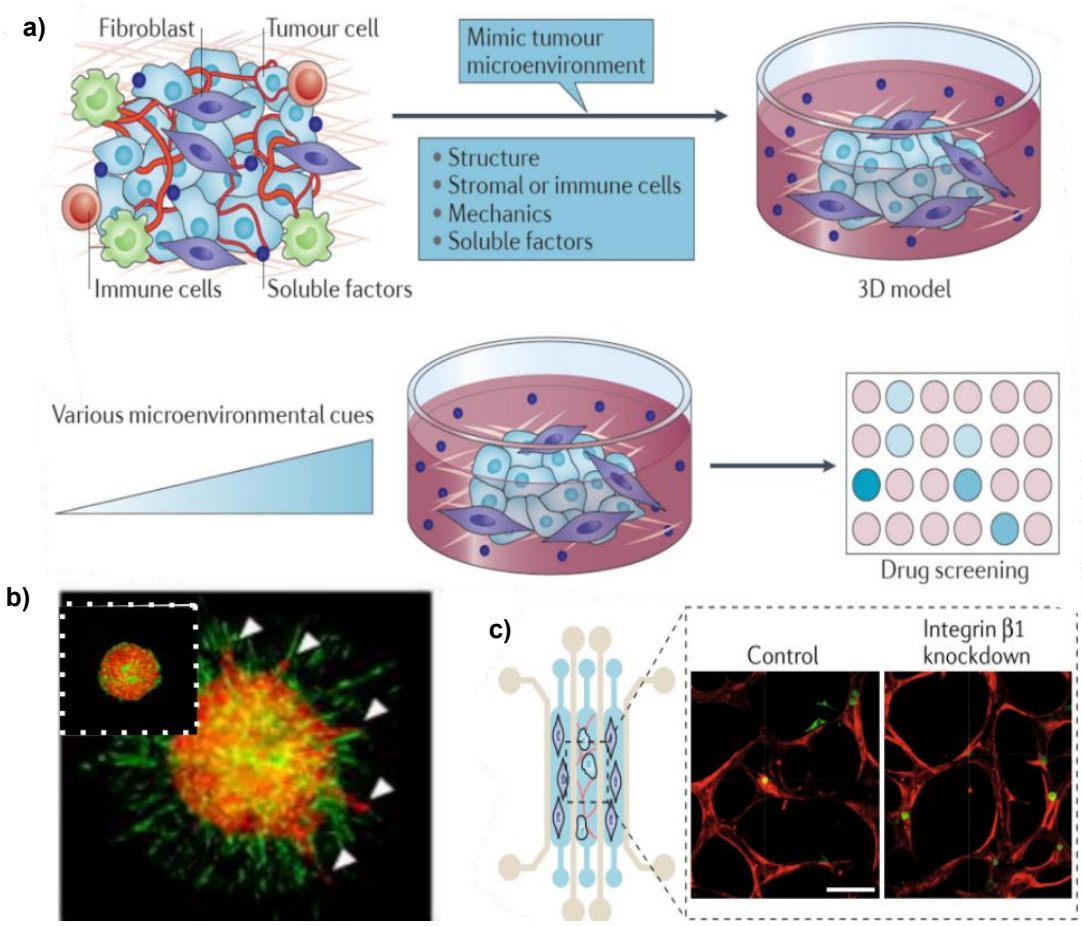

Figure 1.4. a) Engineered 3D in vitro models recreate, as closely as possible, cell-cell and cell -ECM interactions while enabling the recapitulation of diverse microenvironmental cues within human tumors. These 3D models are most likely to resemble the response against anti-cancer drugs in vivo, determining the impact of different cancer niches on the efficacy of a therapeutic approach. Modified from ref. 57. b) Tumor spheroid built by two different cell lines (green and red fluorophore), withe arrows point out cell migration in a collective mode. Adapted from ref. 60. c) Generation of a vascularized system to recreate metastasis in a cancer-on-a-chip device. Modified from ref. 69

With the aim of better mimicking the different features of the TME, different models for 3D cell culture have been deployed. Cellular spheroids represent the first attempt to tackle the third dimension in routine experimentation and are considered as the most simplified reductionist model (an illustrative spheroid is presented in **Figure 1.4b).** Cellular spheroids originate from the natural tendency of many cell types to form aggregates; they can also contain miscellaneous cell types (mono- or multicellular spheroids) or even include cells that have been previously isolated from patients.[60] In cases where cell proliferation is large enough, gradients of oxygen and nutrients are created through the spheroids, so that a necrotic core is formed (in a similar manner as it occurs within central regions of poorly vascularized tumors). Spheroids offer therefore a certain degree of heterogeneity in cell stages, which are of high interest in physiological models – proliferative cells are present in the outer layers while in the central core, cells tend to acquire a quiescent or dying phenotype.[61-63]

The next steps toward a better recreation of 3D tissue architectures endow the incorporation of natural and synthetic materials with the ability to mimic the extracellular matrix, those most routinely employed include: collagen, laminin, hyaluronic acid and the reconstituted basement membrane hydrogel (Matrigel). These 3D matrices not only offer an inherently high cytocompatibility, but also improved cell adhesion properties that facilitate the formation of self-organizing organotypic structures, the so-called organoids.[64-66] In a similar manner, recent studies have described that decellularized matrices from malignant tissues have the ability to recapitulate the features of native tumor.[67,68] Nevertheless, the quality control of these animal-based ECM is very arduous. Examples of such irreproducibility are the batch-to-batch variability, the high molecular complex composition, and the uncontrolled degradation of these materials. To overcome these limitations, synthetic biopolymers (i.e., human-made copies of biopolymers) can be customized to better fulfill the quality requirements. These artificial matrices can be otherwise 3D printed toward the fabrication of cellular scaffolds, which allow the replication of biological structures and higher reproducibility standards. Particularly, the direct printing of hydrogel inks has become a common approach that allows the design of porous, aqua-based environments, thus supporting nutrients and oxygen transportation across cell cultures. Similar models as the one presented in **Figure 1.4c** can also be perfused with nutrient-rich medium or anticancer drugs, incorporating essential biochemical and mechanical cues for a more realistic cell behavior.[69] Overall, the increasing reliability of current cancer models will enable more accurate in vitro studies of the TME, in which the tumor heterogeneity and its metabolism could be exhaustively interrogated.

1.4b Optical methods to monitor tumor environments

Owing to their physiological relevance, the 3D cell models presented in the previous section emerge as promising tools in cancer biology. However, the included third dimension is still a significant hurdle to successfully monitor cancer cells and their associated processes in situ, especially for the detection of small metabolites. Conventionally, laboratory assays for metabolomics studies have been carried out by means of techniques that entail tissue-destructive procedures, such as immunohistochemistry or liquid chromatography coupled to mass spectrometry (LC-MS). Even though a wide variety of components have been identified in biological fluids, both techniques cannot be deployed to assess different samples without irreversible damage; their ability to capture dynamic and heterogeneity profiles at the point of interest in 3D cell cultures is therefore limited. Other alternatives such as nuclear magnetic resonance (NMR) spectroscopy, which do not require elaborate sample preparation, are prone to low sensitivity and complex interpretation, in addition to bulky instrumentation and low

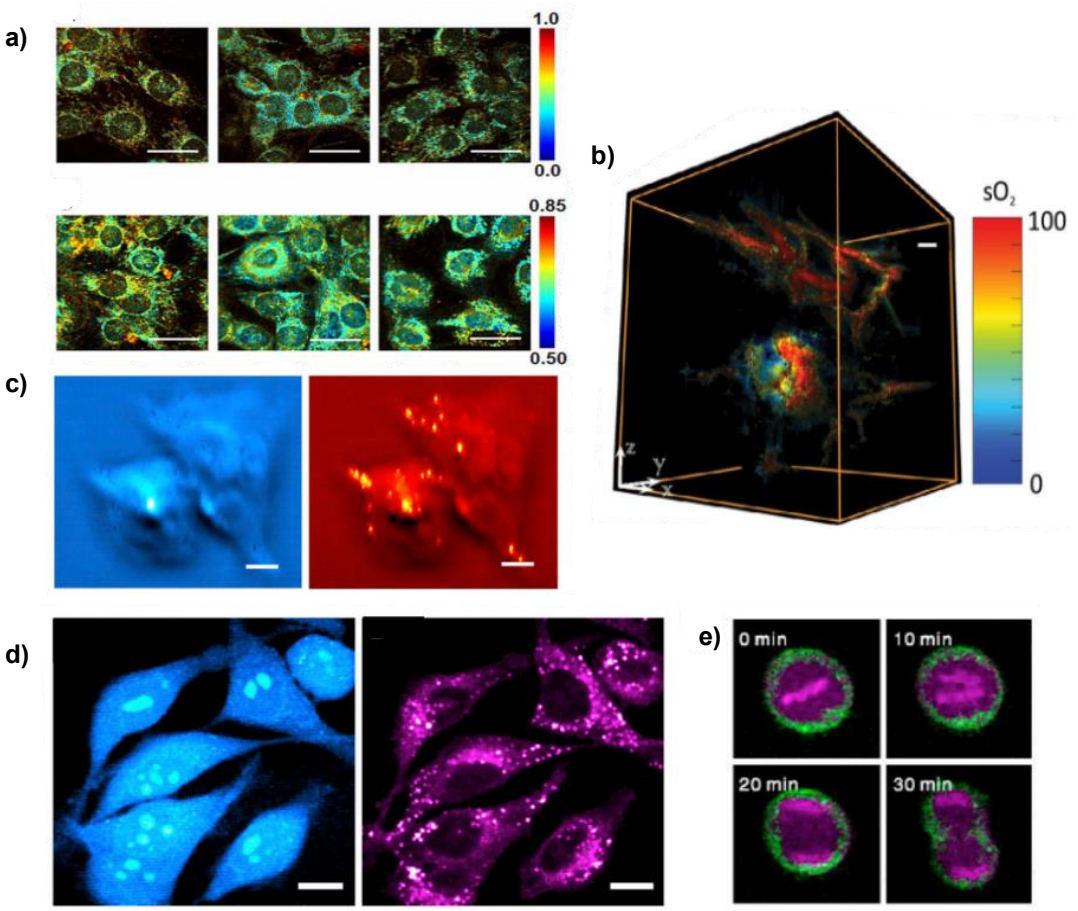

Figure 1.5. a) Intensity ratios between the endogenous fluorescence signals of NAD(P)H and FAD are employed as an optical source of contrast to evaluate metabolic alterations under various conditions. b) Multispectral and volumetric optoacoustic images of O_2 saturation of the tumor, showing the presence of a hypoxic core and its highly oxygenated feeding vessels. c) Metabolic imaging of lipid distribution at the single-cell scale, using mid-infrared photothermal microscopy. d) Metabolic imaging of single cells using Raman scattering microscopy, protein (blue) and lipid (violet) maps of living HeLa cells are shown. e) Time-lapse images of DNA and lipids in a HeLa cell during mitosis, directly monitored by Raman microscopy. Reproduced from ref. 70.

portability. In this context, optical methods, which use light to non-invasively probe matter, offer a valuable alternative to unravel the presence of specific metabolites with high spatiotemporal resolution, as well as representing a cheaper and faster approach.[70,71]

Among all available optical techniques, fluorescence microscopy arguably represents the most popular, commercially available technology to advance toward non-invasive monitoring of biological samples. The combination of a great variety of fluorescent probes with confocal techniques has been extensively employed to visualize the TME. Accordingly, the development of novel fluorescence probes with different binding properties has attracted widespread interest.[72] Thus, with the adequate molecule, this method is capable of capturing cancer and related metabolic processes in the TME, with high resolution and enhanced contrast. Examples of such fluorescence applications range from well-established live/dead assays and pH sensors to specific labelling of metabolic events.[73]

Unfortunately, confocal fluorescence microscopy still presents many drawbacks that limit the conditions under which growing cells and metabolic processes can be monitored in real time. Generally, the range of illumination lasers is only within visible wavelengths, which implies phototoxicity upon extended periods of illumination and restricts the penetration depth in 3D biological samples (over 1-2 mm for light in the visible).[74] Additionally, the strong dependency on fluorescent dyes, which may suffer from photobleaching and be degraded by chemicals inside the cells, impairs long-term TME monitoring.[75,76] With a view of avoiding the use of fluorescent dyes, the auto-fluorescence of FAD and NADH molecules has been traditionally utilized to screen different events in the TME, as represented in **Figure 1.5a**.[77] Nevertheless, auto-fluorescence from cells is typically weak and very unspecific in complex measurements, containing other naturally occurring fluorophores that emit in similar wavelengths. Label-free optical techniques with high specificity and sensitivity are thus in high demand, and therefore, non-traditional modalities are being explored for biological analysis.[78]

Among the different optical modalities, optoacoustic imaging is one of the emerging fields in TME imaging. Photoacoustic technology is a powerful approach that relies on the illumination of samples containing optical absorbers, and the subsequent conversion of light into acoustic waves due to thermoelastic expansion. The resulting acoustic signal is finally detected by an ultrasound sensor.[79,80] Label-free applications can be performed by optoacoustics thanks to its ability to detect and separate oxygenated and deoxygenated hemoglobin, melatonin, lipids, water and other optical absorbers. For instance, remarkable results are shown in **Figure 1.5b** for gradients of oxygenation along the TME, based on specific changes in the spectra from oxygenated to deoxygenated hemoglobin.[81] Nevertheless, while different responses were successfully monitored even at penetration depths over 2-3 cm, major difficulties arise when applying this label free mode at the cellular and subcellular levels.

Beyond fluorescence and optoacoustics, other label-free optical techniques that have attracted significant attention in the context of biomarker monitoring include mid-infrared (mid-IR) and Raman spectroscopies, which can specifically and directly detect a number of metabolites according to their vibrational modes, with sub-micrometer spatial resolution.[82] On one hand, mid-IR imaging/spectroscopy can be used to record vibrational information from histological samples, which was proven effective for fast cancer diagnosis.[83] However, the strong absorption of mid-IR radiation by water compromises its applications in routine monitoring of the TME in cancer models, and thus few examples can be found in the literature (see **Figure 1.5c)**.

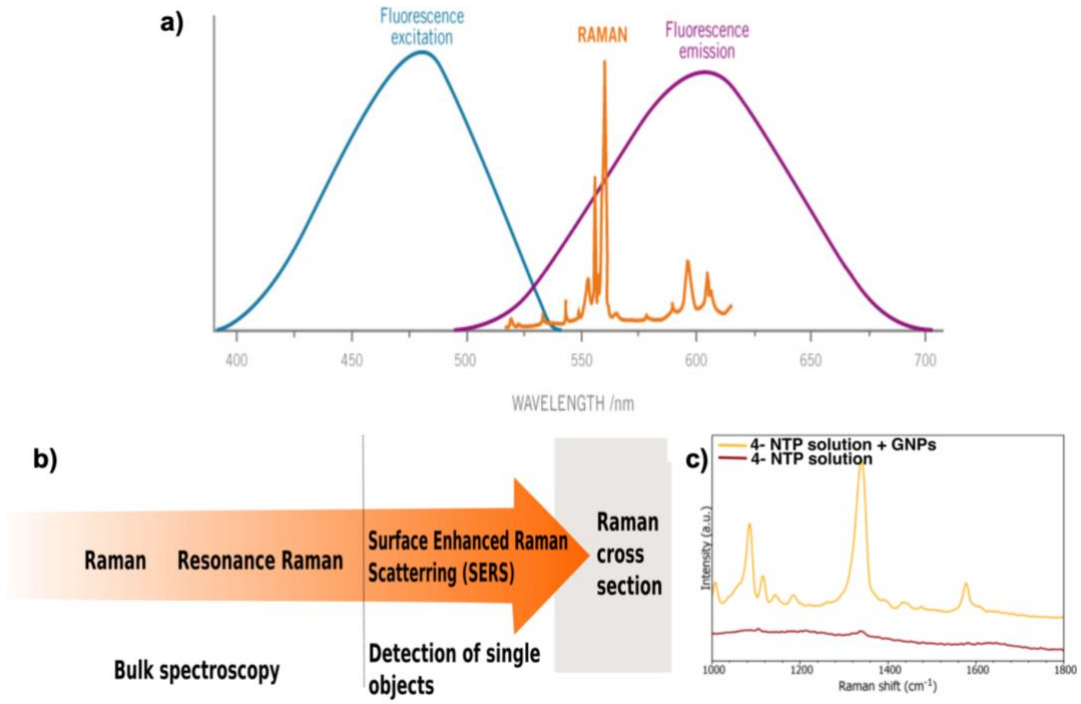

Figure 1.6. a) Fluorescence spectroscopy has a great sensitivity; however, it has limited chemical specificity, so that the distinction between signals from overlapping molecules is typically hard. Conversely, Raman spectroscopy offers information of vibrational states that facilitates multiplex detection, but the efficiency of the process is low; the differences in efficiency between Raman scattering and fluorescence are more than twelve orders of magnitude. b) Plasmonic nanoparticles are known to amplify Raman scattering, with sensitivities that render single molecule detection feasible. For example, in c), the enhancement effect can be observed in comparison with a control sample, i.e., without gold nanoparticles (AuNPs). A significant increase is observed in the SERS spectra enhanced by the presence of plasmonic nanoparticles. Adapted from ref. 87.

Alternatively, the inelastic Raman scattering cross section is very low for water. Hence, this technique can in principle be applied to record the vibrational fingerprints of metabolites under conditions with high water content (e.g., biofluids or intracellular compartments). This technology has shown the capability of imaging numerous metabolites in living cells, as has been reported through different studies about lipid composition and DNA imaging in cancer cells (see images in **Figure 1.5d**, 1.**5e**).[84-86] Unfortunately, the Raman cross sections for most metabolites are also very low and therefore the usual limits of detection in Raman spectroscopy are above 1 mM, posing a major drawback against monitoring of biomolecules at lower concentrations. Consequently, approaches toward increasing the intensity in Raman measurements have been implemented (for example, Resonance Raman and Tip-enhanced Raman). Arguably, the surface-enhanced Raman scattering (SERS) effect, a modality of Raman involving the presence of plasmonic materials, has been the most successful of these techniques, with plenty of examples of application in the biomedical field. Thanks to enhancement of the Raman signal when molecules are adsorbed onto metal surfaces, SERS is a very sensitive technique with the capacity to generating intensity values that exceed those recorded in Raman in many orders of magnitude, as depicted in **Figure 1.6**.[87-91] Since the main subject of this thesis consists of monitoring

metabolic alterations within tumor niches by SERS, we present in what follows an overview of the state of art in SERS technology.

1.5 Surface-enhanced Raman scattering: a powerful tool for biomedical sensing

The discovery of surface-enhanced Raman scattering (SERS) and its subsequent development and application is relatively recent. The initial evidence of the SERS effect was accidentally observed in the early 1970's, when Fleischmann and co-workers registered the Raman signal of pyridine on rough silver electrodes and obtained intensity values that exceeded by far those previously considered as standard.[92] Such unexpectedly high intensities were subsequently investigated and rapidly identified as a potential solution to the main hurdle in Raman spectroscopy: poor sensitivity hindering molecular detection at low concentrations.[93,94] On this account, understanding the basis of SERS to achieve suitable Raman signal enhancement became one of the major study subjects in the field. Although significant progress has been made toward mechanistic understanding, it remains under intense investigation -as explained below in section 1.5.b.

The ability to enhance the Raman signal of molecules adsorbed onto metal surfaces, while preserving the rich vibrational information, has raised further interest on SERS technology toward its integration into functional sensors. Recent advances in SERS have thus been closely connected to the development of purposely devised plasmonic structures toward optimal amplification of the Raman signal – up to 11 orders of magnitude.[95] The fabrication of such tailored substrates, typically comprising nanostructured metals such as gold or silver, has allowed the detection of extremely low molecular concentrations within multiple environments.[96] SERS thus comprises an extensive area of research ranging from theoretical studies of the mechanisms underlying signal enhancement, to the development of plasmonic substrates and devices for real-world applications. The wealth of progress in SERS technology has laid the foundation toward its future expansion into different disciplines (e.g., biomedicine, food safety, or environmental monitoring).[97,98] Notwithstanding, additional developments are still required to achieve a successful and reliable implementation, in which all the variables that influence the SERS performance are properly considered, especially in biomedical applications. Hereunder, the fundamentals of the technique are introduced; subsequently, the applications of SERS in biology, with special emphasis on the sensors design, are covered.

1.5a The Raman effect

When light interacts with matter, the oscillating electro-magnetic (EM) field of light perturbs the charge distribution in the matter, and therefore leads to different processes that involve the exchange of energy (see **Figure 1.7a**). Within this scenario, the incident photons may not only be absorbed, populating an excited state, but they may also interact with matter by distorting the electron cloud around the nuclei, this creates a higher energy state - typically referred as "virtual state". Indeed, the "virtual state" is not stable, and the photons are rapidly re-radiated, generating the phenomenon of light scattering. Such emitted photons can be classified in three different groups according to their derived frequencies: the first term and the most likely event, known as Rayleigh scattering, corresponds to the elastic dispersion of light that occurs when, upon the system being excited to a "virtual state", it drops back to the same initial state and thus the frequency of scattered light is equal to that of the incident beam. The second and third terms (Stokes and anti-Stokes Raman scattering) represent inelastic dispersion of light, in which the energy of the scattered photon is different from that of the incident one, as a result of a molecular vibration of the molecule.[99] This phenomenon provides characteristic information of the chemical nature of the illuminated molecules. However, the low probability of the involved spectroscopic events largely hindered their study; it has been estimated that only one in every 10^8 photons undergoes inelastic scattering upon light-matter interaction.[100] Therefore, the Raman effect is considered to be a very inefficient process, and the acquired intensities are typically lower than in the other light-matter interaction events, e.g. when the energy of the scattered photon is conserved – Rayleigh scattering – or real excited states are involved – as in fluorescence emission. The light path followed through these processes has been schematically depicted in **Figure 1.7b**.[101]

To better view all these elements, a complete Raman spectrum can be observed in **Figure 1.7c**. Excitation of molecules at their ground states typically leads to scattered radiation photons of lower energies than the original one (Stokes radiation), whereas excited states produce scattered photons of higher energy (anti-Stokes radiation). Noteworthily, molecules are mainly populating the ground state at room temperature (Boltzmann distribution), so that anti-Stokes scattering is a relatively rare event and its corresponding intensity is weaker than that of Stokes scattering, which explains why Stokes radiation is typically the main subject of study in Raman spectroscopy.[86] The wavenumber of the Raman response only depends on the vibrational energy states within the molecule and is not affected by the wavelength of the incident light source. The region of the Raman spectra captured by a spectrograph is called the spectral range and it typically displays vibrations within 0-4000 cm^{-1}.[102] In summary, the Raman signal involves the initial interaction of

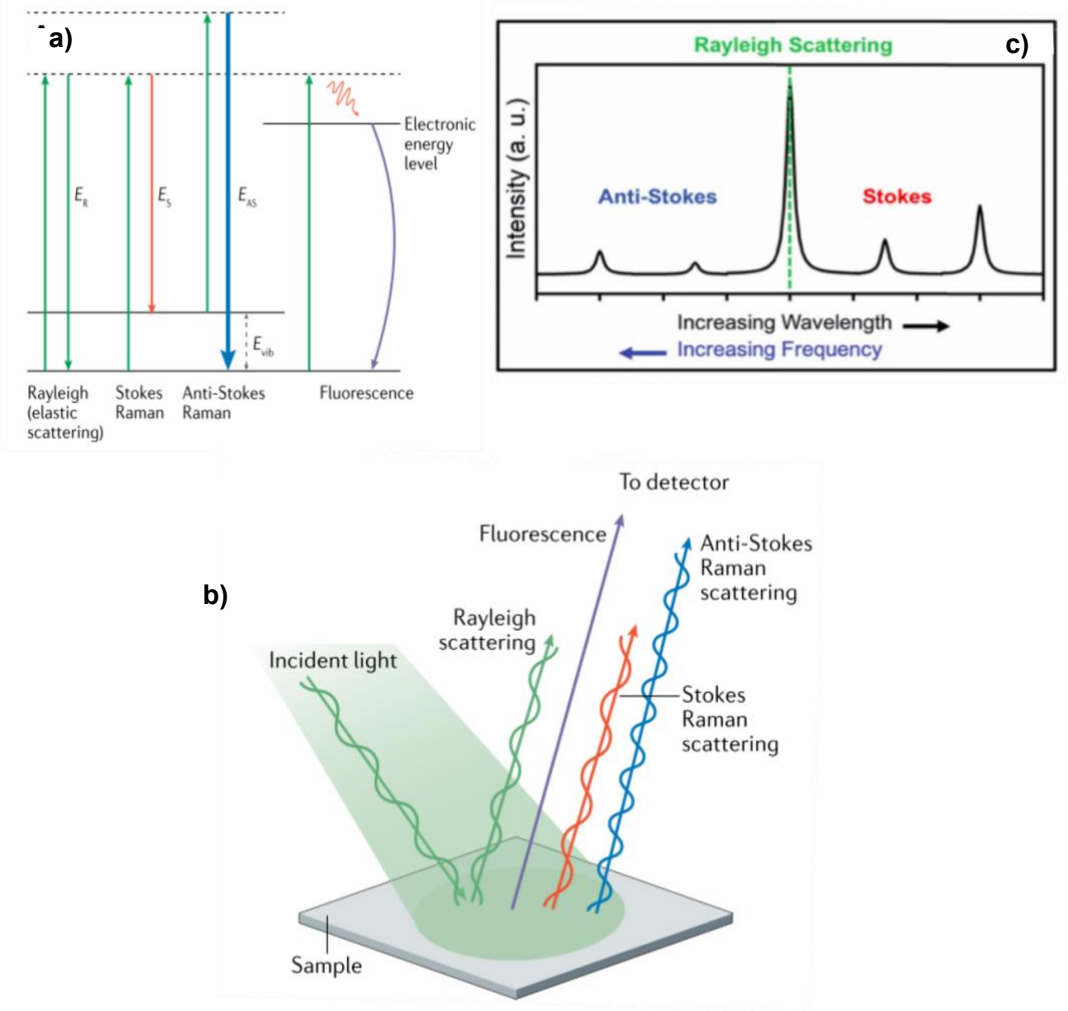

Figure 1.7. a) Energy diagram showing different physical phenomena resulting from light-matter interactions. b) Schematic of light scattering after laser irradiation on a sample surface. When photons interact with the sample, electrons are excited to virtual energy levels. Subsequently, they return to the original energy level by emitting a photon of light, known as Rayleigh scattering, or can undergo an energy shift and return to lower (stokes) or higher (anti-Stokes) energy levels, which is known as Raman scattering. Adapted from ref. 99 c) A typical Raman spectrum displaying the relative intensities of the different scattering processes. Modified from ref. 89.

an incident photon of frequency ω_{in}, which couples to an internal degree of freedom of the molecule (typically, a molecular vibration of frequency ω_{vib}), and finally reemission at different frequencies, ω_{em}. Equation 1 implies that a single excitation wavelength, which must not necessarily be in resonance with the molecule, is sufficient to obtain the entire spectrum.

$$\omega_{em} = \omega_{in} \pm \omega_{vib} \qquad (Equation\ 1)$$

In contrast with IR spectroscopy, where the dipole moment is crucial for the activity of the vibration, a Raman active vibration is determined by a change in polarizability during the vibration. Polarizability refers to the ease of distorting electrons from their original position.

Thus, the polarizability of a molecule decreases with increasing electron density, increasing bond strength, and decreasing bond length. Bonds with a weak dipole moment display a low IR activity, whereas they present a higher degree of polarizability that boosts Raman scattering. This effect explains the previously mentioned low Raman signal of water and its high activity in IR spectroscopy.[103] In addition, each chemical bond has a different Raman scattering wavelength; multiplexing detection of several molecules is therefore more easily achieved in Raman, which is very valuable for molecule identification. Both Raman features, low water activity and multiplexing capability, facilitate a great number of applications to extract biological information.[104,105]

However, it should be noticed that not all molecules display Raman scattering; this effect follows some selection rules that depend on molecular symmetry. Additionally, in the absence of a structured environment (e.g., in solution), the Raman process is considered a low probability phenomenon, quantified in terms of the optical cross-section (i.e., the value that describes the amount of incident light that is effectively converted into emitted photons) as 10^{31}-10^{29} cm^2/molecule.[106] In this context, different strategies are deployed to boost Raman signal. For example, Resonance Raman spectroscopy is a common approach for specific molecules in which the laser excitation frequency is close to the frequency of its electronic transition, enhancing thereby the Raman scattering intensity from these molecules by a factor of 10^2-10^6. In contrast to the limited application of resonance Raman (restricted to molecules absorbing within the excitation wavelength), the use of plasmonic materials to promote the enhancement of Raman intensities is most beneficial for general applications. The interactions of light with surface plasmons in metals generate additional effects, as detailed below, which allow an increase in the scattering cross-section of nearby molecules.[107,108]

1.5b Mechanisms of SERS

The ability of plasmonic materials to dramatically enhance the Raman effect renders SERS a very promising spectroscopic tool. Plasmonic properties of metallic materials are related to their electronic structure, presenting a strong delocalization of electrons.[109] Therefore, under a static electric field, the response of metallic materials depends on the behavior of such free electrons, which move toward the positive poles and create positive and negative net charges at the surface of the bulk. As a consequence, in those cases where the size of metallic particles is lowered to dimensions smaller than the wavelength of the incoming light, the light interacts with the conduction band electrons of nanoparticles (NPs) and induce a coherent oscillation.[110-112] This effect creates the so-called Localized Surface Plasmon Resonance (LSPR), which amplifies the

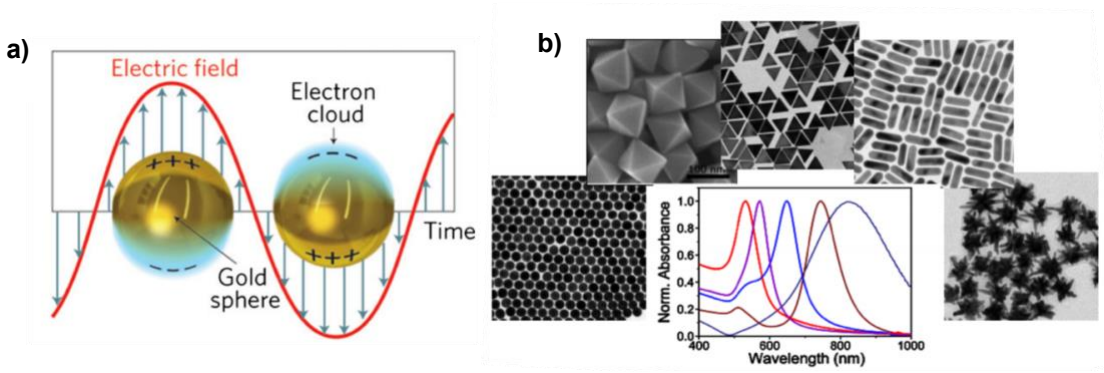

Figure 1.8. a) Localized surface plasmon resonance in metal nanoparticles. The scheme represents the oscillating electrons under influence of an electromagnetic radiation. b) UV-vis-NIR spectra and TEM images of gold nanoparticles with various morphologies, displaying LSPR tunability within the visible and NIR spectral range.

local electric field intensity, as represented in **Figure 1.8a**. Additionally, the LSPR resonance frequency, which results in a spectral peak, is strongly influenced by the type of metal, the size and the shape of the NPs (for instance, between gold nanospheres (AuNPs) and nanorods (AuNRs)) and their dielectric environment. Silver and gold nanoparticles are most commonly utilized for plasmonic materials because of their large LSPR extinction cross sections in the visible range, whereas for other metals, the LSPR is usually shifted to the UV regime; examples of nanoparticles with different size and shape, along with their corresponding LSPR are displayed in **Figure 1.8b**.[113,114]

Particularly for SERS spectroscopy, the intensity of the registered signal is proportional to the intensity of the local electric field around the molecule. In this manner, it is widely accepted that the enhancement of the local electric field by LSPR alters the polarizability of adsorbed molecules, which in turns leads to a higher probability of inelastic scattering events and increased Raman signals. Moreover, the scattered light from the molecule is also boosted by the plasmon resonance. Taken together, the sum of these effects in the SERS emission can be expressed as:

$$I_{SERS} = \alpha_{mol}^2 \times \left|E_p(\omega_{in})\right|^2 \times \left|E_p(\omega_{in} - \omega_{vib})\right|^2 \qquad \textit{(Equation 2)}$$

Where α_{mol} is the polarizability of the molecule, $E_p(\omega_{in})$ is the induced plasmonic electric field at the wavelength of the incident light, and $E_p(\omega_{in} \pm \omega_{vib})$ is the resulting electric field after the interaction with the probe molecule. In addition to the electromagnetic enhancement, the adsorbed molecule on the metallic surface can also get excited through charge transfer from the metal to the molecule, resulting in the phenomenon known as chemical enhancement. Another important aspect is that, the SERS intensity exhibits a strong power dependence on the distance to the metal surface, which clearly evidences that is a surface selective effect. As a consequence, SERS spectra

are determined by the orientation of the molecules relative to the surface, thus involving different spatial components of the molecule's polarizability.[87,115]

Quantification of the signal enhancement by a plasmonic structure, compared to the non-enhanced Raman signal, constitutes one of the main challenges of SERS spectroscopy. These measurements require the calculation of SERS and Raman signals per molecule (N_{SERS} and N_{Raman}), which in practice turns out to be experimentally complex, not only due to the requisite of precise control over the number of molecules per irradiated area, but also because a uniform distribution of plasmon resonances is needed to generate field enhancements of same magnitude (**Figure 1.9a**).[116,117] Consequently, the SERS Enhancement Factor (EF), which indicates the efficiency of the process, can be represented as:

$$EF = \frac{I_{SERS}/N_{SERS}}{I_{Raman}/N_{Raman}} \qquad (Equation\ 3)$$

Although effective SERS can be directly obtained from the electric field enhancement at a single NP, it is advantageous to involve a more sophisticated structure that, for instance, could consist of assembled nanoparticles with nanometer-sized gaps in between (so-called hotspots). These structures enable routinely reaching EF $\approx 10^5$-10^6. Whereas the EF of colloidal plasmonic nanospheres is in the order of 10^3, it may increase up to 10^{10}-10^{11} inside hotspots (represented in **Figure 1.9b**).[118-120] Such a dramatic increase in the EF is created as a result of a high confinement of the electromagnetic field at the junction of nanoparticles. When the distance between two nanoparticles is in order of their radius, the plasmon coupling between the nanoparticles leads to a higher electric field enhancement that impacts the SERS signal.[121] In this context, the fabrication of accurate plasmonic substrates with multiple hotspots is therefore of significance within the field of SERS sensing for medical and environmental applications (i.e., the structure of plasmonic substrates has an impact on the signal enhancement). Therefore, biosensing represents one of the main motivations for the intense research on fabrication, functionalization and self-assembly of metal nanoparticles.[122-124]

1.5c Plasmonic heating

In addition to their use for Raman signal amplification, plasmonic nanoparticles have been employed as heating agents to elevate the temperature of selected system under optical excitation. Plasmonic heating occurs as a result of the increased absorption cross-section of metallic nanoparticles at their plasmonic resonance.[125] On the basis of the amplified movement of electrons

at resonance, heating by Joule dissipation is largely amplified and temperature can thereby increase over 70ºC in solution. Notably, applications of plasmonic heating for cancer treatment are already in clinical trials, while expanding its implementation to other fields, such as drug delivery or gene-expression.[126,127]

1.5d SERS substrates, the main pillar for technological advancement

Based on their ability to concentrate the electric field within a nanoscale volume, a wide variety of metal nanoparticles and nanostructured films have been explored as plasmonic substrates. Such plasmonic structures may differ in composition, morphology, size, and spatial arrangement, pursuing higher enhancement factors and fine tuning of their LSPRs.[128,129] Many efforts are still being devoted to this line of research, through the fabrication of increasingly more sophisticated sensors, as introduced below.

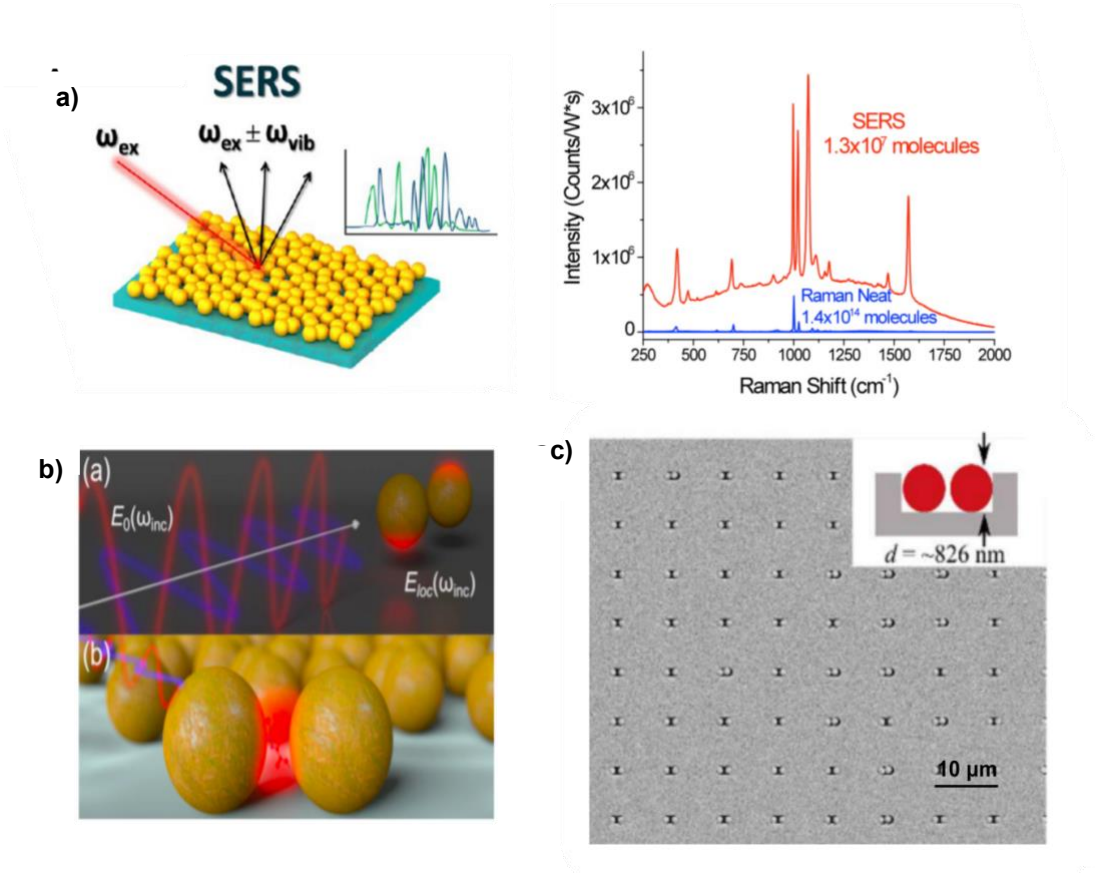

Figure 1.9. a) The formation of hotspots between gold nanoparticles that are separated by small distances leads the molecules located at this position to feel an increase of the electric field up to ten orders of magnitude. As a consequence, high EF can be achieved allowing for detection of small molecule concentrations. Adapted from ref 87. b) Schematic representation of the induced electric dipole in two gold spheres by an incident electromagnetic radiation (upper picture) and hotspot formation in the gap between two nanoparticles (lower picture). Adapted from ref 147. c) SEM image of assembled particles on PDMS templates. The inset displays a schematic side view of the traps. Adapted from ref 160.

Fabrication methods of efficient plasmonic substrates are typically classified within two categories (see **Figure 1.10a**). On one hand, i) nanostructures that are directly built on the surface of solid materials by top-down approaches, such as electron beam lithography.[130,131] On the other hand, ii) bottom-up approaches comprising nanoparticles that can be applied either in a colloidal dispersion or as various types of supported substrates.[132-134] Representative examples from these categories usually exhibit significant differences regarding homogeneity of the geometrical structure, instrumentation and know-how required for fabrication/synthesis, as well as the potential to scale-up.[135-140] Top-down approaches can yield high-resolution nanostructures on demand, but upscaling these processes is arduous and hinders their final integration into biosensors. Still, compelling examples of application of such top-down structures have endowed valuable biological information in some scenarios.[141-143] Of note, densely spaced nanometer-sized pillars have been used as SERS substrates with meaningful biological applications.[144] Upon exposure to a liquid sample and subsequent evaporation, metal-coated nanopillars can form clusters due to collective leaning of the pillars, thereby creating hotspots with high electric field enhancement. A reasonable uniformity in the arrangement of plasmonic structures renders such substrates attractive toward the detection of various biomolecules, such as beta amyloids in Alzheimer's disease or small oligonucleotides.[145,146]

Notwithstanding, most applications have been developed by using substrates that were obtained from colloidal nanoparticles, i.e. through the bottom-up approach. As already mentioned, the assembly of metal nanoparticles to build plasmonic substrates typically gives rise to plasmon coupling/hybridization effects, which are responsible for the greatest SERS enhancement factors.[147,148] Extremely high electric fields are confined within tiny interparticle distances in such structures; even if such hotspots represent a small fraction of the irradiated surface, they contribute most significantly to the recorded SERS signal.[149-151] Methods as simple as drop casting or precipitation of colloidal dispersions enable the production of plasmonic substrates with hotspots that can efficiently amplify the Raman signals from analyte molecules.[152,153] However, the nature and efficiency of hotspots are strongly dependent on the specific arrangement of the individual NPs, interparticle spacing and orientation. In turn, as has been commented, small changes or perturbations in electric field enhancement would drastically alter SERS intensity.[154-156] Unfortunately, the source of SERS sensitivity may also be the predominant cause of poor reproducibility. Sensors based on random nanoparticle aggregation typically exhibit a poor performance, in terms of repeatability and reproducibility. Hence, the development of procedures aiming to define ordered nanoparticle architectures has acquired strong relevance. In this context, self-assembly processes can be used to drive dispersed colloidal systems into organized structures or patterns, without additional guidance.[157] By tailoring the functionality and affinity between

nanoparticles and solvent, the self-assembly of individual components in solution can be precisely controlled.[158-160] On the other hand, nanostructured templates can also be used to guide the self-assembly of nanoparticles into predefined structures, ranging from thin films (2D) to colloidal crystals or supercrystals (3D).[161-163] Custom-made molds of different materials, such as poly-dimethylsiloxane (PDMS) or poly-methylmethacrylate (PMMA) (**Figure 1.9c**), have been used to trap NPs inside the wells of the template, thereby forming organized nanostructures that replicate the mold.[164] As a result, not only a higher reproducibility in the SERS signal can be obtained, but also an exquisite definition of the optical response toward achieving maximum enhancement.[165] Purposely matching the plasmon resonances of the substrate to the incoming

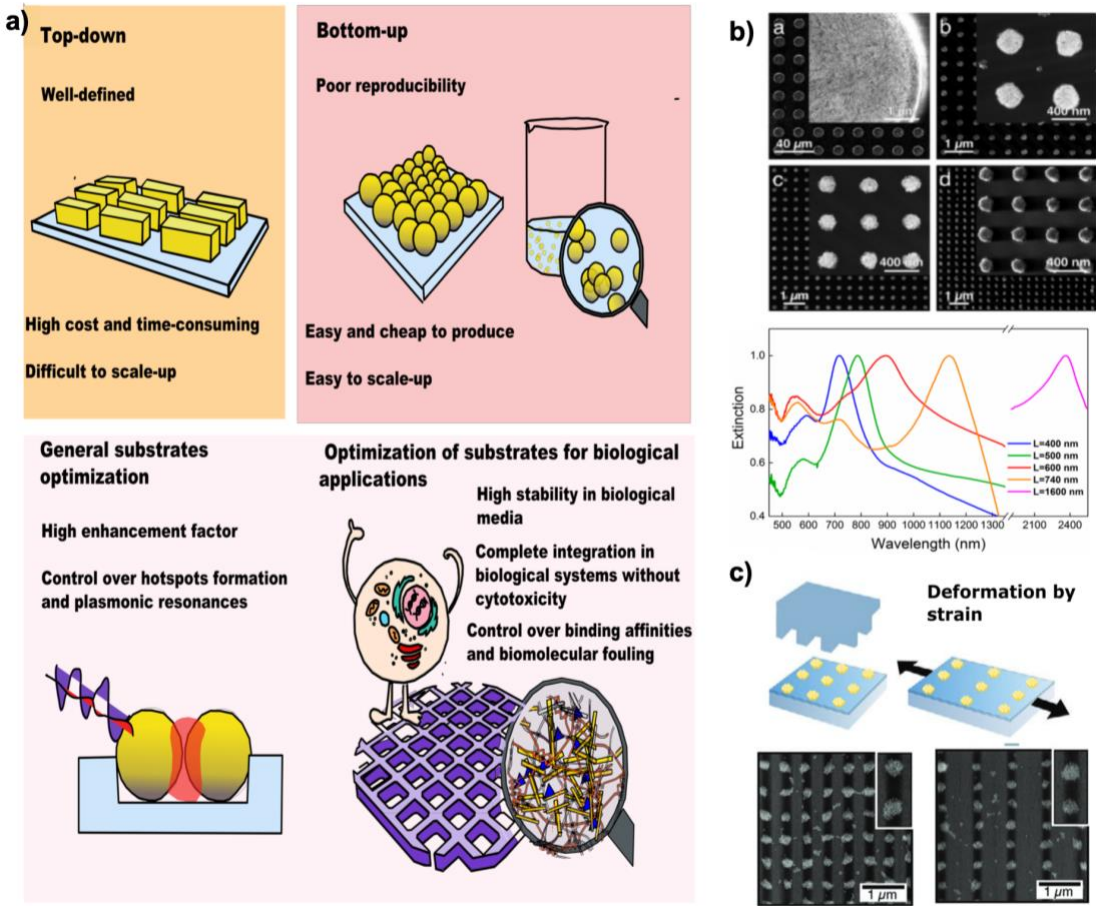

Figure 1.10. a) Schematic representation of top-down and bottom-up fabrication of plasmonic substrates: top-down strategies yield metal nanostructures with high resolution; bottom-up strategies provide the simplicity and scale-up possibilities of colloidal nanoparticles. The scalability of bottom-up substrates, obtained by self-assembly of individual nanoparticles, makes them appealing as sensors in biological applications. As the main responsible component for SERS signal enhancement, optimization of plasmonic substrates is constantly being reported. General improvements are mainly oriented to increasing the enhancement factor, i.e. generating more intense electric fields around nanoparticles, or to better control hotspot formation and plasmonic tunability. Substrates aimed for biological applications have additional requirements (stability, biocompatibility, etc.) due to their constant interaction with biological media. Current efforts attempt to maximize substrate stability and full sensor integration, while minimizing the undesired perturbations induced during the acquisition of SERS spectra. Controlling the binding affinity between nanoparticles and biomolecules may also facilitate detection at low concentrations, even when other biomolecules are present at orders-of-magnitude higher. b) Engineering plasmonic nanoparticle arrays to tune lattice plasmon modes, i) SEM images of AuNP arrays with variation of the distance between NP clusters. Reproduced with permission from ref. 176 ii) Extinction spectra of different AuNP cluster arrays displaying variations in the lattice parameter (L). i) Adapted from ref. 175. b) The optical response of AuNP arrays can be dynamically tuned by applying extension or contraction forces onto flexible plasmonic substrates. Reproduced with permission from ref. 177.

photon (laser) wavelength is of especial interest for biomedical applications. SERS spectra should be collected upon irradiation with an excitation wavelength that is harmless to cells and, ideally, that can propagate through tissue, typically within the first transparency window, between 680 nm and 920 nm.[166,167] Modulation of plasmon resonances has been primarily realized by varying either the chemical nature or the morphology of the nanostructured plasmonic component (the NP).[168-170] Other strategies can be used to dynamically dictate plasmon resonances, based on application of external electrical,[171] magnetic,[172] thermal,[173] or light stimuli.[174] In a recent example, a template-assisted self-assembly process was used to obtain hierarchical nanostructured substrates, comprising square arrays of hexagonally packed AuNP clusters. These highly ordered substrates generate intense lattice plasmon resonances, which can be engineered by tuning geometrical parameters, in particular the lattice parameter or separation distance between AuNP clusters.[175] This effect was deployed to extend the spectral window, from the visible to the near-infrared, without variation of the NP building blocks (**Figure 1.10b**).[176] In a variation of the same method, the plasmonic substrates were transferred onto elastomeric PDMS-based supports, thereby allowing real-time modification of the lattice plasmon resonances by extension or contraction of the substrate, upon application of macroscopic strain (**Figure 1.10c**).[177]

During the development of this thesis, diverse methods for the fabrication of plasmonic substrates have been used. On this account, we describe hereafter some additional features of SERS sensors for biomedical applications (**Figure 1.10a**), especially when in situ measurements are targeted.

1.5e Monitoring of biomolecules and optimization of substrates for biological applications

1.5e I) Label-free and indirect SERS

Label-free SERS applications – also known as direct SERS – have been primarily used for the detection of small molecules, ranging from relevant metabolites in bacteria or eukaryotic cells to diverse neurotransmitters and drugs.[178-183] Although macromolecules can also be detected by SERS, larger biomolecules (usually about 10^{-2} μm) are formed by combinations of the same building blocks, thus registering very similar SERS spectra among members of the same class (e.g., proteins or DNA).[184-187] As a consequence, specific labels must be incorporated for accurate SERS identification. The resulting indirect approaches, in which the detected SERS signal comes from a probe or label, typically involve traditional immunoassays or oligo-microarrays and allow the detection of both proteins and nucleic acids.[188,189] Regarding indirect sensors, SERS probes

must comprise, in their simplest version, a noble metal (again, typically Au or Ag) nanoparticle and a monolayer of reporter molecules acting as fingerprint labels. The background produced by biological fluids can be systematically reduced by carefully designing the nanoprobe (e.g., by including a protecting outer shell) and including washing steps. Thus, only few modifications are required on conventional assays – for instance, a SERS probe instead of a fluorescence dye – and therefore indirect sensors are closer to being integrated into commercial diagnostic tools.

In contrast to macromolecules, the characteristic fingerprint of small metabolites can be recorded and distinctly recognized by SERS, as long as these species can get in contact with the plasmonic substrate.[190] Each chemical bond has a characteristic vibrational frequency, which determines a Raman scattering wavenumber, so that SERS barcodes can be defined for specific metabolites, thereby facilitating their identification in complex mixtures. Thus, small molecules of interest are more likely to be accurately traced in the absence of a tag, reporter, or indicator molecule. The number of molecules ultimately adsorbed onto the plasmonic structure is otherwise controlled by their surface affinity, which in combination with the identity of the sample – its Raman scattering cross-section – determine the SERS spectral fingerprint.[191] However, it should also be taken into account that the high complexity of biological samples, containing a wide and dynamic range of biomolecules that interfere with each other as well as interacting with the plasmonic substrate, may compromise the prediction of SERS spectra resulting from the contribution of individual components (**Figure 1.11a**). In other words, quantification of analytes, especially in complex

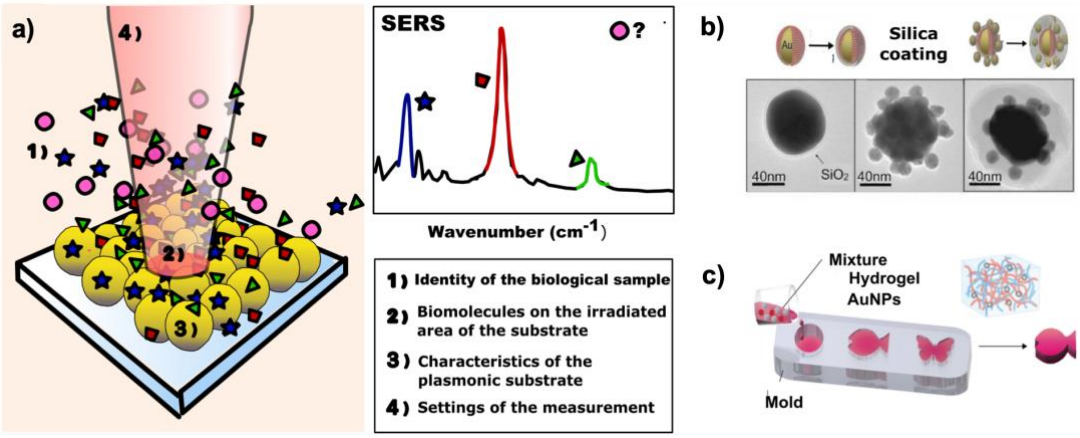

Figure 1.11. a) The SERS spectra of biological samples are defined by a combination of four main parameters, as indicated in the scheme. The nature of the interrogated biomolecules and the plasmonic substrate control the interplay between both components, via their binding affinities. Biomolecules present within the irradiated area of the plasmonic substrate, as well as their intrinsic Raman cross sections, will eventually determine the recorded signal. Biomolecules that adsorb weakly onto the metallic surface, or which feature low Raman cross-sections, are unlikely to be detected (pink dots in the scheme). Optimization of plasmonic substrates and measurement settings are commonly required for an efficient response of SERS platforms in various label-free scenarios. b) Silica coating of dispersed AuNPs and overcoating of core-satellite superstructures, as observed in the TEM images of 3D self-assembled plasmonic superstructures. Silica shells enhance the stability and allow SERS monitoring of molecules in the proximity. Reproduced with permission from ref. 198. c) Hydrogel polymerization in a colloidal dispersion result in polymeric nanocomposites that can be adapted to different shapes, while enhancing the stability of the embedded nanoparticles. Reproduced from ref. 204.

biological mixtures, poses a great challenge, as the composition of the analytes adsorbed on the metallic structure might largely differ from those observed in solution.[192]

Additionally, unlike indirect measurements, the sensitivity of label-free experiments cannot be modulated by either varying the type or the number of reporter molecules (e.g., increasing dye concentration or other attempts with different reporter molecules). On this account, the Raman intensity in label-free approaches can only be boosted by optimizing the plasmonic nanostructures for different scenarios – apart from modifying instrument settings, common for all types of Raman measurements. Overall, optimization of plasmonic substrates to the specific running application is an early-stage strategy that can significantly improve SERS performance for monitoring of biomolecules. The following characteristics have been considered as the most relevant requirements for biomedical applications, and thus will be accordingly discussed through this thesis: i) efficiency must be maintained within biological media, along extended exposure times; ii) the sensor must be fully integrated at the point of interest, while avoiding the presence of external cytotoxic agents that could harm living tissues; and iii) the possibility of controlling binding affinities between biomolecules and the surface of the plasmonic substrate. While bearing these concepts in mind, the development of plasmonic substrates should always pursue a sensitivity matching the specific problem at play, in this case typically the physiological concentration range of the biomolecules of interest.

1.5e II) Stability and reproducibility in biological media

When plasmonic nanostructures are immersed in biological media, their physicochemical properties may dramatically change over time.[193] The combination of multiple factors affects the stability of the system through degradation of surface functionalities, adsorption of proteins and other (bio)molecules, and even morphological changes.[194,195] These unwanted effects lead to changes in the plasmonic response and are prone to providing misrepresentative and irreproducible results. This phenomenon particularly hinders the use of nanoparticles in suspension as SERS sensors in biomedicine. Uncontrolled aggregation of nanoparticles occurs frequently within biological environments, resulting in the formation of clusters with largely variable SERS signal enhancements. Several studies have demonstrated that biological media can also induce the release of ions from metallic particles, which in turn would modify their biocompatibility.[196] Hence, it should be stressed that significant differences can be found in SERS platforms, between their ideal behavior in pure water and their practical performance in biological media, even if compared with commonly used isotonic buffers (e.g., phosphate-buffered saline (PBS) solution). The stability and performance of substrates should be carefully evaluated in the selected biological environment under defined characteristics, as an intermediate step prior to the real-world, uncontrolled sample. Different approaches have been explored to enhance the

biological stability of Au NPs, such as coating with silica or polymer shells (**Figure 1.11b**).[197,198] However, enhanced stability may come at the expense of compromising the interaction of nanoparticles with the target molecules, thus hindering the SERS monitoring performance.[199] On the other hand, the routine approach of immobilizing the nanoparticles on solid supports (mainly glass, silicon or quartz, but even paper), is still sustaining innovation, with novel strategies based on sophisticated functionalization, to strongly retain the nanoparticles.[200-202] Recent approaches have succeeded in tailoring polymer nanocomposites to function as SERS substrates displaying highly tunable features. Plasmonic nanocomposites are formed by embedding plasmonic nanoparticles in polymeric materials, which further assist in preserving the intrinsic properties of the NPs in complex environments (**Figure 1.11c**).[203] The polymer would act by enhancing the robustness of the whole sensor over time, while preventing aggregation of the embedded nanoparticles[204], fostering a new generation of SERS sensors.[205-208]

1.5e III) Integration into biological systems

Key features of direct SERS are its noninvasive character and the absence of sample preparation requirements, which promise the potential of implementing measurements at the point of care (POC), i.e., in the clinic or in cell cultures and artificial organs. However, conventional substrates are rigid and thus barely adaptable to be used in the context of arbitrary surfaces, which dramatically limits their complete integration into real-world scenarios. In this context, emerging SERS substrates formed by materials with soft, flexible, and transparent features, open new avenues toward exploiting a rapid screening of analytes within the complexity of real systems. Specifically, flexible substrates allow an intimate contact with surfaces that are barely accessible to rigid platforms, to an extent that the sensor could provide real-time information on nearby perturbations in a non-invasive manner. Multiple strategies have been explored to adhere metal nanoparticles on different flexible supporting materials, including polymers, graphene oxide, and nanowires.[209-211] In a recent example of application, a paper-based substrate in which NPs were adsorbed onto cellulose fibers, was used to collect human tears directly from the human eye and monitor their composition by SERS. Of particular interest are applications of flexible plasmonic materials as wearable devices – also known as smart tattoos – to monitor biomolecules directly in the body, while maintaining their plasmonic activity under various deformations (**Figure 1.12a**). These SERS substrates can be attached onto the skin or other body surfaces (e.g. the eyeballs), to uncover the presence of trace molecules in sweat and other biofluids (**Figure 1.12b**).[212-214] By engineering such plasmonic tattoos with microneedle structures, one could even register intradermal information by SERS.[215,216] It should be emphasized that, the precise thickness control and high transparency of SERS platforms are also required for in situ measurements, as laser radiation must penetrate through the support layer before reaching the

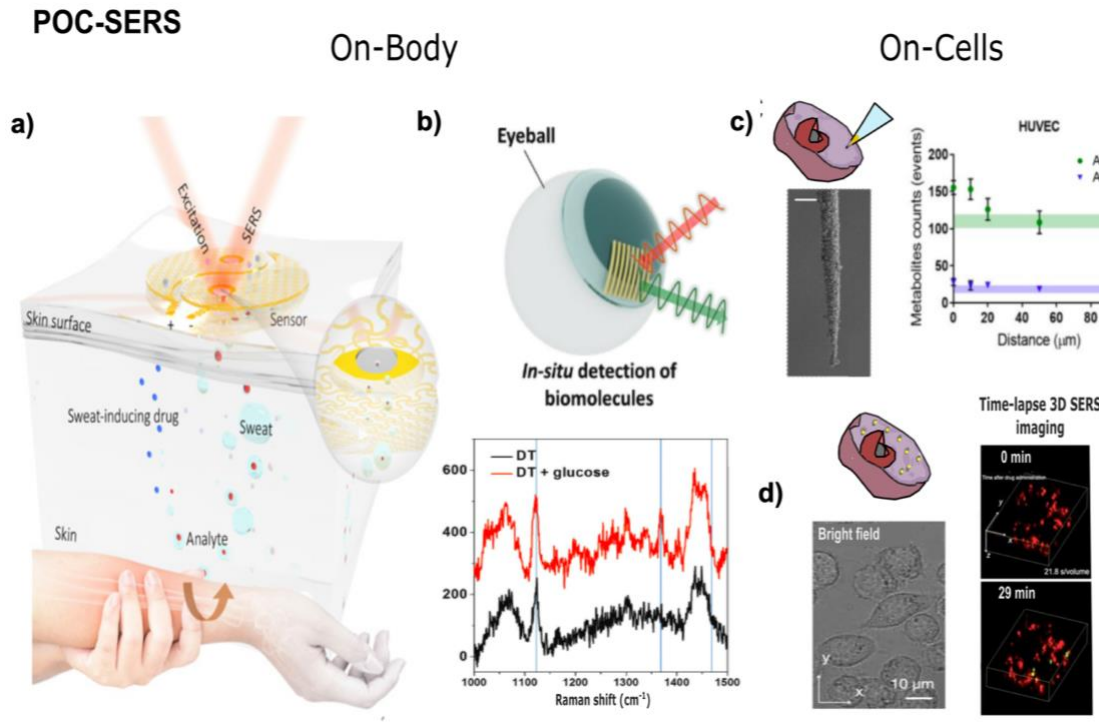

Figure 1.12. On body SERS: a) Sketch depicting the operation of smart tattoos to monitoring metabolites in sweat. The flexible character of the sensor enables a suitable implant on human skin, therefore contacting the sensor with the secreted sweat and the present metabolites. Adapted with permission from ref. 212 b) Schematic illustration of a contact lens combined with a plasmonic nanostructure for their final integration on an eyeball via transfer printing for in situ detection. Comparison of SERS spectra before and after dropping glucose solution over the contact lens sensor, showing their ability to register changes in glucose concentration. Adapted with permission from ref. 214. c) On-cell sensors to monitor intracellular environments by plasmonic nanopipettes, with similar shapes as that in the SEM image (scale bar 1 μm), which can pierce cell membranes with minimum invasion or be used to monitor extracellular gradients in the vicinity of cells, as plotted for ATP and ADP gradients, or in d) by internalized nanoparticles, which typically accumulate into vesicles such as lysosomes. For the example represented in (d), the SERS images are reconstructed from two SERS spectral windows at two different times; the red color is the average Raman intensity from endogenous molecules, and the green color is the average SERS intensity from 1960 to 2010 cm^{-1} assigned to the traced lysosomal drug, which contains alkyne peaks. Adapted with permission from refs. 225, 221.

sample. Recent outcomes underpin such devices as powerful tools to bridge the daunting gap between personalized therapy and real-time tracking of meaningful molecules inside the body.

Other plasmonic substrates have also been devised to evaluate cell activity, adapting their design to the challenges imposed by the interaction with cells and other biological components. Initial attempts involved the internalization of nanoparticles by cells, followed by the acquisition of SERS spectra.[217-219] Unfortunately, this strategy often results in considerably altered cell behavior, as well as low control on nanoparticle stability and location within the ever-changing intracellular milieu. Recent studies have explored the specific interactions between certain nanoparticles and cells, to achieve more uniformly enhanced SERS signals at defined locations, e.g. at cell membranes or in lysosomes (**Figure 1.12d**).[220,221] However, nanoparticle internalization itself is a complex step, due to a strong dependence on variable aspects, such as the state of the cells or the specific cell line.[222] Therefore, as intracellular particles are the source of signal enhancement, significant differences are typically encountered in SERS spectra from different cells. To

overcome this source of inaccuracy, the development of plasmonic nanotips or nanopipettes proved essential to interrogate intracellular compartments with minimum cell damage, while controlling the nature of the plasmonic components. Optimization of the geometry in plasmonic tips, so that nanoparticles are adhered on the surface, facilitates cell membrane penetration toward intracellular compartments in living cells (**Figure 1.12c**).[223,224] The position of the plasmonic component is thus directed by an external operator, thereby reducing signal variability. This setup configuration was also used to monitor metabolites in extracellular media, capturing the formation of chemical gradients near cells. [225]

The integration of efficient Raman signal enhancers inside cellular environments is still in its infancy, which impairs capturing by SERS real-time events that influence cell responses and phenotypes. SERS-active cell culture platforms, which combine different 3D-culture strategies (mentioned in section 1.4a) with the presence of plasmonic NPs, are foreseen to provide devices where different cell types, or even human explants (e.g., organoids grown from patients' tumor samples) could be monitored over extended growth times, with high spatial resolution. As a result, multiple drugs could be tested on these 3D-printed devices, revealing by SERS how the cultured cells would respond to each treatment.

1.5e IV) Control over biomolecular fouling

Notwithstanding the ability of SERS toward the direct detection of different analytes at the point of interest, various steps of sample enrichment and isolation are frequently used prior to collecting SERS measurements.[226,227] Such prerequisites (e.g. centrifugation or chromatography purification) are typically needed to remove, or significantly lessen, those components in biological media that may end up masking the presence of target analytes/biomarkers.[228] The adsorption of biomolecules at high concentrations will likely block the access of target analytes to plasmonic hotspots. Such a competitive adsorption drastically impairs the enhancement of the Raman signal, and, as a result, reduces assay sensitivity and specificity. It is well-known that native proteins in biofluids are particularly prone to binding onto bare nanoparticles, forming a so-called protein corona that yields substantial background noise and may even prevent the detection of smaller-size biomolecules.[229] Numerous strategies have been developed to modulate the adsorption of biomolecules onto metallic surfaces, according to their size and charge, and even to regulate such interactions upon controlled exposure of the substrate. At this point, it is important to emphasize that SERS is a surface technique: a SERS spectrum consistently results from the interaction between sample and substrate, so that, for the same biofluid sample, substrates with different characteristics – e.g., built by nanoparticles stabilized with different ligands (citrate, CTAB…) – may yield different spectra.

A common approach to prevent competitive binding while promoting the interaction of target analyte molecules with the sensor, involves tailoring the surface chemistry of the plasmonic substrate. Many studies have reported the conjugation of plasmonic surfaces with different molecular probes that specifically react with target analytes, which are then detected through the vibrational changes derived from their interaction with pre-tagged Raman reporters.[230-231] Although such sensor configurations successfully repress signal overlap, they are limited to the established target-binding entities and can hardly be applied to multiplexed detection, a valuable feature of SERS sensing (**Figure 1.13a**). A broadly applied strategy involves self-assembled monolayers (SAM) to promote the binding of analytes with distinct affinities to SERS sensors, as well as minimizing non-specific fouling.[232-235] SAM functionalized substrates lead to specific physicochemical interactions between plasmonic substrates and different sample constituents.

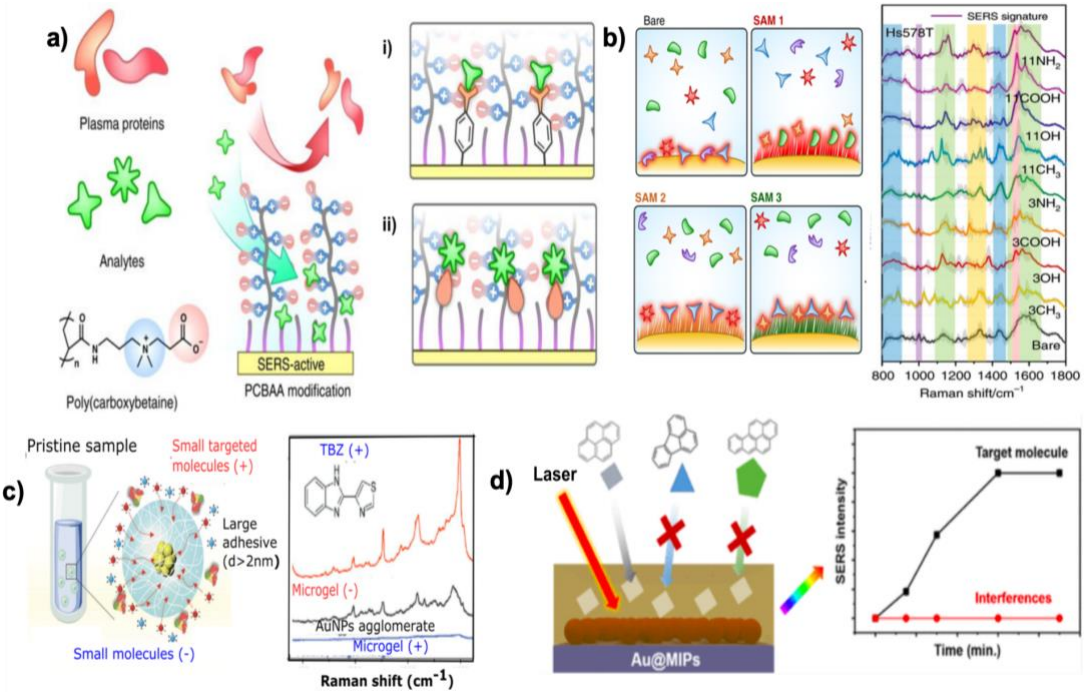

Figure 1.13. a) Schematic representation of the modification of plasmonic surfaces to prevent fouling by proteins present in biological media, while containing: i) probes that interact directly with the target analyte, thereby inducing changes in SERS spectra upon reaction of probe molecules with target analytes; or ii) molecules that only promote the adsorption of a group of targets with similar characteristics. Adapted with permission from ref. 233. b) Arrays of plasmonic surfaces for label-free SERS with different self-assembled monolayers which are depicted as brushes on the metallic support with different color, they also reflect that different sets of metabolites interact with the metallic surface as a function of the deposited SAM. Hence, a range of molecular interactions takes place within complex biological media at each sensor unit, where mildly selective SERS enhancement of the constituents yields multiplex spectral datasets. Such an effect occurs in the presented example with the cell lysates of Hs578Tfibroblast, obtaining a SERS spectrum from each functionalized Au-nanopillars. This strategy enables to diversify the detectable SERS signatures in complex environments and to increase data dimensionality. Reproduced with permission from ref. 235. c) Schematic view of the direct detection of small, charged molecules using oppositely charged hydrogels containing nanoparticles. Large proteins and like-charged molecules are excluded from the microgel, while concentrating oppositely charged molecules, thereby facilitating SERS monitoring. Adapted from ref. 239. d) Creation of a plasmonic platform based on the combination of a molecularly imprinted polymer (MIP) thin film with Au nanoparticle (NPs) assemblies. While the MIP allows the trapping of diverse polycyclic aromatic hydrocarbons close to the Au surface, which endows high specificity, the plasmonic NPs enhance the molecule's Raman signal. Reproduced from ref. 240.

The nature of the selected SAM can be tailored to either improve specificity – the SAM may enhance binding of a small subset of molecules[233] – or to increase multiplexing capabilities.[235] For the latter approach, SAMs providing interactions with low specificity (i.e., biasing the diffusion of molecules with different properties to the proximity of the SERS substrate) can be used to diversify the SERS signatures that can be detected in complex environments (**Figure 1.13b**).

Other strategies exploit the coverage of plasmonic substrates with shells made of porous materials that exclude the diffusion of certain molecules toward the plasmonic nanostructure. In these systems, contamination of the plasmonic surface with macromolecules can be avoided by using mesoporous silica coatings, which block the transport of molecules larger than their pore size. [236,237] In addition to size-dependent impediments, hydrogel networks can additionally facilitate the selective penetration of molecules by electrostatic attraction, while preventing like-charged small molecules from reaching the plasmonic component (**Figure 1.13c**).[238,239] In particular, the combination of molecularly imprinted polymers (MIPs) – which can be devised to display a predetermined selectivity for a given analyte – with SERS sensors, has attracted a significant interest (**Figure 1.13d**).[240-242] In this configuration, the MIP layer renders the SERS substrate capable to deliberately capture target molecules on the surface with high selectivity, thereby mimicking the interaction between bioreceptors and antibodies.

1.6 SERS in cancer metabolomics and artificial intelligence diagnosis

By the implementation of the described procedures, different studies have already been used for the interrogation of dynamic events in cancer cells by SERS. Examples of such SERS applications for cancer metabolomics range from the description of an increase in phenylalanine metabolites upon plasmonic hyperthermia,[217] to the recording of metabolic gradients in the vicinity of malignant cells.[225] Furthermore, a recent study has efficiently reported the use of plasmonic nanostructures (also named as goldnanofève, GNF) to monitor metabolic alterations across tumor xenografts by SERS, thus representing an illustrative example of SERS for direct visualization of unknown metabolic events in the TME.[143] By a careful characterization of the signals obtained from cryo-sections of different tissues, key metabolites in TME as glutathione or hypotaurine were identified. Remarkably, a subsequent SERS analysis of different tumors models revealed that increases in the levels of glutathione correlated with more aggressive cancer metastases (see **Figure 1.14a** for more details).

Although SERS has been applied to monitor different metabolites in cancer, direct addition of such complex biological media to the plasmonic substrate – even if it has been thoroughly optimized – may yield spectra from which individual biomarkers cannot be easily identified. Indeed, as reported above, most successful studies are typically based on the screening of biomarkers displaying both high affinity to gold surfaces and high Raman cross-sections (e.g. metabolites with aromatic moieties). When such molecules are present in the probe solution, they can readily dominate the SERS signal, meaning that they significantly mask the presence of other analytes and their characteristic fingerprint is directly peeked in the spectra. This screening – even at very low concentrations – is then largely advantageous, therefore reaping the reward of fast SERS monitoring. This is the underlying explanation for reporting similar biomolecules in most ongoing applications; many other studies have demonstrated that SERS can become extremely effective for monitoring nitrogenous bases (mainly purine derivatives or the nicotinamide ring), aromatic amino acids or metabolites (tryptophan, phenylalanine, tyrosine, and their derivative products, and thiolated biomolecules (glutathione, cystine, among others).[243,244] In contrast, the identification of other metabolites with implications in cancer disease (e.g., lactate) has not been achieved in similar terms so far. In this scenario, there are studies that, instead of following specific metabolites, seek to determine whether a patient is prone to suffer from cancer, using SERS analysis of selected biofluids, even including additional predictions such as the stage of the tumor and its origin. [245-247] In this approach, classical methods for SERS spectral analysis, in which one can establish a direct correlation between vibrational peaks and the presence of individual metabolites, are no longer sufficient. Chemometrics methods have therefore emerged as a reliable and attractive alternative to be combined with SERS monitoring.[248]

A wide range of multivariate statistic and machine learning methods are currently available in order to decipher the optically rich and complex information contained in SERS spectra from cancer patients. To this end, multiple strategies from a 'simple' exploratory analysis, up to machine learning methods have been exploited for pattern-recognition and classification of SERS spectra.[249,250] In particular, unsupervised methods, such as principal component analysis (PCA), are routinely used in the first place, to visualize variations in the data by compressing the dimension of the SERS spectra – with minimal loss of information. Remarkably, by applying PCA, one could discover hidden patterns in the original data with a minimal intervention (see **Figure 1.14b**). [251-253] However, as long as labeled data have been available, which is most of the cases in normal and altered conditions (e.g. classification of normal vs cancer cells), supervised algorithms displayed more reliable results in SERS analysis. Indeed, the separation of classes is

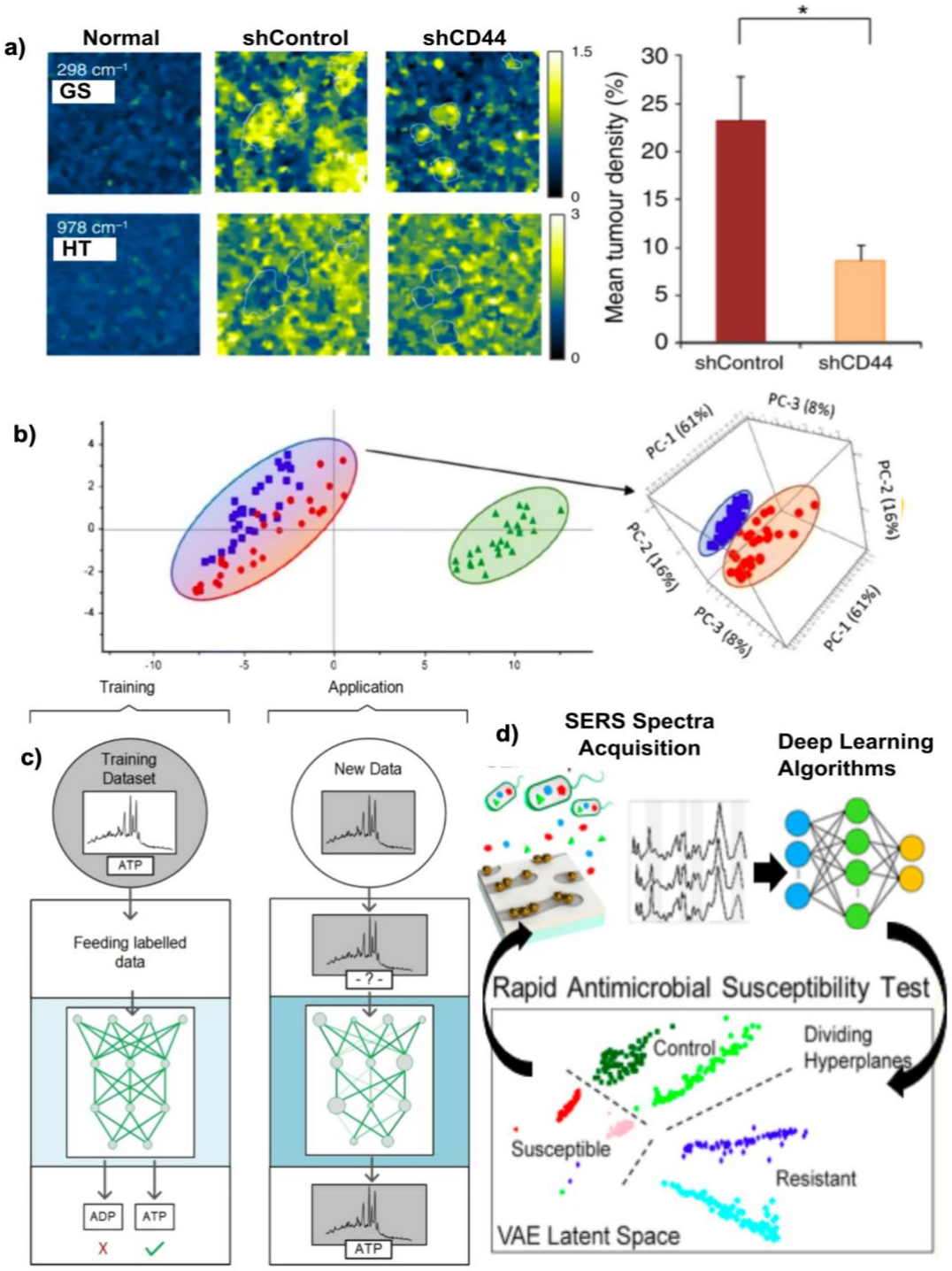

Figure 1.14. a) Results registered by gold-nanofève (GNF) substrates, imaging large-area of different cancer tissue cryosections (5 µm thickness) by SERS. Three representative sections of tissues with (Normal and shControl) or without (shCD44) CD44 expression, a molecule stabilizing and controlling cystine transporter (xCT), are shown. SERS mappings were generated in every case using the characteristic peaks of glutathione (GS) and hypotaurine (HT) at 298 and 897 cm-1, respectively. These results uncover a decrease in glutathione density in tumor lacking CD44, which was exhibited along with significant tumor suppression. Adapted from ref 143 b) Unsupervised analysis of SERS spectra obtained from 3 bacterial strains of *L. monocytogenes*, revealing the existence of different clusters and their proximity. Strains represented by blue and red dots express a similar set of genes, while the green strain does not. Reproduced with permission from ref. 253. c) General scheme of a supervised, machine-learning-based approach to analyze data sets of SERS spectra. Training data are initially fed into the system to create the network. At this point, each data point is labeled according to its metabolites or condition. Subsequently, unknown data are classified by the trained machine-learning algorithm. Reproduced from ref. 254. d) VAE latent space depicting the SERS spectra of bacteria after a rapid antimicrobial susceptibility test. The method achieves a high accuracy (≥95%) in discriminating between susceptible versus resistant to antibiotic cultures. Modified from ref. 256.

not a trivial task because even spectra from the same class may vary significantly, for example, one single metabolite might exhibit different spectra depending on its molecular orientation on the SERS substrate. On the other hand, vibrational features from various classes are likely to overlap, which would hamper the visualization of the classes by simple unsupervised analysis (**Figure 1.14c**).[254] Sophisticated machine learning methods, such as deep-learning, have been widely adopted by the SERS community as a result of being less harsh for a non-specialist and the accessibility of a large number of friendly and open-source frameworks and libraries- unlike other strategies based on shallow artificial neural networks, which requires extensive feature extraction procedures to avoid over-fitting.

Noteworthily, a number of studies have robustly shown the ability of deep learning to outperform other approaches, due to intrinsic interpatient variability, without needing feature extraction or reduce-variance methods, as illustrated, for example, in the analysis of spectra obtained from exosomes of cancer patients.[255] In this direction, a recent study about drug susceptibility in bacteria cultures(**Figure 1.14d**),[256] applied a machine learning method that was not only able to discriminate the metabolome after treated from untreated with an accuracy greater than 95%, but also to identify some important vibrational features in the outputs obtained from the trained model. Still, there is a need for new methodologies to open the access to high-throughput approaches for SERS screening in cancer diagnosis, which will be relevant towards its clinical translation. In this way, combining a portable SERS spectrometer with deep-learning was proved effective as a point-of-care automatic approach, making an early diagnosis of multiple diseases in a single run, including breast cancer.[257] A combination of supervised and unsupervised analysis were implemented along this thesis, so that all the information contained in the SERS spectra could be fully explored.

In the following chapters, we will address the topics presented throughout this introduction, with the intention to expand the application of SERS sensors for upcoming challenges in biomedical disciplines, but particularly, in cancer metabolomics for 3D cell environments.

1.7 References

1. Faguet, G. B. A brief history of cancer: Age-old milestones underlying our current knowledge database. *Int. J. Cancer* **136**, 2022–2036 (2015).
2. Weinberg, R. A. How cancer arises. *Sci. Am.* **275**, 62–70 (1996).
3. Gupta, G. P. & Massagué, J. Cancer Metastasis: Building a framework. *Cell* **127**, 679–695 (2006).
4. Palmer, Adam C. *et al*. Combination cancer therapy can confer benefit via patient-to-patient variability without drug additivity or synergy. *Cell* **171**, 1678-1691 (2017)

5. Hanahan, D. & Weinberg, R. A. The hallmarks of cancer. *Cell* **100**, 57–70 (2000).
6. Hanahan, D. & Weinberg, R. A. Hallmarks of cancer: The next generation. *Cell* **144**, 646–674 (2011).
7. Hanahan, D. Biological Hallmarks of cancer: New dimensions. *Cancer Discov.* **12**, 31 - 46 (2022)
8. Mellman, I., Coukos, G. & Dranoff, G. Cancer immunotherapy comes of age. *Nature* **480**, 480–489 (2011).
9. Byeon, H. K., Ku, M. & Yang, J. Beyond EGFR inhibition: Multilateral combat strategies to stop the progression of head and neck cancer. *Exp. Mol. Med.* **51**, 1-14 (2019).
10. Capdeville, R., Buchdunger, E., Zimmermann, J. & Matter, A. Glivec (ST1571, imatinib), a rationally developed, targeted anticancer drug. *Nat. Rev. Drug Discov.* **1**, 493–502 (2002).
11. Balkwill, F. R., Capasso, M. & Hagemann, T. The tumor microenvironment at a glance. *J. Cell Sci.* **125**, 5591–5596 (2012).
12. Wang, M. *et al.* Role of tumor microenvironment in tumorigenesis. *J. Cancer* **8**, 761–773 (2017).
13. Barcellos-Hoff, M. H., Lyden, D. & Wang, T. C. The evolution of the cancer niche during multistage carcinogenesis. *Nat. Rev. Cancer* **13**, 511–518 (2013).
14. Egeblad, M., Nakasone, E. S. & Werb, Z. Tumors as organs: Complex tissues that interface with the entire organism. *Dev. Cell* **18**, 884–901 (2010).
15. Hanahan, D. & Coussens, L. M. Accessories to the crime: Functions of cells recruited to the tumor microenvironment. *Cancer Cell* **21**, 309–322 (2012).
16. Joyce, J. A. & Pollard, J. W. Microenvironmental regulation of metastasis. *Nat. Rev. Cancer* **9**, 239–252 (2009).
17. Hinshaw, D. C. & Shevde, L. A. The tumor microenvironment innately modulates cancer progression. *Cancer Res.* **79**, 4557–4567 (2019).
18. Fane, M. & Weeraratna, A. T. How the ageing microenvironment influences tumour progression. *Nat. Rev. Cancer* **20**, 89–106 (2020).
19. Liu, T., Zhou, L., Li, D., Andl, T. & Zhang, Y. Cancer-associated fibroblasts build and secure the tumor microenvironment. *Front. Cell Dev. Biol.* **7** (2019).
20. Calon, A., Tauriello, D. V. F. & Batlle, E. TGF-beta in CAF-mediated tumor growth and metastasis. *Semin. Cancer Biol.* **25**, 15–22 (2014).
21. Fang, M., Yuan, J., Peng, C. & Li, Y. Collagen as a double-edged sword in tumor progression. *Tumor Biol.* **35**, 2871–2882 (2014).
22. Sapudom, J. *et al.* The phenotype of cancer cell invasion controlled by fibril diameter and pore size of 3D collagen networks. *Biomaterials* **52**, 367–375 (2015).
23. Plou, J. *et al.* From individual to collective 3D cancer dissemination: roles of collagen concentration and TGF-β. *Sci. Rep.* **8**, 12723 (2018).
24. Binnewies, M. *et al.* Understanding the tumor immune microenvironment (TIME) for effective therapy. *Nat. Med.* **24**, 541–550 (2018).
25. Lyssiotis, C. A. & Kimmelman, A. C. Metabolic Interactions in the Tumor Microenvironment. *Trends Cell Biol.* **27**, 863–875 (2017).
26. Pavlova, N. N. & Thompson, C. B. The Emerging Hallmarks of Cancer Metabolism. *Cell Metab.*

23, 27–47 (2016).

27. Arruabarrena-Aristorena, A., Zabala-Letona, A. & Carracedo, A. Oil for the cancer engine: The cross-talk between oncogenic signaling and polyamine metabolism. *Sci. Adv.* **4**, 1–12 (2018).
28. Brandon, F., Solmonson, A. & DeBerardinis, R.J. Metabolic reprogramming and cancer progression. *Science **368**.* eaaw5473 (2020).
29. Pavlova, N.N. *et al.* The hallmarks of cancer metabolism: Still emerging, *Cell Metab.* **34**, 1-23 (2022).
30. Lyssiotis, C. A. & Nagrath, D. Metabolic reprogramming and vulnerabilities in cancer. *Cancers* **12** (2020).
31. Platten, M., Wick, W. & Van Den Eynde, B. J. Tryptophan catabolism in cancer: Beyond IDO and tryptophan depletion. *Cancer Res.* **72**, 5435–5440 (2012).
32. Triplett, T. A. *et al.* Reversal of indoleamine 2,3-dioxygenase–mediated cancer immune suppression by systemic kynurenine depletion with a therapeutic enzyme. *Nat. Biotechnol.* **36**, 758–764 (2018).
33. Nguyen, N. T. *et al.* Aryl hydrocarbon receptor negatively regulates dendritic cell immunogenicity via a kynurenine-dependent mechanism. *Proc. Natl. Acad. Sci.* **107**, 19961–19966 (2010).
34. Qian, S. *et al.* IDO as a drug target for cancer immunotherapy: Recent developments in IDO inhibitors discovery. *RSC Adv.* **6**, 7575–7581 (2016).
35. Munn, D. H. & Mellor, A. L. IDO in the tumor microenvironment: Inflammation, counter-regulation, and tolerance. *Trends Immunol.* **37**, 193–207 (2016).
36. Blay, J., White, T. D. & Hoskin, D. W. The extracellular fluid of solid carcinomas contains immunosuppressive concentrations of adenosine. *Cancer Res.* **57**, 2602–2605 (1997).
37. Antonioli, L. *et al*. Immunity, inflammation and cancer: a leading role for adenosine. *Nat Rev Cancer* **13**, 842–857 (2013)
38. Chen, J. *et al.* Inosine released from dying or dead cells stimulates cell proliferation via adenosine receptors. *Front. Immunol.* **8**, (2017).
39. Hernandez, C., Huebener, P. & Schwabe, R. F. Damage-associated molecular patterns in cancer: A double-edged sword. *Oncogene* **35**, 5931–5941 (2016).
40. Michaud, M. *et al.* Autophagy-dependent anticancer immune responses induced by chemotherapeutic agents in mice. *Science.* **334**, 1573–1577 (2011).
41. Di Virgilio, F. & Adinolfi, E. Extracellular purines, purinergic receptors and tumor growth. *Oncogene* **36**, 293–303 (2017).
42. Palanichamy, K. *et al.* Methionine and kynurenine activate oncogenic kinases in glioblastoma, and methionine deprivation compromises proliferation. *Clin. Cancer Res.* **22**, 3513–3523 (2016).
43. Barekatain, Y. *et al*. Homozygous MTAP deletion in primary human glioblastoma is not associated with elevation of methylthioadenosine. *Nat. Commun.* **12**, 4228 (2021)
44. Madden, E. C., Gorman, A. M., Logue, S. E. & Samali, A. Tumour cell secretome in chemoresistance and tumour recurrence. *Trends Cancer*. **6,** 489-505 (2020).
45 van Schaik, T. A., Chen, K. S. & Shah, K. Therapy-induced tumor cell death: Friend or foe of immunotherapy? *Front Oncol.* **1,** 678562 (2021).

46 Yan, G., Elbadawi, M., & Efferth, T. Multiple cell death modalities and their key features. *World Acad. Sci*. **2**, 39-48 (2020).

47 Medina, C. B.*et al* Metabolites released from apoptotic cells act as tissue messengers. *Nature* **580,** 130–135 (2020).

48. Kleinman, H. K., Philp, D. & Hoffman, M. P. Role of the extracellular matrix in morphogenesis. *Curr. Opin. Biotechnol.* **14**, 526–532 (2003).

49. Butcher, D. T., Alliston, T. & Weaver, V. M. A tense situation: forcing tumour progression. *Nat. Rev. Cancer* **9**, 108–122 (2009).

50. Li, R. *et al.* Macrophage-secreted TNFα and TGFβ1 influence migration speed and persistence of cancer cells in 3D tissue culture via independent pathways. *Cancer Res.* **77**, 279–290 (2017).

51. Friedl, P. & Alexander, S. Cancer invasion and the microenvironment: Plasticity and reciprocity. *Cell* **147**, 992–1009 (2011).

52. Rozario, T. & DeSimone, D. W. The extracellular matrix in development and morphogenesis: A dynamic view. *Dev. Biol.* **341**, 126–140 (2010).

53. Doyle, A. D., Carvajal, N., Jin, A., Matsumoto, K. & Yamada, K. M. Local 3D matrix microenvironment regulates cell migration through spatiotemporal dynamics of contractility-dependent adhesions. *Nat. Commun.* **6**, 8720 (2015).

54. Gjorevski, N., Piotrowski, A. S., Varner, V. D. & Nelson, C. M. Dynamic tensile forces drive collective cell migration through three-dimensional extracellular matrices. *Sci. Rep.* **5**, 11458 (2015).

55. Papalazarou, V. *et al.* The creatine–phosphagen system is mechanoresponsive in pancreatic adenocarcinoma and fuels invasion and metastasis. *Nat. Metab.* **2**, 62–80 (2020).

56. Park, J. S. *et al.* Mechanical regulation of glycolysis via cytoskeleton architecture. *Nature* **578**, 621–626 (2020).

57. Gu, L. & Mooney, D. Biomaterials and emerging anticancer therapeutics: engineering the microenvironment. *Nat. Rev. Cancer* **16**, 56–66 (2016).

58. Boussommier-Calleja, A., Li, R., Chen, M. B., Wong, S. C. & Kamm, R. D. Microfluidics: A new tool for modeling cancer–immune interactions. *Trends in Cancer* **2**, 6–19 (2016).

59. Pampaloni, F., Reynaud, E. G. & Stelzer, E. H. K. The third dimension bridges the gap between cell culture and live tissue. *Nat. Rev. Mol. Cell Biol.* **8**, 839–845 (2007).

60. Carey, S.P. *et al*. Leading malignant cells initiate collective epithelial cell invasion in a three-dimensional heterotypic tumor spheroid model. *Clin. Exp. Metastasis* 30, 615–630 (2013)

61. Kopanska, K. S., Alcheikh, Y., Staneva, R., Vignjevic, D. & Betz, T. Tensile forces originating from cancer spheroids facilitate tumor invasion. *PLoS One* **11**, e0156442 (2016).

62. Haeger, A., Krause, M., Wolf, K. & Friedl, P. Cell jamming: Collective invasion of mesenchymal tumor cells imposed by tissue confinement. *Biochim. Biophys. Acta - Gen. Subj.* **1840**, 2386–2395 (2014).

63. Jeong, S. Y., Lee, J. H., Shin, Y., Chung, S. & Kuh, H. J. Co-culture of tumor spheroids and fibroblasts in a collagen matrix-incorporated microfluidic chip mimics reciprocal activation in solid tumor microenvironment. *PLoS One* **11**, e0159013 (2016).

64. Shin, Y. *et al.* Microfluidic assay for simultaneous culture of multiple cell types on surfaces or within hydrogels. *Nat Protoc* **7**, 1247–1295 (2014).
65. Kenny, P. A. *et al.* The morphologies of breast cancer cell lines in three-dimensional assays correlate with their profiles of gene expression. *Mol. Oncol.* **1**, 84–96 (2007).
66. Nguyen-Ngoc, K.-V. *et al.* ECM microenvironment regulates collective migration and local dissemination in normal and malignant mammary epithelium. *Proc. Natl. Acad. Sci.* **109**, E2595–E2604 (2012).
67. Yi, H. G. *et al.* A bioprinted human-glioblastoma-on-a-chip for the identification of patient-specific responses to chemoradiotherapy. *Nat. Biomed. Eng.* **3**, 509–519 (2019).
68. Piccoli, M. *et al.* Decellularized colorectal cancer matrix as bioactive microenvironment for in vitro 3D cancer research. *J. Cell. Physiol.* **233**, 5937–5948 (2018).
69. Sontheimer-Phelps, A., Hassell, B. A. & Ingber, D. E. Modelling cancer in microfluidic human organs-on-chips. *Nat. Rev. Cancer* **19**, 65–81 (2019).
70. Ntziachristos, V., Pleitez, M. A., Aime, S. & Brindle, K. M. Emerging technologies to image tissue metabolism. *Cell Metab.* **29**, 518–538 (2019).
71. Clemens, G., Hands, J. R., Dorling, K. M. & Baker, M. J. Vibrational spectroscopic methods for cytology and cellular research. *Analyst* **139**, 4411–4444 (2001).
72. Drummen, G. P. C. Fluorescent probes and fluorescence (microscopy) techniques-illuminating biological and biomedical research. *Molecules* **17**, 14067–14090 (2012).
73. Ueno, T. & Nagano, T. Fluorescent probes for sensing and imaging. *Nat. Methods* **8**, 642–645 (2011).
74. Hong, G., Antaris, A. L. & Dai, H. Near-infrared fluorophores for biomedical imaging. *Nat. Biomed. Eng.* **1**, 0010 (2017).
75. Lippincott-Schwartz, J., Snapp, E. & Kenworthy, A. Studying protein dynamics in living cells. *Nat. Rev. Mol. Cell Biol.* **2**, 444–456 (2001).
76. Berezin, M. Y. & Achilefu, S. Fluorescence lifetime measurements and biological imaging. *Chem. Rev.* **110**, 2641–2684 (2010).
77. Liu, Z. *et al.* Mapping metabolic changes by noninvasive, multiparametric, high-resolution imaging using endogenous contrast. *Sci. Adv.* **4**, eaap9302 (2018).
78. Andreana, M., Sentosa, R., Erkkilä, M. T., Drexler, W. & Unterhuber, A. Depth resolved label-free multimodal optical imaging platform to study morpho-molecular composition of tissue. *Photochem. Photobiol. Sci.* **18**, 997–1008 (2019).
79. Stoffels, I. *et al.* Metastatic status of sentinel lymph nodes in melanoma determined noninvasively with multispectral optoacoustic imaging. *Sci. Transl. Med.* **7**, 317ra199 (2015).
80. Ron, A., Deán-Ben, X. L., Gottschalk, S. & Razansky, D. Volumetric optoacoustic imaging unveils high-resolution patterns of acute and cyclic hypoxia in a murine model of breast cancer. *Cancer Res.* **79**, 4767–4775 (2019).
81. Reber, J. *et al.* Non-invasive measurement of brown fat metabolism based on optoacoustic imaging of hemoglobin gradients. *Cell Metab.* **27**, 689-701.e4 (2018).
82. Baker, M. J. *et al.* Using Fourier transform IR spectroscopy to analyze biological materials. *Nat.*

Protoc. **9**, 1771–1791 (2014).

83. Bai, Y., Zhang, D., Li, C., Liu, C. & Cheng, J. X. Bond-selective imaging of cells by mid-infrared photothermal microscopy in High Wavenumber Region. *J. Phys. Chem. B* **121**, 10249–10255 (2017).
84. Cheng, J. X. & Xie, X. S. Vibrational spectroscopic imaging of living systems: An emerging platform for biology and medicine. *Science* **350**, aaa8870 (2015).
85. Yorucu, C. *et al.* Raman spectroscopy detects melanoma and the tissue surrounding melanoma using tissue-engineered melanoma models. *Appl. Spectrosc. Rev.* **51**, 243–257 (2016).
86. Butler, H. J. *et al.* Using Raman spectroscopy to characterize biological materials. *Nat. Protoc.* **11**, 664–687 (2016).
87. Langer, J. *et al.* Present and future of surface-enhanced Raman scattering. *ACS Nano* **14**, 28–117 (2020).
88. Schlücker, S. Surface-enhanced raman spectroscopy: Concepts and chemical applications. *Angew. Chemie - Int. Ed.* **53**, 4756–4795 (2014).
89. Ding, SY., *et al*. Nanostructure-based plasmon-enhanced Raman spectroscopy for surface analysis of materials. *Nat. Rev. Mater.* 1, 16021 (2016)
90. Zheng, X. S., Jahn, I. J., Weber, K., Cialla-May, D. & Popp, J. Label-free SERS in biological and biomedical applications: Recent progress, current challenges and opportunities. *Spectrochim. Acta - Part A Mol. Biomol. Spectrosc.* **197**, 56–77 (2018).
91. Byrne, H. J. *et al.* Spectropathology for the next generation: Quo vadis? *Analyst* **140**, 2066–2073 (2015).
92. Fleischmann, M., Hendra, P. J. & McQuillan, A. J. Raman spectra of pyridine adsorbed at a silver electrode. *Chem. Phys. Lett.* **26**, 163–166 (1974).
93. Jeanmaire, D. L. & Van Duyne, R. P. Surface Raman spectroelectrochemistry part1. heterocyclic, aromatic, and aliphatic amines adsorbed on the anodized silver electrode. *J. Electroanal Chem.* **84**, 1-20 (1977).
94. Albrecht, M. G. & Creighton, J. A. Anomalously intense Raman spectra of pyridine at a silver electrode. *J. Am. Chem. Soc.* **99**, 5215–5217 (1977).
95. Ji-Xin, C. & Sunney, X. X. Vibrational spectroscopic imaging of living systems: an emerging platform for biology and medicine. *Science* **350**, aaa8870 (2015).
96. Shiohara, A.; Langer, J.; Polavarapu, L. & Liz-Marzán, L. M. Solution processed polydimethylsiloxane/gold nanostar flexible substrates for plasmonic sensing. *Nanoscale* **6**, 9817–9823 (2014).
97. Lafuente, M. *et. al.* In situ synthesis of sers-active Au@POM nanostructures in a microfluidic device for real-time detection of water pollutants. *ACS Appl. Mater. Interfaces **12***, 36458–36467 (2020).
98 Zhou, H.; Li, X.; Wang, L.; Liang, Y.; Jialading, A.; Wang, Z.; Zhang, J. Application of sers quantitative analysis method in food safety detection. *Rev. Anal. Chem.* **40**, 173–186 (2021)
99. Ferraro, J. R., Nakamoto, K. & Brown, C. W. *I*ntroductory Raman spectroscopy: Second edition. (2003).

100. Mosca, S., Conti, C., Stone, N. & Matousek, P. Spatially offset Raman spectroscopy. *Nat. Rev. Methods Prim.* **1**, (2021).
101. Raman, C. V. & Krishnan, K. S. A new type of secondary radiation. *Nature* **121**, 501–502 (1928).
102. Kudelski, A. Analytical applications of Raman spectroscopy. *Talanta* **76**, 1–8 (2008).
103. Testa-Anta, M., Ramos-Docampo, M. A., Comesaña-Hermo, M., Rivas-Murias, B. & Salgueiriño, V. Raman spectroscopy to unravel the magnetic properties of iron oxide nanocrystals for bio-related applications. *Nanoscale Adv.* **1**, 2086–2103 (2019).
104. Ellis, D. I., Cowcher, D. P., Ashton, L., O'Hagan, S. & Goodacre, R. Illuminating disease and enlightening biomedicine: Raman spectroscopy as a diagnostic tool. *Analyst* **138**, 3871–3884 (2013).
105. Downes, A. & Elfick, A. Raman spectroscopy and related techniques in biomedicine. *Sensors* **10**, 1871–1889 (2010).
106. Moskovits, M. & Suh, J. S. Surface selection rules for surface-enhanced Raman spectroscopy: Calculations and application to the surface-enhanced Raman spectrum of phthalazine on silver. *J. Phys. Chem.* **88**, 5526–5530 (1984).
107. Kneipp, K., Kneipp, H., Itzkan, I., Dasari, R. R. & Feld, M. S. Surface-enhanced Raman scattering and biophysics. *J. Phys. Condens. Matter* **14**, (2002).
108. Liang, Z., Sun, J., Jiang, Y., Jiang, L. & Chen, X. Plasmonic Enhanced Optoelectronic Devices. *Plasmonics* **9**, 859–866 (2014).
109. Maier, S. A. Plasmonics: Fundamentals and Applications. *Springer New York* **677** (2004).
110. Willets, K. A. & Van Duyne, R. P. Localized Surface Plasmon Resonance Spectroscopy and Sensing. *Annu. Rev. Phys. Chem.* **58**, 267–297 (2007).
111. Enoch, S. & Bonod, N. Plasmonics: From basics to advanced topics. *Springer Ser. Opt. Sci.* **167**, 321 (2012).
112. Gramotnev, D. K. & Bozhevolnyi, S. I. Plasmonics beyond the diffraction limit. *Nat. Photonics* **4**, 83–91 (2010).
113. Liz-Marzán, L. M. Tailoring surface plasmons through the morphology and assembly of metal nanoparticles. *Langmuir* **22**, 32–41 (2006).
114. Lohse, S. E., Burrows, N. D., Scarabelli, L., Liz-Marzán, L. M. & Murphy, C. J. Anisotropic noble metal nanocrystal growth: The role of halides. *Chem. Mater.* **26**, 34–43 (2014).
115. Stiles, P. L., Dieringer, J. A., Shah, N. C. & Van Duyne, R. P. Surface-enhanced Raman spectroscopy SERS: Inelastic scattering of a photon from a molecule in which the frequency change precisely matches the difference in vibrational energy levels. *Annu. Rev. Anal. Chem* **1**, 601–626 (2008).
116. Xie, Y. *et al.* Adsorption and photon-driven charge transfer of pyridine on a cobalt electrode analyzed by surface enhanced Raman spectroscopy and relevant theories. *J. Electroanal. Chem.* **554**, 417–425 (2003).
117. Arunkumar, K. A. & Bradley, E. B. Theory of surface enhanced Raman scattering, *J. Chem. Phys.* **78**, 2882-2888 (1983)
118. Xu, H., Bjerneld, E. J., Käll, M. & Börjesson, L. Spectroscopy of single hemoglobin molecules by

surface enhanced raman scattering. *Phys. Rev. Lett.* **83**, 4357–4360 (1999).

119. Stockman, M. I., Li, K. & Bergman, D. J. Self-similar chain of metal nanospheres as efficient nanolens. *OSA Trends Opt. Photonics Ser.* **97**, 993–995 (2004).

120. Alvarez-Puebla, R., Liz-Marzán, L. M. & García De Abajo, F. J. Light concentration at the nanometer scale. *J. Phys. Chem. Lett.* **1**, 2428–2434 (2010).

121 Jain, P: K.; Huang, W.; El-Sayed, M. A. On the universal scaling behavior of the distance decay of plasmon coupling in metal nanoparticles pairs: A plasmon ruler equation. *Nano Lett.* **7**, 2080-2088 (2007).

122. Aizpurua, J. *et al.* Optical properties of coupled metallic nanorods for field-enhanced spectroscopy. *Phys. Rev. B - Condens. Matter Mater. Phys.* **71**, 1–13 (2005).

123. Tian, C., Deng, Y., Zhao, D. & Fang, J. Plasmonic silver supercrystals with ultrasmall nanogaps for ultrasensitive sers-based molecule detection. *Adv. Opt. Mater.* **3**, 404–411 (2015).

124. Kim, D. S., Honglawan, A., Yang, S. & Yoon, D. K. Arrangement and SERS applications of nanoparticle clusters using liquid crystalline template. *ACS Appl. Mater. Interfaces* **9**, 7787–7792 (2017).

125 Brongersma, M. L., Halas, N. J. & Nordlander, P. Plasmon-induced hot carrier science and technology. *Nat. Nanotechnol.* **10**, 25–34 (2015).

126 Meng, F. *et al.* 3D Bioprinted in vitro metastatic models via reconstruction of tumor microenvironments. *Adv. Mater.* **31**, e1806899 (2019).

127 Miller, I. C. *et al.* Enhanced intratumoural activity of CAR T cells engineered to produce immunomodulators under photothermal control. *Nat. Biomed. Eng* **5,** 1348–1359 (2021).

128 Luo, S.C. *et. al*. Nanofabricated SERS-active substrates for single-molecule to virus detection in vitro: A review. *Biosens. Bioelectron*. **61**, 232–240 (2014).

129 Vo-Dinh, Tuan., Hiromoto, M. Y. K., Begun, G. M. & Moody, R. L. Surface-enhanced Raman spectrometry for trace organic analysis. *Anal. Chem.* **56**, 1667–1670 (1984).

130 Wang, X.; Huang, S.-C.; Hu, S.; Yan, S.; Ren, B. Fundamental understanding and applications of plasmon-enhanced Raman spectroscopy. *Nature Rev. Phys.* **2,** 253–257 (2020)

131 Yang, A. *et. al.* W. Real-time tunable lasing from plasmonic nanocavity arrays. *Nat. Commun.* **6**, 6939 (2015).

132 Isaacoff, B. P. & Brown, K. A. Progress in top-down control of bottom-up assembly. *Nano Lett.* **17**, 6508–6510 (2017).

133 Han, Y., Wu, S.-R., Tian, X.-D. & Zhang, Y. Optimizing the SERS performance of 3D substrates through tunable 3D plasmonic coupling toward label-free liver cancer cell classification. *ACS Appl. Mater. Interfaces* **12**, 28965–28974 (2020).

134 Haidar, I. *et.al*. Bottom-up assembly of Au@Ag plasmonic nanocrystals: Issues to be addressed to achieve a good SERS substrate. *Appl. Mater. Today* **15**, 462–471 (2019).

135 Milliken, S., Fraser, J., Poirier, S., Hulse, J. & Tay, L.-L. Self-assembled vertically aligned au nanorod arrays for surface-enhanced Raman scattering (SERS) detection of cannabinol. *Spectrochimica Acta A* **196**, 222–228 (2018).

136 Zhang, L., Guan, C., Wang, Y. & Liao, J. Highly effective and uniform SERS substrates fabricated

by etching multi-layered gold nanoparticle arrays. *Nanoscale* **8**, 5928–5937 (2016).

137 Montjoy, D. G., Bahng, J. H., Eskafi, A., Hou, H. & Kotov, N. A. Omnidispersible hedgehog Particles with multilayer coatings for multiplexed biosensing. *J. Am. Chem. Soc*. **140**, 7835–7845 (2018).

138 Baranov, D. G., Verre, R., Karpinski, P. & Käll, M. Anapole-enhanced intrinsic Raman scattering from silicon nanodisks. *ACS Photonics* **5**, 2730–2736 (2018).

139 Sharma, B. *et. al*. High-performance SERS substrates: Advances and challenges. *MRS Bull*. **38**, 615–624 (2013).

140 Mueller, N. S. *et. al*. Dark interlayer plasmons in colloidal gold nanoparticle bi- and few-layers. *ACS Photonics* 5, 3962–3969 (2018).

141 Li, J. *et. al.* Digital single-molecule nanopillar SERS platform for predicting and monitoring immune toxicities in immunotherapy. *Nat. Commun.* **12**, 1087 (2021).

142 Hu, M., *et. al*. Gold nanofingers for molecule trapping and detection. J. *Am. Chem. Soc.* **132**, 12820–12822 (2010).

143 Shiota, M. *et. al.* Gold-nanofève surface-enhanced Raman spectroscopy visualizes hypotaurine as a robust anti-oxidant consumed in cancer survival. *Nat. Commun.* **9**, 1561 (2018).

144 Yang, J. *et. al*. Surface-enhanced Raman spectroscopy based quantitative bioassay on aptamer-functionalized nanopillars using large-area Raman mapping. *ACS Nano* **7**, 5350–5359 (2013).

145 Altuntas, S. & Buyukserin, F. Fabrication of thioflavin-t-modified nanopillared SERS substrates for ultrasensitive beta-amyloid peptide detection. *J. Raman Spectrosc.* **49,** 1247–1256 (2018).

146 Chen, K. H., Pan, M. J.; Jargalsaikhan, Z., Ishdorj, T. O. & Tseng, F. G. Development of surface-enhanced Raman scattering (SERS)-based surface-corrugated nanopillars for biomolecular detection of colorectal cancer. *Biosensors* **10**, 163 (2020).

147 Xie, Y. *et. al*. Adsorption and photon-driven charge transfer of pyridine on a cobalt electrode analyzed by surface enhanced Raman spectroscopy and relevant theories. *J. Electroanal. Chem.* **554**, 417–425 (2003).

148 Arunkumar, K. A. & Bradley, E. B. Theory of surface enhanced Raman scattering. *J. Chem. Phys*. **78**, 2882–2888 (1983).

149 Xu, H., Bjerneld, E. J., Käll, M. & Börjesson, L. Spectroscopy of single hemoglobin molecules by surface enhanced Raman scattering. *Phys. Rev. Lett.* **83**, 4357–4360 (1999).

150 Stockman, M. I., Li, K. & Bergman, D. J. Self-similar chain of metal nanospheres as efficient nanolens. *OSA Tr. Opt. Photonics Ser.* **97**, 993–995 (2004).

151 Alvarez-Puebla, R. & Liz-Marzán, L. M.; García de Abajo, F. J. Light concentration at the nanometer scale. J. *Phys. Chem. Lett.* **1**, 2428–2434 (2010).

152 Aizpurua, J. Bryant, G. W. & Richter, L. J.; García de Abajo, F. J.; Kelley, B. K.; Mallouk, T. Optical properties of coupled metallic nanorods for field-enhanced spectroscopy. *Phys. Rev. B* **71**, 235420 (2005).

153 Tian, C., Deng, Y., Zhao, D. & Fang, J. Plasmonic silver supercrystals with ultrasmall nanogaps for ultrasensitive sers-based molecule detection. *Adv. Optical Mater.* **3**, 404–411 (2015).

154 Kim, D. S., Honglawan, A., Yang, S. & Yoon, D. K. Arrangement and SERS applications of

nanoparticle clusters using liquid crystalline template. *ACS Appl. Mater. Interfaces* **9**, 7787–7792 (2017).

155 Wei, H. & Xu, H. Hot spots in different metal nanostructures for plasmon-enhanced Raman spectroscopy. *Nanoscale* **5**, 10794–10805 (2013).

156 Shiohara, A., Wang, Y. & Liz-Marzán, L. M. Recent approaches toward creation of hot spots for SERS detection. *J. Photochem. Photobiol. C* **21**, 2–25 (2014).

157 Asiala, S. M. & Schultz, Z. D. Characterization of hotspots in a highly enhancing SERS substrate. *Analyst* **136**, 4472–4479 (2011).

158 García-Lojo, D. *et. al*. Plasmonic supercrystals. *Acc. Chem. Res.* **52**, 1855–1864 (2019).

159 Severoni, E. *et. al*. Plasmon-enhanced optical chirality through hotspot formation in surfactant-directed self-assembly of gold nanorods. *ACS Nano* **14**, 16712–16722 (2020).

160 Ni, S., Leeman, J., & Wolf, H. Insight into mechanism of capillary assembly. *Faraday Discuss.* **181**, 225–242 (2015).

161 Kim, J. *et. al.* Polymorphic assembly from beveled gold triangular nanoprisms. *Nano Lett.* **17**, 3270–3275 (2017).

162 Alba, M. *et. al*. Macroscale plasmonic substrates for highly sensitive surface-enhanced Raman scattering. *Angew. Chem. Int. Ed.* **52**, 6459–6463 (2013).

163 Gómez-Graña, S. *et. al.* Gold nanooctahedra with tunable size and microfluidic-induced 3D assembly for highly uniform SERS-active supercrystals. *Chem. Mater.* **27**, 8310–8317 (2015).

164 Bodelón, G. *et. al.* Detection and imaging of quorum sensing in Pseudomonas Aeruginosa biofilm communities by surface-enhanced resonance Raman scattering. *Nat. Mater.* **15**, 1203–1211 (2016).

165 Hanske, C. *et. al*. Large-scale plasmonic pyramidal supercrystals via templated self-assembly of monodisperse gold nanospheres. *J. Phys. Chem. C* **121**, 10899–10906 (2017).

166 Lin, L., Bi, X., Gu, Y., Wang, F. & Ye, J. Surface-enhanced Raman scattering nanotags for bioimaging. *J. Appl. Phys.* **129**, 191101 (2021).

167 Pilot, R. & Massari, M. Silver nanoparticle aggregates: wavelength dependence of their SERS properties in the first transparency window of biological tissues. *Chem. Phys. Impact* **2**, 100014 (2021).

168 Alexander, K. D., Skinner, K., Zhang, S., Wei, H. & Lopez, R. Tunable SERS in gold nanorod dimers through strain control on an elastomeric substrate. *Nano Lett.* **10**, 4488–4493 (2010).

169 Lee, J.-E. *et. al.* Viable stretchable plasmonics based on unidirectional nanoprisms. *Nanoscale* **10**, 4105–4112. (2018)

170 Xu, K., Zhou, R., Takei, K. & Hong, M. Toward flexible surface-enhanced Raman scattering (SERS) sensors for point-of-care diagnostics. *Adv. Sci.* **6**, 1900925 (2019).

171 Rudé, M. *et. al*. Ultrafast and broadband tuning of resonant optical nanostructures using phase-change materials. *Adv. Optical Mater*. **4**, 1060–1066 (2016).

172 Geryak, R., Geldmeier, J., Wallace, K. & Tsukruk, V. V. Remote giant multispectral plasmonic shifts of labile hinged nanorod array via magnetic field. *Nano Lett.* **15**, 2679–2684 (2016).

173 Lee, E. *et. al*. Fine golden rings: tunable surface plasmon resonance from assembled nanorods in topological defects of liquid crystals. *Adv. Mater.* **28**, 2731–2736 (2016).

174 Lu, X. *et. al.* Light-controlled shrinkage of large-area gold nanoparticle monolayer film for tunable SERS activity. *Chem. Mater.* **30**, 1989–1997 (2018).

175 Matricardi, C. *et. al*. Gold nanoparticle plasmonic superlattices as surface enhanced Raman spectroscopy substrates. *ACS Nano* **12**, 8531-8539 (2018).

176 Hanske, C. *et. al*. Solvent-assisted self-assembly of gold nanorods into hierarchically organized plasmonic mesostructures. *ACS Appl. Mater. Interfaces* **11**, 11763–11771 (2019).

177 Charconnet, M. *et. al*. Mechanically tunable lattice-plasmon resonances by templated self-assembled superlattices for multi-wavelength surface-enhanced Raman spectroscopy. *Small Methods* **5**, 2100453 (2021).

178 Premasiri, W. R., Lee, J. C. & Ziegler, L. D. Surface-enhanced Raman scattering of whole human blood, blood plasma, and red blood cells: Cellular processes and bioanalytical sensing. *J. Phys. Chem. B* **116**, 9376–9386 (2012).

179 Premasiri, W. R. *et. al.* The biochemical origins of the surface-enhanced Raman spectra of bacteria: A metabolomics profiling by sers. *Anal. Bioanal. Chem.* **408**, 4631–4647 (2016).

180 Cervo, S. *et. al.* SERS Analysis of serum for detection of early and locally advanced breast cancer. *Anal. Bioanal. Chem.* **407**, 7503–7509 (2015).

181 Lee, W. *et. al*. spread spectrum SERS allows label-free detection of attomolar neurotransmitters. *Nat. Commun.* **12**, 159 (2021).

182 Cho, H. *et. al*. Surface-enhanced Raman spectroscopy-based label-free insulin detection at physiological concentrations for analysis of islet performance. *ACS Sens*. **3**, 65–71 (2018).

183 Shalabaeva, V. *et. al*. Time resolved and label free monitoring of extracellular metabolites by surface enhanced Raman spectroscopy. *PLoS One*, **12**, e0175581 (2017).

184 Feliu, N. *et. al.* SERS quantification and characterization of proteins and other biomolecules. *Langmuir* **38**, 9711–9730 (2017).

185 Garcia-Rico, E., Alvarez-Puebla, R. A. & Guerrini, L. Direct surface-enhanced Raman scattering (SERS) spectroscopy of nucleic acids: From fundamental studies to real-life applications. *Chem. Soc. Rev.* **47**, 4909–4923 (2018).

186 Huang, J.-A. *et. al*. SERS Discrimination of single DNA bases in single oligonucleotides by electro-plasmonic trapping. *Nat. Commun*. **10,** 5321 (2019).

187 Almehmadi, L. M., Curley, S. M., Tokranova, N. A., Tenenbaum, S. A. & Lednev, I. K. Surface enhanced Raman spectroscopy for single molecule protein detection. *Sci. Rep.* **9**, 12356 (2019).

188 Sun, Y., Xu, F., Zhang, Y., Shi, Y., Wen, Z. & Li, Z. Metallic Nanostructures assembled by DNA and related applications in surface-enhancement Raman scattering (SERS) detection. *J. Mater. Chem.* **21**, 16675–16685 (2011).

189 Kamińska, A. *et. al.* SERS-Based immunoassay in a microfluidic system for the multiplexed recognition of interleukins from blood plasma: Towards picogram detection. *Sci. Rep.* **7**, 10656 (2017).

190 Bell, S. E. J. *et. al.* Towards reliable and quantitative surface-enhanced Raman scattering (SERS): from key parameters to good analytical practice. *Angew. Chem. Int. Ed*, **59**, 5454–5462 (2020).

191 Genova, A. *et. al.* SERS of cells: What can we learn from cell lysates? *Anal. Chim. Acta* **1005**, 93–

100 (2018).

192 Weiss, R. *et. al.* Surface-enhanced Raman spectroscopy of microorganisms: limitations and applicability on the single-cell level. *Analyst*, **144**, 943–953 (2019).

193 Feliu, N. *et. al.* In vivo degeneration and the fate of inorganic nanoparticles. *Chem. Soc. Rev.* **45**, 2440–2457 (2016).

194 Moore, T. L. *et. al*. Nanoparticle colloidal stability in cell culture media and impact on cellular interactions. *Chem. Soc. Rev.* **44**, 6287–6305 (2015).

195 Milić, M. *et. al.* Cellular uptake and toxicity effects of silver nanoparticles in mammalian kidney cells. *J. Appl. Toxicol.* **35**, 581–592 (2015).

196 Loza, K. *et. al.* The dissolution and biological effects of silver nanoparticles in biological media. J. *Mater. Chem. B* **2**, 1634–1643 (2014).

197 Li, J. F. *et. al.* Q. Surface analysis using shell-isolated nanoparticle-enhanced Raman spectroscopy. *Nat. Protocols* **8**, 52–65 (2013).

198 Gellner, M. *et. al.* 3D Self-assembled plasmonic superstructures of gold nanospheres: Synthesis and characterization at the single-particle level. *Small* **7**, 3445–3451 (2011).

199 Cha, M. G. *et. al.* Thin silica shell coated ag assembled nanostructures for expanding generality of SERS analytes. *PLoS One* **12**, e0178651 (2017).

200 Kim, W. *et. al.* Paper-based surface-enhanced Raman spectroscopy for diagnosing prenatal diseases in women. *ACS Nano* **12**, 7100–7108 (2018).

201 Teixeira, A. *et. al*. Microfluidics-driven fabrication of a low cost and ultrasensitive SERS-based paper biosensor. *Appl. Sci.* **9**, 1387 (2019).

202 Hahm, E. *et. al.* β-CD dimer-immobilized ag assembly embedded silica nanoparticles for sensitive detection of polycyclic aromatic hydrocarbons. *Sci. Rep.* **6**, 26082 (2016).

203 Ogundare, S. A. & van Zyl, W. E. A Review of cellulose-based substrates for SERS: Fundamentals, design principles, applications. *Cellulose* **26**, 6489–6528 (2019).

204 Song, J. & Cho, E. Dual-responsive and multi-functional plasmonic hydrogel valves and biomimetic architectures formed with hydrogel and gold nanocolloids. *Sci Rep* **6**, 34622 (2016).

205 Yu, W. *et. al.* Light-Addressable nanocomposite hydrogels allow plasmonic actuation and in situ temperature monitoring in 3D cell matrices. *Adv. Funct. Mater.* **29**, 2108234 (2021).

206 Miranda, B. *et. al.* A PEGDA hydrogel nanocomposite to improve gold nanoparticles stability for novel plasmonic sensing platforms. *J. Appl. Phys.* **129**, 33101 (2021).

207 Pastoriza-Santos, I., Kinnear, C., Pérez-Juste, J.;,Mulvaney, P. & Liz-Marzán, L. M. Plasmonic polymer nanocomposites. *Nat. Rev. Mater.* **3**, 375–391 (2018).

208 García-Astrain, C. *et. al.* 3D-printed biocompatible scaffolds with built-in nanoplasmonic sensors. *Adv. Funct. Mater.* **30**, 2005407 (2020).

209 Kumar, A. & Santhanam, V. Paper swab based SERS detection of non-permitted colourants from dals and vegetables using a portable spectrometer. *Analytica Chim. Acta* **1090**, 106–113 (2019).

210 Li, H., Dai, H., Zhang, Y., Tong, W., Gao, H. & An, Q. Surface-enhanced Raman spectra promoted by a finger press in an all-solid-state flexible energy conversion and storage film. *Angew. Chem. Int. Ed.* **56**, 2649–2654 (2017).

211 Jeong, J. W. *et. al.* High-Resolution nanotransfer printing applicable to diverse surfaces via interface-targeted adhesion switching. *Nat. Commun.* **5**, 5387 (2014).

212 Yingli, W. *et. al.* Wearable plasmonic-metasurface sensor for noninvasive and universal molecular fingerprint detection on biointerfaces. *Sci. Adv*, **7**, eabe4553 (2021).

213 Koh, E. H. *et. al.* A wearable surface-enhanced Raman scattering sensor for label-free molecular detection. *ACS Appl. Mater. Interfaces* **13**, 3024–3032 (2021).

214 Jeong, J. W. *et. al.* 3D cross-point plasmonic nanoarchitectures containing dense and regular hot spots for surface-enhanced Raman spectroscopy analysis. *Adv. Mater.* **28**, 8695–8704 (2016).

215 Linh, V. T. N. *et. al*. Bioinspired plasmonic nanoflower-decorated microneedle for label-free intradermal sensing. *Appl. Surf. Sci.* **551**, 149411 (2021).

216 Park, J. E. *et. al.* Plasmonic microneedle arrays for in situ sensing with surface-enhanced Raman spectroscopy (SERS). *Nano Lett.* **19**, 6862–6868 (2019).

217 Aioub, M. & El-Sayed, M. A. A real-time surface enhanced Raman spectroscopy study of plasmonic photothermal cell death using targeted gold nanoparticles. *J. Am. Chem. Soc.* **138**, 1258–1264 (2016).

218 Kang, B., Austin, L. A. & El-Sayed, M. A. Observing real-time molecular event dynamics of apoptosis in living cancer cells using. *ACS Nano* **8**, 4883–4892 (2014).

219 Zhu, J. *et. al.* surface-enhanced Raman spectroscopy investigation on human breast cancer cells. *Chem. Central J.* **7**, 37 (2013).

220 Tadesse, L. F. *et. al*. Plasmonic and electrostatic interactions enable uniformly enhanced liquid bacterial surface-enhanced Raman scattering (SERS). *Nano Lett.* **20**, 7655–7661 (2020).

221 Koike, K. *et. al.* Quantitative drug dynamics visualized by alkyne-tagged plasmonic-enhanced Raman microscopy. *ACS Nano* **14**, 15032–15041 (2020).

222 Rees, P., Wills, J. W., Brown, M. R., Barnes, C. M. & Summers, H. D. The origin of heterogeneous nanoparticle uptake by cells. *Nat. Commun.* **10**, 2341 (2019).

223 Hanif, S. *et. al.* Nanopipette-Based SERS aptasensor for subcellular localization of cancer biomarker in single cells. *Anal. Chem.* **89**, 9911–9917. (2017)

224 Vitol, E. A. *et. al.* In situ intracellular spectroscopy with surface enhanced Raman spectroscopy (SERS)-enabled nanopipettes. *ACS Nano* **3**, 3529–3536 (2009.

225 Lussier, F., Brulé, T., Vishwakarma, M., Das, T., Spatz, J. P. & Masson, J.-F. Dynamic-SERS optophysiology: a nanosensor for monitoring cell secretion events. *Nano Lett.* **16**, 3866–3871 (2016).

226 Markina, N. E., Markin, A. V., Weber, K., Popp, J. & Cialla-May, D. Liquid-liquid extraction-assisted SERS-based determination of sulfamethoxazole in spiked human urine. *Analytica Chim. Acta 1109*, 61–68 (2020).

227 Torul, H., Çiftçi, H., Çetin, D., Suludere, Z., Boyac, I. H. & Tamer, U. Paper membrane-based SERS platform for the determination of glucose in blood samples. *Anal. Bioanal. Chem. 407*, 8243–8251 (2015).

228 Dumont, E. *et. al.* Development of a prototype device for near real-time surface-enhanced Raman scattering monitoring of biological samples. *Talanta* **224**, 121866 (2021).

229 Szekeres, G. P. & Kneipp, J. SERS probing of proteins in gold nanoparticle agglomerates. *Front. Chem* 2019, **7**, 30 (2019).

230 Kumar, S. *et. al.* Myoglobin and polydopamine-engineered raman nanoprobes for detecting, imaging, and monitoring reactive oxygen species in biological samples and living cells. *Small* **13**, 1701584 (2017).

231 Li, D.-W. *et. al.* Reaction-based SERS nanosensor for monitoring and imaging the endogenous hypochlorous acid in living cells. *Analytica Chimica Acta* **1018**, 104–110 (2018).

232 Klutse, C. K., Mayer, A., Wittkamper, J. & Cullum, B. M. Applications of self-assembled monolayers in surface-enhanced Raman scattering. *J. Nanotechnology* **20**, 319038 (2012).

233 Sun, F. *et. al.* Hierarchical zwitterionic modification of a SERS substrate enables real-time drug monitoring in blood plasma. *Nat. Commun.* **7**, 13437 (2016).

234 Leong, Y. X. *et. al.* Surface-enhanced Raman scattering (SERS) taster: A machine-learning-driven multireceptor platform for multiplex profiling of wine flavors. *Nano Lett.* **21**, 2642–2649 (2021).

235 Kim, N. *et. al.* M. M. Surface enhanced Raman scattering artificial nose for high dimensionality fingerprinting. *Nat. Commun.* **11**, 207 (2020).

236 Kang, H. & Haynes, C. Interactions between silica-coated gold nanorod substrates and hydrophobic analytes in colloidal surface-enhanced Raman spectroscopy. *J. Phys. Chem. C* **123**, 24685–24697 (2019).

237 Gao, Z. *et. al.* In solution SERS sensing using mesoporous silica-coated gold nanorods. *Analyst* **141**, 5088–5095 (2016).

238 Shin, Y. *et. al.* Facile microfluidic fabrication of 3D hydrogel SERS substrate with high reusability and reproducibility via programmable maskless flow microlithography. *Adv. Optical Mater.* **8**, 2001586 (2020).

239 Kim, D. J., Park, S.-G., Kim, D.-H. & Kim, S.-H. SERS-active-charged microgels for size- and charge-selective molecular analysis of complex biological samples. *Smal* **14**, 1802520 (2018).

240 Castro-Grijalba, A. *et. al.* SERS-based molecularly imprinted plasmonic sensor for highly sensitive PAH detection. *ACS Sens.* **5**, 693–702 (2020).

241 Guo, Y. Kang, L., Chen, S. & Li, X. High performance surface-enhanced Raman scattering from molecular imprinting polymer capsulated silver spheres. Phys. *Chem. Chem. Phys.* **17,** 21343–21347 (2015).

242 Guo, X. *et. al.* Molecular-imprinting-based surface-enhanced Raman scattering sensors. *ACS Sens.* **5**, 601–619 (2020).

243 Zhang, Q. & Reinhard, B. M. Characterizing nanoplastics-induced stress and its SERS fingerprint in an intestinal membrane model. *Nano Select* **2**, 1707–1722 (2021).

244 Fornasaro, S. *et. al*. Ergothioneine, a dietary amino acid with a high relevance for the interpretation of label-free surface enhanced Raman scattering (SERS) spectra of many biological samples. *Spectrochim. Acta A* **246**, 119024 (2021).

245 Zhou, W. *et. al*. Plasmonically calibrated label-free surface-enhanced Raman spectroscopy for improved multivariate analysis of living cells in cancer subtyping and drug testing. *Anal. Chem.* **93**, 4601–4610 (2021).

246 Lin, D. *et. al*. Label-free blood plasma test based on surface-enhanced Raman scattering for tumor stages detection in nasopharyngeal cancer. *Sci. Rep.* **4**, 4751 (2014).

247 Erzina, M. *et. al*. Precise cancer detection via the combination of functionalized SERS surfaces and convolutional neural network with independent inputs. *Sens. Actuators B* **308**, 127660 (2020).

248 Goodacre, R., Graham, D. & Faulds, K. Recent developments in quantitative SERS: moving towards absolute quantification. *TrAC Anal. Chem.* 102, 359-368 (2018)

249 Lussier, F. *et. al*. Deep learning and artificial intelligence methods for Raman and surface-enhanced Raman scattering. *TrAC Trends Anal. Chem.* **124**, 115796 (2020).

250 Barucci, A. *et. al*. Label-free SERS detection of proteins based on machine learning classification of chemo-structural determinants. *Analyst* **146**, 674–682 (2021).

251 Witkowska, E. *et. al*. Strain-level typing and identification of bacteria – a novel approach for SERS active plasmonic nanostructures. *410*, 5019–5031 (2018).

252 Czaplicka, M. *et. al*. Kamińska, A. Raman spectroscopy and surface-enhanced Raman spectroscopy (SERS) spectra of salivary glands carcinoma, tumor and healthy tissues and their homogenates analyzed by chemometry: towards development of the novel tool for clinical diagnosis. *Analytica Chim. Acta* **1177**, 338784 (2021).

253 Tang, J.-W. *et. al*. comparative analysis of machine learning algorithms on surface enhanced Raman spectra of clinical staphylococcus species. *Front. Microbiol.* **12**, 2424 (2021).

254 Lussier, F., Missirlis, D., Spatz, J. P. & Masson, J.-F. machine-learning-driven surface-enhanced Raman scattering optophysiology reveals multiplexed metabolite gradients near cells. *ACS Nano* **13**, 1403–1411 (2019).

255 Shin, H. *et. al*.. Early-stage lung cancer diagnosis by deep learning-based spectroscopic analysis of circulating exosomes. *ACS Nano* **14**, 5435–5444 (2020).

256 Thrift, W. J. *et. al*. Deep learning analysis of vibrational spectra of bacterial lysate for rapid antimicrobial susceptibility testing. *ACS Nano* **14**, 15336–15348 (2020).

257 Lin, X. *et. al.* High throughput blood analysis based on deep learning algorithm and self-positioning super-hydrophobic SERS platform for non-invasive multi-disease screening. *Adv. Funct. Mater.* **31**, 2103382 (2021).

CHAPTER 2

“Multiplex SERS Detection of Metabolic Alterations in Tumor Extracellular Media”

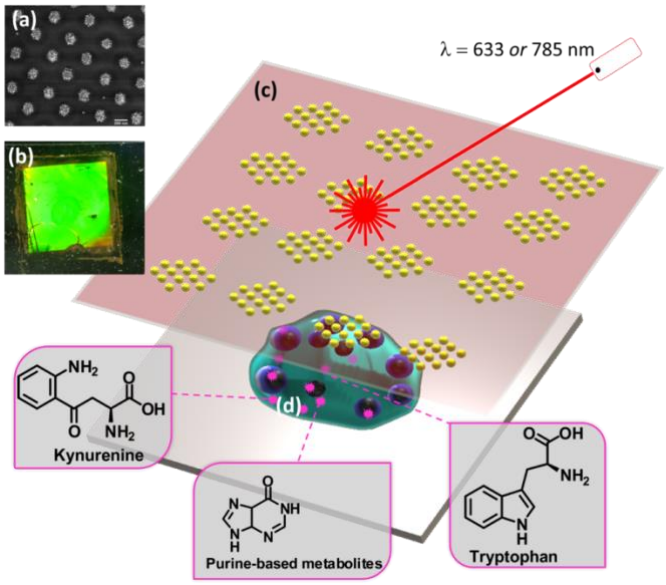

The composition and intercellular interactions of tumor cells within tissues dictate the biochemical and metabolic properties of the tumor microenvironment, to an extent that monitoring such perturbations could harbor diagnostic and therapeutic relevance. Growing interest on these phenomena has inspired the development of novel technologies with sufficient sensitivity and resolution to monitor metabolic alterations in the tumor microenvironment. In this context, surface-enhanced Raman scattering (SERS) can be used for the label-free detection and imaging of diverse molecules of interest among extracellular components. We present in this chapter the application of nanostructured plasmonic substrates comprising ordered gold nanoparticle superlattices, to the SERS detection of selected tumor metabolites. We demonstrate the potential of this technology through the analysis of kynurenine, a secreted immunomodulatory derivative of the tumor metabolism and the related molecules tryptophan and purine derivatives. SERS enabled the unambiguous identification of the metabolites of interest and allowed the multiplexed detection of their characteristic fingerprints under different conditions. Finally, we combined the effective plasmonic SERS substrate with a hydrogel-based 3D system, as a model of the tumor microenvironment, for real-time imaging of metabolite alterations and cytotoxic effects in tumor cells.

2.1 Introduction

Cancer cells and the stroma create dynamic pseudo-organs that contain a unique niche with distinct biochemical and physiological properties.[1] Mutations and signaling alterations in tumor cells modify the composition of the microenvironment, whereas changes in the microenvironment can also influence the fitness of cancer cells, eventually reprogramming cancer cell metabolism (examples of such metabolic interactions were explained in section 1.3a).[2,3,4] Consequently, the assessment of tumor-secreted metabolites becomes instrumental for monitoring the response of tumors upon therapeutic challenges, the stratification of cancer patients and the identification of novel therapeutic strategies. In this regard, imaging and fast detection of metabolites may play a critical role to accomplish these aims.[5,6,7]

Conventionally, extracellular metabolic studies have been carried out by means of colorimetric techniques, which involve the addition of chemical groups that specifically react with the molecule of interest. This method is rapid and convenient but also has significant drawbacks, as it is invasive and does not allow the long-term simultaneous detection of multiple analytes.[8] More recently, LC- MS, and at a lesser extent NMR, have been the techniques of choice for the majority of high- and low-throughput metabolic analysis, due to their robustness and multiple detection capability. However, LC-MS involves time-consuming, expensive, and destructive procedures,[9] while NMR suffers from weak sensitivity.[10,11] Hence, the development of alternative label-free methods to rapidly detect multiple tumor-secreted metabolites in extracellular media is required toward understanding metabolic alterations in the extracellular environment of tumor cells.[12]

In this scenario, SERS can be applied non-invasively for label-free detection and imaging of a wide range of analytes, standing as a promising technique that fulfills several of the above mentioned requirements.[13] SERS facilitates the identification of vibrational fingerprints of probe molecules in contact with a plasmonic nanostructure, to the extent that it can be used to characterize biological molecules in solution and within cells, for cancer diagnosis.[14-16] This chapter abounds in a SERS-based strategy that succeeded in monitoring the extracellular accumulation of metabolites relevant to tumor biology, by applying nanostructured plasmonic substrates comprising a superlattice of gold nanoparticles (AuNPs), as the source of enhancement for the Raman signal from the analytes.

The employed plasmonic superlattices were previously reported to display an intense plasmon resonance, thanks to the periodic arrangement of the constituent AuNPs (see section 1.5c). This physical phenomenon emerges when, arrays of AuNPs into particular gratings diffract light in-

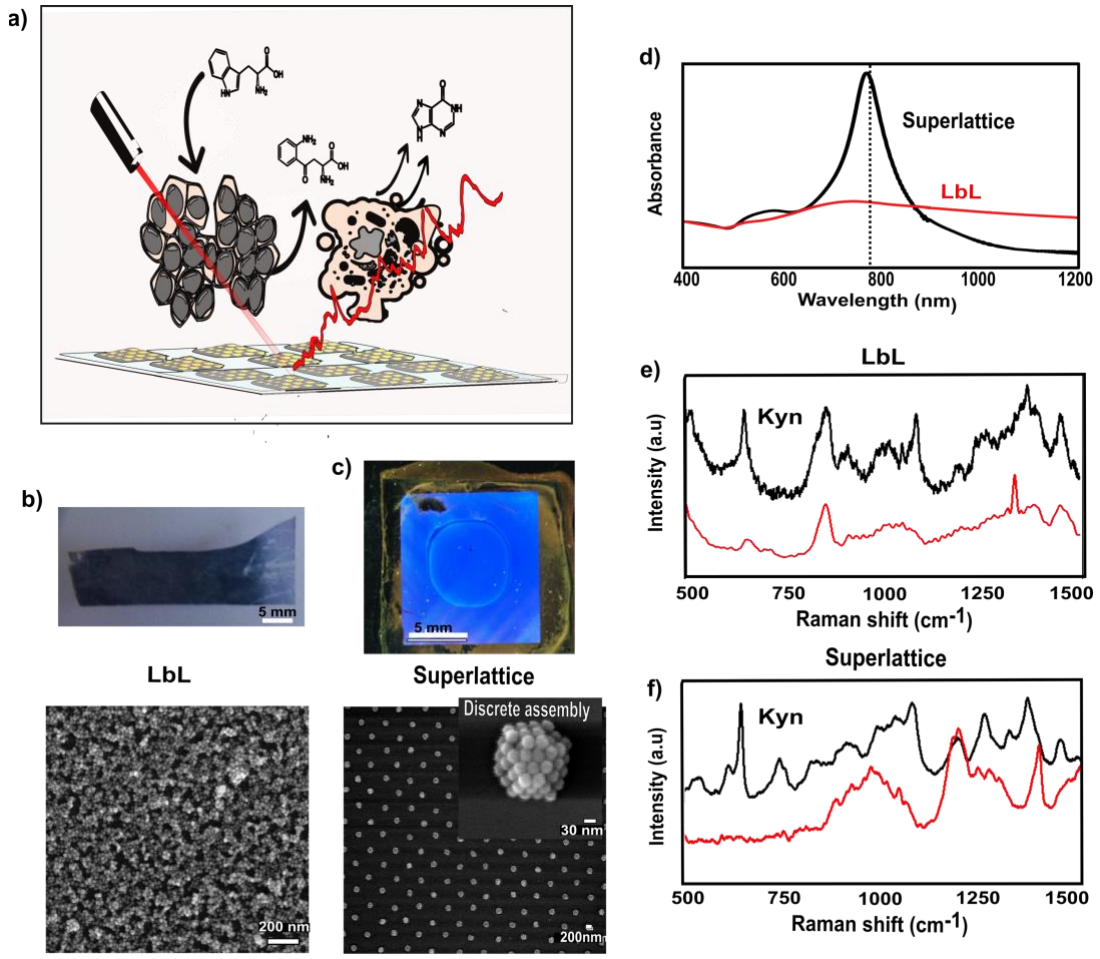

Figure 2.1 a) Sketch of the deployed strategy to monitor extracellular metabolites by SERS. b,c) Representative optical image of LBL (b) and superlattice substrates (c), with the corresponding SEM images of AuNPs distribution on a glass support. The inset in (c, lower panel) shows the structure of a representative NP cluster. d) Vis-NIR spectra, normalized at 400 nm, for both LbL and superlattice plasmonic substrates; the vertical line indicates the excitation wavelength used for SERS measurements (785 nm). e,f) SERS spectra for kynurenine (Kyn) measured in 100 µM aqueous solution deposited on LBL (e) and superlattice (f) substrates. Red spectra show the background signal of both pristine substrates All measurements were performed with a 50× objective, 10 s acquisition time, maximum power of the 785 nm laser 8.48 mW.

plane (also known as Rayleigh-Wood anomaly). Due to this in-plane diffraction event, a sudden drop in reflectivity is observed at a wavelength dictated by the lattice period (L) of the 2D crystalline array. In addition, such in-plane diffracted waves interact with AuNPs clusters at each lattice spot, resulting in an enhancement of the plasmon resonance around the wavelength of the Rayleigh anomaly, which in turn creates an additional increase of the electric field within each AuNP cluster, boosting the SERS signal (this is also known as lattice plasmon resonance).[17] Hence, by varying the lattice period, we can have an additional handle to manipulate the plasmonic behavior of such SERS substrates (**see Equation 2.1**), leveraging their use under different excitation wavelengths.

$$a)\ \lambda_0 = L\eta_{substrate}$$

$$b)\ \eta_{superstrate}\sin(\theta_{inc}) + {}^{\lambda_0}/_{L} = \eta_{substrate}\sin(\theta_{dif})$$

Equation 2.1. a) Given a specific light wavelength (λ_0), we can calculate the periodicity of the superlattice (L) that originates in-plane light diffraction (η represents the refractive index of the substrate, 1.5 for glass supports). It should be taken into account, however, that this simplified equation can only be applied for Rayleigh anomaly, when the diffractive angle is 90º ($\theta_{dif} = 90°$), and with excitation light at normal incidence ($\theta_{inc} = 0$). Original granting equation found in (b)

By using these plasmonic superlattices (along with substrates fabricated by alternative strategies), we monitored the activity of the commonly overexpressed IDO-1 enzyme in solid tumors, which consumes Trp to generate Kyn, thereby reducing Trp and increasing Kyn concentrations in the extracellular environment. This metabolic process has attracted much attention due to the recently discovered association between high Kyn/Trp ratios in plasma from cancer individuals and poor patient prognosis.[18,19] We consider that the implementation of a SERS detection platform can offer an efficient tool to perform a fast monitoring of Kyn/Trp ratio in the extracellular environment, and in turn to evaluate the extrapolation of IDO-1 expression. On the basis of the crucial role elicited by purine derivative metabolites within the TME (see section 1.3b),[20,21] we also envision the biological value of monitoring variations of such purine derivatives by SERS. For the screening of such metabolites, we devised a SERS-based detection system to image the accumulation of metabolites in 3D cancer-on-a-chip models, which would retrieve spatial information about different cell events over time. The quality of the recorded SERS spectra reinforced confidence on the efficiency (i.e., the ability to detect μM-concentrations of target analytes in complex media) and versatility of the method for the label-free molecular detection of small metabolites, and its potential contribution to understanding the fluctuations of such molecules within the tumor microenvironment (see **Figure 2.1a**).[22,23]

2.2 Results and discussion

2.2 I) Plasmonic substrates for SERS detection of kynurenine and tryptophan

As a starting point, we tested two types of plasmonic substrates, which had been optimized, prior to the realization of this thesis, for the detection of bacterial Quorum Sensing signaling molecules and offered a high stability in biological media (see section 1.5.d II in Chapter 1).[24,25] Although both strategies involved the deposition of 30 nm spherical AuNPs on glass substrates, the different methodologies and concentrations resulted in radically different distributions on the substrate (see images of both plasmonic substrates in **Figure 2.1b,c**). The standard polyelectrolyte-based layer-by-layer (LbL) assembly methodology was followed to fabricate homogenous (disordered) multilayers of AuNPs on a glass cover slip (see Chapter 6 for experimental methods, in particular

section 6.2 for SERS substrates fabrication) a schematic description of the process can be found in Figure 6.1a (Chapter 6). In contrast, the fabrication of plasmonic superlattices, was carried out via a template-assisted method that guides the self-assembly of AuNPs into hierarchical nanostructured substrates (the protocol is depicted in Figure 6.1b)

The different AuNP organization resulted in significant variations in the extinction spectra of the substrates. Comparison of the spectra (normalized to the amount of gold) for both substrates in **Figure2.1d** unveiled that the plasmonic superlattices endowed a sharp resonance around 760 nm, which closely matched the 785 nm SERS excitation laser wavelength, whereas LbL films exhibited a much broader extinction band, while retaining a maximum within the same wavelength range. This significant difference is explained due to the Rayleigh anomalies occurring in periodic plasmonic structures, as previously explained.[17,26] The lattice plasmon resonance was thus devised to match the excitation wavelength of the 785 nm laser, by selection of plasmonic substrates with a lattice period (L) of 500 nm (based on **Equation 2.1**). Upon incubation with the selected metabolite (Kyn), both substrates (**Figure 2.1 e,f**) demonstrated their responsiveness by revealing additional vibrational modes that were not present in the background signal of pristine SERS substrates (red spectra in **Figure 2.1 e,f)**.

Shown in **Figure 2.2a** are Raman and SERS spectra of commercial Kyn and Trp, recorded in the solid state and in solution, respectively. For SERS measurements, 100 μL of a 100 μM analyte solution was drop-casted on the corresponding nanostructured plasmonic substrate and subsequently illuminated with the 785 nm laser. The obtained results showed that the Kyn SERS spectrum is dominated by a narrow peak at 560 cm^{-1}, corresponding to the aminophenyl group.[27] The SERS spectrum of Trp was otherwise characterized by broader peaks, including one localized around 760 cm^{-1}, which corresponds to the indole moiety.[28] Moreover, SERS spectra of commercial Kyn at different concentrations were collected and compared to the SERS spectrum of phosphate buffered saline (PBS) on the same plasmonic support, used as a blank (namely, 0 μM). As noted in **Figure 2.2b**, 1μM was the lowest concentration that could be safely distinguished from the blank, which was sufficient for its detection in the extracellular space at physiological concentrations (10-100 μM).[29] To determine the ratio between Kyn and Trp (Kyn/Trp) by SERS, solutions of the commercial metabolites were co-incubated on superlattice substrates at varying relative concentrations. The characteristic SERS spectral features enabled simultaneous determination of both metabolites, using the peak at 560 cm^{-1} for Kyn and that at 760 cm^{-1} for Trp, which were sufficiently well differentiated despite being a closely related pair of analytes. As shown in **Figure 2.2d**, the relative contribution of the selected peaks gradually changed for different Kyn/Trp ratios. We could therefore approximate the Kyn/Trp coefficient as a function of the ratio between the SERS intensities of these main peaks. Our results confirmed

that semi-quantitative monitoring of both analytes could be achieved, at least within the selected combinations of Kyn-Trp (**Figure 2.2c**), which were further employed to determine IDO-1 activity in cancer cells by SERS.

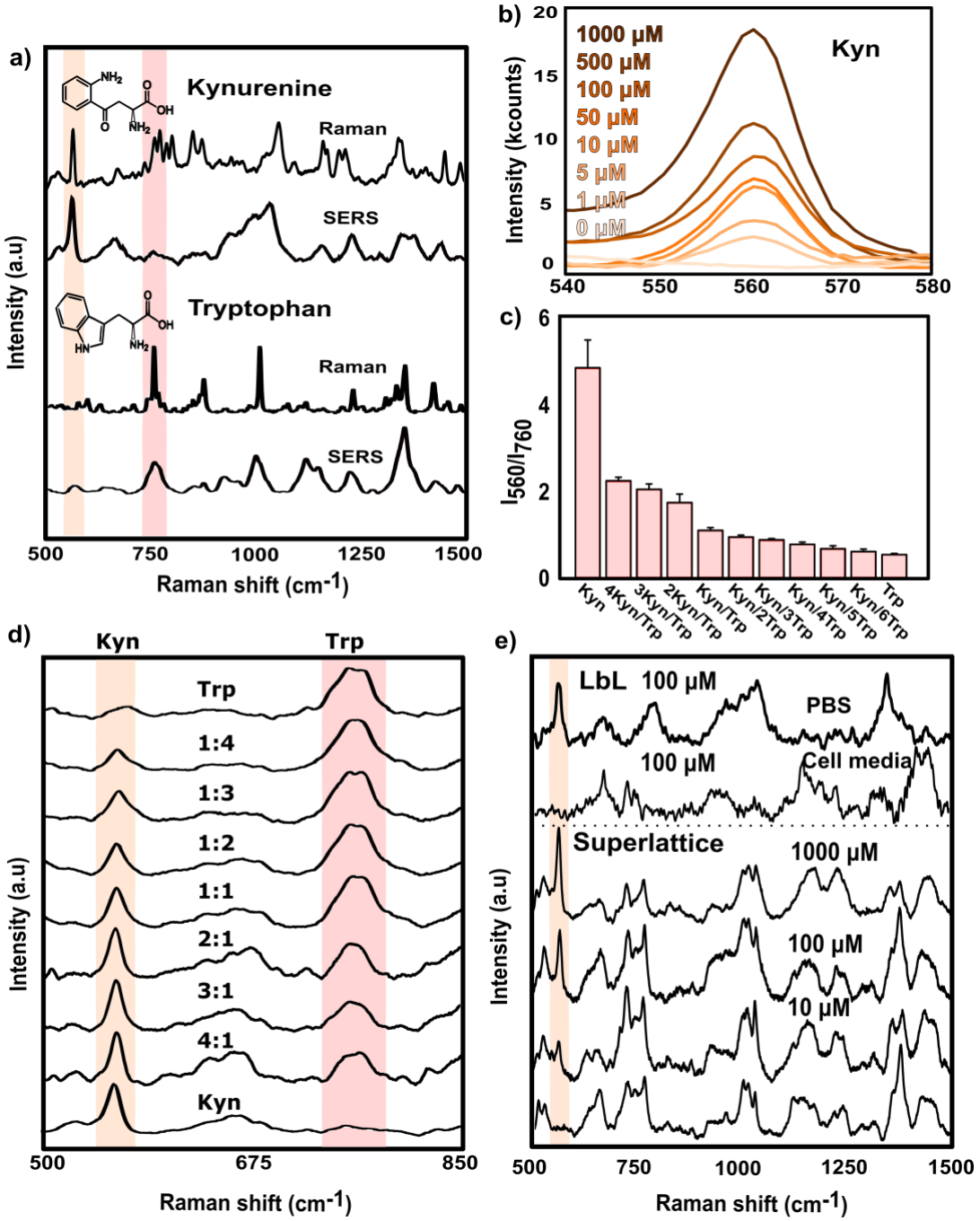

Figure 2.2. a) Comparison of Raman and SERS spectra for kynurenine (Kyn) and tryptophan (Trp), measured in the solid state and in 100 µM aqueous solutions deposited on superlattice substrates. b) Kynurenine SERS spectra at gradually increasing concentrations (0 µM, 1 µM, 5 µM, 1 µM, 50 µM, 100 µM, 500 µM, 1000 µM) in PBS, measured on superlattice substrates. c) Calculated ratio (I_{560}/I_{760}) between SERS spectra intensities at 560 cm^{-1} and 760 cm^{-1}, obtained from the different tryptophan-kynurenine combinations, the error bars show the standard deviation of three independent assays (n=3). d) SERS spectra of kynurenine-tryptophan mixtures with different ratios; the kynurenine characteristic peak (560 cm^{-1}) is highlighted with an orange bar, the tryptophan peak (760 cm^{-1}) with a pink bar. e) SERS spectra from different plasmonic substrates, in PBS and cell media. The presence of cell media masks the signal of the kynurenine peak at 560 cm^{-1} (orange label) and prevents its quantification in LbL substrates. All SERS measurements were performed with a 50× objective, 10 s acquisition time, maximum power of the 785 nm laser 8.48 mW.

It should be noted, however, that these experiments were carried out in PBS solutions, far from the complexity found in real biofluids, where Kyn and Trp are a minor fraction and the likelihood of interferences from other components would significantly increase. Indeed, detection of specific metabolites within complex environments is still considered as one of the major challenges to be addressed by optical detection systems. Although both plasmonic substrates (LBL and superlattices) were sufficiently efficient to identify Kyn in PBS, we observed discrepancies between the spectra obtained using both substrates when incubating different concentrations of Kyn in cell media (Dulbecco's Modified Eagle Medium, DMEM, in 10% fetal bovine serum, FBS). As shown in **Figure 2.2e**, only the superlattice substrate was reliable toward the detection of Kyn in complex media, whereas no significant bands at 560 cm^{-1} could be easily peeked using LBL substrates. This result could be due to the combination of different factors such as the improved performance of plasmonic superlattices, as well as the preferential adsorption of Kyn onto these metallic structures. For the latter, it should be noted that both substrates differ in their surface chemistry, owing to the different functionalization of the employed nanoparticles (see section 6.1 for details of nanoparticles synthesis and their use in substrate fabrication). Moreover, as specified in section 6.2, a combined cleaning step with oxygen plasma followed by UV-ozone was carried out for plasmonic superlattices (just before sample incubation), intended to remove the organic molecules remaining on metallic structures, and thus altering their surface chemistry (note the impact of this procedure on final SERS signal in Figure 6.2). Importantly, when we employed plasmonic superlattices, the detection of Kyn was confirmed at concentrations as low as 10 μM in cell media.

2.2 II) Analysis of metabolic alterations induced by IDO-1 expressing cells

We therefore selected the superlattice substrates to monitor extracellular metabolic alterations, as well as screening the activity of IDO-1 in tumor cells under different conditions. For this purpose, HeLa cells (cell line derived from cervical cancer) were challenged with interferon-gamma (IFN-γ) which reportedly activates IDO-1 expression, as depicted in **Figure 2.3b (** see section 6.7, for cell culture procedures**)**.[30,31] IFN-γ has long been recognized as a pro-inflamatory cytokine that can induce, upon binding to the target cell surface repector, the expression of a battery of genes in the interior of the cell, including that encoding for the IDO-1 enzyme.[32] Noteworthily, those HeLa cells that had been treated with IFN- γ (100 ng/mL) consistently induced IDO-1 expression (**Figure 2.3a**). Cells challenged with IFN-γ were rinsed and fresh media was supplemented with

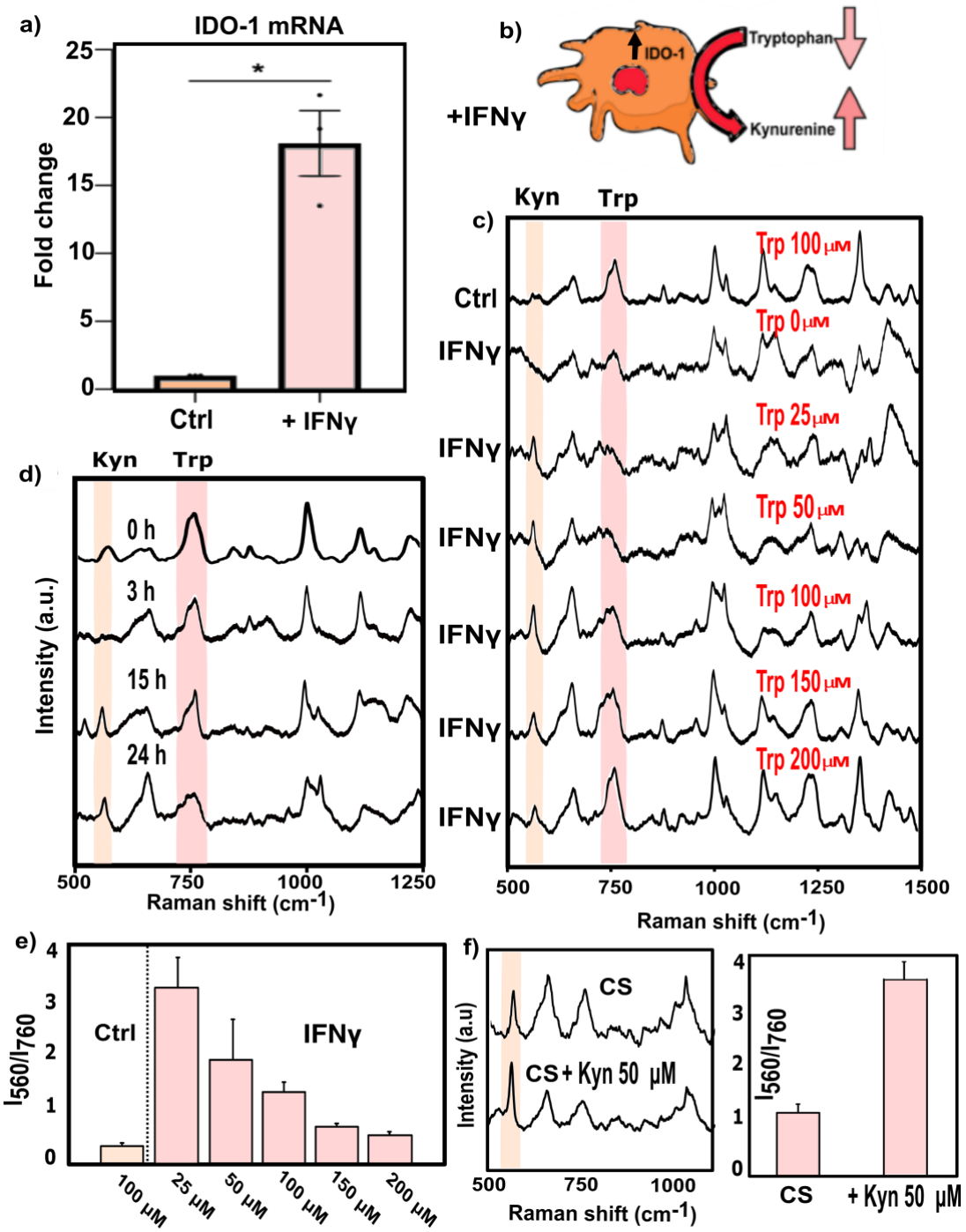

Figure 2.3. a) Changes in IDO expression in the control, compared to IFN-γ activation, observed by RT-qPCR. Results show that, the expression of IDO was significantly increased ($p<0.001$), 18-fold compared to non-activated cells. Error bars represent the standard deviation of three independent experiments. b) Schematic view of the catalytic activity of IDO-1 enzyme overexpressed in tumor cells, upon incubation with IFN- γ, which consumes tryptophan (Trp) and releases kynurenine (Kyn). Fluctuations of Trp and Kyn concentrations in extracellular media can be then tracked by SERS. c) SERS spectra of cell supernatants after 24h. Cells were harvested, upon IFN- γ activation (100ng/mL), except in control, and varying the initial tryptophan concentrations. The orange bar marks the kynurenine peak while the tryptophan signal is indicated by a pink bar. The spectra are the average of 25 measurements from a representative sample. d) SERS spectra of cell supernatants extracted at different times. Cells were previously activated with IFN-γ and incubated with 100 µM of Trp. e) Ratio between Kyn (560 cm^{-1}) and Trp (760 cm^{-1}) in control and after 3 days of IFN-γ conditions (100ng/mL) and Trp supplementation from 25 to 200 µM, as calculated from SERS data. The error bars show the standard deviation of three independent cell assays (n=3). f) SERS spectra of cell supernatant after 24h, namely as CS (IFN-γ, 100 µM Trp). Once the cell supernatant was measured by SERS, a defined concentration of kynurenine was added to the samples and measured again (+ Kyn 50 µM).

varying Trp concentrations, to later monitoring its conversion to Kyn. It should be noted that media was also supplemented with 10 μM of Hemin, a cofactor of IDO-1 enzyme, which is necessary for the tryptophan catalytic conversion.[33] LC-MS-based metabolic measurements of Trp and Kyn confirmed the IFN-γ-elicited conversion of Trp to Kyn, owing to induced IDO-1 expression (see Appendix **S2.1-S2.4**). As shown in **Figure 2.3c**, consistent differences were observed among SERS spectra acquired from media at various conditions. IFN-γ treatment of HeLa cells resulted in the detection of a molecular vibration indicating the presence of Kyn (560 cm^{-1}), whereas no signal could be identified in control experiments. In addition, the absence of supplemented Trp in media prevented the accumulation of Kyn, in line with the lack of IDO-1 substrate. Subsequently, we calculated the Kyn/Trp ratio as described above, obtaining semiquantitative data for the ratio between both metabolites (**Figure 2.3e**). Increasing Trp was consistently accompanied by lower Kyn SERS signal. Additionally, SERS measurements allowed us to study time-dependent changes in a straightforward manner over 24 hours, observing thereby a gradual increment in the collected intensity from the peak at 560 cm^{-1} (**Figure 2.3d**). Finally, to fully validate these results, we enriched the supernatant of HeLa cells overexpressing IDO-1 (CS), with commercial Kyn (+ 50 μM). As expected, the results in **Figure 2.3f** showed an increase in the SERS intensity only at the characteristic wavenumbers of Kyn, as compared with the results obtained before Kyn supplementation. In a similar manner, consistently higher values for the Kyn/Trp ratio were obtained for Kyn-enriched supernatants.

As a complementary strategy to trigger the production of Kyn, we chose to challenge HeLa cells with increasing doses of an IDO-1 co-activator analog, Hemin, which is a commercial analog of the heme group - a non-polypeptide unit required for the biological function of IDO-1 (enzymatic activity represented in **Figure 2.4a**).[33] As illustrated in **Figure 2.4b**, we confirmed that Hemin supplementation is required for Kyn production, since it is involved in the activation of IDO-1. We additionally noticed that Hemin supplementation affected the SERS profile in a dose-dependent manner, beyond the sharp signal at 560 cm^{-1}. **Figure 2.4c** shows that high Hemin concentrations (100 μM) result in an intense SERS band at 725 cm^{-1}, typically assigned to purine derivative metabolites.[34] We also noted an increment in cell death at high Hemin concentration, which suggested a cytotoxic effect of this co-factor (**Figure 2.5a**). This process drove us to speculate that both events, cell death and the release of purine derivatives, were correlated and could be investigated by SERS.

From the unexpected SERS band collected at 725 cm^{-1} in the above described experiments, we performed the measurements of a number of representative purine derivative metabolites, such as ATP, adenine (A), adenosine (Ado), inosine (Ino), and hypoxanthine (HX), which had been

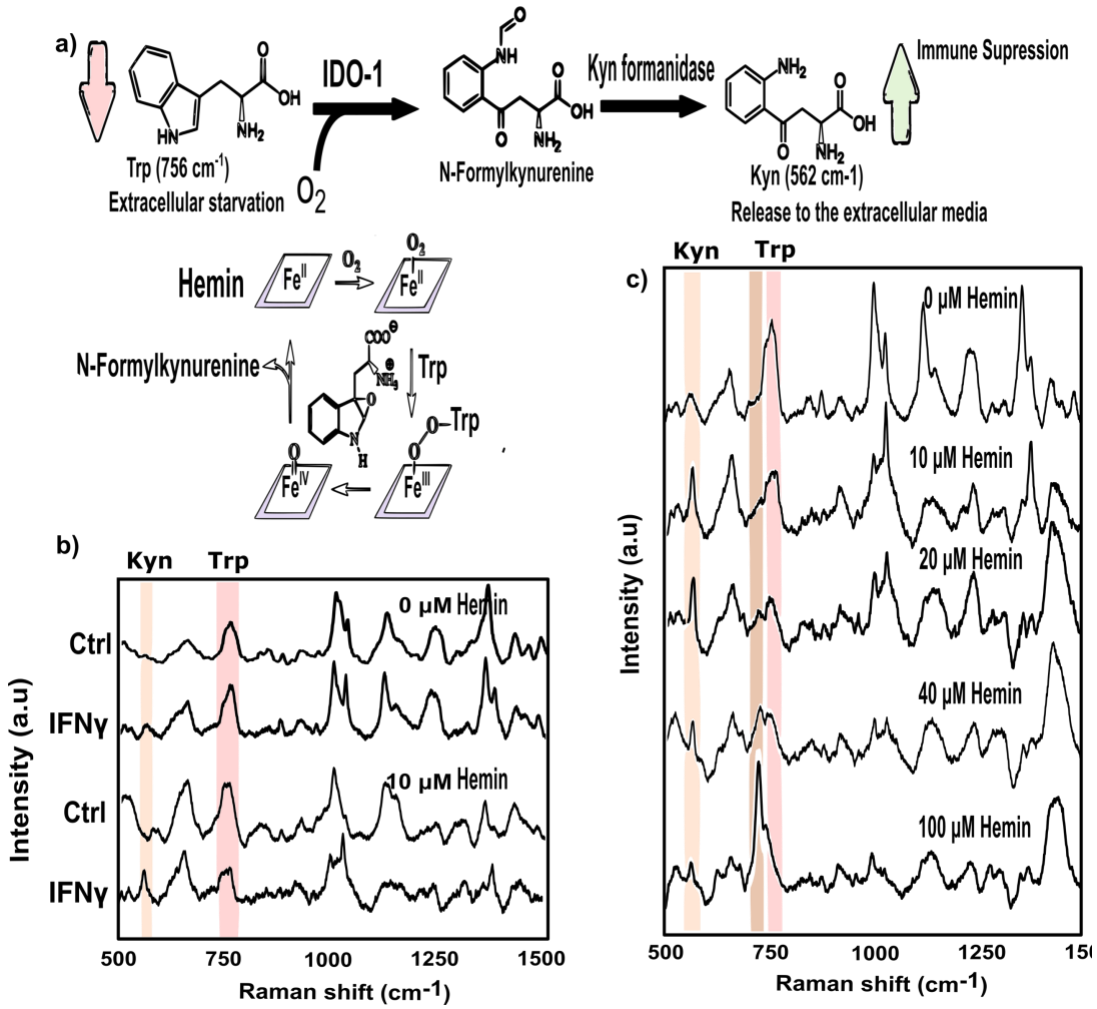

Figure 2.4. a) Schematic view of the catalytic activity of IDO-1 enzyme. Functional activity might be regulated at the level of substrate concentration and holoenzyme assembly (that is, incorporation of the heme prosthetic group) by cofactor availability. b) SERS spectra of cell supernatants obtained from cells which were challenged with 100 µM of Trp and Hemin concentrations (0 or 10 µM), under control or IFN-γ conditions. c) SERS spectra of cell supernatants of IFN-γ activated cells and incubated with 100 µM of Trp and varying concentrations of Hemin (0, 10, 20, 40, 100 µM). The brown bar marks the peak at 725 cm^{-1}. SERS measurements were performed with a 50× objective and 10s acquisition time, the maximum power of the 785 nm laser was 8.48 mW.

reported to display intense bands in similar regions of the SERS spectra.[35] The recorded SERS signals facilitated a moderate distinction between A and HX, as shown in **Figure 2.5c**. Specifically, a mild shift was observed in the main peak, from 735 cm^{-1} in adenine-related molecules (black) to 725 cm^{-1} in HX derivatives (red), attributed to the deamination process between both nitrogenous bases.[36] These results suggest that the SERS fluctuations in **Figure 2.4c** could in principle be attributed to the accumulation of extracellular HX under stressing high concentrations of Hemin.

2.2 III) Detection of extracellular Hypoxanthine accumulation during cell death events

To further examine whether SERS can be employed for the detection of purine bases in the extracellular milieu, we exposed HeLa cells to different stress conditions, such as high concentrations of hydrogen peroxide (H_2O_2) and Staurosporine (STP), which are well-defined inducers of cell stress and death (see stress conditions assays in section 6.7).[37] We measured the SERS spectra from cell supernatants after 24 hours under the selected conditions. We found that, indeed, SERS signals corresponding to the accumulation of purine derivatives were markedly altered under both conditions, in an analogous manner as previously observed in Hemin addition experiments (**Figure 2.5d**). We then tested whether drug concentration would correlate with the intensity of the peak at 725 cm^{-1}, which, as previously stated, can be partly attributed to extracellular HX accumulation. From the results displayed in **Figure 2.5e**, we observed a rising trend, which reached a maximum at 10 μM of STP, when a high percentage of the cells were dead (**Figure 2.5b**). It should be mentioned that the percentage of cell death obtained from cell viability assays showed a good correlation with the trend observed from the SERS intensity of the peak at 725 cm^{-1} (see section 6.8 for details about cell viability quantification) This similarity, together with the results obtained by LC-MS analysis (see Appendix **S2.5-S2.6**), reinforced the idea that both events were connected.

In view of these positive results, we moved toward the application of SERS for in situ sensing of analytes in hydrogel-based cancer models. To this end, we devised a configurable cancer-on-a-chip system containing a more physiologically relevant 3D structure of collagen,[38,39] and then explored the combination of this platform with plasmonic substrates **(Figure 2.5f).** We initially deposited HeLa cells, which had been embedded in collagen, inside printed silicone chambers, which were then filled with cell media (see 3D cell culture protocols in section 6.7). At selected times, the chamber was stacked with a plasmonic substrate and illuminated with the 785 nm laser for SERS measurements **(**images of the final chip configuration can be found in the section 6.4**,** Figure 6.3**).** We found that SERS signals corresponding to the accumulation of HX in the extracellular media could still be tracked with this system under stressing conditions, namely 5 μM STP (**Figure 2.5g**). On the other hand, SERS mapping of control cells (no STP addition) did not reveal any significant signal of HX release after 24 hours. SERS monitoring of HX molecules could be performed by following the intensity of the peak at 725 cm^{-1} over millimeter-scale regions of the extracellular environment (**Figure 2.5h**). The uniformity of HX levels in the recorded maps indicated a suitable diffusion of HX from the hydrogel-based cancer model to the plasmonic substrate.

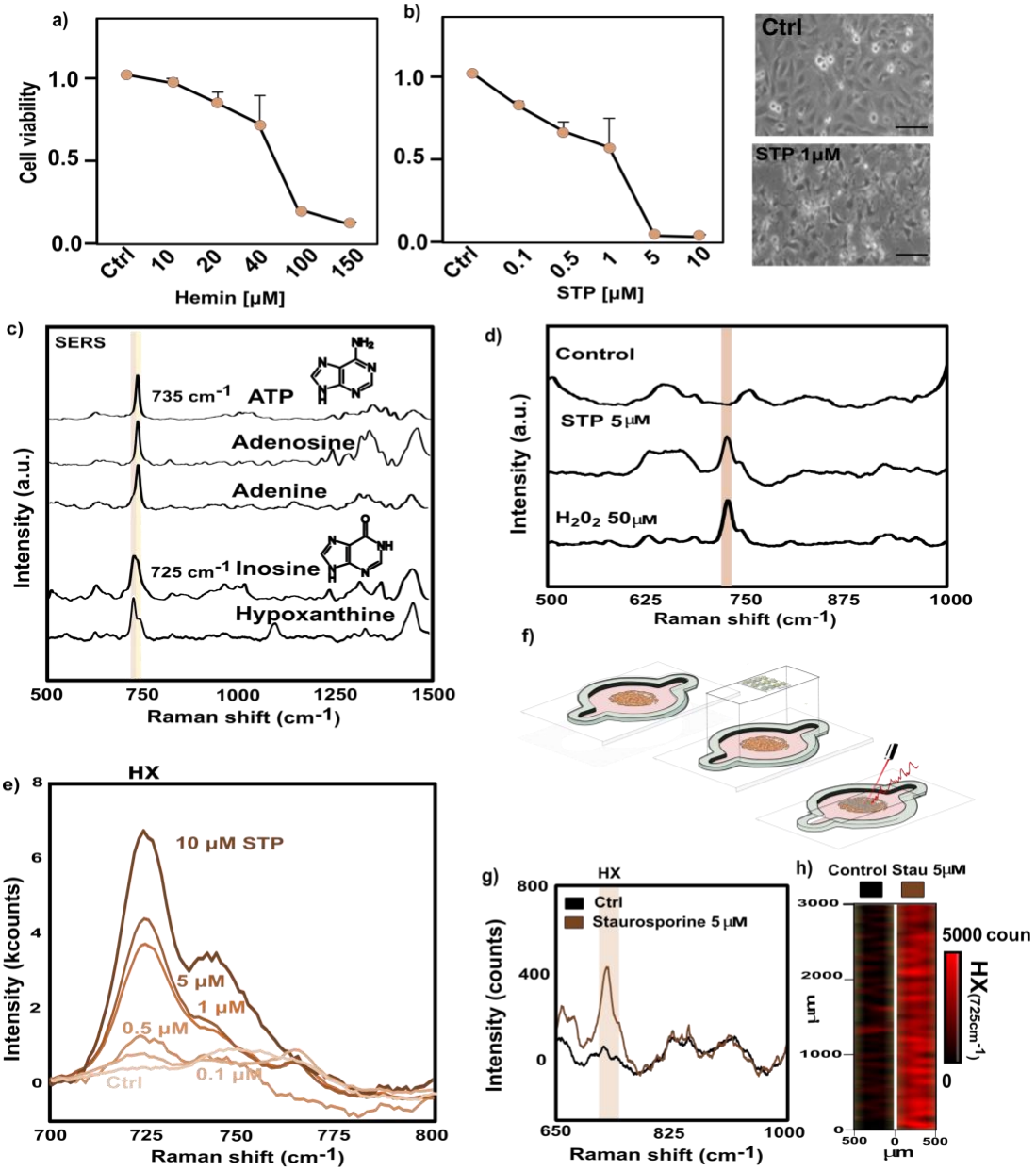

Figure 2.5. a,b) Dose-effect curve of Hemin (a) and STP (b) represented as number of live cells attached (Crystal Violet staining method) normalized to control conditions; error bars represent the standard error of three independent experiments (n = 3). Bright-field (scale bar of 50 µm, 100x magnification) images of control HeLa cells and those exposed to 1 µM STP. c) SERS spectra of A and HX derivative metabolites, brown and yellow bars identify the characteristic peak of HX (725 cm^{-1}) and A (735 cm^{-1}) respectively. SERS measurements were performed with a 50× objective, the maximum power of the 785 nm laser was 8.48 mW, and 10 s of acquisition time. d) SERS spectra of cell supernatants extracted after 24 hours of cell culture, under different stress conditions. The contribution to the averaged spectra of HX related molecules is highlighted by a brown bar. The spectra are the average of 25 measurements on a representative sample. e) SERS spectra of cell supernatants after 24 hours of cell incubation with different STP concentrations. The spectra are the average of 25 measurements on a representative sample. f) Schematic view of the methodology used to combine a 3D cell culture inside a silicon chamber with SERS measurements. g) Average of SERS spectra recorded after 24 hours of control and 5 µM STP incubation. h) SERS mapping (725 cm^{-1}) acquired with an excitation laser wavelength of 785 nm, 10× objective and a laser power of 15.15 mW, for 5 s.

2.2 IV) Imaging of Hemin cytotoxic effect in 3D cell culture

We finally exploited the developed system to monitor Hemin concentration and its cytotoxic effect by SERS. As shown in **Figure 2.6a**, Hemin molecules exhibited a broad absorption band

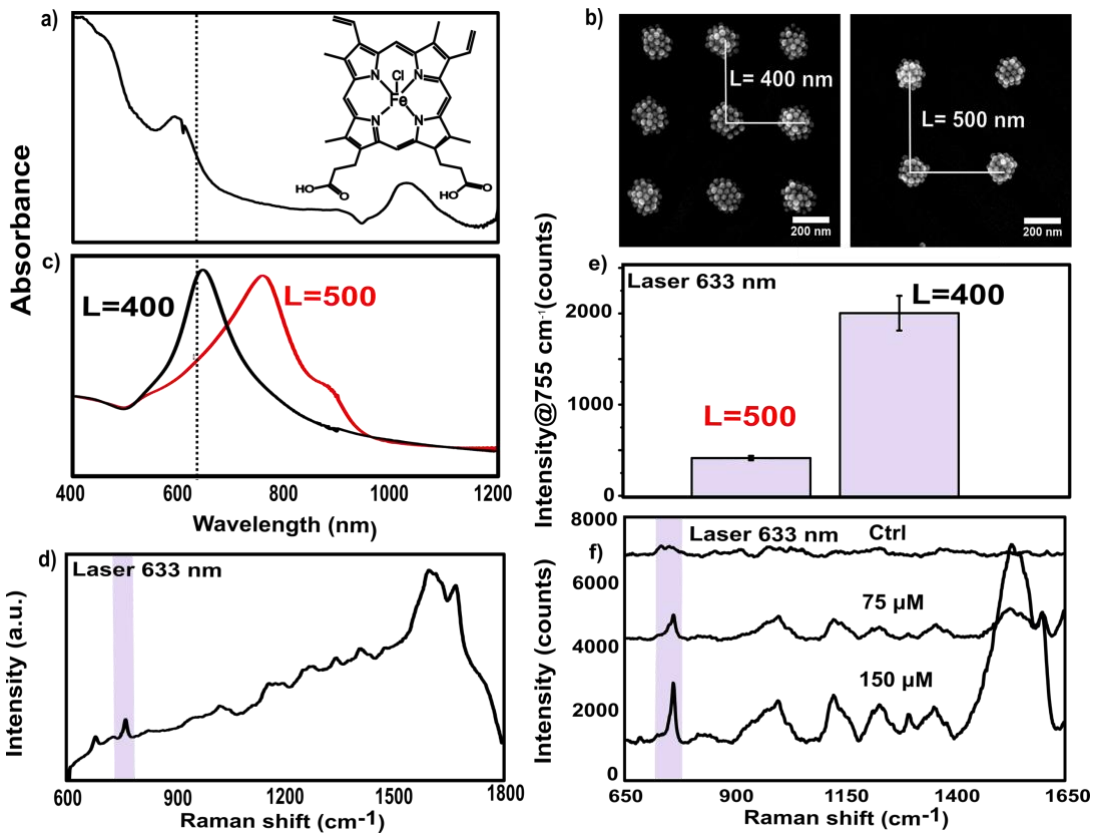

Figure 2.6. a) Normalized Vis-NIR spectrum and chemical structure of Hemin. b) SEM images of two plasmonic superlattices with different lattice parameters, i.e. the distance between AuNPs clusters denoted as "L". c) Normalized Vis-NIR spectra of plasmonic superlattices with different lattice parameters, as labeled. The dotted vertical line indicates the excitation wavelength (633 nm) used for the SERRS measurements of Hemin. d,e) SERRS spectrum of Hemin, 100 µM (d) and the corresponding intensities of the peak at 755 cm^{-1} (purple bar), as a function of the lattice parameter (e). The measurements were recorded with a 50× objective, maximum laser (633 nm) power of 6.54 mW and acquisition time of 10 s. The spectrum is the average of 25 measurements. f) SERRS spectra of cell media after addition of different Hemin concentrations: 1 (0 µM), 2 (75 µM) and 3 (150 µM), displayed spectra are the average of 25 measurements taken from a representative sample, acquired with a 50× objective, a maximum power of 6.54 mW of 633 nm laser and an acquisition time of 10 s. The plasmonic superlattices used as SERRS substrates presented a lattice parameter of 400 nm, to be in resonance with the 633 nm laser.

in the visible, which dropped at 700 nm, so that illumination of an aqueous solution of commercial Hemin with a 633 nm laser led to resonant Raman conditions (explained in section 1.5a). Thus, SERRS (surface-enhanced resonance Raman scattering) rather than SERS spectra of Hemin were recorded (**Figure 2.6d**). Our choice of plasmonic superlattices as SERS substrates offered the possibility of modifying the lattice parameter (L) to obtain a lattice plasmon mode in resonance with the 633 nm laser. By changing the lattice parameter from 500 nm to 400 nm (**Figure 2.6b**), the lattice plasmon mode approached the laser excitation of 633 nm (see **Figure 2.6c** for comparison between both plasmonic superlattices).[17] The results plotted in **Figure 2.6e** demonstrated the achieved improvement in Hemin detection when the lattice plasmon wavelength of the substrate matched the 633 nm excitation laser, through the SERRS pyrrole ring vibration signal of Hemin. Importantly, such a measurement configuration facilitated the monitoring of Hemin at different concentrations in complex media, as shown in **Figure 2.6f**. Hence, in the

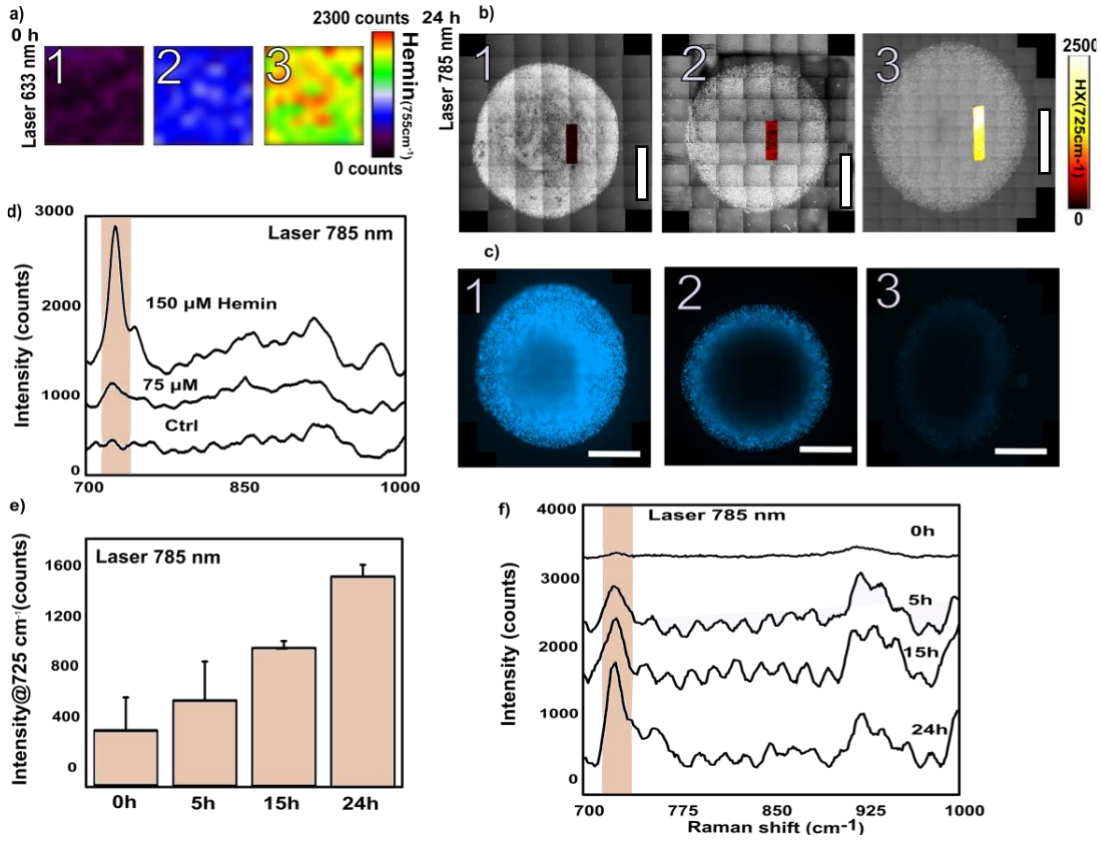

Figure 2.7. a) SERRS mapping (755 cm^{-1}) after addition of different Hemin concentrations: 1 (0 µM), 2 (75 µM) and 3 (150 µM) into the cancer-on-a-chip, over an area of 100x100$µm^2$ on plasmonic superlattices (L = 400 nm). Acquired with a 50× objective, a maximum power of 6.54 mW of 633 nm laser and an acquisition time of 10s. b) Optical image of 24-hours hydrogel-based cancer models captured with a cell observer microscope and superimposed with the corresponding HX SERS mapping (725 cm^{-1}) of a selected area. Numbers at upper corner indicate different initial Hemin concentrations: 1 (0 µM), 2 (75 µM) and 3 (150 µM); scale bar: 2 mm. c) Fluorescence image of tumor cells embedded in collagen at varying Hemin concentrations, namely 1 (0 µM), 2 (75 µM), 3 (150 µM). Live cells were stained with Cytocalcalcein (blue), images were taken with a 100x magnification. Scale bar is 2.5 mm. d) Average of the SERS spectra (200 measurements) recorded in the hydrogel-based cancer models after 24 hours of treatment with varying Hemin concentrations with 785 nm laser and L = 500 nm e) Relative SERS intensities at 725 cm^{-1}, recorded at 0, 5, 15 and 24h of incubation with the highest Hemin concentration (150 µM); error bars refer to standard deviation of three different measurements (n=3). All measurements were acquired with an excitation laser wavelength of 785 nm, 10× objective, and a laser power of 15.15 mW for 10 s. f) Average of the SERS spectra (25 measurements) recorded over the time in the hydrogel-based cancer models at 150 µM Hemin.

following experiments, we had to reconfigure the cancer-on-a-chip system over the course of the experimental protocol, alternating plasmonic substrates with different lattice parameters (L = 400 nm or 500 nm), to efficiently match the different laser wavelengths (633 nm and 785 nm), and thereby facilitating the detection of both metabolites - Hemin and HX.

We challenged the 3D cell cultures with different Hemin concentrations (Control, 75, 100 µM) and measured them in the cancer-on-a-chip platform by SERRS (633 nm laser; L = 400nm), as shown in **Figure 2.7a.** After 24 hours, we reconfigured the system by replacing the plasmonic substrates (L=500 nm) and subsequently irradiated with the 785 nm laser. The results shown in **Figure 2.7b** illustrate the effect of Hemin on the extracellular HX concentration (average SERS spectra in **Figure 2.7d**), again confirming that higher Hemin concentrations correlated with higher

cytotoxicity, measured by fluorescence microscopy in **Figure 2.7c** (live cells were labeled with a blue probe). We finally evaluated the impact of the highest Hemin concentration over time. Notably, the SERS fingerprint of HX was clearly identified as early as five hours after initiating the treatment, and the signal intensity increased over time, as can be seen in the SERS spectra recorded at 15 and 24 hours (**Figure 2.7e** and **2.7f**). These results indicated that high Hemin concentrations can also have an early cytotoxic effect on cancer cells, which eventually altered the extracellular milieu.

2.3 Conclusions

The present chapter demonstrates the application of SERS for the detection of extracellular tumor metabolites under diverse cell culture conditions. Significantly, IDO-1 activity in tumor cells was monitored by SERS, measuring simultaneously extracellular changes in both the substrate and the product of its enzymatic activity (Trp and Kyn, respectively). By using highly efficient nanostructured plasmonic substrates, we were able to estimate by SERS the Kyn/Trp ratio, which is well known to correlate with bad prognosis in cancer patients. Moreover, we observed that the cofactor of the IDO-1 enzyme, Hemin, affects the SERS profile in a dose-dependent manner and this SERS signal was further associated with the induction of cell death at toxic concentrations of Hemin. Additionally, the levels of purine derivative metabolites were directly related to cell death induction, thus working as a suitable biomarker of cell death. We consider that the tools and methods presented throughout this chapter can be incorporated into the next-generation diagnostic SERS technologies.

The reported approach notably provided an additional tool for the spatiotemporal analysis of metabolite alterations and their response under different conditions. We demonstrated that these label-free studies can be extended to in situ imaging of metabolite exchanges in tumor microenvironments. This sensitive and cost-effective plasmonic substrate was therefore effectively combined with 3D cell culture models, which more closely recreate the biochemical and biophysical cues in the TME and are considered as paramount tools for future diagnosis and therapy. Still, more complex cell models are required to better examine metabolic interactions among different cell types. Moreover, although this approach has validated the use of SERS as an alternative strategy for metabolomics, the focus was only centered on known metabolic processes, already described by other technologies (e.g., LC-MS or fluorescence). Given the fast assessment and high sensitivity that SERS technology has shown, we foresee that different co-cultures of cancer and stromal cells could be established on purposely devised cancer-on-a-chip platforms to elucidate novel mechanisms of cell-to-cell communication.

Additionally, the development of standardized protocols and data processing programs for multiple metabolite quantification in complex environments is still a pending challenge. The implementation of multivariate and artificial intelligence AI (machine learning in particular) algorithms appears, at this moment, as a crucial advancement to extend these SERS-based metabolomics studies to a greater variety of applications. To take steps in this direction, we will cover in Chapter 4 the analysis of similar SERS spectra by methods based upon machine learning techniques, unveiling additional information contained in such spectra.

2.4 References

1. Lyssiotis, C. A. & Kimmelman, A. C. Metabolic interactions in the tumor microenvironment. *Trends Cell. Biol.* **27**, 863–875 (2017).
2. Martinez-Outschoorn, U. E., Peiris-Pagés, M., Pestell, R. G., Sotgia, F. & Lisanti, M. P. Cancer metabolism: a therapeutic perspective. *Nat. Rev. Clin. Oncol.* **14**, 11–31 (2017).
3. Arruabarrena-Aristorena, A., Zabala-Letona, A. & Carracedo, A. Oil for the cancer engine: The cross-talk between oncogenic signaling and polyamine metabolism. *Sci. Adv.* **4**, eaar2606. (2018).
4. Wegiel, B., Vuerich, M., Daneshmandi, S. & Seth, P. Metabolic switch in the tumor microenvironment determines immune responses to anti-cancer Therapy. *Front. Oncol.* **8**, 284 (2018).
5. Wang, H., Franco, F. & Ho, P. C. Metabolic regulation of Tregs in cancer: opportunities for immunotherapy. *Trends Cancer* **3**, 583–592 (2017).
6. Murray, P. J. Amino acid auxotrophy as a system of immunological control nodes. *Nat. Immunol.* **17**, 132–139 (2016).
7. Anastasiou, D. Tumour microenvironment factors shaping the cancer metabolism landscape. *Br. J. Cancer* **116**, 277–286 (2017).
8. Yamazaki, F. & Kid, R. Mechanism of interferon-gamma action. Characterization of indoleamine 2,3-dioxygenase in cultured human cells induced by interferon-gamma and evaluation of the enzyme-mediated tryptophan degradation in its anticellular activity. *J. Biol Chem* **263**, 2041-2048. (1988).
9. Yong S, L. S. Rapid separation of tryptophan, kynurenines, and indoles using reversed-phase high-performance liquid chromatography. *J Chromatogr.* **175**, 343–346 (1979).
10. Edison, A. S. *et al.* The future of NMR-based metabolomics. *Curr. Opin. Biotechnol.* **43**, 34–40 (2017).
11. Lu, W. *et al.* Metabolite measurement: Pitfalls to avoid and practices to follow. *Annu. Rev. Biochem.* ***86***, 277–304 (2017).
12. Ntziachristos, V., Pleitez, M. A., Aime, S. & Brindle, K. M. Emerging technologies to image tissue Metabolism. *Cell Metab.* **29**, 518–538 (2019).
13. Langer, J. *et al.* Present and future of surface-enhanced Raman scattering. **14**, 28–117 (2020)
14. Bodelón, G. *et al.* Detection and imaging of quorum sensing in Pseudomonas aeruginosa biofilm communities by surface-enhanced resonance Raman scattering. *Nat. Mater.* **15**, 1203–1211 (2016).

15. Feliu, N. *et al.* SERS quantification and characterization of proteins and other biomolecules. *Langmuir* **38**, 9711–9730 (2017).
16. Kang, B., Austin, L. A. & El-sayed, M. A. Observing real-time molecular event dynamics of apoptosis in living cancer cells using. *ACS Nano* **8**, 4883–4892 (2014).
17. Matricardi, C. *et al.* Gold nanoparticle plasmonic superlattices as surface-enhanced Raman spectroscopy substrates. *ACS Nano* **12**, 8531–8539 (2018).
18. Cheong, J. E. & Sun, L. Targeting the IDO1/TDO2–KYN–AhR pathway for cancer immunotherapy – challenges and opportunities. *Trends Pharmacol. Sci.* **39**, 307–325 (2018).
19. Nguyen, N. T. *et al.* Aryl hydrocarbon receptor negatively regulates dendritic cell immunogenicity via a kynurenine-dependent mechanism. *Proc. Natl. Acad. Sci.* **107**, 19961–19966 (2010).
20. Antonioli, L., Blandizzi, C., Pacher, P. & Haskó, G. Immunity, inflammation and cancer: A leading role for adenosine. *Nat. Rev. Cancer* **13**, 842–857 (2013).
21. Hernandez, C., Huebener, P. & Schwabe, R. F. Damage-associated molecular patterns in cancer: A double-edged sword. *Oncogene* **35**, 5931–5941 (2016).
22. Renner, K. *et al.* Metabolic hallmarks of tumor and immune cells in the tumor microenvironment. *Front. Immunol.* **8**, 248 (2017).
23. Singer, K., Cheng, W.-C., Kreutz, M., Ho, P.-C. & Siska, P. J. Immunometabolism in cancer at a glance. *Dis. Models Mech.* **11**, dmm034272 (2018).
24. Bodelón, G. *et al.* Imaging bacterial interspecies chemical interactions by surface-enhanced Raman scattering. *ACS Nano* **11**, 4631–4640 (2017).
25. Hanske, C. *et al.* Solvent-assisted self-assembly of gold nanorods into hierarchically organized plasmonic mesostructures. *ACS Appl. Mater. Interfaces* **11**, 11763–11771 (2019).
26. Lenzi, E., Jimenez de Aberasturi, D. & Liz-Marzán, L. M. Surface-enhanced Raman scattering tags for three-dimensional bioimaging and biomarker detection. *ACS Sen.s* **4**, 1126−1137 (2019).
27 Nie, C. G. Castillo, K. L. Bergbauer, J. F. R. Kuck, I. R. Nabiev & N. T. Yu. Surface-Enhanced Raman Spectra of Eye Lens Pigments. *Appl. Spectrosc.* **44**, 571 (1990).
28 Q. Tu, J. Eisen, C. Chang, Surface-enhanced Raman spectroscopy study of indolic molecules adsorbed on gold colloids *J. Biomed. Opt.* **15**, 20512 (2010).
29 Munn, D. H. & Mellor, A. L. IDO in the tumor microenvironment: Inflammation, counter-regulation, and tolerance. *Trends Immunol.* **37**, 193–207 (2016).
30. De Ravin, S. S. *et al.* Tryptophan/kynurenine metabolism in human leukocytes is independent of superoxide and is fully maintained in chronic granulomatous disease. *Blood* **116**, 1755–1760 (2010).
31 Walter, D. *et al.* A new, simple , bioassay for human IFN-y. *J. Immunol. Methods* **205**, (1994).
32. Nelp, M. T. *et al.* Immune-modulating enzyme indoleamine 2,3-dioxygenase is effectively inhibited by targeting its apo-form. *Proc. Natl. Acad. Sci.* **115**, 3249–3254 (2018).
33. Basran, J. *et al.* The mechanism of formation of N-formylkynurenine by heme dioxygenases. *J Am. Chem. Soc.* **133**, 16251–16257 (2011).
34. Premasiri, W. R. *et al.* The biochemical origins of the surface-enhanced Raman spectra of bacteria : a metabolomics profiling by SERS. *Anal. Bioanal. Chem.* **408**, 4631–4647 (2016).

35. Chiang, S., Chen, S. & Chang, L. A dual role of Heme oxygenase-1 in cancer cells. *Int. J. Mol. Sci.* **20**, 39 (2019).

36 Premasiri, W. R., Lee, J. C. & Ziegler, L. D. Surface-enhanced Raman scattering of whole human blood, blood plasma, and red blood cells: cellular processes and bioanalytical sensing. *J. Phys. Chem. B* **116**, 9376–9386 (2012)

37. Kabir, J., Lobo, M. & Zachary, I. Staurosporine induces endothelial cell apoptosis via focal adhesion kinase dephosphorylation and focal adhesion disassembly independent of focal adhesion kinase proteolysis. *Biochem. J.* **367**, 145–155 (2002).

38. Yi, H. *et al.* A bioprinted human-glioblastoma-on-a-chip for the identification of patient-specific responses to chemoradiotherapy. *Nat. Biomed. Eng.* **3**, 509–519 (2019).

39. Yu, J. *et al.* Reconfigurable open microfluidics for studying the spatiotemporal dynamics of paracrine signalling. *Nat. Biomed.l Eng.* **3**, 830–841 (2019).

CHAPTER 3

"Preventing Memory Effects in SERS Substrates by Polymer Coating and Laser-Activated Deprotection with Time and Space Resolution"

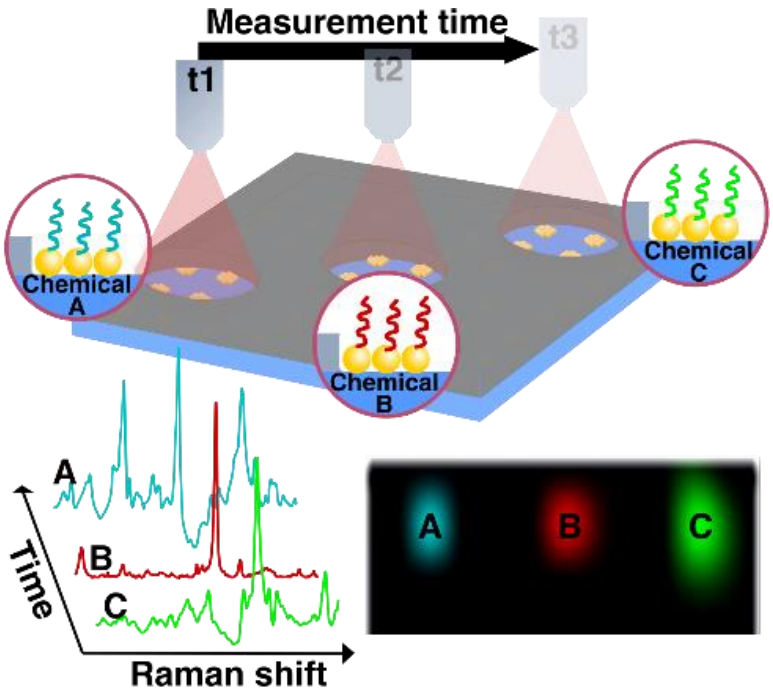

This Chapter abounds in the potential of SERS for in situ biomonitoring, through the analysis of cell events at the point of interest, to retrieve accurate metabolic information in real time. Such in situ measurements are often accompanied by underlying problems when recording successive measurements within complex environments. A common source of uncertainty in real-time SERS measurements originates from the irreversible adsorption of (analyte) molecules onto the plasmonic substrate, which may interfere in subsequent measurements. This so-called "SERS memory effect" leads to measurements that do not accurately reflect varying conditions of the sample over time. We introduced a strategy that overcomes this detrimental effect, by applying a thermolabile sheathing layer of poly(lactic co-glycolic acid) (PLGA) over state-of-the-art plasmonic substrates. The presence of the PLGA layer prevents unwanted adsorption of analyte molecule(s) from solution, whereas SERS measurements can be subsequently made by locally etching the sheathing layer. By using this approach, we could not only perform real time sensing of multiple analytes flowing into microfluidic devices, but we were also able to improve the detection of metabolites in real time.

3.1 Introduction

SERS spectroscopy has been proven to facilitate the identification of trace analytes through the detection of their characteristic vibrational fingerprints, even in a multiplex fashion.[1] On this account, SERS has emerged as a promising chemical monitoring method, with applications in various fields including biosensing,[2] food control,[3] and detection of hazardous materials,[4] among others. As explained in detail in Chapter 1, SERS relies on the plasmonic properties of noble metal nanostructures to enhance the Raman signal of adsorbed molecules. The confinement of light at nanoscale volumes by plasmonic nanomaterials is thus responsible for a dramatic increase in sensitivity, which can go as far as single-molecule detection.[5]

Indeed, key features of SERS are its non-invasive character and label-free detection, which promise the potential of performing in situ measurements, e.g. in the clinic or in the field. Still, to achieve in situ monitoring not only further development in portable Raman spectrometers is required, but also long-term SERS detection in real time represents a complex challenge. An example of application would be the implementation of real-time SERS measurements in flow for monitoring water pollutants.[6,7,8] On the other hand, we have demonstrated that SERS detection of biomolecules released by living organisms uncovers highly valuable information, e.g. on their cellular state and function.[9] Thus, real-time measurements are likely to impact a wide variety of fields, from medical diagnosis to the biotechnology industry. However, an additional drawback arises when molecules adsorb strongly on the surface of the plasmonic substrate,[10,11] so that their corresponding Raman signal would remain in subsequent measurements, even at later stages of incubation with different analytes. This so-called "memory effect" limits real-time detection using standard SERS strategies, in which analyte solutions are continuously in direct contact with the plasmonic substrate. A common approach to reliably monitor changes in the chemical composition of a solution involves the use of a freshly-made substrate every time a measurement is to be made. Even if it works, this strategy does not allow continuous in-flow SERS measurements without operator intervention, or automation. Arguably, using a fresh SERS substrate for every measurement imposes a heavy economic handicap, particularly when measurements for extended periods of time or detection of different analytes are required.

Different solutions have been proposed to fabricate re-usable SERS substrates and thus eligible for real-time sensing. The main strategy typically consists of cleaning the substrate to remove molecular adsorbates. Some cleaning techniques based on physicochemical treatments, such as UV-ozone, or incubation with different solvents have allowed the recycling of plasmonic substrates for SERS measurements.[12,13] It should be noted that such techniques still do not allow for in situ measurements, since the substrates must be removed from the solution of interest during

the cleaning process. Different examples utilize photocatalytic materials to degrade sulfur bonds between the analyte and the metallic surface by photocatalysis.[14,15] Other authors have otherwise shown in situ SERS measurements in microfluidic channels by electrical regeneration of silver wires.[16] Whereas these methods enable the monitoring of chemical species in real time, they can barely be translated into efficient plasmonic systems. In addition, these procedures typically entail long cleaning periods, which slows down the detection process and thereby the likelihood of affecting the quality of the substrate. A different strategy, followed by Gao and coworkers, comprises the in situ synthesis of plasmonic nanoparticles inside a microfluidic channel, meaning that a specific synthesis must take place for each measurement point. Although it does resolve the SERS memory effect, such an approach requires a high consumption of material and leaves "useless" nanoparticles in the microfluidic outlet, causing an additional limitation for real-time sensing.[17,18]

We propose in this chapter an alternative concept, based upon the initial covering of the entire plasmonic surface with a thermolabile sheathing layer, which not only would allow long-term monitoring through the identification and/or quantification of analyte(s), but also efficient spatial and temporal control over the adsorption of biomolecules (see section 1.5d IV). The devised method involves as a first step the spin-coating of a layer of poly(lactic co glycolic acid) (PLGA) – a polymer that has been broadly utilized for biological applications – on a selected plasmonic substrate.[19,20] Besides its biocompatibility, it has been previously demonstrated that site-selective PLGA degradation can be achieved by laser irradiation.[21] In this particular implementation, photodegradation was attained by first embedding AuNRs within the polymeric material, so that PLGA could be disrupted by photothermal heating caused upon the irradiation of AuNRs with a resonant laser (see section 1.5c).[22] In a similar context, other studies have demonstrated that the photothermal effect can be exploited to alter the permeability of different polymers, such as poly-(N-isopropylacrylamide) (pNIPAM), upon NIR irradiation.[23]

We hypothesized that the deposited PLGA layer should protect the SERS substrate by preventing the adsorption of analyte molecule(s) from solution. Upon laser irradiation at a sufficiently high fluence, the plasmonic photothermal effect would open a micron-sized hole in the PLGA layer. The so-created cavity would then act as an open window in the PLGA layer, rendering the plasmonic substrate underneath accessible to the target analyte(s) at that particular spot. By repeated irradiation at different locations (and different times), multiple windows can be opened at will, so that freshly exposed areas of the plasmonic substrate are used each time for new SERS measurements and chemical analysis of the solution. The versatility of this technique would warrant its implementation into multiple experimental setups, including real-time measurements

of fluids within microfluidic channels or monitoring of metabolite fluctuations in biological environments.

Conventionally, the design and optimization of plasmonic substrates has been one of the major subjects of study in the field, underpinning the development of sensors with greater SERS performance.[24,25] Such substrates are intended to provide high and uniform near-field enhancements, so that intense SERS signals can be recorded from arbitrary spots, even for low concentrations of the target analytes.[26,27] However, sensitivity enhancement is often accompanied by limitations in reproducibility, multiplexing ability and reusability in practical applications. Whereas the optimization of enhancement factors has been extensively studied, issues connected with real-time measurements and reusability have not been adequately addressed so far. Hence, although current technology allows the ultrasensitive detection of multiple analytes,[28] its practical implementation for continuous monitoring is still in its infancy. In this context, we introduce a simple methodology that allows the transformation of state-of-the-art SERS substrates into long-term detection platforms for in situ sensing applications (**Figure 3.1**)

3.2. Results and discussion

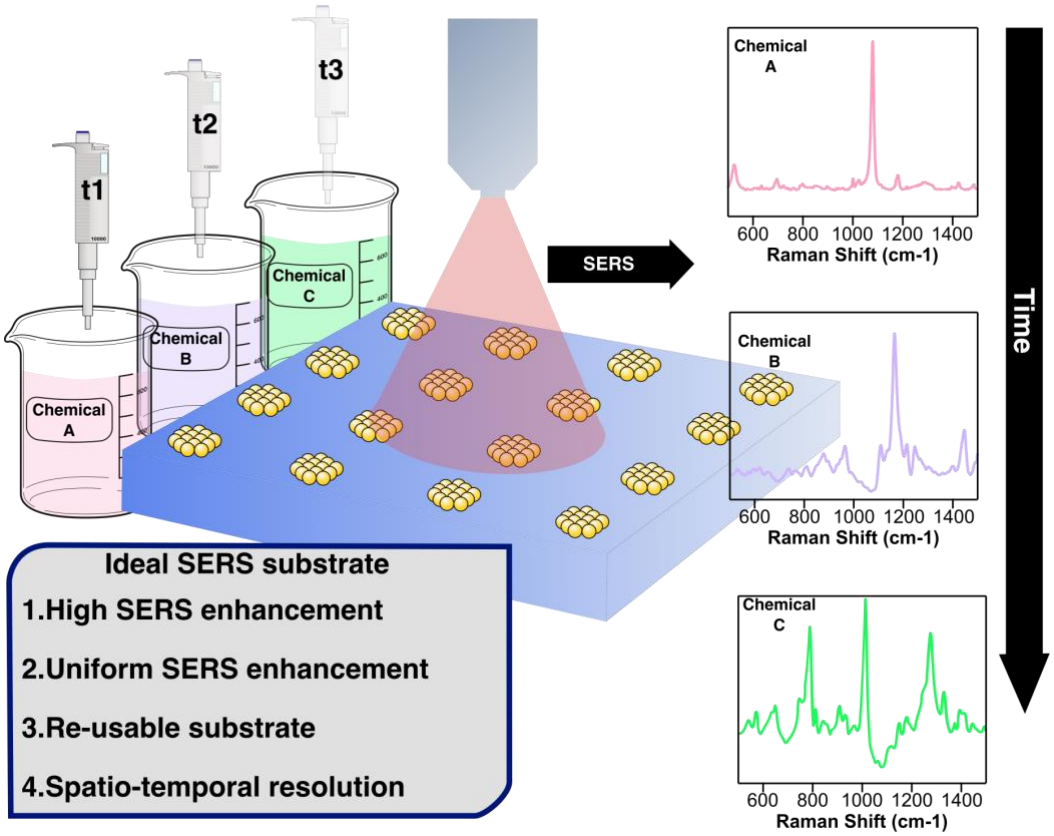

Figure 3.1. Requisites for real-time SERS substrates. An ideal SERS-based system would allow for continuous monitoring of chemical variations in solution, with time and space resolution.

3.2 I) Plasmonic superlattices coated with PLGA for SERS sensing

We initially aimed at providing additional features to the plasmonic substrates described in Chapter 2 – known as plasmonic superlattices –, which comprise regular arrays of clusters made of hexagonally packed nanospheres (**Figure 3.2b**).[29] However, they also suffered from the above-described shortcomings, related to reliable measurements over time (**Figure 3.2a**). This issue could be directly observed in **Figure 3.2c**. Upon incubation with a 100 μM solution of 4-mercaptobenzoic acid (4-MBA), its characteristic vibration at 1078 cm^{-1}, corresponding to the ν_{12}(C-C) ring stretching mode[30] (pink highlighted region in **Figure 3.2c**), was unequivocally detected. However, the SERS memory effect did not allow us to re-use the same plasmonic superlattice. Therefore, the 4-MBA peak still dominated the SERS spectrum, even after extensive rinsing with water and incubation with 100 μM nicotinamide (NAm). In contrast, no peak associated to NAm (expected at the position marked by the orange bar in **Figure 3.2c**) could be identified under these conditions. Similarly, when adding a mixture of 4-MBA + NAm after 4-MBA incubation, only the signal of 4-MBA was registered. We interpreted these results in terms of 4-MBA molecules remaining anchored on the superlattice substrate; the irreversible adsorption of 4-MBA not only leads to an intense SERS signal, but also compromises the adsorption of NAm molecules onto the AuNPs. Such an unsatisfactory performance was repeatedly observed with different types of plasmonic substrates, analytes and concentrations, even with various biomolecules (see **Figure 3.2d,e**), indicating a widespread impact of the observed phenomenon.

As a solution to this commonly unwanted effect, and in general to the single-use limitation of SERS substrates, we proposed the deposition of a polymer coating to protect the plasmonic substrate. The dispensed cover should then act as a sheathing layer that can be readily disrupted by laser irradiation and photothermal degradation. Removal of the polymer layer at the irradiation spot would render the underlying AuNPs available for interaction with the probe solution, thereby avoiding potential interferences derived from continuous exposition. To this aim, we first selected PLGA with a lactic/glycolic content ratio of 75:25 because of its well-described thermal degradation[31] and biocompatibility.[32] For the deposition of a PLGA thin film over the superlattice, we spin-coated a solution of 12 wt% PLGA/ethyl acetate (200 μL; 1500 rpm; 30s) on top of the plasmonic substrate. Of note, the solvent of the PLGA solution was found to strongly affect the degree of sample coverage. Whereas the use of PLGA/acetone solutions only provided

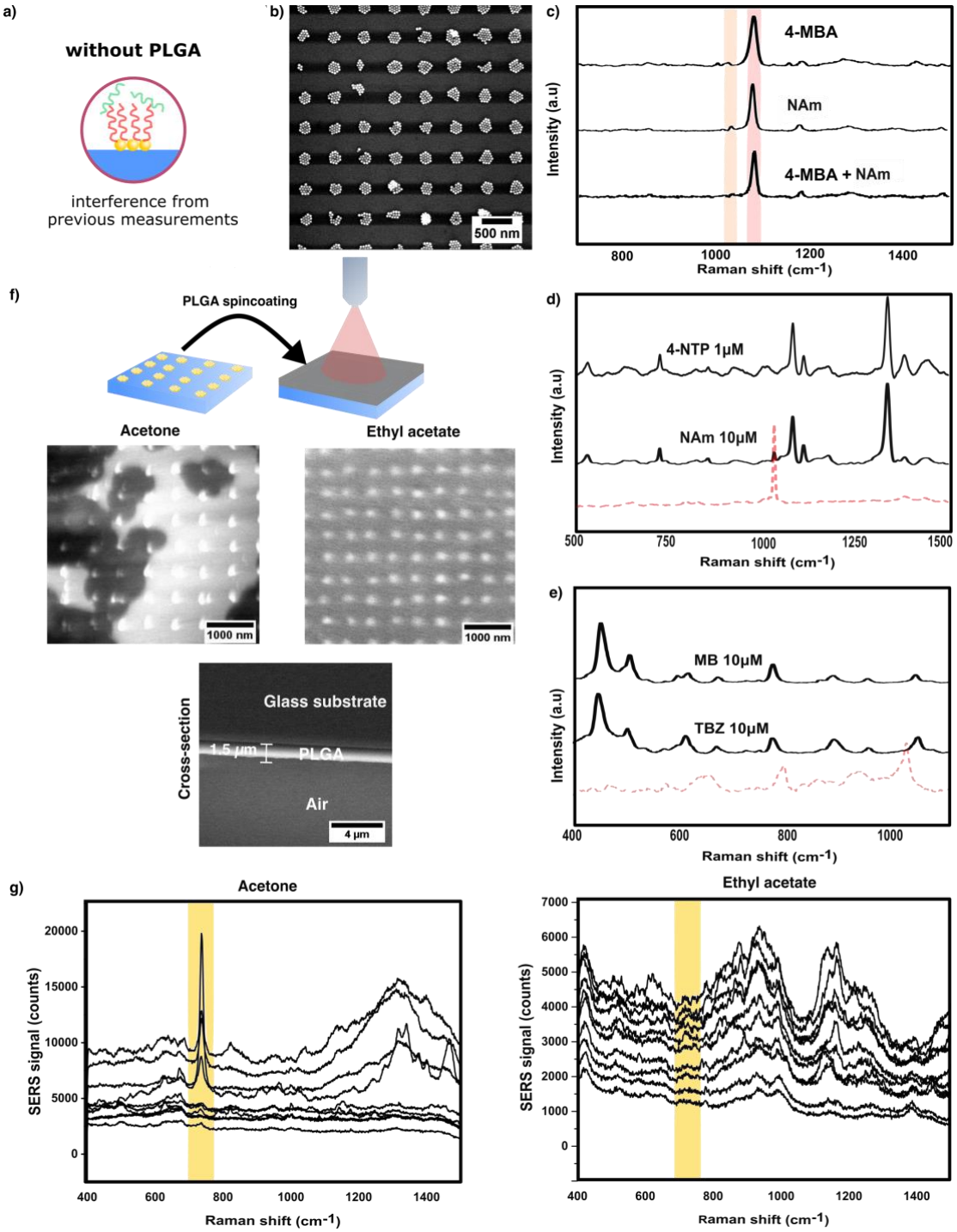

Figure 3.2. a) Scheme of an uncoated plasmonic substrate: the adsorbed red analyte prevents the attachment of subsequently added green analyte. b) Representative SEM image of a plasmonic superlattice. c) SERS spectra from a superlattice, upon the sequential addition of 100 μM solutions of 4-MBA, nicotinamide, and finally a 50:50 mixed solution of 4-MBA and NAm. All measurements were performed with a 50× objective, 1 s acquisition time, and a maximum power of the 785 nm laser of 0.018 mW/μm^2. d) e) Example of SERS memory effect after incubation with various analytes; a sequential combination of 4-NTP with NAm (d) and MB followed by TBZ. The dotted red lines indicate the signal of the analytes NAm and TBZ. acquired on pristine substrates. f) PLGA-SERS strategy: a plasmonic superlattice is covered with PLGA by spin coating. SEM images of PLGA coatings made from PLGA dissolved in acetone and ethyl acetate. Besides, SEM image of the cross section of a PLGA coating film made from PLGA dissolved in ethyl acetate. In g) the signal of the incubated analyte (Adenosine, 100 μM) is observed at various areas over the plasmonic superlattice spin-coated with PLGA dissolved in acetone, due to the inhomogeneous coverage of the plasmonic component by the PLGA film. On the other hand, a perfect coverage was obtained by spin-coating from PLGA dissolved in ethyl acetate. In this case, the SERS spectra show no trace of adenosine from the same solution incubated on top of the substrate.

a partial coating of the plasmonic surface, PLGA/ethyl acetate solutions yielded homogenous films with a uniform thickness of 1.5 μm on the whole substrate (measured by cross-sectional SEM images, see **Figure 3.2f**). Homogenous PLGA coatings made the plasmonic substrates inaccessible to analytes in solution, as demonstrated by the absence of SERS signals from arbitrary spots on the sample, upon incubation with a 4-MBA solution (**Figure 3.2g**). Conversely, irregular coating of the plasmonic substrates by PLGA yielded some impermeable regions, while others areas of the substrate were accessible to the probe solution, as exemplified by the corresponding SEM image and SERS spectra of PLGA/acetone solutions in **Figure 3.2f,g**. Hence, we prepared all the following samples by using ethyl acetate as the solvent, which consistently resulted in complete coverage of the gold nanoparticle superlattices.

PLGA is a thermodegradable polymer, meaning that it can be degraded into its building blocks (glycolic acid and lactic acid) upon heating.[33] In our experimental design, heat is generated by photothermal conversion upon irradiation of the plasmonic superlattice with an intense laser beam –as generally described in Chapter 1 for plasmonic nanomaterials. In the designed configuration, such a plasmonic heating effect would eventually cause a localized degradation of the PLGA layer at the illumination area, leading to local diffusion of dissolved molecules toward the underlying plasmonic substrate.[34,35] By using a laser excitation with a high enough irradiance, we can provoke a sufficient increase in local temperature to degrade the PLGA layer, precisely at the irradiated area. On this account, plasmonic heating was assessed by means of an infrared camera, which showed a local temperature increase from 30 ºC to 38 °C on the plasmonic superlattice, during the excitation with a 785 nm laser at an irradiance of 0.064 mW/μm^2 (**Figure 3.3a**). In contrast, no temperature increase was observed when the laser beam was focused outside of the plasmonic superlattice, which confirmed that both the Au nanoparticles and the laser are required to cause the heating. It should be however noted that, even if a consistent temperature increase was measured by the thermal camera, such measurements did not reflect the actual temperature next to the AuNPs at the nanoscale, which has been reported to be considerably higher.[36–38]

The proposed SERS-PLGA strategy is depicted in **Figure 3.3b.** As a first experimental demonstration of this method, we incubated a plasmonic substrate, which had been covered with a PLGA (75:25) film, into a 100 μM 4-MBA aqueous solution. Subsequently, the substrate was irradiated with a 785 nm laser at 0.018 mW/μm^2 for 1 s through a 50x objective (the same conditions for SERS measurements as in **Figure 2.2c**). This laser irradiance was not of sufficient intensity to induce a plasmonic heating that degrades the polymeric chains of the PLGA layer. As a result, no trace of 4-MBA signal was registered in the SERS spectra (see spectrum *i* in **Figure 3.3c**). The sample was again irradiated with a higher laser power, 0.064 mW/μm^2 for 1s, leaving

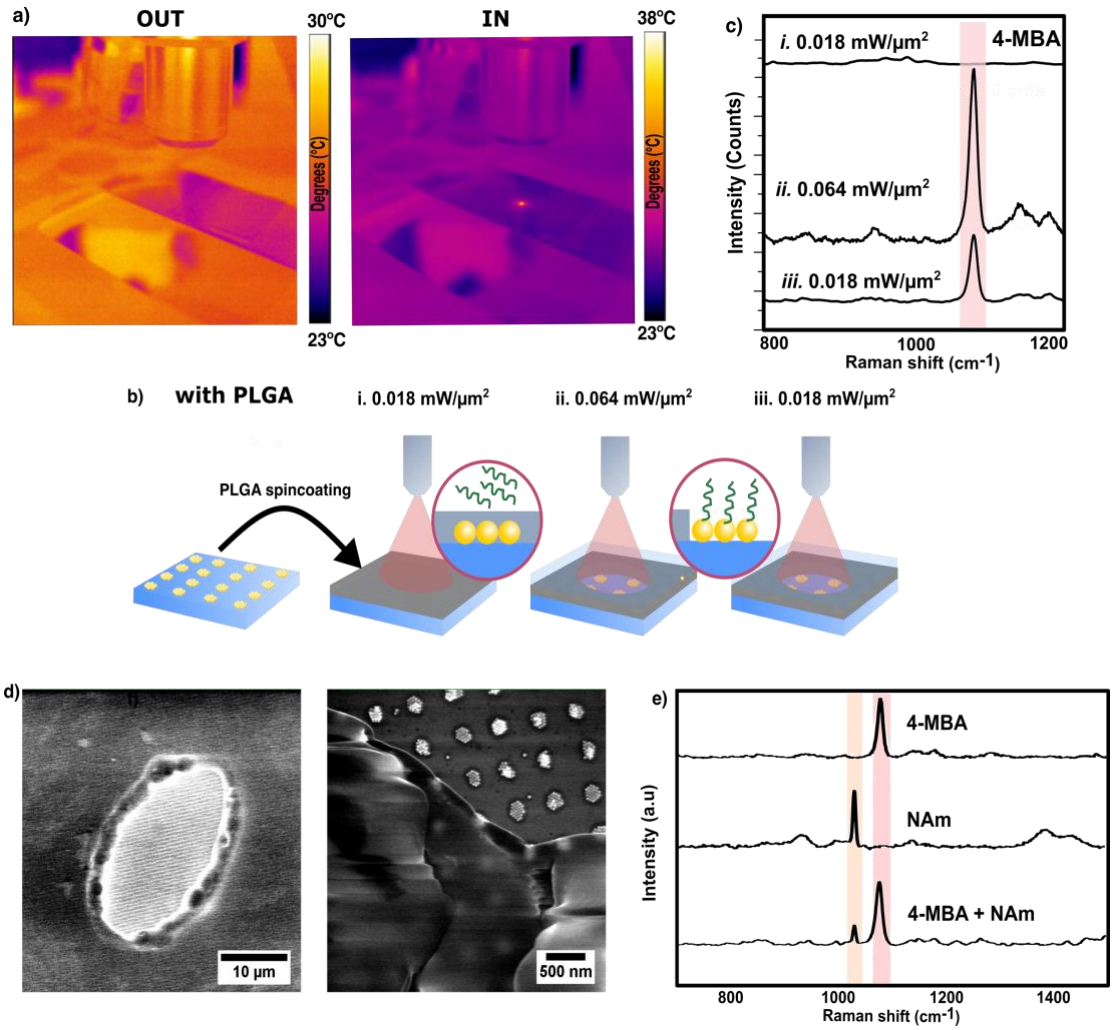

Figure 3.3. a) Infrared thermal camera images of a plasmonic substrate under laser irradiation at 0.064 mW/μm², out of the plasmonic area (left) and inside the plasmonic area (right). A temperature increase is detected at the laser spot when focused inside the plasmonic area. b) Upon spin coating the substrate with PLGA, only laser irradiation at a high fluence leads to local degradation of the PLGA layer, rendering the nanoparticles available to analytes present in the solution; finally, SERS is measured at a low laser fluence. c) SERS spectra from a PLGA-superlattice incubated in 100 μM of 4-MBA solution, at each step described in (b), as labeled; the 4-MBA vibrational fingerprint is registered just after opening a window by laser irradiation. d) SEM images of a window created in the PLGA layer by laser irradiation (0.064 mW/μm², 785 nm), at different magnifications. e) SERS spectra from a PLGA-coated superlattice, overcoming the memory effect that occurred after sequential addition of 4-MBA, NAm and a 50:50 mixed solution of 4-MBA and NAm. Each SERS spectrum was recorded after addition of a new analyte solution, first creating a window in the PLGA layer and then measuring SERS on the same spot.

an open window in the PLGA film because of polymer degradation by plasmonic heating. As soon as the hole was created, the SERS signal from 4-MBA was acquired (spectrum *ii* in **Figure 3.3c**), owing to molecular diffusion through the open window toward the uncovered area of the AuNP superlattice. Although a consistent SERS signal of 4-MBA was recorded after 1s of irradiation at 0.064 mW/μm², the laser illumination was prolonged until the SERS signal was stabilized, which was usually achieved after 5 s. The irradiance of the 785 nm laser could then be lowered, back to 0.018 mW/μm², and used to evaluate the detection of 4-MBA with a lower laser power, at the created measurement window (spectrum *iii* in **Figure 3.3c**). A SERS map of a PLGA-covered substrate was captured upon creating the measurement window by recording the

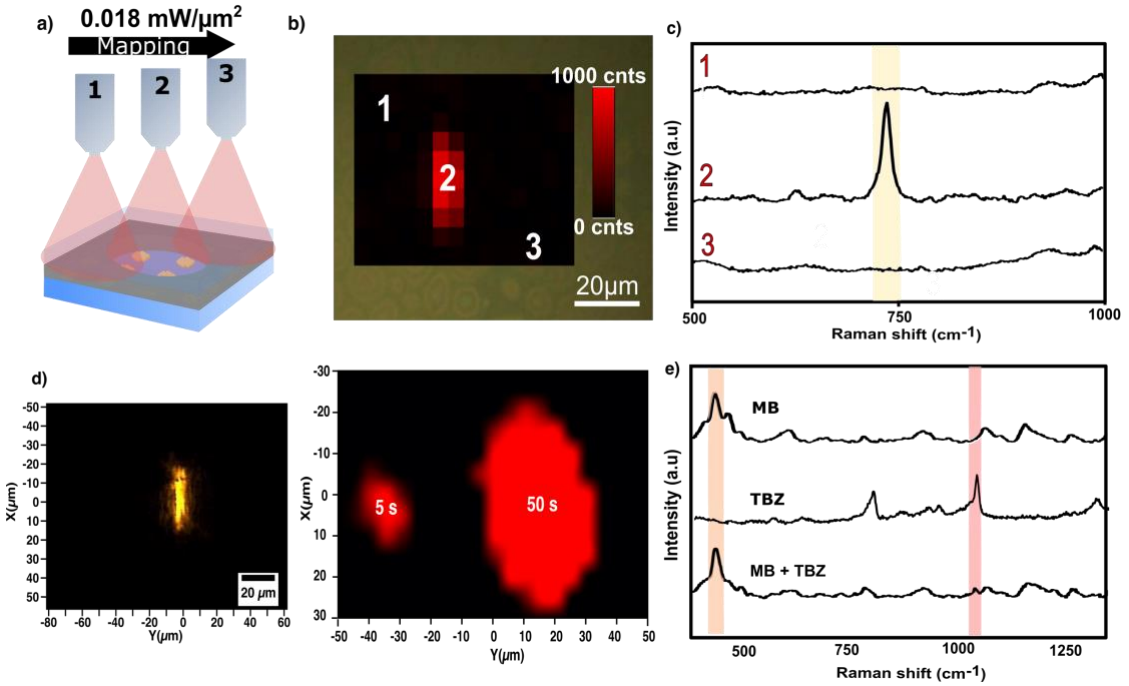

Figure 3.4. a) Schematic view of the scanning process with lower laser power over a previously created measurement window, generating the corresponding SERS map. b) SERS mapping of the selected area, presenting a measurement window within the sheathing layer. The signal from the incubated analyte (Adenosine, 100 μM) was monitored by the presence of a SERS signal at 735 cm^{-1} and could be recorded only over the region where the window was created. The SERS map was acquired with a 785 nm laser power of 0.018 mW/μm^2 to prevent unnecessary PLGA degradation. c) Representative SERS spectra of selected spots over the mapped area. d) Optical microscopy image of the laser spot illuminated through a 50x objective and focused on a silicon substrate. The impact of such a laser spot upon different irradiation times on the size of the forming windows. Two different areas were irradiated with the same 0.064 mW/μm^2 irradiance and through 50x objective, while varying the exposure time of the laser from 5s to 50s. Subsequently, the two areas were scanned with a 785 nm laser power of 0.018 mW/μm^2, imaging the created windows by the signal observed from the incubated analyte (NAm, 100 μM) at 1030 cm^{-1}. As illustrated, longer irradiation times (50s) originate windows with larger areas. e) Illustration of the efficiency of the PLGA-SERS method for other pair of analytes. In this case, Methylene Blue (MB) was first added, followed by the addition of thiabendazole (TBZ) and finally by the addition of a MB:TBZ 50:50 mixture. Using the PLGA-SERS method, all analytes were perfectly identified.

intensities of the indicated peak at the region around the irradiated spot – with a laser power of 0.018 mW/μm^2, confirming that the signal is circumscribed to the open window (**Figure 3.4a,b,c**). SEM imaging of the same area unveiled an opening in the PLGA film, with an elliptical shape of around 20x10 μm^2, as illustrated in **Figure 3.3d.** It should be also noted that changes of the irradiation time (e.g, 5s or 50s) induce variations in the accumulated heat, which affected in turn the shape of the cavity. As observed in **Figure 3.4d,** longer exposition times enlarged the size of the forming window in comparison with the cavity created at initial moments, which more closely matched the laser spot size. Importantly, higher magnification SEM images of windows created after 5s (**Figure 3.3d**) clearly revealed the lattice of plasmonic clusters underneath the PLGA film. No reshaping[39] or melting of the nanoparticles was observed, which is paramount to achieving an enhanced SERS signal**.**

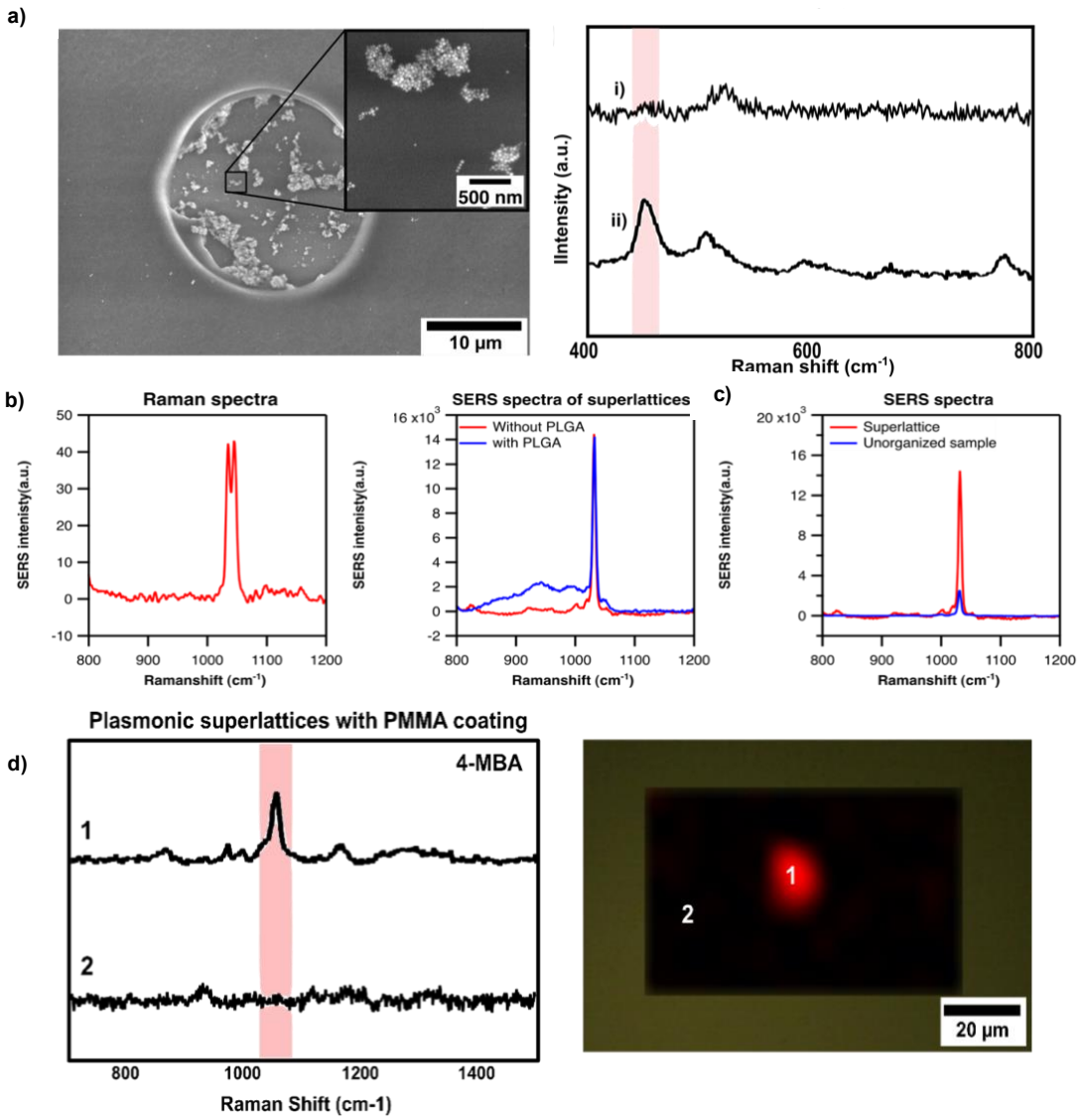

Figure 3.5. Transferability of the PLGA-SERS method to simple systems wherein plasmonic substrates were produced by drying a 50 μL droplet solution of AuNPs (2 mM) in CTAC (500 μM). a) Representative SERS obtained from random NP clusters at spots out (i) or on (ii) of the created window, which is imaged on the right panel by SEM microscopy. b,c) Acquired spectra for the calculation of the analytical SERS enhancement factor. Raman spectra of a 1M solution of NAm, and the corresponding SERS spectra of 100 µM NAm, using (b) a plasmonic superlattice with or without PLGA or (c) a random NP cluster. d) Modification of the polymer coating-SERS method, using PMMA as a coating polymer instead of PLGA. Upon laser irradiation at 0.128 mW/µm^2 for 5 s, SERS mapping (left panel) of the irradiated region by illumination at 0.018 mW/µm^2 indicated the creation of a measurement window in the PMMA film. The SERS map only registered the signal of the incubated analyte (4-MBA, 100 μM) at the specific spot where higher irradiance had been previously applied. At all other points, we only recorded background spectra (right panel), demonstrating the impermeable character of spin-coated PMMA films

Once the performance of the SERS-PLGA method was established, we carried out the same sequence of incubations with different analytes, following the method described above for the uncovered plasmonic substrate – no sheathing PLGA layer. During the sequential incubations of 4-MBA, NAm and a 50:50 4-MBA/NAm mixture, we created different measurement windows for each analyte, at a different position of the PLGA layer. By using the PLGA-SERS strategy, we could monitor accurately the sequential presence of the analytes, as shown in the corresponding SERS spectra (**Figure 3.3e**). Therefore, upon incubation with NAm, only its

vibration at 1030 cm^{-1} (assigned to an aromatic ring bending[40]) was monitored, despite of having incubated the substrate with 4-MBA. Furthermore, irradiation and measurement in the presence of both 4-MBA and NAm (50:50) revealed the SERS signature of both analytes. We additionally validated that a similar performance of the PLGA-protected plasmonic substrate could be obtained with different pairs of analytes (an example is shown in **Figure 3.4e**), in agreement with our initial hypothesis and assessing the efficacy of the method in avoiding memory effects in SERS substrates. Additionally, we witnessed no decrease of the analytical SERS enhancement factor using the PLGA SERS method, as shown in **Figure 3.5b**. Specifically, the EF using the PLGA SERS method with plasmonic superlattices is of $3.38x10^6$, which lies in the upper range found in the literature[41] (see calculation of EF in **Equation 3.1**).

$$EF = \frac{I_{SERS}}{C_{SERS}} \frac{C_{raman}}{I_{Raman}}$$

with $C_{raman} = 1M \;\; C_{SERS} = 100\ \mu M$

$$I_{Raman} = 42 \qquad I_{SERS}(PLGA) = 14200 \qquad I_{SERS}(without\ PLGA) = 14450$$

$EF_{(PLGA)} = 3.38x10^6$ & $EF_{(without\ PLGA)} = 3.44x10^6$

Equation 3.1. The analytical SERS enhancement factor of pristine plasmonic superlattices (without PLGA) and of a plasmonic superlattice covered with the PLGA sheathing layer on a recently created measurement window. More information on this calculation can be found in Chapter 1 (section 1.5b).

We determined above a specific irradiance threshold, which was required to reach a sufficient temperature for PLGA degradation and formation of a measurement window. Such a threshold strongly depended on the light-to-heat conversion efficiency of each specific substrate and thus on its optical absorption properties. On this account, the selected plasmonic material, made of hexagonally packed AuNP clusters gave rise to higher temperatures than single gold nanoparticles under the same laser irradiation conditions. Still, the process could be equally applied to other plasmonic substrates, such as random NP clusters created by simple drop casting of a colloidal dispersion on top of a glass slide, as the one presented in **Figure 3.5a**. Such samples displayed a lower SERS enhancement of $5.8x10^5$, almost an order of magnitude less than plasmonic superlattices, as can be seen in **Figure 3.5c.** However, their simpler fabrication, with no templating process required, rendered them very easy to reproduce and, hence, to be implemented in a variety of applications. This result showed the broad transferability of the PLGA-SERS method, even with arbitrary plasmonic substrates, thus endowing it with a general character.

We additionally noted that other polymers, such as poly(methyl methacrylate) (PMMA), could be spin-coated on top of plasmonic substrates, in line with previous studies.[42,43] PMMA layers

showed a similar behavior as that of PLGA, meaning that a measurement window could be created upon laser irradiation, thereby allowing SERS detection (**Figure 3.5d)**. As a result, multiple designs, which combine different plasmonic substrates and different polymers, can be purposely devised. However, it should be taken into account that additional drawbacks may arise, either from substrates with low photothermal efficiency or from highly thermostable polymers, and therefore these characteristics must be carefully considered for each selected material. For example, polymers with higher thermal resistance would require a higher photothermal heating for the window to be opened, which in turn could cause damage on the plasmonic component.[44] Such damages, e.g., reshaping or degradation, would impact the performance of the plasmonic substrate as a SERS platform in subsequent measurements.

3.2 II) Real-time detection mediated by localized PLGA degradation

The controlled size of the measurement windows created via laser irradiation, along with the precision of the microscope stage, provided a sufficient spatial resolution to perform a large number of sequential measurements at different times. The example displayed in **Figure 3.6a** showed that two windows could be created in close proximity to each other (20 μm), without noticeable perturbation. Moreover, in agreement with the above results for a single window, the SERS signal of NAm was only identified within the two open windows.

We thus propose that such a micron-scale control over PLGA degradation could be beneficial to create multiple windows at defined positions -every time SERS measurements are demanded. This idea was developed in **Figure 3.6,** for the multiplex SERS detection of different analytes. In this example, the analytes – 4-mercaptobenzoic acid (4-MBA), crystal violet (CV), thiabendazole (TBZ) and nicotinamide (NAm) – were sequentially injected at 100 μM concentration inside a silicone chamber ensembled with the plasmonic substrate (similar to that in Chapter 2, see section 6.4). Then, we proceeded as follows: the analyte was added, a laser irradiance of 0.064 mW/μm^2 was applied for 1 s, so that a measurement window was created. Subsequently, the analyte was washed out from the silicone chamber and, the following analyte was injected. It should be stressed that after each incubation, a new window was formed in a selected different spot of the PLGA layer. Finally, we mapped the whole area by using a laser power of 0.018 mW/μm^2. The map was generated by considering the SERS intensities of the characteristic peaks for each analyte (**Figure 3.6c**). The SERS map in **Figure 3.6b** displays four regions (corresponding to the laser-irradiated regions) with meaningful and different signals, which we represented by different colors. Note that, on account of the strong SERS memory

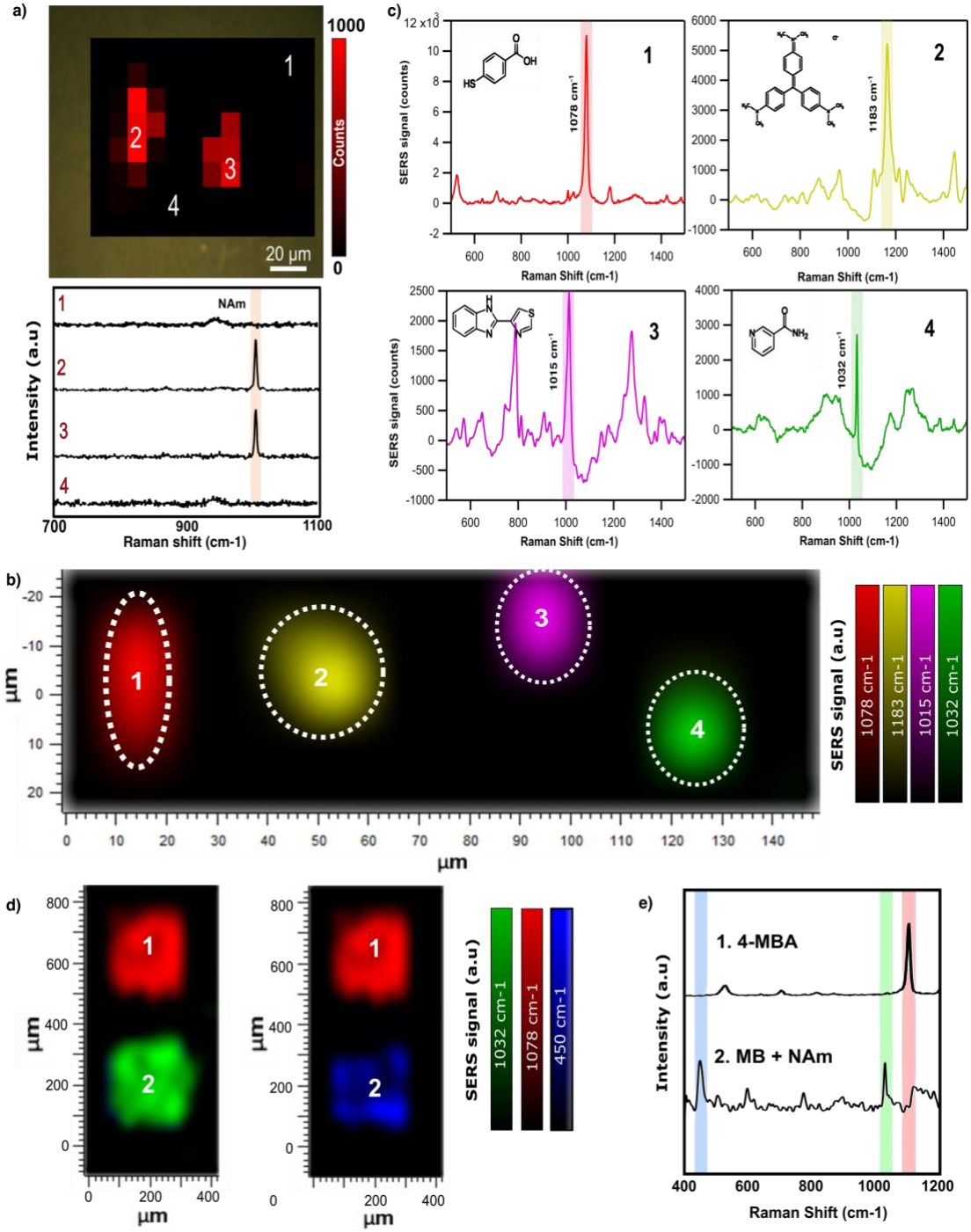

Figure 3.6. Spatial control on the formation of the measurement window in the PLGA layer. a) SERS map recorded at 0.018 mW/m^2 of a PLGA-coated AuNP superlattice, with two windows created by laser irradiation (0.064 mW/µm^2) in the presence of a NAm solution (100 μM). The high resolution achieved in this process can be appreciated by a distance of 20 μm between both measurement windows. The lower panel shows SERS spectra recorded at different positions of the map, whre the signal from NAm was only identified at the created measurement windows. b,c) Multiplex SERS detection with high spatial resolution. b) SERS map of a AuNP superlattice on which 4 windows were created in sequence by laser irradiation and degradation of the PLGA film (see text for details). The map was generated by integration of the characteristic vibrational modes of 4-MBA at 1084 cm^{-1} (1), CV at 1183 cm^{-1} (2), TBZ at 1015 cm^{-1} (3) and NAm at 1032 cm^{-1} (4). We used a laser power of 0.018 mW/µm^2 with 1s integration time and a 50x objective. c) Representative SERS spectra obtained at created windows, only the characteristic Raman signals of the analyte present at the time of laser irradiation were detected in the corresponding new hole. d) SERS map of a AuNP superlattice with 2 unshielded areas of ca. 200x200 µm^2, created by consecutive laser irradiation through a 10x objective, with a power of 0.026 mW/µm^2. e) SERS spectra from each hole in d). Area 1 was created during incubation with 4-MBA; area 2 during incubation with both MB and NAm.

effect, only the characteristic Raman signals of the analyte present at the time of laser irradiation were enhanced in the corresponding new hole (no additional analytes were adsorbed on previously opened areas). This result also indicates that both the plasmonic substrate and the PLGA coating were sufficiently stable to play their corresponding roles during consecutive window opening and SERS mapping steps. As exemplified, four different SERS measurements were recorded from an area of 120x40 μm^2, which could potentially translate into thousands of measurements on a substrate with an area of 1 cm^2. Arguably, this strategy could largely expand the reusability and lifetime of SERS substrates. By using larger plasmonic substrates and smaller laser spots, we could make even more measurements on a single substrate.

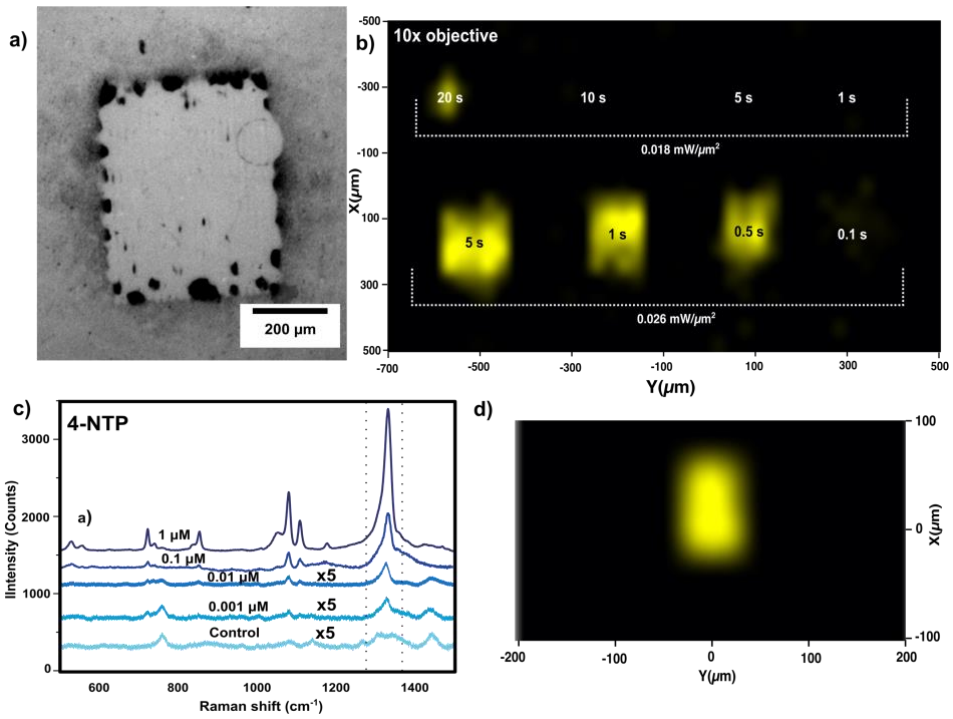

Figure 3.7. a) Optical microscopy images of holes created on a PLGA coating film, captured at 5x magnification. This window was created by irradiation through a 10x objective, with a power of 0.026 mW/μm^2 during 5 s, over an area of 400x400 μm^2. In this case, the space between multiple irradiation points was 20 µm. b) Impact of time and laser irradiance on the process of creating windows by illumination through a lower magnification objective of 10x. 8 different areas of 100x200 μm^2 were irradiated on the PLGA-plasmonic substrate. In each area the sample was irradiated 30 times, moving the spot of 10 µm both in x and y between each successive irradiation. For each area a different irradiation time and intensity was chosen to modify the cumulated irradiation energy. As indicated in the image, every area was illuminated with a specific intensity (dotted lines) and for a defined period of time (the time display at every area). Finally, when the scanning was completed, a SERS map was acquired using a 10x with 1 s integration time, at 0.0039 mW/μm^2 laser power to avoid additional PLGA degradation. c) Average SERS spectra of 4-NTP at different concentrations (between 1 µM and 1 nM with tenfold-increase steps), recorded on measurement windows of 100x100 μm^2 created by consecutive laser irradiation (5s per measurement point) through a 10x objective, with a power of 0.026 mW/μm^2. d) SERS map showing a window created during incubation with 0.1 µM of 4-NTP. To avoid additional PLGA degradation, the scanning was performed using a 10x objective with 1 s integration time, at 0.0039 mW/μm^2 laser power.

On a different example, we demonstrated that PLGA-coated substrates could still be used for multiplex sensing. We show in **Figure 3.6d** the detection of 4-MBA in area 1, while subsequent incubation with a mixture of NAm and Methylene Blue (MB) is readily registered in area 2**.** In this example, we show not only the high spatial control that can be achieved with our PLGA-coated substrates, but also the simultaneous detection of multiple analytes from each hole (**Figure 3.6e**). In **Figure 3.7a**, we additionally demonstrate that the windows in the PLGA film can be easily tailored to different sizes and shapes. Therefore, we created larger holes by reducing the objective magnification through which the laser beam was focused, and then scanning multiple points at the desired area of the substrate. In these particular examples, the irradiance as well as the illumination time were selected based on the results obtained in **Figure 3.7b**. In addition, this strategy facilitated the detection of molecules at concentrations as low as nM (see **Figure 3.7c** for 4-nitrothiophenol (4-NTP) detection). Larger windows in combination with a 10x magnification objective guaranteed that a greater number of molecules were accurately enhanced, so that typical sampling errors at such lower concentrations could be reduced (see **Figure 3.7d**).

3.2 III) Long term SERS monitoring: From microfluidics to cancer-on-a-chip

The spatial and temporal control on SERS measurements of different analytes, enabled by the PLGA-SERS method, can be applied to continuous monitoring of solutions, even in complex environments. As a proof of concept, a microfluidic device was attached on top of a PLGA-coated NP superlattice. The resulting microfluidic plasmonic device was mounted along with a syringe pump system to modulate the flow of an analyte solution in the chip (see section 6.9 for details). A schematic representation of the experiment is shown in **Figure 3.8a**. For each new SERS measurement, we changed the position of the sample using a piezoelectric stage, to find a pristine region of the sample. A new measurement window was then created at this spot and SERS was measured to detect the analytes present in the solution at that precise time. In this manner, changes in the injected solutions with different analytes - here 4-MBA and TBZ - or water, were monitored by SERS, based on the most intense SERS peaks from 4-MBA (1080 cm^{-1}) and TBZ (1014 cm^{-1}). As can be observed in **Figure 3.8c**, the sequential presence of TBZ or 4-MBA in the microfluidic channel was readily identified by the PLGA-SERS method over various cycles of injection. Accordingly, no SERS signal was detected when water was flowing in the microfluidic channel. As a control, we used an uncoated plasmonic superlattice (without PLGA layer), in

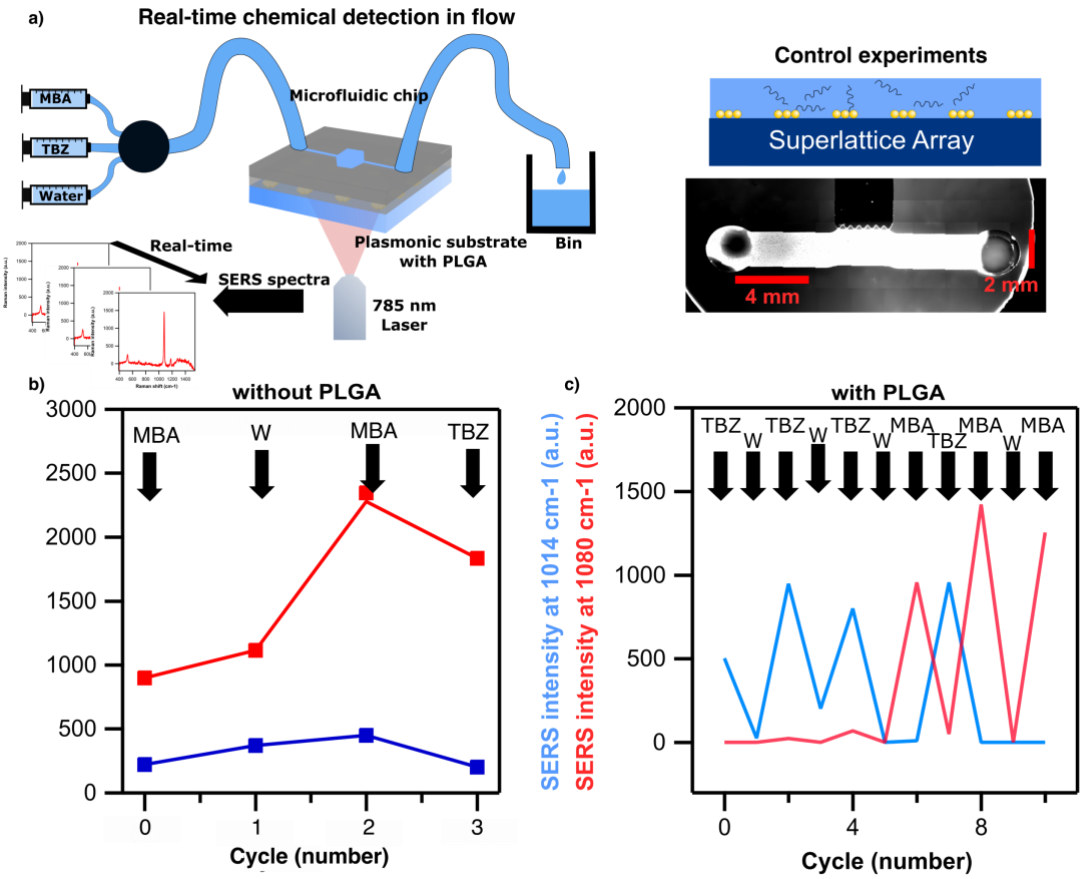

Figure 3.8. a) Scheme of the setup for sensing in flow. The plasmonic substrate was mounted on a microfluidic chip, and the fluid flow was provided by a syringe pump at 20 mL/h. Introduction of water or analyte solutions in the microfluidic channel was also performed by syringe pumps. The control experiment of the microfluidic flow system is also represented on the right, showing the microfluidic channel when containing a fluorescent solution inside (FITC). For b) and c), we plotted the SERS intensity of the characteristic mode of thiabendazole (1014 cm^{-1}) and 4-MBA (1080 cm^{-1}), as a function of the introduction cycles by the syringe pump. The black arrows on top of the plots represent the introduction of a different analyte solution (water (W), TBZ or MBA) in the microfluidic channel. SERS intensity of the characteristic mode of thiabendazole at 1014 cm^{-1} (blue line) and 4-MBA at 1080 cm^{-1} (red line), as a function of the introduction cycles (n) by the syringe pump, for a plasmonic superlattice coated with a PLGA sheathing layer.

which case we found that the signal of the first molecule attaching to the substrate (4-MBA) was persistently recorded, even after flowing water or TBZ solution (**Figure 3.8b**).

In the previous experiments, the versatility of the detection system was probed for short periods of time, i.e. time frames of minutes or few hours. However, other interesting applications of this technology, such as monitoring the extracellular milieu of cell cultures, would likely involve analyses during longer time periods. For such long-term experiments, we proposed to employ a different PLGA (95:5) solution, on account of its higher stability in water.[45] As shown in **Figure 3.9a.*i*,** PLGA 95:5 films maintained their impermeability over longer times, at least for several days. A threshold laser irradiance of 0.064 $mW/\mu m^2$ was also found to be appropriate for this polymer formulation, allowing the molecules in solution to pass through the PLGA 95:5 layer after irradiation (**Figure 3.9a.*ii***). For experiments with cell cultures, we used the same silicone chamber that was manufactured in the previous Chapter 2. HeLa cells ($1x10^6$ cell/mL) were then

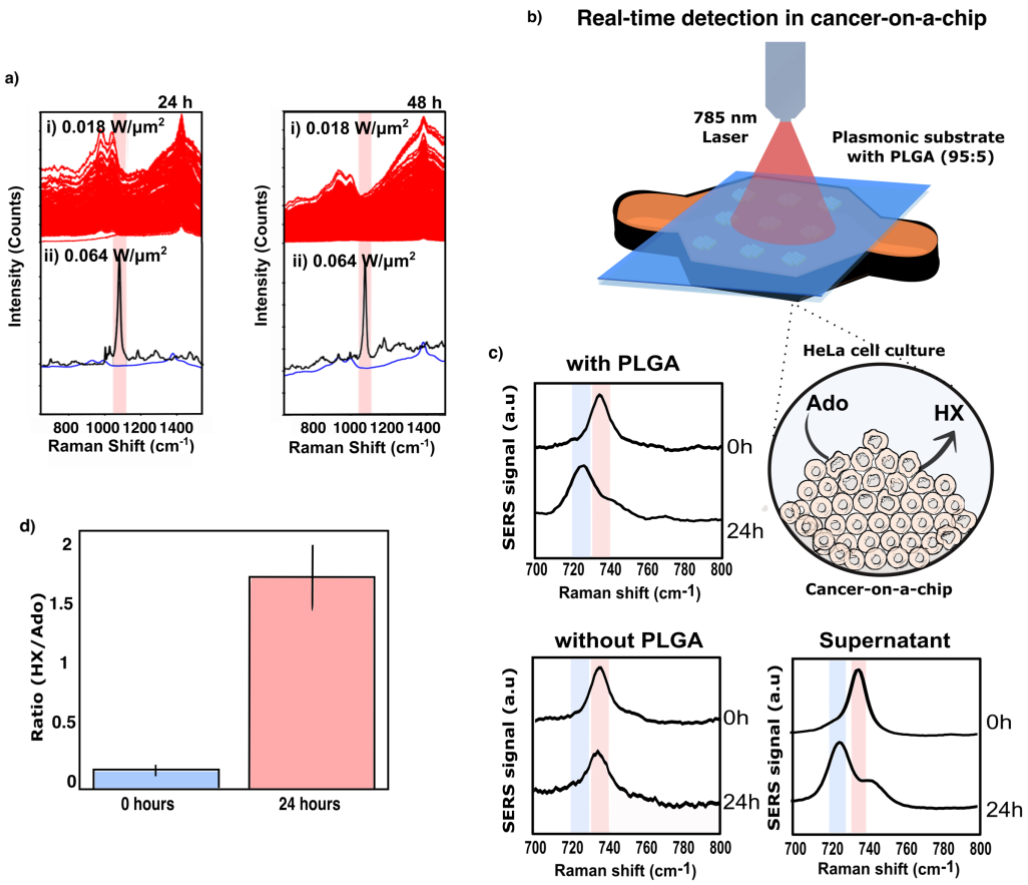

Figure 3.9. a) SERS measurements of an MBA solution (100 µM) recorded on a plasmonic substrate covered with a film of PLGA with a lactic acid/glycolic acid ratio of 95:5. The spectra in (i) were recorded by using a lower laser irradiation (0.018 W/µm^2) and indicated a high stability of the impermeable PLGA layer over time. ii) SERS spectra recorded before (blue) and after (black) laser heating at 0.064 W/µm^2 and subsequent creation of a measurement window in PLGA 95:5 at different times. b) Schematic view of the methodology used to combine a silicone chamber with a plasmonic superlattice to perform SERS measurements, with the laser radiation passing through the support layer. The AuNPs-PLGA side of the plasmonic substrate must be oriented toward the inner compartment. We represent in the inset the incorporation of HeLa cells inside the silicone chamber, thereby generating a cancer-on-a-chip model. The bioactive environment causes the conversion of Adenosine (Ado) and Hypoxanthine (Hx). c) SERS spectra recorded in situ from plasmonic superlattices with and without PLGA sheathing layer, at different times (0 and 24 h) after Ado (200 µM) supplementation into the bioreactor containing HeLa cells. SERS spectra of the extracellular supernatant extracted from the chip and measured on fresh substrates without PLGA layer. d) Confirmation of the metabolic conversion between initial Ado into HX by LC-MS, estimated as the ratio between HX and Ado concentrations, at time 0h and 24 h after 200 µM Ado supplementation.

laden inside the silicone chamber and, again, the whole system was assembled with the plasmonic substrate, placing the side with the AuNP clusters directly in contact with the extracellular milieu (**Figure 3.9b**). In Chapter 2, we have shown that this configuration was capable to accurately monitor changes in a cell milieu, as long as the plasmonic component were renewed prior to every measurement, which was likely to alter the sample under investigation, even if moderately. In this regard, we came up with the PLGA-SERS strategy as a smarter solution to such an invasive procedure.

As a proof of concept and on the basis of previous results, we investigated purine derivative fluctuations in the cell milieu of the cancer-on-a-chip system.[46,47] As stated earlier, the continuous

monitoring of extracellular purine levels can provide valuable information about the cellular state within biological systems (e.g., bioreactors or other cancer-on-a-chip devices). To this end, we initially challenged the culture media with Ado, reaching a high extracellular concentration of 200 μM. Under such conditions, the presence of active enzymes in the bioreactor caused a quick decrease of the extracellular Ado, converting it into HX,[48] as validated by high-performance liquid chromatography (LC-MS) (see Appendix Chapter, **Figure S3.1**). For SERS studies, we measured in situ the spectra of the cultured medium at different incubation times (0 and 24 hours) after Ado supplementation. As detailed below, we followed three different strategies for recording these measurements, the results of which are presented in **Figure 3.9c**. For completeness, the SERS spectra of the pure metabolites: adenosine and hypoxanthine can be found in **Figure 2.5c**. For the experiments performed with the cancer-on-a-chip model and 95:5 PLGA coating of the plasmonic substrate (with PLGA**),** irradiation with a 785 nm laser at 0.064 mW/μm^2 for 5 s, through a 50x objective, ensured complete degradation of the sheathing layer at the selected spots. Once this procedure was completed, we could readily monitor by SERS the high concentration of Ado at time zero, responsible for an intense peak at 735 cm^{-1} in the SERS spectrum. After 24 hours and upon generation of a new measurement window, the metabolic conversion of Ado was recorded, as indicated by a significant peak shift to 725 cm^{-1}. On the other hand, SERS spectra of cell devices without the protective PLGA layer were still dominated by the characteristic Ado peak after 24 hours and could not sense any metabolic activity in the medium surrounding the cell culture (without PLGA in **Figure 3.9c**). To verify these contradictory results, cell supernatants were collected and re-evaluated on fresh plasmonic sensors, which were not found to present interferences from adsorbed molecules. As observed, SERS spectra of collected supernatants were in agreement with those obtained by 95:5 PLGA-coated plasmonic substrates, while confirming the lack of accuracy of the results obtained without the PLGA layer, attributable to a SERS memory effect. Such results validate SERS-PLGA as a strategy to consistently measure varying conditions inside cell cultures, monitoring the conversion of Ado into HX over time, with similar accuracy but much less time-consuming than the LC-MS measurements presented in **Figure 3.9d**. The obtained metabolic parameters may offer highly valuable information on cell environments – without perturbances-, with potential applications in not only TME research, but also in biotechnology processes, such as a remote control of manufacturing requirements.

3.3. Conclusions

The present chapter provides compelling evidence supporting the use of PLGA-coated plasmonic substrates as suitable novel SERS platforms, which will allow the implementation of more versatile sensors in future applications. Thanks to the impermeable PLGA sheathing layer, such

structures were capable to overcome the common problem of "SERS memory effect", which represents a source of uncertainty in real-time measurements. Laser irradiation at high fluence induces plasmonic heating of the underlying nanoparticles, so the sheathing layer degrades under high local temperature and opens a measurement window at the selected measurement time and location. As a result, this system allowed a higher control over the exposed area of a plasmonic surface to the incubated solution, obtaining valuable information regarding the evolution of dynamic systems.

Unlike other previously deployed methodologies, major strengths of our PLGA-SERS strategy are its simplicity and broad transferability that will allow others to easily adopt and exploit this technology. On one hand, the same lasers lines present in conventional Raman equipment were used to raise the local temperature over AuNP clusters, albeit at a higher fluence than in typical SERS measurements, meaning that no additional instrumentation is required for this implementation. On the other hand, this approach has been demonstrated to work successfully with plasmonic substrates or polymers, different to those used in this proof of concept. Based on its wide applicability, we anticipate that other improvements could be readily introduced in the design, for instance, a variation of the developed method could provide a better control over the attained temperatures. Of especial interest would be those modifications in the sheathing layer that might yield lower temperature resistance while maintaining its impermeable character over extended periods of time.

We consider that, in general, this study could contribute to accelerate the development of real-time SERS systems, specially (but not only) in relation to biological applications where this PLGA-SERS approach could facilitate the monitoring of cellular states over time. Still, the final implementation of such PLGA-covered substrates on the ground will be intimately tied to the development of next-generation portable Raman devices, which are indented to provide convenient, flexible hand-held capabilities. Current Raman spectrometer must be adapted to collect continuously high-standard data within a wide range of environments, including outdoor and remote measurements, which may drastically differ from the conditions found at the laboratory,

Finally, we envision that the accuracy in the spatial distribution of created cavities in the sheathing layer might also serve for other applications, such as the selective functionalization of plasmonic substrates with targeting molecules (e.g., antibodies or aptamers). Although not covered in this this thesis, this approach may rguably facilitate the rapid creation of multiplex assays for indirect SERS sensors (introduced in Chapter 1.5d.I), such as immune assays, with multiple possibilities. Hence, an interesting example of application could be the simultaneous quantification of multiple

biomarkers at different spatial positions. For this configuration, each of the recently created windows would be modified with a specific antibody, so that only the targeted antigens woud be immobilized on predefined areas.

3.4. References

1. Langer, J. *et al.* Present and future of surface-enhanced Raman scattering. *ACS Nano* **14**, 28–117 (2020).
2. Bodelón, G. *et al.* Detection and imaging of quorum sensing in Pseudomonas aeruginosa biofilm communities by surface-enhanced resonance Raman scattering. *Nat. Mater.* **15**, 1203–1211 (2016).
3. Shiohara, A., Langer, J., Polavarapu, L. & Liz-Marzán, L. M. Solution processed polydimethylsiloxane/gold nanostar flexible substrates for plasmonic sensing. *Nanoscale* **6**, 9817–9823 (2014).
4. Lin, P. Y., Hsieh, C. W. & Hsieh, S. Rapid and sensitive SERS detection of bisphenol A using self-assembled graphitic substrates. *Sci. Rep.* **7**, 1–6 (2017).
5. Schlücker, S. Surface-enhanced Raman spectroscopy: Concepts and chemical applications. *Angew. Chem., Int. Ed.* **53**, 4756–4795 (2014).
6. Lafuente, M. *et al.* In situ synthesis of SERS-active Au@POM nanostructures in a microfluidic device for real-time detection of water pollutants. *ACS Appl. Mat. Interfaces* **12**, 36458–36467 (2020).
7. Chen, J. *et al.* Flexible and adhesive surface enhance Raman scattering active tape for rapid detection of pesticide residues in fruits and vegetables. *Anal.l Chem.* **88**, 2149–2155 (2016).
8. Rodriguez-Mozaz, S., López De Alda, M. J. & Barceló, D. Monitoring of estrogens, pesticides and bisphenol A in natural waters and drinking water treatment plants by solid-phase extraction-liquid chromatography-mass spectrometry. *J. Chromatogr. A* **1045**, 85–92 (2004).
9. Plou, J. *et al.* Multiplex SERS Detection of metabolic alterations in tumor extracellular Media. *Adv. Funct. Mater.* **30**, 1910335 (2020).
10. Meier, T. A. *et al.* Fast electrically assisted regeneration of on-chip SERS substrates. *Lab Chip* **15**, 2923–2927 (2015).
11. Wachter, E. A., Storey, J. M. E., Sharp, S. L., Carron, K. T. & Jiang, Y. Hybrid dubstrates for real-time SERS-based chemical sensors. *Appl. Spectrosc.* **49**, 193–199 (1995).
12. Ansar, S. M. *et al.* Removal of molecular adsorbates on gold nanoparticles using sodium borohydride in water. *Nano Lett.* **13**, 1226–1229 (2013).
13. Shin, Y. *et al.* Facile microfluidic fabrication of 3D hydrogel SERS substrate with high reusability and reproducibility via programmable maskless flow microlithography. *Adv. Opt. Mater.* **8**, 2001586 (2020).
14. Sinha, G., Depero, L. E. & Alessandri, I. Recyclable SERS substrates based on Au-Coated ZnO nanorods. *ACS Appl. Mater. Interfaces* **3**, 2557–2563 (2011).

15. Guselnikova, O. *et al.* Plasmon-assisted self-cleaning sensor for the detection of organosulfur compounds in fuels. *J. Mater. Chem. C* **7**, 14181–14187 (2019).
16. Höhn, E. M., Panneerselvam, R., Das, A. & Belder, D. Raman spectroscopic detection in continuous microflow using a chip-integrated silver electrode as an electrically regenerable surface-enhanced raman spectroscopy substrate. *Anal. Chem.* **91**, 9844–9851 (2019).
17. Gao, R., Choi, N., Chang, S. I., Lee, E. K. & Choo, J. Real-time analysis of diaquat dibromide monohydrate in water with a SERS-based integrated microdroplet sensor. *Nanoscale* **6**, 8781–8786 (2014).
18. Dugandžić, V., Hidi, I. J., Weber, K., Cialla-May, D. & Popp, J. In situ hydrazine reduced silver colloid synthesis – Enhancing SERS reproducibility. *Anal. Chim. Acta* **946**, 73–79 (2016).
19. Shen, X. *et al.* PLGA-based drug delivery systems for remotely triggered cancer therapeutic and diagnostic applications. *Front. Bioeng. Biotechnol*. **8**, 381 (2020).
20. Strozyk, M. S. *et al.* Spatial analysis of metal–PLGA hybrid microstructures using 3D SERS imaging. *Adv. Funct. Mater.* **27**, 1701626 (2017).
21. Gupta, M. K. *et al.* 3D printed programmable release capsules. *Nano Lett.* **15**, 5321–5329 (2015).
22. Meng, F. *et al.* 3D Bioprinted in vitro metastatic models via reconstruction of tumor microenvironments. *Adv. Mater.* **31**, 1–10 (2019).
23. Sousa-Castillo, A. *et al.* Plasmonic retrofitting of membrane materials: Shifting from self-regulation to on-command control of fluid flow. *Advanced Materials* **30**, 1806899 (2018).
24. Solís, D. M., Taboada, J. M., Obelleiro, F., Liz-Marzán, L. M. & García De Abajo, F. J. Optimization of nanoparticle-based SERS substrates through large-scale realistic simulations. *ACS Photonics* **4**, 329–337 (2017).
25. Polavarapu, L. & Liz-Marzán, L. M. Towards low-cost flexible substrates for nanoplasmonic sensing. *Phy. Chem. Chem. Phys.* **15**, 5288 - 5300 (2013).
26. Hanske, C. *et al.* Solvent-assisted self-assembly of gold nanorods into hierarchically organized plasmonic mesostructures. *ACS Appl. Mater. Interfaces* **11**, 11763–11771 (2019).
27. García-Lojo, D. *et al.* Plasmonic supercrystals. *Acc. Chem. Res.* **52**, 1855–1864 (2019).
28. Kim, N. *et al.* Surface enhanced Raman scattering artificial nose for high dimensionality fingerprinting. *Nat. Commun.* **11**, 207 (2020).
29. Matricardi, C. *et al.* Gold nanoparticle plasmonic superlattices as surface-enhanced Raman spectroscopy substrates. *ACS Nano* **12**, 8531–8539 (2018).
30. Michota, A. & Bukowska, J. Surface-enhanced Raman scattering (SERS) of 4-mercaptobenzoic acid on silver and gold substrates. *J. Raman Spectros.* **34**, 21–25 (2003).
31. Darwish, W. M. A. & Bayoumi, N. A. Gold nanorod–loaded (PLGA-PEG) nanocapsules as near-infrared controlled release model of anticancer therapeutics. *Lasers Med. Sci.* **35**, 1729–1740 (2020).
32. Ghitman, J., Iuliana, E., Stan, R. & Iovu, H. Review of hybrid PLGA nanoparticles: Future of smart drug delivery and theranostics medicine. *Mater Des.* **193**, 108805 (2020).
33. Hirenkumar, M. & Steven, S. Poly Lactic-co-Glycolic acid (PLGA) as biodegradable controlled drug delivery carrier. *Polymers* **3**, 1377−1397 (2012).

34. Brongersma, M. L., Halas, N. J. & Nordlander, P. Plasmon-induced hot carrier science and technology. *Nat. Nanotechnol.* **10**, 25–34 (2015).
35. Quintanilla, M. *et al.* Heat generation by branched Au/Pd nanocrystals: Influence of morphology and composition. *Nanoscale* **11**, 19561–19570 (2019).
36. Borah, R. & Verbruggen, S. W. Coupled plasmon modes in 2D gold nanoparticles clusters and their effect on local temperature control. *The J. Phys Chem. C* **123**, 30594–30603 (2019).
37. Jones, S., Andrén, D., Karpinski, P. & Käll, M. Photothermal heating of plasmonic nanoantennas: influence on trapped particle dynamics and colloid distribution. *ACS Photonics* **5**, 2878–2887 (2018).
38. Baffou, G. *et al.* Photoinduced heating of nanoparticle arrays. *ACS Nano* **7**, 6478–6488 (2013).
39. González-Rubio, G., Guerrero-Martínez, A. & Liz-Marzán, L. M. Reshaping, fragmentation, and assembly of gold nanoparticles assisted by pulse lasers. *Acc. Chem. Res.***49**, 678–686 (2016).
40. Castro, J. L., Arenas, J. F., Lopez-Ramirez, M. R., Soto, J. & Otero, J. C. Surface-enhanced Raman scattering of picolinamide, nicotinamide, and isonicotinamide: Unusual carboxamide deprotonation under adsorption on silver nanoparticles. *J. Colloid Interface Sci.* **396**, 95–100 (2013).
41. Scarabelli, L., Coronado-Puchau, M., Giner-Casares, J. J., Langer, J. & Liz-Marzán, L. M. Monodisperse gold nanotriangles: Size control, large-scale self-assembly, and performance in surface-enhanced raman scattering. *ACS Nano* **8**, 5833–5842 (2014).
42. Fiutowski, J. Mapping of gold nanostructure-enhanced near fields via laser scanning second-harmonic generation and ablation. *J. Nanophotonics* **6**, 063515 (2012).
43. Haas, K. M. & Lear, B. J. Degradation of polypropylene carbonate through plasmonic heating. *Nanoscale* **5**, 5247–5251 (2013).
44. Taylor, A. B., Siddiquee, A. M. & Chon, J. W. M. Below melting point photothermal reshaping of single gold nanorods driven by surface diffusion. *ACS Nano* **8**, 12071–12079 (2014).
45 Makadia, H. K. & Siegel, S. J. Poly Lactic-Co-Glycolic Acid (PLGA) as Biodegradable Controlled Drug Delivery Carrier. *Polymers* **3**, 1377−1397 (2011).
46. Fredholm, B. B. Adenosine, an endogenous distress signal, modulates tissue damage and repair. *Cell Death Differ.* **14**, 1315−1323 (2007).
47. Di Virgilio, F. & Adinolfi, E. Extracellular purines, purinergic receptors and tumor growth. *Oncogene* **36**, 293–303 (2017).
48. Yegutkin, G. G. Nucleotide- and Nucleoside-Converting Ectoenzymes: Important Modulators of Purinergic Signalling Cascade. *Biochim. Biophys. Acta, Mol. Cell Res.* **1783**, 673−694 (2008).

CHAPTER 4

"Label-free SERS Detection of Secreted Metabolite Profiles during Cell Death and Resistance Using Chemometrics Methods"

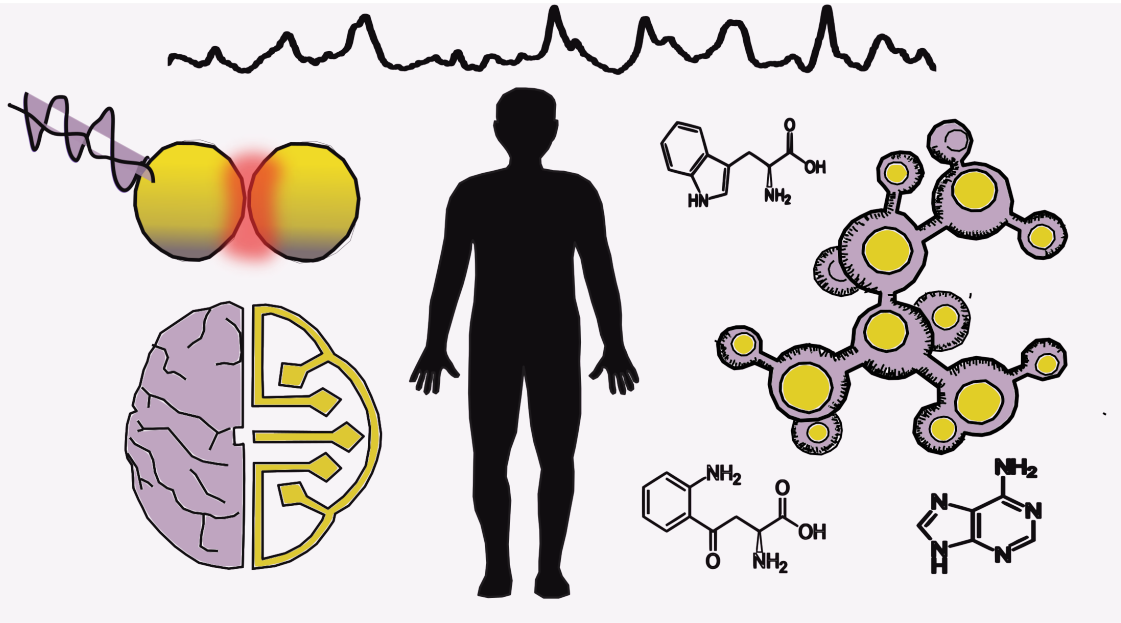

In the previous chapters, we have shown how the characteristic fingerprints of relevant metabolites can be traced through SERS spectroscopy, to an extent that we could monitor variations in their relative concentrations. However, for most metabolites, this strategy, based on the direct correlation between SERS intensities and the presence of individual metabolites, is no longer sufficient. Therefore, chemometrics methods have emerged as a more accurate alternative to conventional approaches, specifically when measurements are made in complex biological media. In this context, we have implemented multivariate and artificial intelligence (AI, machine learning in particular) algorithms to screen variations in the cell secretome, i.e. the subset of metabolites released to the extracellular milieu, under different stressing conditions. In this chapter, we demonstrate that these methods can be devised to substantially improve SERS spectra processing, not only allowing a better classification between control and dying cells – compared to Chapter 2 – but also the identification of specific metabolic profiles for different cell death mechanisms or upon anti-cancer therapy resistance. These results only represent a first approach to this topic, but they consistently show that more sophisticated analysis (supervised or unsupervised) can make the stride to extract complex information contained in the SERS spectra, which will expand current applications and facilitate the analysis of larger data.

4.1 Introduction

Cells respond to stress in a variety of ways, which may conclude with the elimination of the damaged cell. At the dawn of the field of cell biology, cell death had no more implications beyond the absence of cell activity. The valuable insights gained over the last decade, however, unveiled the role of cell death in the process of homeostatic regulation and the overall maintenance of life.[1] In this manner, individual cells have been found to activate different cell death mechanisms to sculpt life in the whole organism, e.g., through preventing uncontrollable cell proliferation.[2] Therefore, by adjusting the cell numbers and eliminating cells with aberrant features, multicellular life forms can modulate physiological events, including embryogenesis or tissue inflammation.[3] In contrast, multiple pathologies will arise under the inhibition of the regulatory checkpoints in such cell death processes.[4] As explained in section 1.3a, the mechanisms orchestrating cell death are typically classified in two general subgroups: programmed cell death (PCD) and accidental cell death (ACD) or non-PCD. Whereas programmed cellular pathways are specifically executed in PCD, therefore generating a time-dependent response to stress (for example, as occurring in apoptosis or ferroptosis), ACD is dominated by an instantaneous cell collapse against unfavorable conditions (non-programmed necrosis by osmotic forces, pH variations, severe oxidative damage, etc.).[5]

In this context, recent reports have supported the notion that, upon triggering cell death, different soluble metabolites are released to the extracellular milieu by a combination of regulated processes and passive diffusion through impaired membranes.[6] This secretome, the subset of molecules released, varies among different types of cell death, and can function as an extracellular messenger with the ability to influence neighboring cells. These released metabolites have been described to transmit either danger signals -alerting the organism about potential threats-, or messages to promote cell proliferation and suppress inflammation within a tissue.[7,8] To this end, cells can regulate (or "program") their death to tailor the responses of nearby cells according to the received stimuli, thereby changing the impact their death would have on the surroundings. Particularly, the secretome of dying cells could play a vital role on the fate of malignant tumors during treatment, transforming immunologically "cold" environments – those that limit immune activity-, into "hot" environments that are capable to stimulate anti-tumoral responses.[9] In this context, the development of new analytical tools for the fast identification of metabolic profiles under different death mechanisms is required. Importantly, accurate classification of varying secretomes could pave the way toward better cancer treatments.[10–13]

The methods currently used for the identification of different cell death mechanisms and related secretomes typically require a set of combined techniques to reach a complete characterization,

such as fluorescence microscopy, western blotting, mass spectrometry, genetic analysis, etc.[14] Still, these techniques are time-consuming and may involve invasive procedures, while relying on experts to handle and interpret the results. In addition to these drawbacks, most of them are expensive and prone to offering poor sensitivity and specificity. Therefore, new strategies are needed to provide a fast, reliable, and straightforward determination of the different cell death types and their associated metabolic profiles. SERS has the potential to overperform current methods on account of its high, label-free sensitivity, which enables the acquisition, within seconds, of the characteristic molecular fingerprint of cell secretomes.[15] In Chapter 2, we have demonstrated that multiplex monitoring of metabolites in the extracellular tumor environment can be carried out by SERS.[16] By using this approach, we could monitor cell death events as a function of the SERS intensity of the peak at 725 cm^{-1} (breathing mode of HX ring), suggesting that specific metabolic profiles can be used as biomarkers of cell death. In a similar direction, other studies have tracked intracellular changes during cell death by SERS, identifying peaks associated with protein denaturation, amino acid residues, changes in protein conformation, and/or lipid degradation. However, as detailed in Chapter 1, an efficient uptake of nanoparticles by cells is required for intracellular monitoring, which may affect cell behavior and ignores the information contained in the extracellular metabolites.[17,18] Overall, although SERS proved its potential for metabolic profiling,[19] the development of new protocols in synergy with advanced data processing is required toward a better classification of secretomes during cell death.[20]

Here, we present different methods for the classification of secretomes, by using SERS and a combination of multivariate and machine learning algorithms for data processing (see scheme in **Figure 4.1**). In particular, a deep-neural network (DNN) framework was developed for this approach.[21] We initially demonstrated the release of a characteristic metabolite secretome depending on the stressing stimuli, which eventually induce cell death in HeLa cells. The results were validated by a set of supervised methods, among which, our DNN classification model showed the highest accuracy, sensitivity, and specificity (≈99%). Second, upon challenging HT1080 cells with two anti-cancer drugs (STP and Erastin), we observed that variations in SERS spectra (and thus in extracellular metabolites) display a time-dependent pattern. Finally, in a different implementation of the developed SERS method, we carried out a long-term study of those breast cancer cells that had shown resistance to radiotherapy treatment, monitoring radiation-induced release of specific metabolites. The recorded metabolic fluctuations over time provided additional insights into the biochemical response of tumors, which may foster future SERS studies to monitor processes associated to tumor cell death or resistance.

4.2 Results and discussion

4.2 I) Secretome monitoring under stress

To induce the release of a distinct subset of metabolites, we challenged HeLa cells with different stress conditions. In the same manner as described in Chapter 2, we initially selected treatments with STP (10 μM) and H_2O_2 (50 μM) because of their well-known properties as strong cytotoxic agents. Specifically, STP is a potent inductor of apoptosis, whereas H_2O_2 activates other molecular pathways that induce cell death by a combination of programmed (necroptosis) and non-programmed necrosis. Interestingly, the apoptotic secretome has been recently described to drive anti-inflammatory responses,[6] while H_2O_2 cell-death was found to elicit the release of certain metabolites that act as mediators of stress-associated inflammation.[22,23] Hence, on the basis of such reported opposite effects, we aimed to monitor differences between the SERS spectra recorded upon incubation with STP and H_2O_2.

For the determination of metabolic profiles in the extracellular medium, we collected the supernatant of HeLa cells after 24 hours of treatment (see section 6.7 for the description of stress assays) and spiked the SERS substrate prior to measurements. Cytotoxicity tests in **Figure 4.2a** showed no significant differences in the percentage of dying cells (≈100%) after 24 h under both conditions (MTT assay, see section 6.8). By using plasmonic superlattice substrates, for which a good reproducibility was demonstrated in previous chapters, we collected approximately 50 spectra per assay and carried out 5 independent biological replicates, using a 785 nm laser through a 50× objective, with 1 s of acquisition time. Next, SERS mappings (50 spectra in an area of

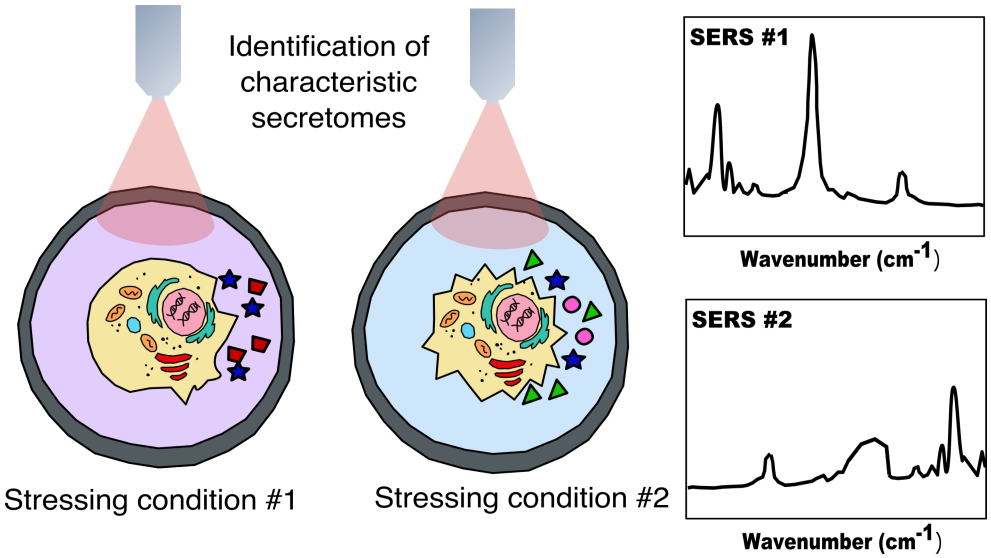

Figure 4.1. Scheme depicting the implemented procedure to evaluate by SERS secretome variations produced under different stress conditions.

250x500 μm^2) were analyzed, and the corresponding average spectra are displayed in **Figure 4.2b.** Although the acquired SERS metabolic profiles are not associated to a single compound and/or biomolecule, but to a combination of them,[24,25] we could demonstrate that consistent vibrational fingerprints were distinctly observed for each condition. In addition, as observed in **Figure 4.2d,** successful discrimination among the three selected conditions (control, STP, and H_20_2) could be visualized by t-Distributed Stochastic Neighbouring Entities (t-SNE) unsupervised analysis.

On the other hand, numerous studies have also reported the role of environmental conditions on the final set of secreted metabolites, not only as a function of the applied treatment. For example, the combination of starvation –lack of nutrients- and certain chemotherapies that typically induce apoptosis, could turn into intense pro-inflammatory responses (known as immunogenic cell death).[26] Therefore, we examined SERS spectra obtained under starvation conditions, with or without addition of STP. It should be noted that a Hanks' Balanced Salt solution (HBBS) buffer,

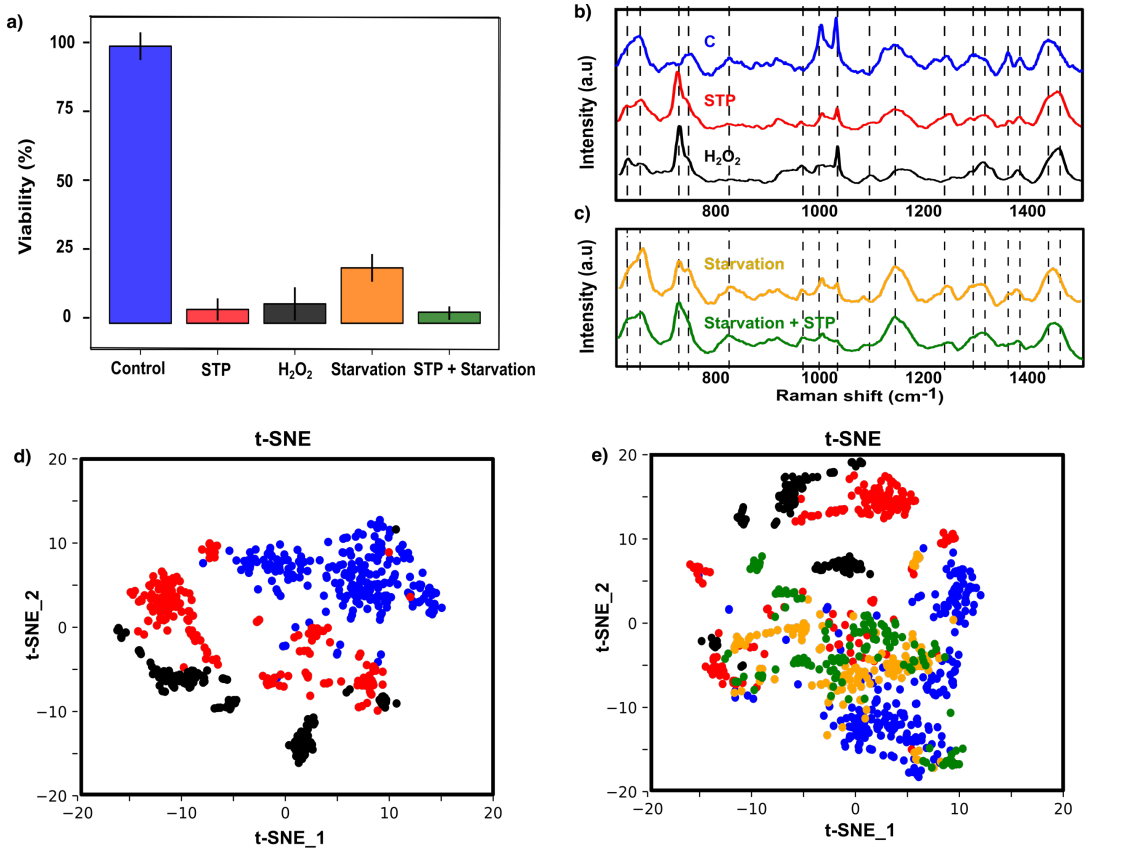

Figure 4.2. a) MTT assays quantifying the % of metabolically active cells (i.e., live cells) in comparison with control conditions b) Average SERS profiles of HeLa cells in control conditions and after 24 hours of Staurosporine 10 μM (STP) or H_20_2 application. SERS measurements were performed with a 50× objective and 10 s of acquisition time, the maximum power of the 785 nm laser was 8.48 mW. c) Average SERS spectra of HeLa cells in starvation for 24 hours, with or without additional STP (10 μM) incubation. d) t-SNE plot providing separation among secretome classes, control (blue), STP (red), and H_20_2 (black). e) t-SNE analysis did not offer an accurate clusterization of the different conditions: control (blue), STP (red) and H_20_2 (black), starvation (orange) and starvation + STP (green). SERS measurements were performed with a 50× objective and 1 s of acquisition time, the maximum power of the 785 nm laser was 8.48 mW.

without nutrients supplied, was used as starvation media in these experiments. In this manner, some of the differences observed in SERS spectra could be directly attributed to changes in cell media; however, the presence of some peaks (or the ratio between different vibrations) could not be explained only through the change of media (**Figure 4.2c**). We thus interpreted this result in terms of a different release of metabolites when both conditions (STP + starvation) are combined. However, by increasing the number of different conditions, vibrational features of various classes may overlap, which significantly hampers the visualization of classes by simple unsupervised analysis (**Figure 4.2d**). Hence, we analyzed the registered SERS profiles by means of machine learning methods, which better address the complexity found during the classification of secretomes as a function of the cell death stimulus (see section 1.6).

4.2 II) DNN architecture optimization

At this step, we deployed a deep neural network (DNN) as a proof-of-concept approach to classify cell secretomes and then compared the performance of our model with those obtained by other supervised methods. In **Figure 4.3a**, we show a scheme of the created network, which comprises a framework based on the input layer (1 × 855) and 4 convolution layers devoted to extract the principal features of SERS spectra. Three of these convolution layers were followed by 1 normalization batch, Relu, and MaxPool (common functions applied in neural networks for

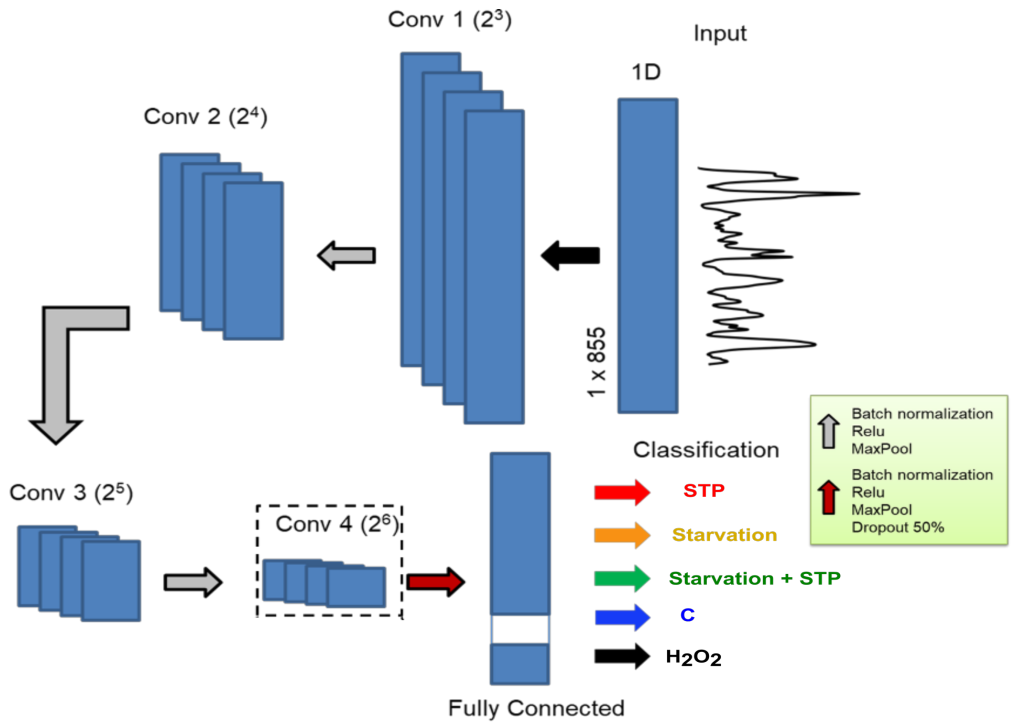

Figure 4.3. Schematics displaying the workflow of the employed deep neural network (DNN)-based classification method.

feature extraction, which are oriented to introduce non-linearity while reducing the number of parameters in the network). The last convolution layer presents an extra dropout of 50% to improve the generalization of the models and a fully connected layer; this fully connected layer represents the last stage in the DNN´s basic architecture, where all the different channels previously created for feature extraction (2^6) are combined to influence the final predictions for data classification. Finally, a softmax layer, which normalizes the output to a probability distribution across the 5 classes, is applied and the maximum is taken as the predicted class. This step contains the five classes that relate to the different stress conditions that induce cell death: Control (live cells), Staurosporine, Starvation media, H_20_2 treatment, Starvation media + Staurosporine; assigned to their respective SERS spectra. Subsequently, we tested the accuracy of the developed strategy to accurately classify secretomes, which could prove the influence of each stress stimulus on the profile of released metabolites.

To build a robust and stable DNN model, its performance was evaluated by changing the sampling ratio between training and validation sets (**Figures 4.4**). A total of 941 SERS spectra from the five different stress conditions were used in this step. For this strategy, we randomly sampled our data set and then split them into training and validation data sets, varying the sampling ratio (e.g., 55% training and 45% validation). Then, the randomly selected training data set was sent to the DNN architecture, so as to optimize the model and subsequently quantify, with the validation data sets, the accuracy (the percentage of samples that were correctly classified) and the loss (the summation of errors made for each sample) values. This process was carried out twenty times (n = 20), meaning that, each time, we changed the SERS spectra selected in the training or the validation groups. The boxplots in **Figure 4.4** thus represent the variability in these outcomes (loss and accuracy), among the 20 repetitions. As expected, the models designed with low ratio

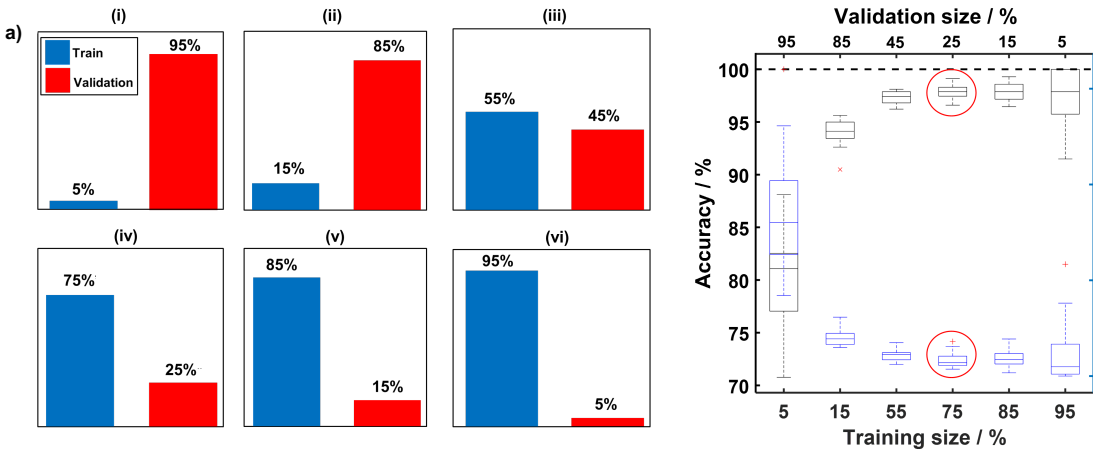

Figure 4.4. Performance evaluation of the different strategies used to build the DNN models for evaluation of their performance**.** Sampling strategy to select the training and validation data sets and their respective boxplot results, (left panel).

sets (5% training, 95% validation) demonstrated low median accuracy and high median loss values (≤95% and ≥0.2, respectively), whereas the model deployed with 95% of the spectra for training presented large variations among the 20 repetitions (i.e., the outcomes strongly depend on the data selected as training or validation). As a consequence, the best results were obtained with the data sets for 75:25 and 85:15 ratios.

a)

Parameters (%)	DA*	DT*	Bag*	SVM*	DNN*
Accuracy	86	82	95	96	**99**
Sensitivity	83	79	94	95	**99**
Specificity	82	79	93	97	**99**

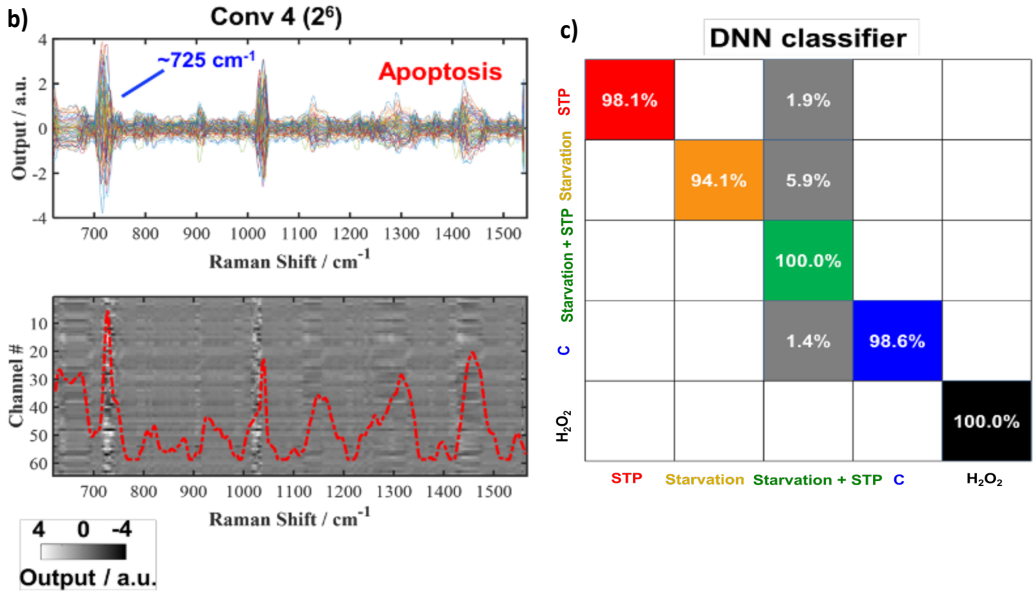

Figure 4.5.. a) Decision Trees; Bag – Bootstrap Aggregation; SVM – Support Vector Machine; DNN – Deep Neural Network. Average of twenty repetitions varying the member of the group training and validation b) Outputs of the last convolution layers from our DNN framework, we plotted the 64 channels contained within the 4th convolutional layer. In addition, to improve visualization, we combined this data in a colormap matrix in the lower panner, shown in red is a SERS spectrum from Apoptosis class used to perform the activations. c) Confusion matrix for the validation data set.

On the basis of the previous outcomes, we separated our data into 671 training (75%) and 223 validation (25%), containing examples of all cell death types, and then we carried out a classification task using the previously optimized DNN framework. This model achieved an accuracy of ~99% and a root mean square error of validation (RMSEV) of 4.3%, which indicates the high quality of our classification DNN models. We also reported our results in terms of confusion matrix, a table that provides a comparison between actual and predicted classification, for each individual class (**Figure 4.5c)** The "off-diagonal" values (in gray) represent the false-positive rates of each individual class of the misclassified samples. Overall, we observed high percentages (close to 100%) in the figures of true positive rates: 98.1%, 94.1% and 98.6% for Apoptosis, Autophagy, and Control classes, respectively, despite of presenting a slightly low

sensitivity with false positive rates of 1.9%, 5.9% and 1.4%, for the classes of STP, starvation and control, respectively

After building the DNN models for classification, we compared the performance of our DNN architecture with other standard supervised methods, such as discriminant analysis (DA),[27] decision trees (DT),[28] bootstrap aggregation (Bag),[29] and support vector machine (SVM)[30] (**Table 4.5a**). Our results clearly indicated that all models were able to perform the classification task with high accuracy. However, slightly superior figures of merit were obtained for the DNN model, which was able to perform a classification with sensitivity and specificity of ~99% of all secretome types. Notwithstanding, Bag and SVM could reach comparable results to those from our DNN method. As expected, they can also deal with the variability present in complex SERS

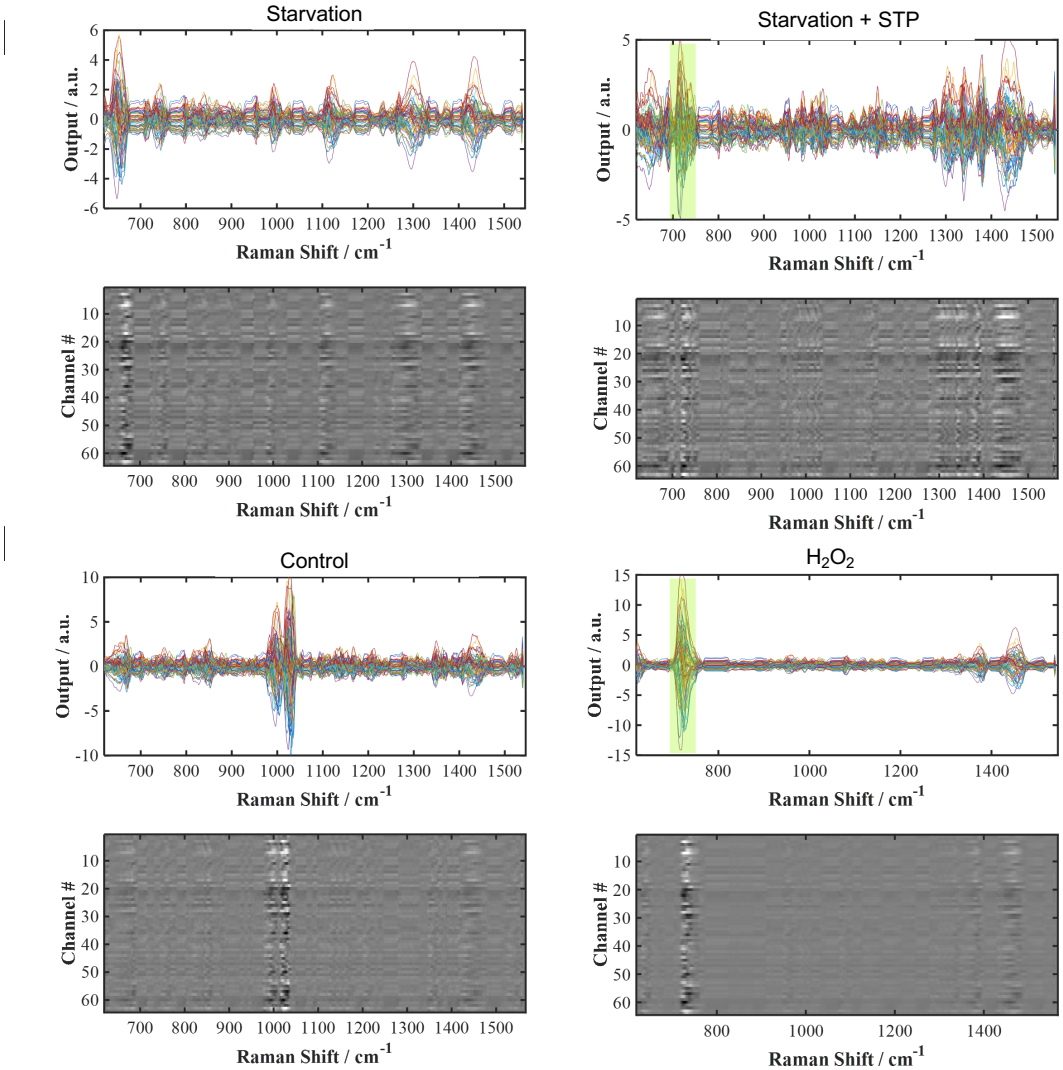

Figure 4.6. Comparison of the outputs of the last convolutional layers (*Conv 4* = 64 channels, see **Figure 4.3a**) after activation of all channels with one validation data from the classes Starvation, STP + Starvation, Control, and H_20_2. The highlighted area in green shows a trend of our DNN framework to give higher weights for the region around 725 cm^{-1}, which could be associated with cell death mechanism.

spectra, but those methods are more time-consuming, which would be a relevant drawback for future cases in which a more complete analysis with larger data sets is projected.

In an attempt to extract more information contained in our DNN architecture, which would help in the identification of specific metabolic profiles, we quantitatively estimated the activation of hidden convolutional layers. This strategy is similarly used to extract features from images by Google DeepDream,[31] but we translated this approach to remove spectral features, aiming at the acquisition of precise information about class assignment in the model. For example, **Figure 4.5b** shows the outputs obtained in the last convolution layer, containing 2^6 (64) different channels, upon testing one sample from the Apoptosis class through our DNN architecture. In the upper panel of Figure4.5b, we plotted all of the 64 channels contained within this convolutional layer. In addition, to improve visualization, we combined this data in a colormap matrix at the lower panel, as follows: colors represent the output of each channel (grey scale; values between -4 and +4), likewise, values in the X-axis reflect the wavenumber in the SERS spectra and, in the Y-axis, each of the 64 channels in the convolutional layer. Remarkably, we can observe, through brighter colors in the matrix, that some bands are being extracted, meaning that the optimized DNN architecture gives higher weight to these vibrations within the SERS spectra. Especially, the region around 725 cm^{-1} obtained higher absolute values for mostly all channels. This result indicates that, this region was also meaningful for other classes, such as Necrosis (H_20_2 treatment) and slightly for Apoptosis + Autophagy (Starvation conditions + STP) (highlighted in **Figure 4.6**). However, not for the Control class; these results are in accordance whit previous results in Chapter 2, where we observed that stress conditions were associated with an increment in the SERS band at 725 cm^{-1}.

4.2 III) Time-dependent evolution of secretomes

In previous experiments, all measurements were recorded from supernatants taken after 24 hours of inducing stress conditions. However, the frequency of death-specific molecules is highly variable and thus dependent on the selected time-point. Different types of regulated cell death mechanisms were thus probed to display characteristic and varying metabolic profiles over time. Interestingly, unlike apoptosis, ferroptosis (a programmed necrosis cell death) has been reported to exert a unique time course with wave-like propagation (i.e., the death of some cells initiates a chain reaction that kills neighboring cells).[32,33] Therefore, Erastin-elicited ferroptosis exhibits a well-characterized timing that dramatically differs from that found in apoptosis – as previously investigated in the literature. In this context, we also carried out experiments to compare the changes in extracellular SERS metabolites profiles between ferroptosis and apoptosis, over time. For these experiments, HT1080 cell lines were used as a cell model, owing to their well-described

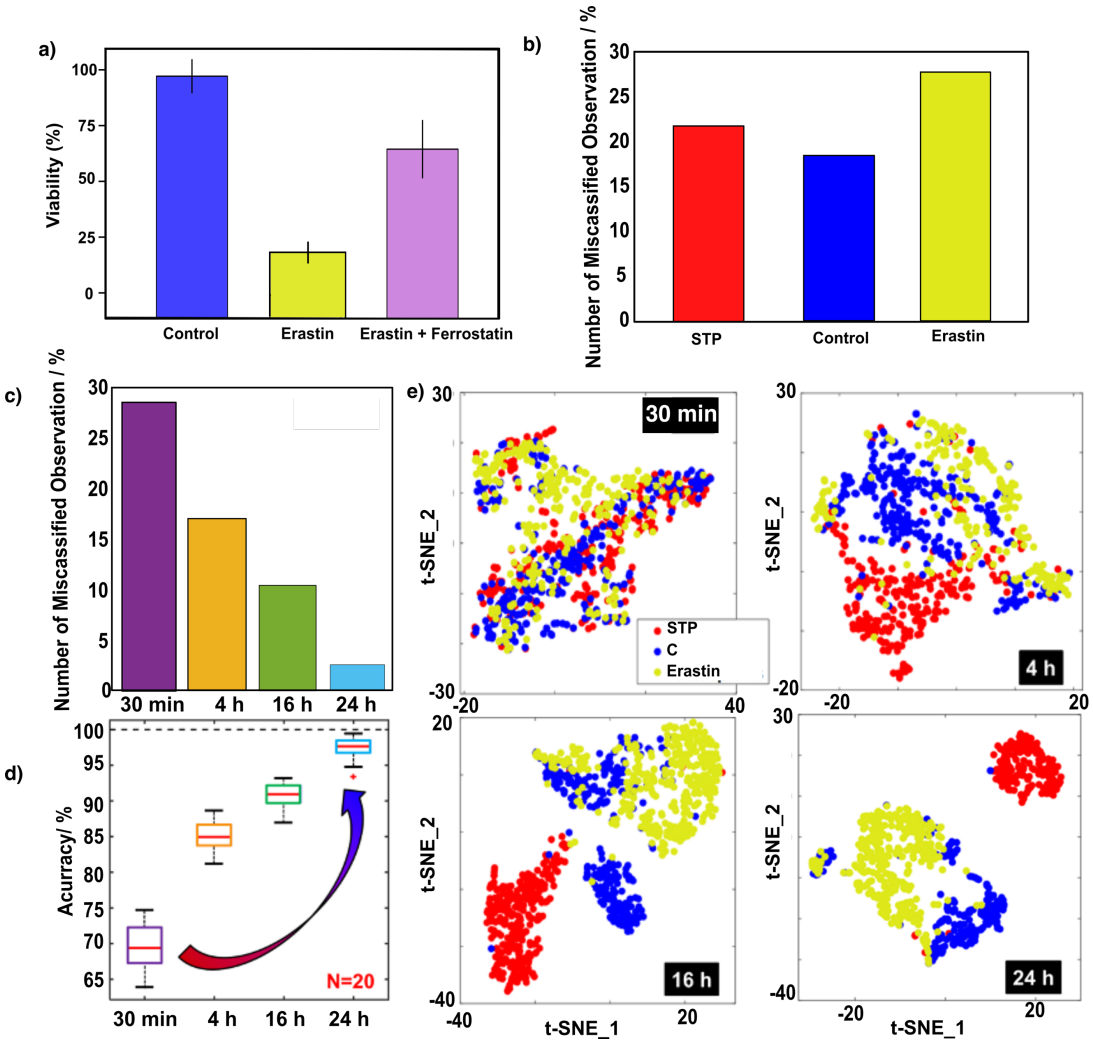

Figure 4.7. a) MTT assay quantifying the percentage of live cells, compared to control conditions (n=3) after 24 hours of Erastin administration with or without Ferrostatin (Ferroptosis cell death inhibitor). b) DNN analysis for the classification of three different conditions: STP (Apoptosis), Erastin (Ferroptosis), and Control in HT1080 cells, combining the spectra collected at different times. c) Total number of misclassified samples among the three classes by DNN architecture, but calculated over each time (30 min, 4h, 16 h and 24h). d) Median of the accuracy acquired in twenty DNN models; N = 20 is the number of DNN models built with randomly sampling the original data set as training:validation (75:25). e) t-SNE analysis of the spectra acquired at successive times: 30 min, 4 h, 16 h, and 24 h. SERS measurements were performed with a 50× objective and 1 s of acquisition time, the maximum power of the 785 nm laser was 8.48 mW.

sensitivity to both STP and Erastin, which induce ferroptosis (**Figure 4.7a**). Initially, we challenged HT1080 by adding Erastin, while also performing control and STP experiments. It should be noted that cell supernatants were collected from these experiments at 30 min, 4h, 16h and 24h, so that changes in the metabolic profile could be registered over time. More information regarding these procedures is provided in the section 6.7 (stress conditions assay). From the previous optimization, we decided to separate the collected data into 2460 samples for training, 819 samples for validation. These data were collected from two different biological experiments (n=2) (3 mappings of approximately 50 spectra in areas 250x500 μm^2 for each time and condition). Subsequently, a classification task was carried out by means of our previously optimized DNN framework.

The results for the classification of selected stress conditions (Control, STP and Erastin) in HT1080 cells are shown in **Figure 4.7b**. Higher numbers (~30%) of misclassified samples were obtained, compared to previous results in Figure 4.5. Notwithstanding, for each group, we included all SERS spectra obtained at different times. Conversely, **Figure 4.7c** plots the average results for the total number of misclassified samples from the Apoptosis, Control and Ferroptosis classes, as a function of time, by running a single DNN model at each point in time. At 30 min, we observed that about 30% of the samples were classified to a wrong class. However, this number of misclassified samples can be reduced by half, after 4 h of having induced the stress conditions, and further reduced to only ≤3% after 24 h. We also quantified the accuracy for each individual class, as the median of 20 DNN models (see boxplots **Figure 4.7d**), to display the variability of the model. The results demonstrated a better agreement with the accuracy presented in Figure 4.5 at 24 h. As could be expected, after 30 min of experiment, the combined results from DNN models reached a median classification accuracy of ~70%, which could be improved at longer times, resulting in an accuracy improvement from 85 to 98% for 4 h and 24 h, respectively. To investigate the effect of each individual sample in the separation of the classes, we carried out a multivariate analysis of the acquired spectra, by using t-SNE method – described in section 6.10. Notably, at starting points (30 min) in **Figure 4.7e**, the samples look very similar, and only a few samples could be distinguished from the others. Then, after 4 hours, different classes start to separate from each other (mostly STP), until they form well-defined clusters at 24 hours. It should be noted that these results could provide meaningful information about the timing of different cell death events. While a clear separation can be obtained with STP after 4 hours – apoptosis occurred in early stages – Erastin triggered a slower dying process, thus registering spectra that are more similar to the control at initial stages.

4.2 IV) Metabolic alterations in tumor resistance upon radiotherapy

Recent studies have explored the use of Raman spectroscopy to monitor variations in the intracellular environment after the application of radiotherapy, providing valuable insights regarding metabolic features capable of conferring radiation sensitivity. Particularly, the accumulation of high concentrations of glycogen has been reported within surviving cells, and then proposed as a prognostic factor of radio-resistance.[34,35] Although Raman spectroscopy has elegantly revealed unique radiation-related signatures in the intracellular milieu, it could not provide information on extracellular metabolites, owing to their lower concentrations. In this context, we aimed at using SERS to account for such biochemical variations in the extracellular milieu after radiotherapy, which may further assist with the elucidation of complementary biomarkers in mechanisms of resistance.

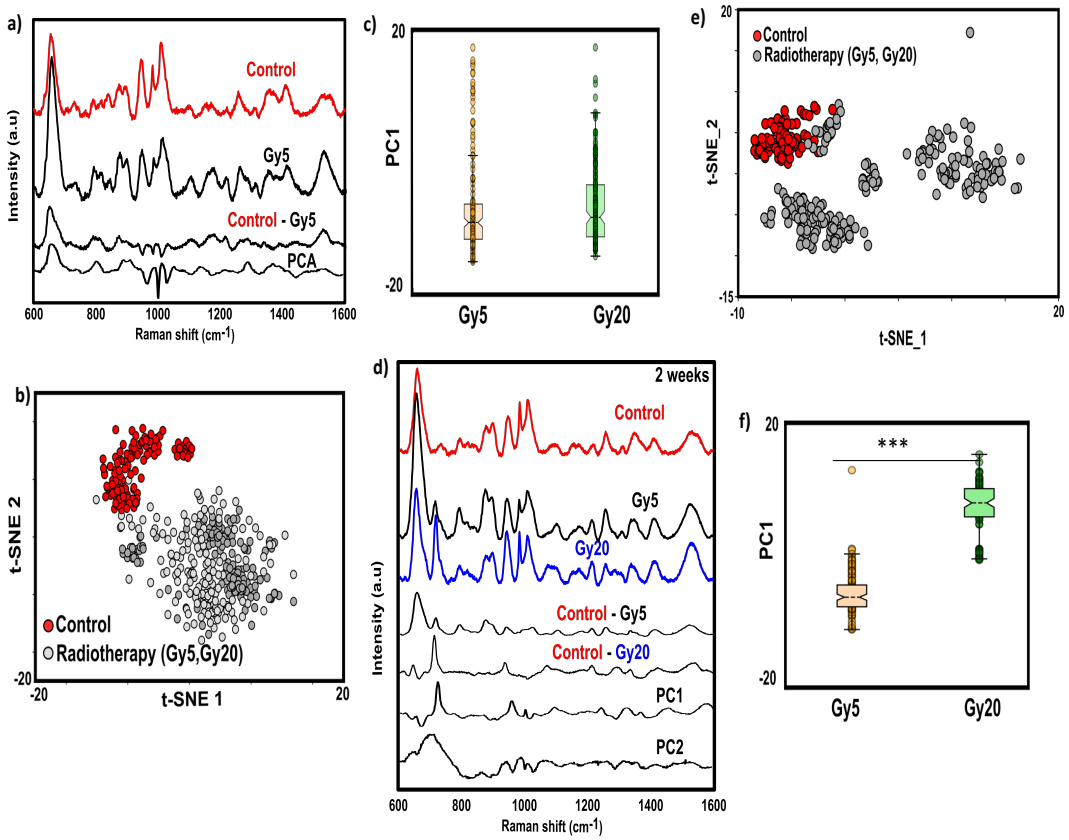

Figure 4.8. a) Mean spectra from supernatants of control and irradiated cells (Gy5) at 4th day post irradiation. The difference spectrum (Control – Gy5) is shown for comparison with the first PCA component from the entire dataset. b)Visualization of the collected signatures in the t-SNE map, each point representing an individual spectrum; two clusters can be distinguished. c) Boxplots representing the mean PCA scores for the first PCA component of Gy5 and Gy20 conditions at 4th day post irradiation. c) Mean spectra of supernatants from control and irradiated cells (Gy5, Gy20) at 17 days post-irradiation. The difference spectra (Control – Gy5; Control – Gy20) are presented, along with the first and second PCA components from the entire dataset. d) t-SNE analysis allows the identification of three different clusters. e) Boxplots representing the mean PCA scores for the first PCA component of Gy5 and Gy20 conditions after 17 days post-irradiation ($p < 0.001$). SERS measurements were performed with a 50× objective and 1 s of acquisition time, the maximum power of the 785 nm laser was 8.48 mW.

Following previous Raman-based studies, we cultured MCF-7 breast cancer cells, selected by their reported high radio-resistance radiotherapy (see section 6.7, radiotherapy treatment). We then exposed them to clinically relevant single fractions of 5 and 20 Gy radiation, while maintaining a group of non-irradiated cells as control. On day 1 post-irradiation, cells were harvested at a density of 15×10^4 cells/mL in 12 well plates. Subsequently, cultured cells were challenged with fresh media (cDMEM, 10% FBS), and allowed to grow for three days. We selected this period of time (3 days) to guarantee a sufficient impact of cell activity on the starting extracellular conditions. Finally, 4-day supernatants were collected and deposited onto plasmonic substrates fabricated by drop-casting (see section 6.3 for fabrication details). As shown in the average spectra of **Figure 4.8a**, we observed marked differences in SERS features for the MCF-7 supernatant after radiation treatment (Gy5)**.** Moreover, the representative point-by-point difference spectrum (Control – Gy5) and the PCA component (see section 6.10) from the entire

data set are both dominated by spectral features around 650 cm^{-1} and 1000 cm^{-1}. From the literature,[36] we could interpret these variations in terms of a higher release of glutathione to the extracellular compartment (principal vibration located at 655 cm^{-1}), as a response to radiotherapy. A meaningful increase (4.7 fold) in glutathione levels after irradiation has also been reported by others groups,[37,38] which reinforces our initial hypothesis. The complete SERS data set represented in **Figure 4.8b** comprised 405 single spectra, recording each condition in 3 different substrates. The first PCA component accounts for 80% of the total variance and represents the dominant observation of variability in the peak around 650 cm^{-1} within the entire SERS data set. It should be noted that the mean PCA scores for the first PCA component (**Figure 4.8c**) do not present any significant differences between radiation doses (5 and 20 Gy), only when comparing with non-irradiated cells. The same conclusion can be drawn from the outcome of t-SNE analysis in **Figure 4.7b**, in which only two clusters were created – one for control and the other for radiotherapy with both doses.

To continue with the screening of biochemical adaptations over time, we repeated the same protocol two weeks after radiotherapy. Cells were again harvested at a concentration of $15x10^4$ cells/mL in 1 mL of fresh media for three days. We then interrogated the collected 3-day supernatant by SERS, and analyzed the acquired spectra using the same methodology (**Figure 4.8d**). We still observed variations in SERS features among the different conditions, with the peak at 650 cm^{-1} displaying higher intensities only upon treatment. In contrast, an intense peak was registered this time at 725 cm^{-1}, mainly for the 20 Gy dose. This vibration has been typically attributed to purine derivative metabolites in various assays along this thesis and could thus indicate a late cell death for the highest radiotherapy dose, among other causes. Three defined clusters were created in the t-SNE analysis of **Figure 4.8e**, meaning that consistent differences can be registered between groups. Remarkably, representation of the mean PCA scores for each dose in **Figure 4.8f** revealed significant differences between 5 Gy and 20 Gy after 2 weeks.

4.3 Conclusions

Undoubtedly, a need remains for new approaches that can trace the information contained in the extracellular milieu, which would avoid time-consuming protocols. In this chapter, we have introduced different applications resulting from the combination of label-free SERS monitoring and either multivariate analysis (such as t-SNE or PCA) or machine learning approaches. The presented studies showed that SERS can readily monitor and distinguish specific biochemical signatures under different conditions, even being capable of registering time-dependent variations. A key feature of our observations was that the deployed DNN model could perform a classification with high sensitivity and specificity of 99%, for different secretomes. Such a high

accuracy demonstrates the efficacy of SERS for assessing changes in extracellular metabolite levels. However, despite of the positive results, further research is still required toward a sufficient validation of the obtained results. In this regard, we discuss in what follows different improvements that could be implemented in the near future.

An important aspect of this study was the initial selection of the stress conditions, which was based on the previous results in Chapter 2, as well as literature analysis that recapitulated stress conditions according to their pro-inflammatory or anti-inflammatory effects. Hence, the selected conditions have already been reported to trigger different responses in the TME. However, validation is still needed by means of additional experiments, for instance, by supplementing the collected supernatants from cancer cells undergoing cell death to other stromal cells (such as macrophages or fibroblasts). Subsequently, we could test whether the metabolites derived from dying cells alter the gene expression of those stromal cells (by RNA sequencing, for example). To further determine whether the influenced gene programs are related to pro- or anti-inflammatory processes, and validate what has been previously reported in the literature.

We have only shown so far the capacity of the DNN algorithms to identify different secretomes. However, once the DNN was optimized, it would be compelling to assess the SERS spectra upon different stress conditions that originate similar secretomes; to then evaluate whether they are classified as a part of the same group by the DNN. In case of positive results, meaning that the algorithm is not only capable of discerning between different secretomes, but also of identifying similar secretomes created in different conditions, SERS monitoring (+ DNN) could potentially lead to a new type of cell death studies, in which the impact of secretomes on the neighboring environment would be more easily accessible (compared to other cumbersome alternatives as the one explained above of RNA sequencing).

In addition, despite of being consistently reported in the literature, further viability studies are required to confirm the different timing between apoptosis or ferroptosis processes. Likewise, the quantification of the registered fluctuations should be performed by other techniques (e.g., LC-MS). In particular, we should investigate the reported increment in the SERS signal associated with glutathione in Figure 4.8. This event could have significant implications both to monitor biochemical changes within a TME environment upon therapy, and to identify new mechanisms responsible for radiotherapy resistance. Overall, we consider that this chapter opens up new challenges to be explored in the future.

4.4 References

1. Ameisen, J. C. On the origin, evolution, and nature of programmed cell death: a timeline of four billion years. *Cell Death Differ*. **9**, 367–393 (2002).
2. Jacobson, M. D., Weil, M. & Raff, M. C. Programmed cell death in animal development. *Cell* **88**, 347–354 (1997).
3. Fuchs, Y. & Steller, H. Programmed cell death in animal development and disease. *Cell* **147**, 742–758 (2011).
4. Galluzzi, L. *et al*. Molecular mechanisms of cell death: recommendations of the Nomenclature Committee on Cell Death 2018. *Cell Death Differ*. **25**, 486–541 (2018).
5. Yan, G., Elbadawi, M. & Efferth, T. Multiple cell death modalities and their key features. *World Acad Sci J* **2**, 39–48 (2020).
6. Medina, C. B. *et al*. Metabolites released from apoptotic cells act as tissue messengers. *Nature* **580**, 130–135 (2020).
7. van Schaik, T. A., Chen, K.-S. & Shah, K. Therapy-induced tumor cell death: friend or foe of immunotherapy? *Front. Oncol*. vol. 11 678562 (2021).
8. Madden, E. C., Gorman, A. M., Logue, S. E. & Samali, A. Tumour cell secretome in chemoresistance and tumour recurrence. *Trends Cancer* **6**, 489–505 (2020).
9. Tan, C.-P., Lu, Y.-Y., Ji, L.-N. & Mao, Z.-W. Metallomics insights into the programmed cell death induced by metal-based anticancer compounds. *Metallomics* **6**, 978–995 (2014).
10. Ouyang, L. *et al*. Programmed cell death pathways in cancer: a review of apoptosis, autophagy and programmed necrosis. *Cell Prolif*. **45**, 487–498 (2012).
11. Gaber, T., Strehl, C. & Buttgereit, F. Metabolic regulation of inflammation. *Nat. Rev. Rheumatol*. **13**, 267–279 (2017).
12. Rastinehad, A. R. *et al*. Gold nanoshell-localized photothermal ablation of prostate tumors in a clinical pilot device study. *Proc. Natl. Acad. Sci. U.S.A* **116**, 18590 LP – 18596 (2019).
13. Labi, V. & Erlacher, M. How cell death shapes cancer. *Cell Death Dis*. **6**, e1675–e1675 (2015).
14. Zheng, J. *et al*. Sorafenib fails to trigger ferroptosis across a wide range of cancer cell lines. *Cell Death Dis*. **12**, 698 (2021).
15. Langer, J. *et al*. Present and future of surface-enhanced Raman scattering. *ACS Nano* **14**, 28–117 (2020).
16. Plou, J. *et al*. Multiplex SERS detection of metabolic alterations in tumor extracellular media. *Adv. Funct. Mater*. **30**, 1910335 (2020).
17. Aioub, M. & El-Sayed, M. A. A real-time surface enhanced Raman spectroscopy study of plasmonic photothermal cell death using targeted gold nanoparticles. *J. Am. Chem. Soc*. **138**, 1258–1264 (2016).
18. Kang, B., Austin, L. A. & El-Sayed, M. A. Observing real-time molecular event dynamics of apoptosis in living cancer cells using nuclear-targeted plasmonically enhanced Raman nanoprobes. *ACS Nano* **8**, 4883–4892 (2014).

19. Lussier, F., Missirlis, D., Spatz, J. P. & Masson, J. F. Machine-learning-driven surface-enhanced Raman scattering optophysiology reveals multiplexed metabolite gradients near cells. *ACS Nano* **13**, 1403–1411 (2019).
20. Thrift, W. J. *et al*. Deep learning analysis of vibrational spectra of bacterial lysate for rapid antimicrobial susceptibility testing. *ACS Nano* **14**, 15336–15348 (2020).
21. Mozaffari, M. H. & Tay, L.-L. A review of 1D convolutional neural networks toward unknown substance identification in portable Raman spectrometer. *http://arxiv.org/abs/2006.10575* (2020).
22. Filomeni, G., de Zio, D. & Cecconi, F. Oxidative stress and autophagy: the clash between damage and metabolic needs. *Cell Death & Differentiation* **22**, 377–388 (2015).
23. Wang, Q., Tang, X. N. & Yenari, M. A. The inflammatory response in stroke. *Journal of Neuroimmunology* **184**, 53–68 (2007).
24. El-Khoury, P. Z. & Schultz, Z. D. From SERS to TERS and Beyond: Molecules as Probes of Nanoscopic Optical Fields. *The Journal of Physical Chemistry C* **124**, 27267–27275 (2020).
25. Lussier, F., Missirlis, D., Spatz, J. P. & Masson, J.-F. Machine-Learning-Driven Surface-Enhanced Raman Scattering Optophysiology Reveals Multiplexed Metabolite Gradients Near Cells. *ACS Nano* **13**, 1403–1411 (2019).
26. Mickaël, M. *et al*. Autophagy-Dependent Anticancer Immune Responses Induced by Chemotherapeutic Agents in Mice. *Science* **334**, 1573–1577 (2011).
27. Villa, J. E. L., Quiñones, N. R., Fantinatti-Garboggini, F. & Poppi, R. J. Fast discrimination of bacteria using a filter paper–based SERS platform and PLS-DA with uncertainty estimation. *Analytical and Bioanalytical Chemistry* **411**, 705–713 (2019).
28. Seifert, S. Application of random forest based approaches to surface-enhanced Raman scattering data. *Scientific Reports* **10**, 5436 (2020).
29. Kanno, N. *et al*. Machine learning-assisted single-cell Raman fingerprinting for in situ and nondestructive classification of prokaryotes. *iScience* **24**, 102975 (2021).
30. Li, S.-X. *et al*. Study of support vector machine and serum surface-enhanced Raman spectroscopy for noninvasive esophageal cancer detection. *Journal of Biomedical Optics* **18**, 1–9 (2013).
31. Simonyan, K., Vedaldi, A. & Zisserman, A. Deep inside convolutional networks: Visualising image classification models and saliency maps. *arXiv preprint arXiv:1312.6034* (2013).
32. Davidson, A. J. & Wood, W. Igniting the spread of ferroptotic cell death. *Nature Cell Biology* **22**, 1027–1029 (2020).
33. Riegman, M. *et al*. Ferroptosis occurs through an osmotic mechanism and propagates independently of cell rupture. *Nature Cell Biology* **22**, 1042–1048 (2020).
34. Harder, S. J. *et al*. Raman spectroscopy identifies radiation response in human non-small cell lung cancer xenografts. *Scientific Reports* **6**, 21006 (2016).
35. Matthews, Q. *et al*. Radiation-Induced Glycogen Accumulation Detected by Single Cell Raman Spectroscopy Is Associated with Radioresistance that Can Be Reversed by Metformin. *PLOS ONE* **10**, e0135356 (2015).
36. Genova, E. *et al*. SERS of cells: What can we learn from cell lysates? *Analytica Chimica Acta* **1005**, 93–100 (2018).

37. Navarro, J. *et al*. Blood glutathione as an index of radiation-induced oxidative stress in mice and humans. *Free radical biology & medicine* **22**, 1203–1209 (1997).
38. Daukantienė, L. *et al*. The significance of reduced glutathione and glutathione S-transferase during chemoradiotherapy of locally advanced cervical cancer. *Medicina* **50**, 222–229 (2014).

CHAPTER 5

“Nanocomposite Scaffolds for Monitoring of Drug Diffusion in Three-Dimensional Cell Environments by SERS”

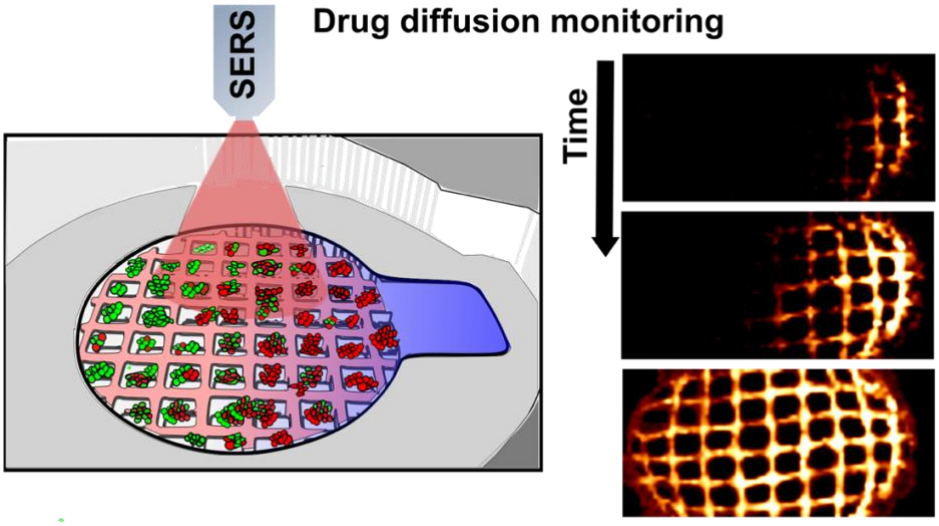

The strategies described in previous chapters entailed 2D plasmonic substrates supported on rigid materials, primarily glass coverslips. However, to better capture dynamic processes in complex cellular environments, the integration of flexible detectors with a homogenous distribution within well-defined three-dimensional (3D) networks would be required, to an extent that the sensor could provide more precise information about nearby perturbations in a non-invasive manner. In this context, the development of 3D-printed structures that can function as both sensors and cell culture platforms emerges as a promising strategy, not only for mimicking a specific cell niche but also toward identifying its characteristic physico-chemical conditions, such as concentration gradients. We present in this chapter a 3D cancer model that incorporates a hydrogel-based scaffold containing gold nanorods. In addition to sustaining cell growth, the printed nanocomposite inks display the ability to uncover drug diffusion profiles by SERS, with high spatiotemporal resolution. We additionally demonstrate that the acquired information could pave the way to designing novel strategies for drug discovery in cancer therapy, through correlation of drug diffusion with cell death.

5.1 Introduction

As emphasized throughout this thesis, the extracellular environment and its impact on cell fitness is a growing area of research, which has initially focused on mimicking microenvironments by tissue-like cell-culture systems in three dimensions (3D).[1,2,3] However, monitoring parameters of interest within these structures, such as spatio-temporal heterogeneity or molecular gradients, imposes additional experimental challenges. Hence, not only more realistic in vitro models are required, but also new imaging technologies should be implemented to assess them accurately.[4,5,6,7]

In section 1.4, we discussed the limitations of 2D cell cultures, including the lack of the cell-cell and cell-extracellular matrix interactions that are required to generate specific 3D microenvironments.[8,9] Whereas biomolecules can diffuse freely in the extracellular milieu of 2D cell culture models, gradients of soluble molecules are established along tissues by a combination of cellular activity and restricted extracellular diffusion.[10,11] Such gradients, along with the 3D internal structure, strongly influence cell responses and phenotypes in solid tissues, including tumors.[12,13]

Indeed, during the design of 3D cell environments, biological structures can be tailored through the technology used to build them.[14,15,16] Thus, different approaches can be combined to improve the outcome and better mimic the features of a native niche.[17,18] Recent experiments involving hydrogels and scaffold-based systems have reproduced with high precision the 3D physiology of selected human tissues.[19] Still, even though these approaches have revealed new elements in cell biology,[20] the incorporated third dimension drastically hampered the efficient capture of dynamic aspects, such as drug or nutrient transport, by optical methods. For instance, the ability of optical microscopy to map large extracellular concentration profiles in 3D is limited, especially if other fluorescent labels are present, which may cause signal overlap – e.g., in combination with cell-viability dyes.[21,22] Ordinary sensing techniques involve otherwise invasive procedures, which prevent continuous monitoring of gradually evolving processes. As a consequence, dynamic parameters are not routinely registered in 3D experiments and their potential effects on cell behavior are thus ignored. The development of alternative analytical methods to rapidly detect gradients in extracellular media is therefore required toward a better understanding of cellular niches and their implications in the effectiveness of therapeutic methods.

In this context, we have demonstrated in previous chapters that SERS can be employed to evaluate changing environments. By enhancing the Raman signal of molecules adsorbed onto plasmonic nanostructures, we could identify the trace analytes upon laser irradiation, in a fast and label-free

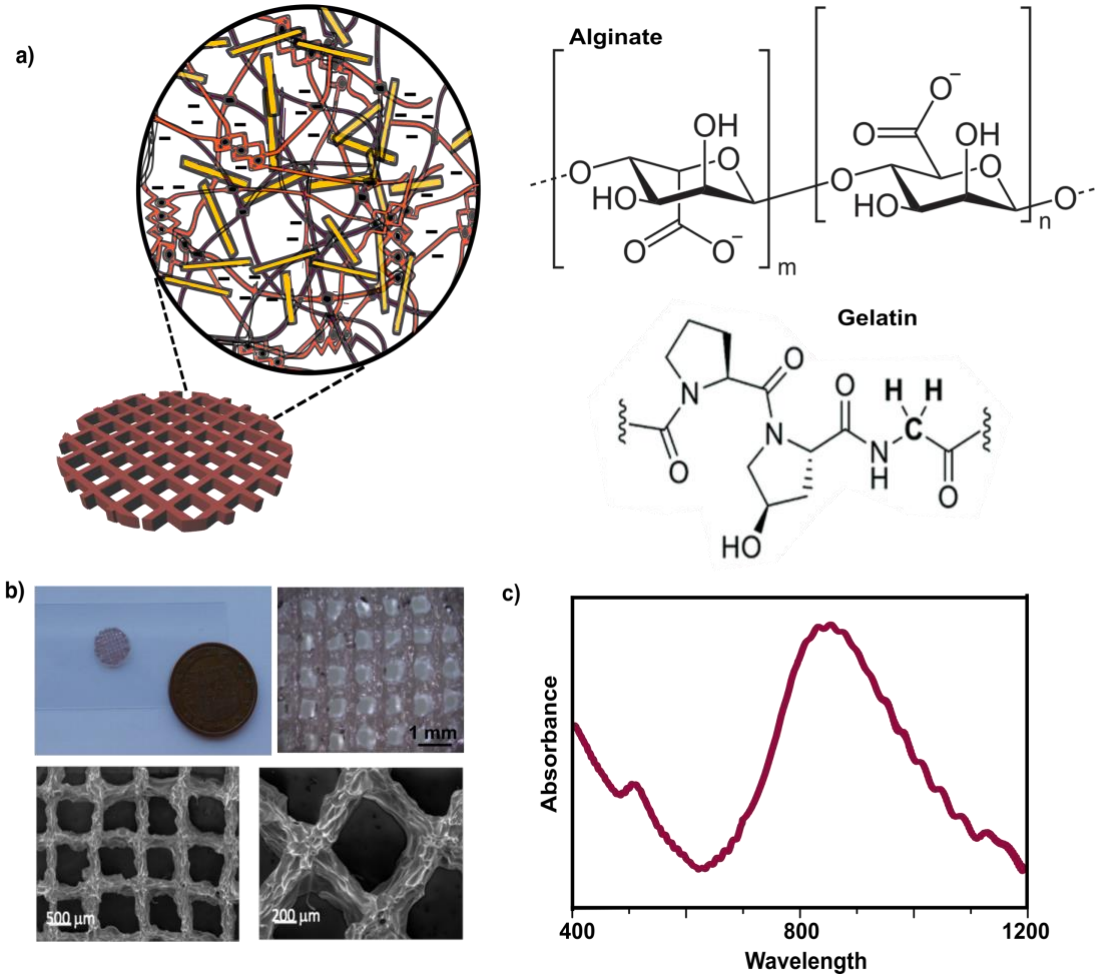

Figure 5.1. a) Scheme of a 3D-printed nanocomposite hydrogel scaffold comprising gelatin and alginate, represented by purple and orange fibers respectively (monomer structures shown on the right). The homogenous distribution of gold nanorods (AuNRs) within the polymer matrix is represented by yellow bars. b) Photographs of an illustrative nanocomposite scaffold from the front, a 5-€ cent coin is incorporated in the picture for comparison, and higher magnification image of the scaffold obtained through a Greenough stereo microscope. In the lower panel, SEM images of the grid-like scaffolds with mesh size of 600 µm. c) Vis-NIR spectrum of a gelatin-alginate (10% and 2%, respectively) ink containing 1 mM of AuNRs

manner.[23,24] However, the complete integration of efficient Raman signal enhancers inside cellular environments was not achieved; in most of the previous cases the sensor was not in intimate contact with the cells, thereby hindering the spatiotemporal resolution in SERS bioimaging.[25,26] In this direction, the fabrication of SERS-active scaffolds from inks containing plasmonic gold nanoparticles has been recently reported by our laboratory, as highly efficient platforms for SERS monitoring in 3D.[27] We thus hypothesized that similar systems could be employed to screen biorelevant compounds in 3D environments, while analysing the extracellular gradients created upon drug exposure by SERS. For this purpose, we selected Methylene Blue (MB) as a drug candidate, because it features a high Raman cross-section and has been used as a photosensitizer agent in antitumor therapy.[28,29,30]

We formulated a biocompatible gelatin-alginate hydrogel containing gold nanorods (AuNRs), which could be 3D-printed to fabricate cell culture scaffolds (see **Figure 5.1a)**.[31,32] As briefly introduced in section 1.4, 3D-printing strategies can be particularly efficient at recreating the tumor niche, due to their ability to control geometric structures with milli-/microscale resolution. Specifically, 3D-printed grid-like scaffolds can recapitulate the architecture of tissues while creating porous inks, which support nutrients and oxygen transport for water-based environments in cell cultures.[33,34] Hence, using biocompatible hydrogels renders printed structures suitable for cell growth, with a tailored physiological architecture, so that complex in vitro systems can be accurately reconstructed. Among various natural polymers typically employed in biomedicine, we selected alginate-gelatin mixtures because of their outstanding water retention, facilitated by alginate content, and cell adhesion, promoted by the peptide-binding domains of gelatin.[35] Moreover, alginate is a polysaccharide formed by the blocks of β-D-mannuronate and α-L-guluronate that provide a strongly anionic character to the hydrogel ink, which enhances the adsorption – and subsequent SERS detection – of oppositely charged molecules through electrostatic interactions. The resulting fast and sensitive response to MB would yield a suitable spatiotemporal resolution. Our results demonstrate real-time monitoring of drug diffusion in 3D cell cultures, through the detection of MB gradients within different environments.

5.2 Result and discussion

5.2 I) SERS performance of nanocomposite scaffolds

Since our objective requires SERS-active inks, we incorporated AuNRs within selected mixtures of gelatin-alginate hydrogels. A representative extinction spectrum of the nanocomposite inks is shown in **Figure 5.1c**. The AuNRs loading resulted in an extinction band over 800 nm, which closely matched the 785 nm SERS excitation laser wavelength. It is important to keep in mind that the SERS-active nanoparticles were embedded in a porous matrix, and therefore we could not take advantage of nanoparticle aggregation effects, so that the selection of AuNRs (instead of AuNPs) as single NP enhancers was found to better match the laser excitation. Moreover, gelatin and alginate are optically transparent at this wavelength, which was required for near-IR light penetration and therefore for the acquisition of the SERS signal within the hydrogel (see section 1.5d). Upon printing, the obtained nanocomposite scaffolds were crosslinked with $CaCl_2$, so divalent cations (Ca^{2+}) bind anionic blocks in different chains of alginate, resulting in stable 3D grid-like networks with a mesh size between 500 and 700 μm according to SEM measurements (**Figure 5.1b;** note that the dimensions of the scaffold varied from hydrated to drying state).

We then evaluated the SERS performance of printed scaffolds, as a function of two key parameters of the ink composition: concentration of AuNRs and percentage of alginate (maintaining always constant the percentage of gelatin at 10%). MB was thus incubated with the scaffolds at 1 µM concentration. It should be noted that prior to using the AuNRs suspension, the nanoparticles were gently washed to remove excess CTAB, which might impair cell viability. Furthermore, during

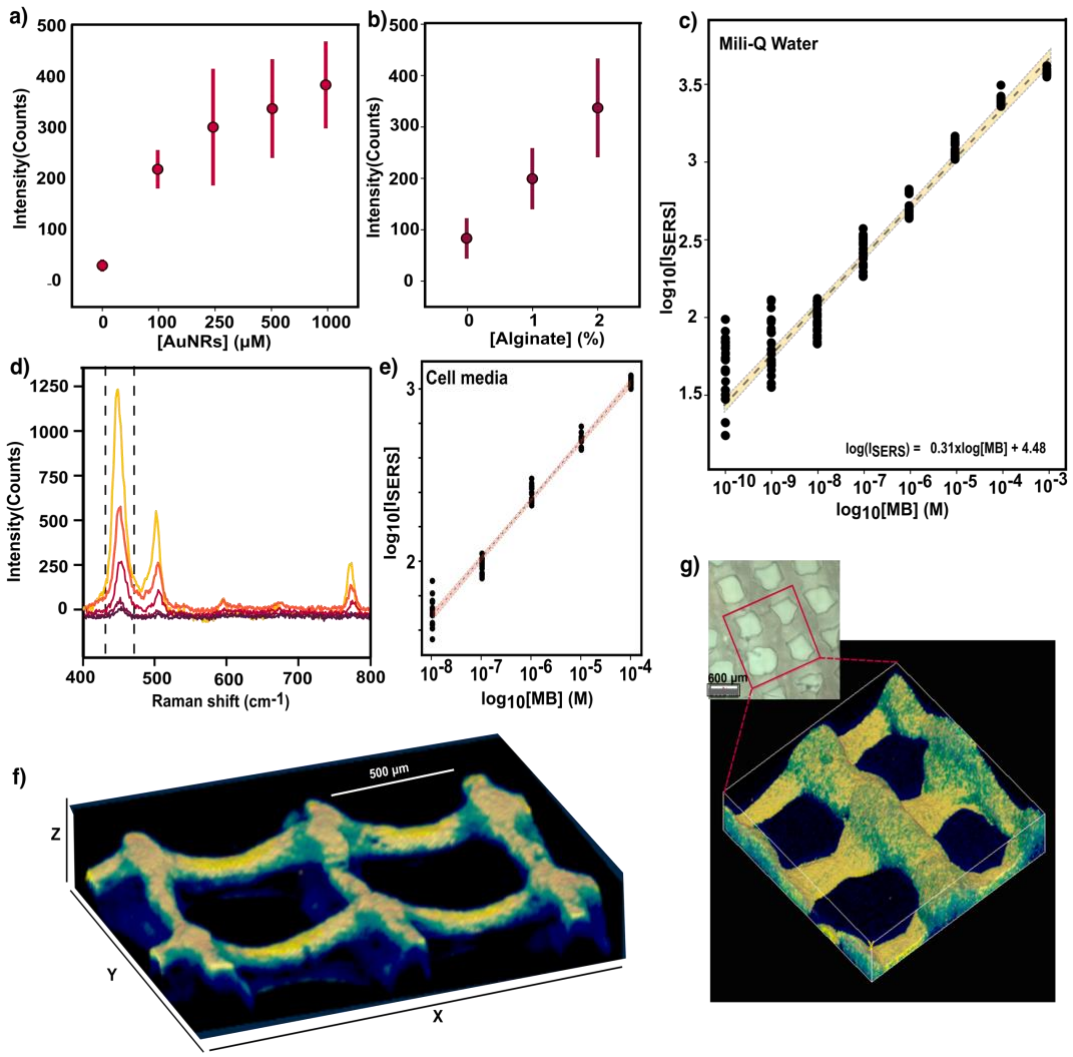

Figure 5.2. a) SERS intensity of 1 µM Methylene Blue (MB) at 450 cm^{-1} registered by scaffolds (10% gelatin + 2% alginate) with varying concentrations of AuNRs, from bare scaffolds (no nanoparticles) to 1000 µM AuNRs solution. Error bars show standard deviations from ten different measurements with three different scaffolds (N=3, n=10). b) SERS intensity of 1 µM MB obtained from scaffolds with 500 µM AuNRs and an increasing alginate percentage up to 2%, (N=3, n=10). c) SERS intensity (at 450 cm^{-1}) as a function of MB concentration. The yellow bar is a linear fit in the quantitative detection region, including a regression line (dotted line) and 95% confidence interval. Each data point corresponds to the signal from 10 spectra collected from three different scaffolds (N=3, n=10). d) SERS spectra of MB at different concentrations (between 10 nM and 10 µM with tenfold-increase steps) in cell media, DMEM 10% FBS. e) SERS intensity of MB at 450 cm^{-1} (the red line is a linear fit with 95 % confidence interval) in the presence of cell media components (N=2, n=10). An excitation laser at 785 nm through a 10× objective, with a power of 15.15 mW for 1 s, was used for all measurements. f) 3D Z-stack reconstruction of SERS intensity at 450 cm^{-1} upon MB incubation at 10 µM, recorded with a 785 nm excitation laser through a 20× immersion objective in confocal mode, with a power of 7 mW and 10 ms of integration time. g) SERS signal of 10 µM MB solution in cell media (DMEM, 10% FBS) scanned within the area labelled by the red square in the left-hand optical microscope image. The measured cube presented the following dimensions in X, Y and Z: (1.5 x 1.5 x 0.5) mm^3. The SERS map in the right-hand panel was again acquired with a 20x immersion objective and a spatial resolution of 10 in XY and 20 µm in Z. To visualize the 3D image, the different Z-stacks were reconstructed to produce a three-dimensional rendering.

the cleaning step, comprising centrifugation and resuspension in Mili-Q water, the amount of AuNRs was adjusted to reach the desired final concentration within the hydrogel inks. Increasing AuNR concentrations inside the hydrogel was found to directly correlate with higher SERS intensities of the MB vibration at 450 cm^{-1} (C-N-C skeletal bending[36]). The SERS results in **Figure 5.2a** are consistent with an increase in the number of plasmonic hotspots for Raman signal amplification, so that the MB signal was negligible for an ink formulation without nanoparticles. On the other hand, when the percentage of alginate was increased from 0% to 2%, with constant AuNR concentration, the registered SERS intensities were significantly affected. As illustrated in **Figure 5.2c**, scaffolds containing 2% alginate showed the greatest SERS performance for MB detection. Although a low MB signal could be acquired by inks lacking alginate, the influence of this polymer component on signal enhancement was even more intense than that observed at varying AuNR concentrations. We interpreted these results in terms of electrostatic interactions between positively charged MB and the anionic alginate-based ink, facilitating analyte penetration through the scaffold. As a consequence, MB molecules are more likely to adsorb on the plasmonic nanoparticles embedded within the hydrogel, resulting in a higher SERS signal

(a) $\log(I_{SERS}) = 0.31x\log([MB]) + 4.48$

(b) $\log(I_{SERS}) = 0.33x\log([MB]) + 4.39$

Equation 5.1. Formulae correlating the concentration of MB with recorded SERS intensity in Mili-Q water (a) and in cDMEM (b). [MB] is the molar concentration of MB and I_{SERS} is the SERS intensity (expressed in counts).

enhancement.[37,38] All scaffolds were thus prepared using inks containing 2% alginate and 1 mM AuNRs, thereby achieving a fast, sensitive detection of MB signal – no long pre-incubation times with the analyte were needed, in contrast with previous studies using different analyte-polymer combinations.[27]

SERS spectra collected from varying MB concentrations showed that semi-quantitative detection could be achieved in the range from 1 mM down to 0.1 nM (see **Figure 5.2c**). Within this range, MB concentration could be approximated with SERS intensity, by the empirical **Equation 5.1a.** Interestingly, the negatively charged hydrogel may additionally hinder the interaction of large proteins with AuNRs,[39] which in combination with the above-mentioned electrostatic attraction effect would facilitate a reproducible detection of MB in complex cell media (DMEM, 10% FBS). As shown in **Figure 5.2d**, the characteristic peak of MB at 450 cm^{-1} dominates the SERS spectra, even at low concentrations and when other biomolecules are present at orders of magnitude higher concentration than that of MB. We proposed that our scaffolds can be used for direct, real-time

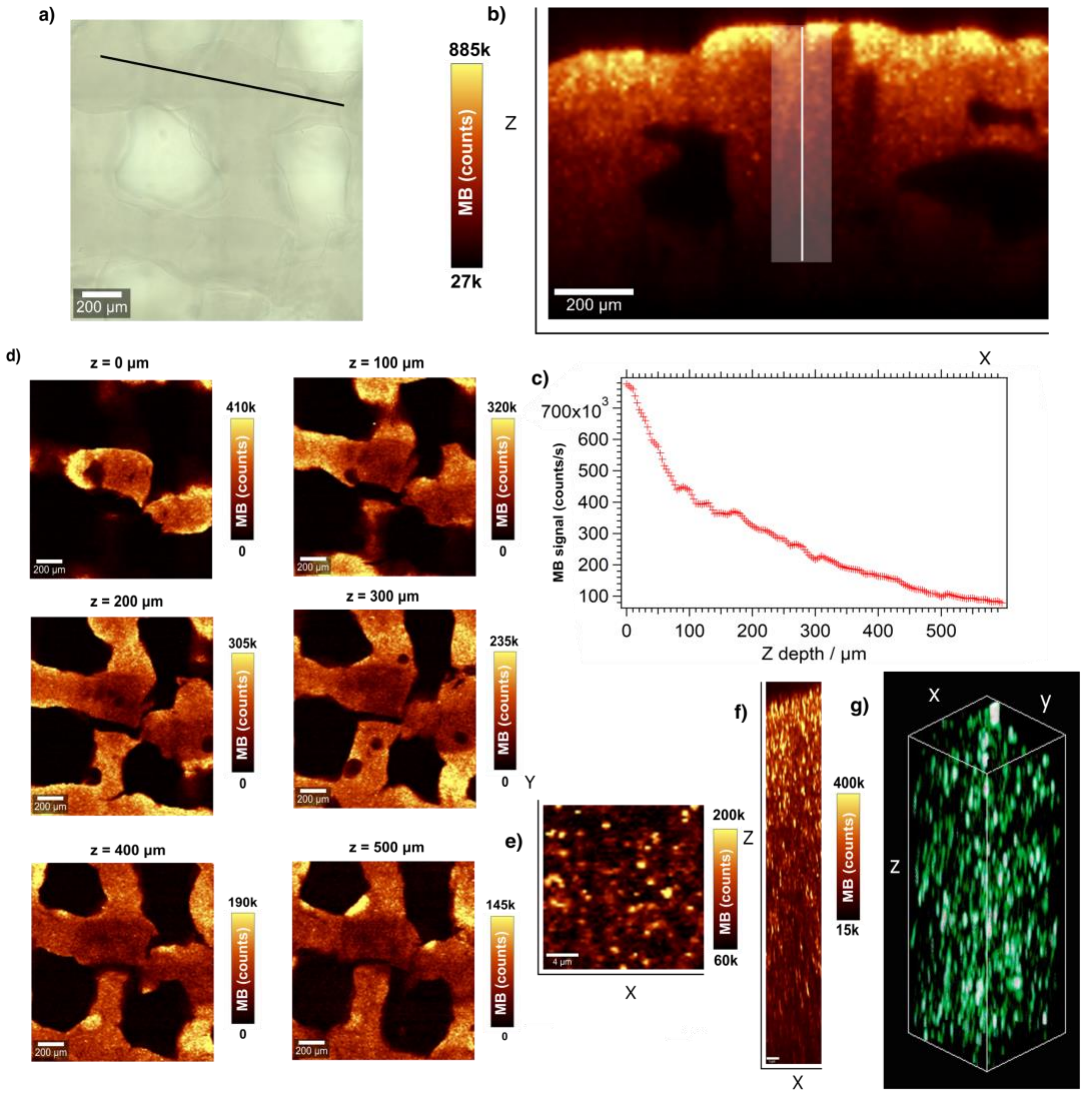

Figure 5.3. SERS signal decay of MB (10 µM) solution at deeper imaging planes along the Z-axis in gelatin-alginate (2%) scaffolds: a) Bright-field (reflection) image of the scaffold. b) Confocal MB SERS profile up to 800 µm scaffold depth, recorded along a 1.26 mm line corresponding to the black line indicated in (a), with a 785 nm excitation laser, power of 30 mW, integration time of 10 ms and using a 20x (NA=0.4) air objective. The scanning step size was set to 10 µm in XZ. c) Cross section profile of the MB signal averaged within the area marked by the white rectangle in (b) showing the SERS intensity with increasing depth. d) MB SERS images recorded from different planes (depths) with excitation at 785 nm, laser power of 30 mW, integration time of 10 ms and using a 20x (NA=0.4) air objective. Scanning step size was set to 10 µm in XZ. The SERS signal was normalized for each image individually. Additionally, three different high magnification images were acquired with 63x water immersion objective (NA=1) and 785 nm laser: e) MB SERS imaging along Y-axis (scale bar = 4 µm) and f) Z-axis (profile map) recorded both by 20 mW power and integration time of 10 ms and scanning step sizes of 1 µm in XY and 5 µm in Z (scale bar = 9 µm). g) High resolution SERS imaging of MB by 3D reconstruction of a Z-stack. The images were recorded with a 785 nm laser, power of 10 mW, integration time of 10 ms and with a scanning step size of 0.333 µm in XY and 2 µm in Z. The dimensions of the recorded cube were (25 x 25 x 60) μm^3.

analysis of biological samples with no need for pre-treatment separation and concentration steps, which are common requisites for SERS analysis in complex media.[40] Although a decreased sensitivity was observed as compared to aqueous samples, semi-quantitative measurements could be recorded between 100 mM and 10 nM, covering the therapeutic window range for MB, i.e. the drug dosage typically used for therapy.[41] Therefore, changes in MB concentration would

correspond to changes in SERS intensity in a predictable manner, which in turn was found to follow a slightly different trend (see **Equation 5.1b**), as illustrated in **Figure 5.2e**.

We show in **Figure 5.2f** the result of scanning the SERS signal of 10 μM MB (within the therapeutic range for cancer treatment) in Mili-Q water. [29,41] A confocal Raman microscope with a 20x water immersion objective and scanning steps of 13.3, 10 and 20 μm in X,Y and Z, respectively, were employed for precise MB 3D screening throughout a total volume of (2.0 x 1.5 x 0.3) mm^3. The intensity recorded along the XY-plane in **Figure 5.2g** showed that constant intensity values were also obtained for 10 μM MB in cDMEM, thus not only accounting for a homogenous distribution of MB, but also of AuNRs within the hydrogel at this measurement scale – 10 μm of spatial resolution. On the contrary, a SERS intensity decay was registered at deeper imaging planes, due to laser spot broadening, decrease of collection efficiency and other factors, as illustrated in **Figure 5.3a-c.** Generally, whereas the highest SERS intensity was observed close to the surface of the scaffold - depicting its morphology, the acquired signal decreased as the focus of the laser is located deeper in the sample; small alterations of this behavior can be due to local structure inhomogeneities and/or to the presence of bigger aggregates within the scanned area. Interestingly, large pores and cavities within the scaffold below the surface can still be imaged by SERS. The morphology of the scaffolds at different heights was also investigated in more detail in **Figure 5.3d** by recording different planes with a step size of 100 μm in Z-axis, up to a depth of 0.5 mm. A higher spatial resolution could be otherwise obtained using a 63x water immersion objective, allowing us to visualize the local AuNR hot-spots distribution along the scaffold (**Figure 5.3e-f**). However, this strategy restricted imaging to much smaller (μm -sized) areas, since longer measurement times were required to obtain high spatial resolution at large scales.

5.2 II) Nanocomposite scaffolds as cell culture platforms

Aiming at the integration of the nanocomposite scaffolds into 3D cell environments, we characterized the rheological behavior of the hydrogels to be used as inks for 3D printing, followed by the biocompatibility and mechanical stability of the scaffolds for extended periods of time (more than one week in vitro). On one hand, the results presented in **Figure S5.1** of the Appendix section demonstrated a shear-thinning behavior of the inks within the usual shear rate range for 3D printing, thus rendering them readily extrudable. These mechanical properties facilitated the injection of inks with high spatial resolution owing to their viscous behavior upon shear stress application, which makes them flow under modest pressure and set rapidly at the target site. In addition, the printed scaffolds offered consistent stability over time: maximum swelling was recorded after 7 days of incubation in cDMEM and hydrolytic degradation was only noticeable after 14 days of incubation.

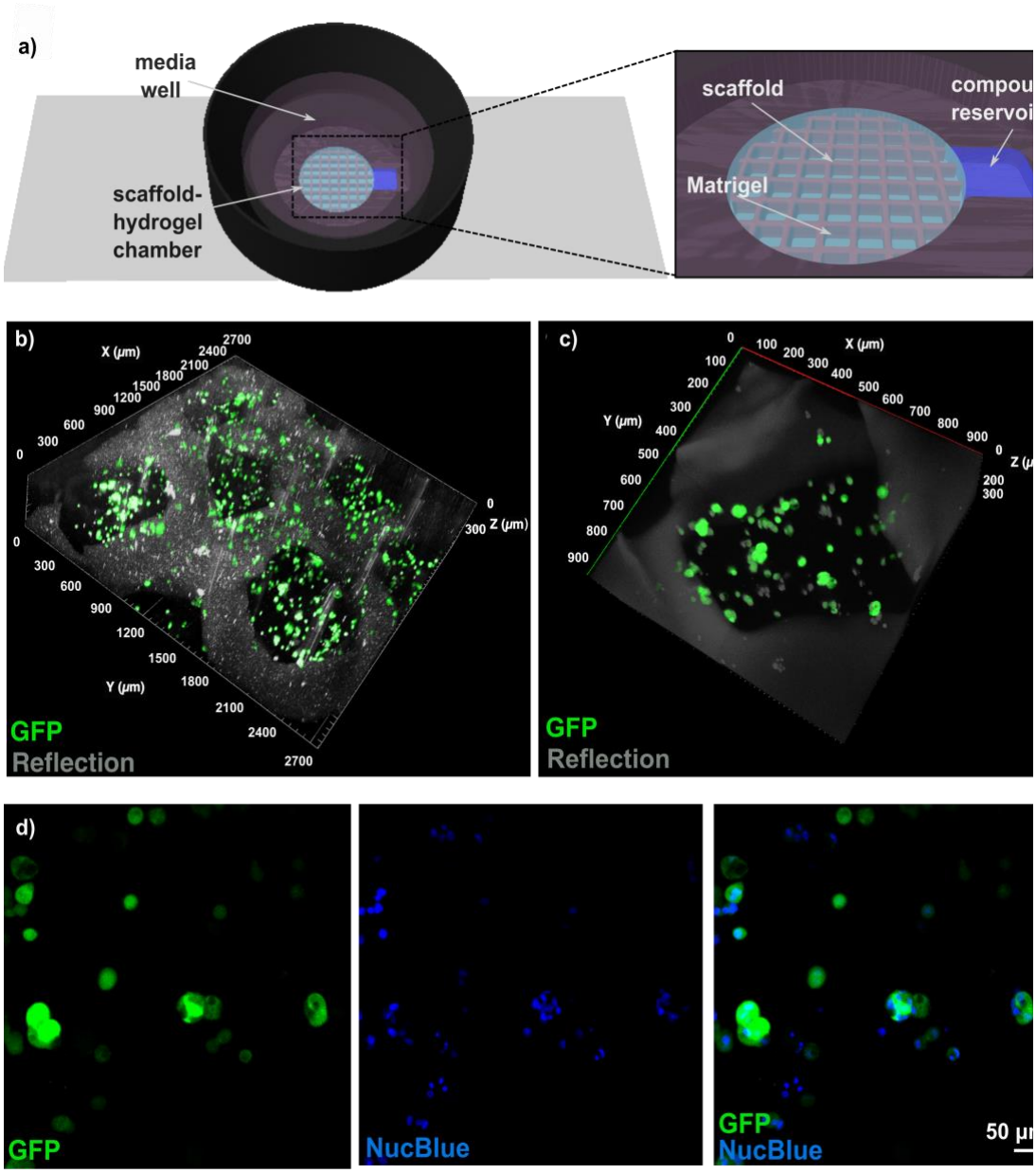

Figure 5.4. a) Scheme of a custom-made device to integrate nanocomposite scaffolds within a 3D tumor cell environment, comprising MCF-7 cells and Matrigel. The presence of a lateral reservoir (see inset) allows for controlled MB delivery. b) 3D reconstruction of confocal images of growing MCF-7 cells embedded in Matrigel within the supporting scaffold. Dimensions XYZ = 2700 x 2700 x 300 µm. c) Higher magnification image showing cancer cell clusters formed under these conditions. Dimensions XYZ = 900 x 900 x 300 µm. d) MCF-7 cell aggregates embedded in Matrigel were formed in 3D after 3-4 days in vitro within the nanocomposite scaffold. MCF-7 cells with eGFP were labeled with NucBlue for visualization of individual nuclei.

On the other hand, MCF-7 cancer cells, which exhibit features of mammary epithelium, were selected as the biological model based on their well-described behavior in 3D cell cultures and their sensitivity to MB therapy.[29,42] Using a purposely devised cell culture device was essential, in this scenario, toward successfully implementing a homogenous cell distribution within 3D-printed plasmonic scaffolds. The system represented in **Figure 5.4a** comprised a central chamber where the supporting scaffolds could be fixed, while using a commercial extracellular matrix

(Matrigel) to uniformly sustain the cells. A lateral reservoir was incorporated into the device (**Figure 5.4a**, inset) to challenge the 3D cell environment with reproducible MB gradients. Meanwhile, the media well, located above the scaffold/hydrogel chamber, provided the necessary nutrients to the 3D culture and supported the use of dip-in immersion objectives during SERS measurements (dimensions of the device can be found in the section 6.5). Following this approach, MCF-7 cells were efficiently seeded in the device and remained viable for several days, forming tumor-like cell aggregates after 3-4 days in vitro, throughout the entire 3D extracellular matrix (see confocal microscopy images in **Figures 5.4b,c**). Moreover, the labelling of individual nuclei in **Figure 5.4d** confirmed the formation of such aggregates with more than one cell – observing multiples nucleus, stained in blue, in confocal images of cell aggregates.

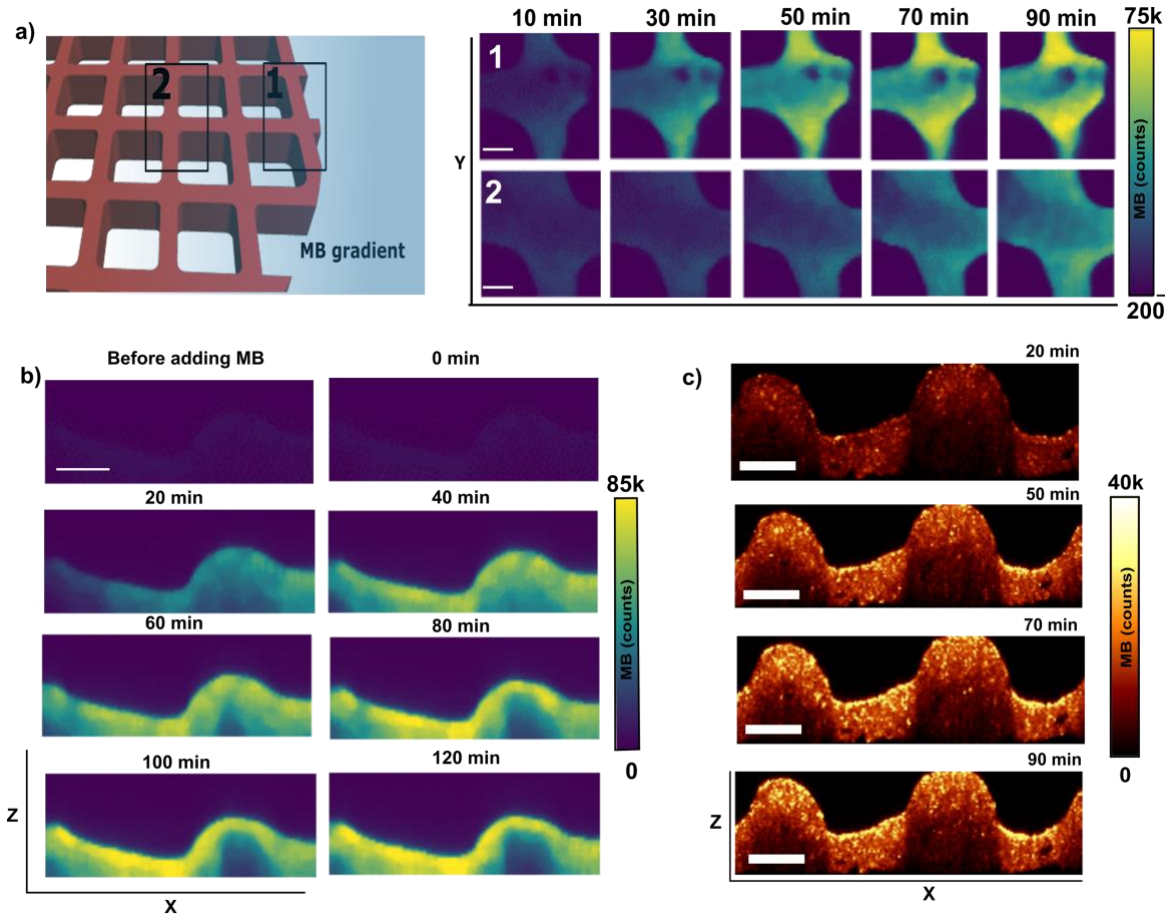

Figure 5.5. a) Schematic view of the experimental setup to monitor MB diffusion by SERS. Two neighboring areas of the plasmonic scaffold, separated from each other by 1 mm in X, were selected to register the SERS intensity at successive times upon MB administration. Maps were recorded with a 785 nm laser through a 20x objective with laser power of 15 mW, 10 ms integration time and a step size of 16 µm. Scale bars: 200 µm b) Time-resolved mapping, every 20 minutes, of the MB-SERS signal in the XZ plane (profile). MB (10 µM) was delivered to the scaffold at the compound reservoir incubated in Mili-Q water. SERS profiles were measured at laser excitation of 785 nm with a power of 15 mW, integration time of 10 ms and a scanning step size of 10 µm, using a 20x air objective (NA=0.4), scale bars: 200 µm. c) SERS mappings were registered through successive times upon MB (10 µM) administration from the top media well. SERS signals were recorded with a 785 nm excitation laser through a 20x immersion objective in confocal mode, with a power of 7 mW, 50 ms of integration time, and a step size of 10 µm. Scale bars: 200 µm

As a first example of application, we assessed the potential of the deployed system to visualize MB diffusion. In these experiments, scaffolds were placed within our home-made devices, followed by addition of MB from the lateral reservoir. As illustrated in **Figure 5.5a**, the localized drug delivery created a MB gradient that could be imaged by SERS. We initially selected two neighboring areas in the plasmonic scaffold, separated by 1 mm from each other, to register SERS intensity upon MB administration (10 μM). The area located closer to the compound reservoir – labeled as 1 – showed a rapid response to MB (shorter than 30 minutes), whereas the farthest area -labeled as 2- exhibited a significant delay (one hour) to reach a comparable signal. These results, in addition to those presented in **Figure 5.5b** for X and Z axis**,** demonstrated a suitable spatio-temporal resolution in SERS imaging, which may account for MB gradients along the scaffold, in three dimensions. Of note, different gradients in X and Z axis were created if the MB was administrated from the top media well (**Figure 5.5c**), rather than at the compound reservoir.

We then analyzed the impact of the ECM, in this case Matrigel, and of the presence of cells, on MB diffusion. To this end, we performed a similar experiment (localized drug delivery from the compound reservoir), but incorporating Matrigel, either with or without embedded MCF-7 cells. Upon MB administration, we scanned sufficiently large areas (8 mm x 3 mm) of the scaffold at different incubation times (1h, 2h and 24 h). The corresponding maps in **Figure 5.6a** unveiled the formation of MB gradients (at different conditions and times) with meaningful and varying SERS profiles. In contrast to the control conditions, significantly restricted MB diffusion occurred in the presence of both Matrigel and MCF-7 cells. We observed in the SERS profiles of **Figure 5.6b** that such a hindered diffusion strongly affects MB distribution profiles at early time points – 1 and 2 hours. Notwithstanding, a similar equilibrium situation (homogenous distribution of MB along the X and Y axes) was reached for all experimental conditions within 24 hours, meaning that no significant variations were registered in SERS intensities at different spots of the same scaffolds (**Figure 5.6c**). Similar effects are shown in **Figure 5.6e**, in which the administration of MB was directly performed from the top of the media well, so as to establish a gradient along the Z-axis. Using the confocal microscopy mode, we additionally observed that the presence of MCF-7 not only hindered MB diffusion but also originated a more heterogeneous distribution along the XZ-plane, clearly noticeable in comparison with control conditions in **Figure5.5c.** Besides, the total SERS intensity at 24 hours was consistently lower in experiments with cells (**Figure 5.6d**). To clarify these results, we investigated whether MCF-7 cells were effectively taking up MB from the extracellular milieu, thereby affecting its diffusion. In this context, MB could also serve as a fluorophore probe with emission around 690 nm, so that cells uptaking MB would display higher emission intensities at this wavelength. We thus interrogated MCF-7 cells upon Matrigel depolymerization and subsequent cell retrieval, via flow cytometry (**Figure 5.6f**). To do so, the obtained cell solution was measured using a 695/40 filter (PerP-CY5) that discerned between cells

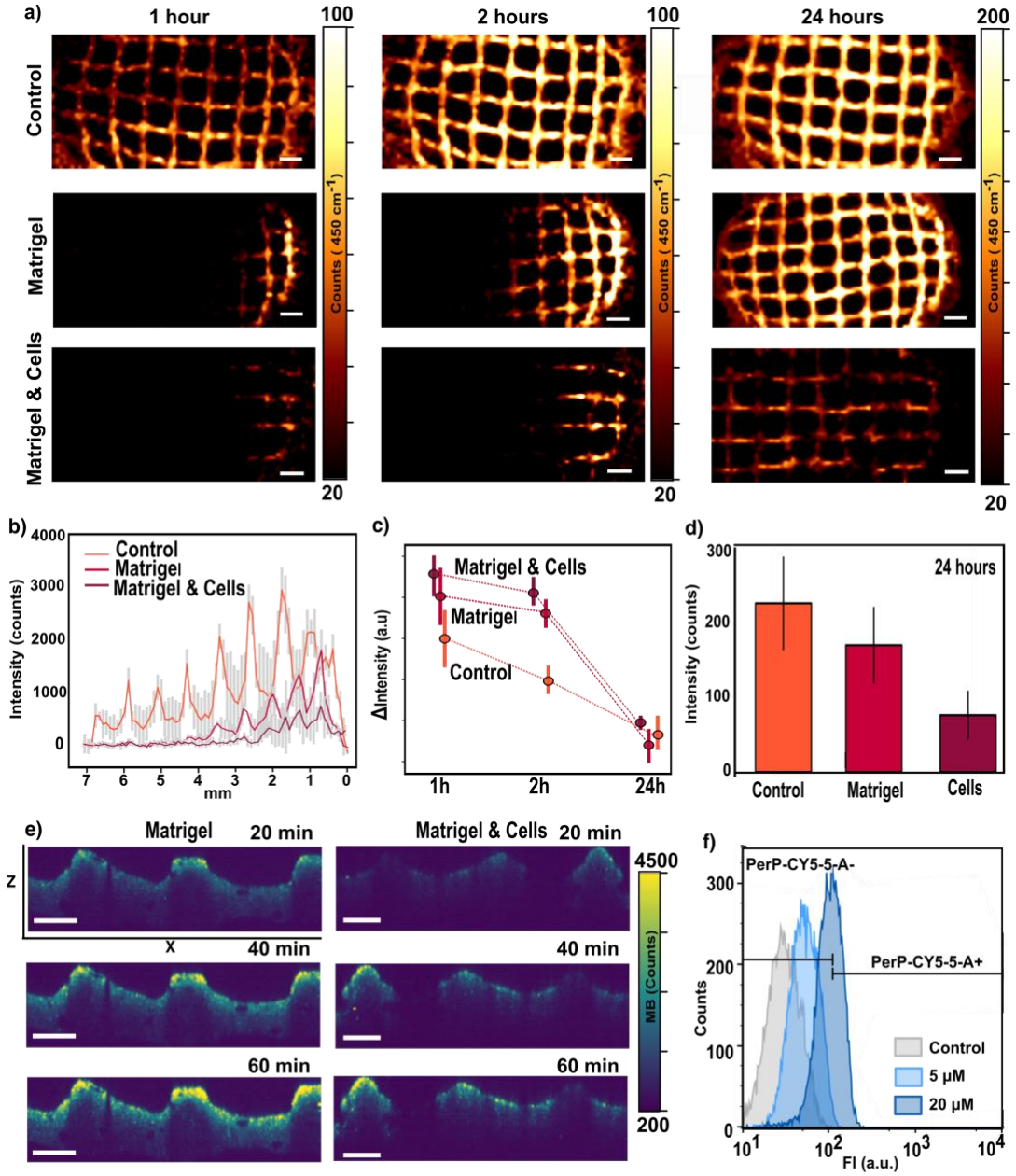

Figure 5.6. a) MB diffusion patterns along the X-axis in pristine nanocomposite scaffolds, scaffolds embedded in Matrigel, and Matrigel loaded with high cell density ($2x10^6$ cells/mL). The SERS signal (at 450 cm^{-1}) was acquired at indicated times (1 hour, 2 hours and 24 hours). An excitation laser at 785 nm through a 10x objective, with a power of 15.15 m*W* for 0.1 s was used for all measurements. Scale bars: 600 µm. b) Diffusion profiles of MB along the X-axis after 2 hours of its administration. Each point represents the average and the standard deviation obtained from SERS intensities along the Y-axis. The step size is 100 µm. c) Plot comparing the differences in SERS intensity between two areas of the scaffold located at 3000 µm away in the X-axis from each other. Each point denotes the average value from three independent experiments. d) Average of the SERS intensity at 450 cm^{-1} after 24 hours of MB administration (10 µM) at the compound reservoir, once equilibrium was reached. Each data point corresponds to the average signal from 200 collected points within two independent experiments (n = 200, N = 2). e) SERS profile maps (XZ plane) of the nanocomposite scaffold within Matrigel and cell-containing Matrigel, after MB administration from the top media well. Confocal SERS mappings were recorded with a 785 nm excitation laser through a 20× water immersion objective, 7 mW power, 50 ms integration time, and a step size of 10 µm. Scale bars: 200 µm. f) Flow cytometry analysis of the uptake of MB by cells retrieved from the 3D culture. The fluorescence from MB increased in a dose-dependent manner. The gating indicates positive and negative cell populations after applying the PerCP-Cy5.5 emission filter (670/40).

with or without intracellular MB. In this manner, we could measure an increase in cell fluorescence at higher MB concentrations, monitoring thereby a dose-dependent accumulation of

MB inside MCF-7 cells. Finally, on the basis of the recorded SERS mappings, we interpreted the creation of different diffusion profiles as the result of 3 main factors: drug diffusivity, extracellular matrix permeability and intracellular accumulation of MB.[43,44]

5.2 III) Monitoring drug distribution and cell death

We finally sought to monitor the SERS signal at different MB concentrations over time, and their consequences on cell viability. It should be noted that the use of MB as an anti-cancer drug requires an extra step of drug activation by light exposure at an appropriate wavelength (close to 640 nm).[45] Upon illumination, the photosensitizer (MB molecules) would start generating reactive oxygen species (ROS), eventually inducing cell death (see **Figure 5.7a**). In the experiments discussed so far, MB was applied without light activation (dark conditions) so that no significant cytotoxic activity was observed. This was further tested by cell viability studies with different

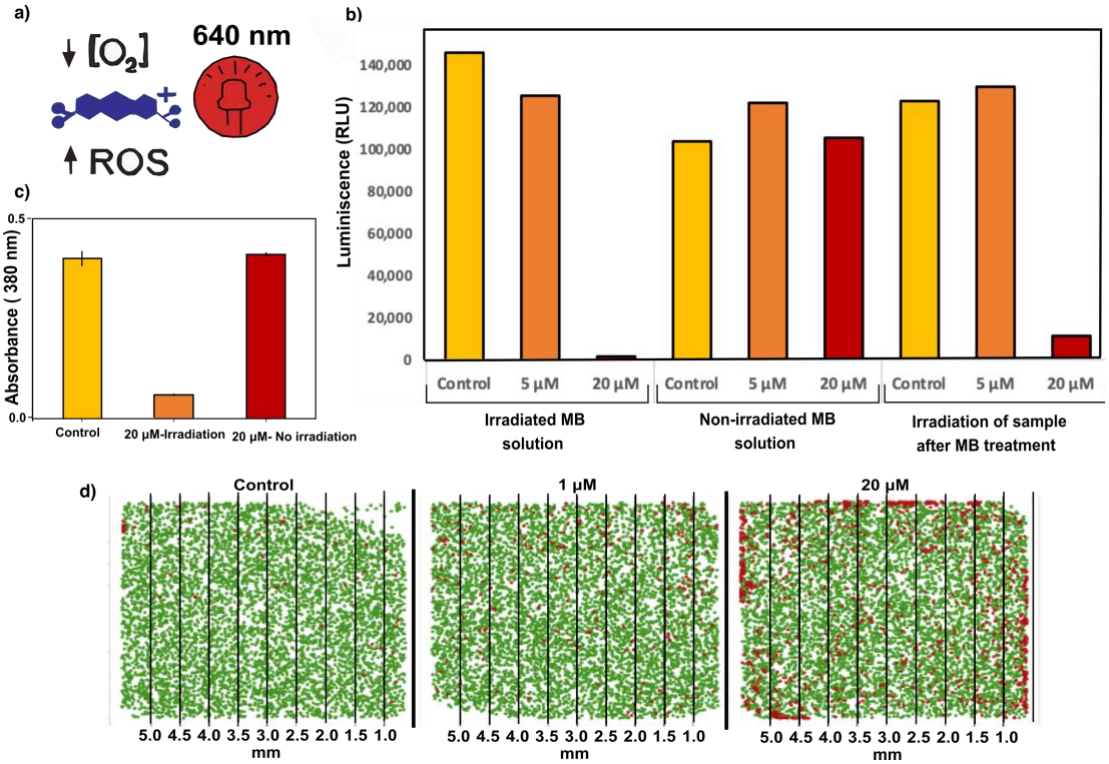

Figure 5.7. a) Sketch of the photoactivation procedure of MB by irradiation with 640 nm light, generating reactive oxygen species (ROS) from O_2. b) Luminescence output 24h after MB challenging at two different concentrations (5 µM and 20 µM), with or without red-lamp irradiation for 1 hour. For this viability assay, cell supernatants were mixed with CellTiter-Glo reagent. The resulting luminescence, which correlates with the number of live cells, was recorded by means of a 965 Luminometer. c) ROS generation by MB (20 µM) after 60 min of red lamp illumination (640 nm). The production of ROS acted by reducing ABDA molecules, present in the solution at 0.2 mM, which eventually leads to a decay in the absorbance at 380 nm. d) Viable cells under control conditions, 1 µM, 20 µM of MB after 24 hours of MB administration at the compound reservoir; MB was previously activated by red lamp illumination for 60 min. The images were acquired by confocal microscope and then processed to represent in two dimensions the Z-stack projection of 3D live confocal images and quantify the distribution of GFP (green) and PI (red) signal. Lines indicate columns into which the images were divided to study the measured area. The obtained results did not display a well-defined gradient of cell death along the X-axis

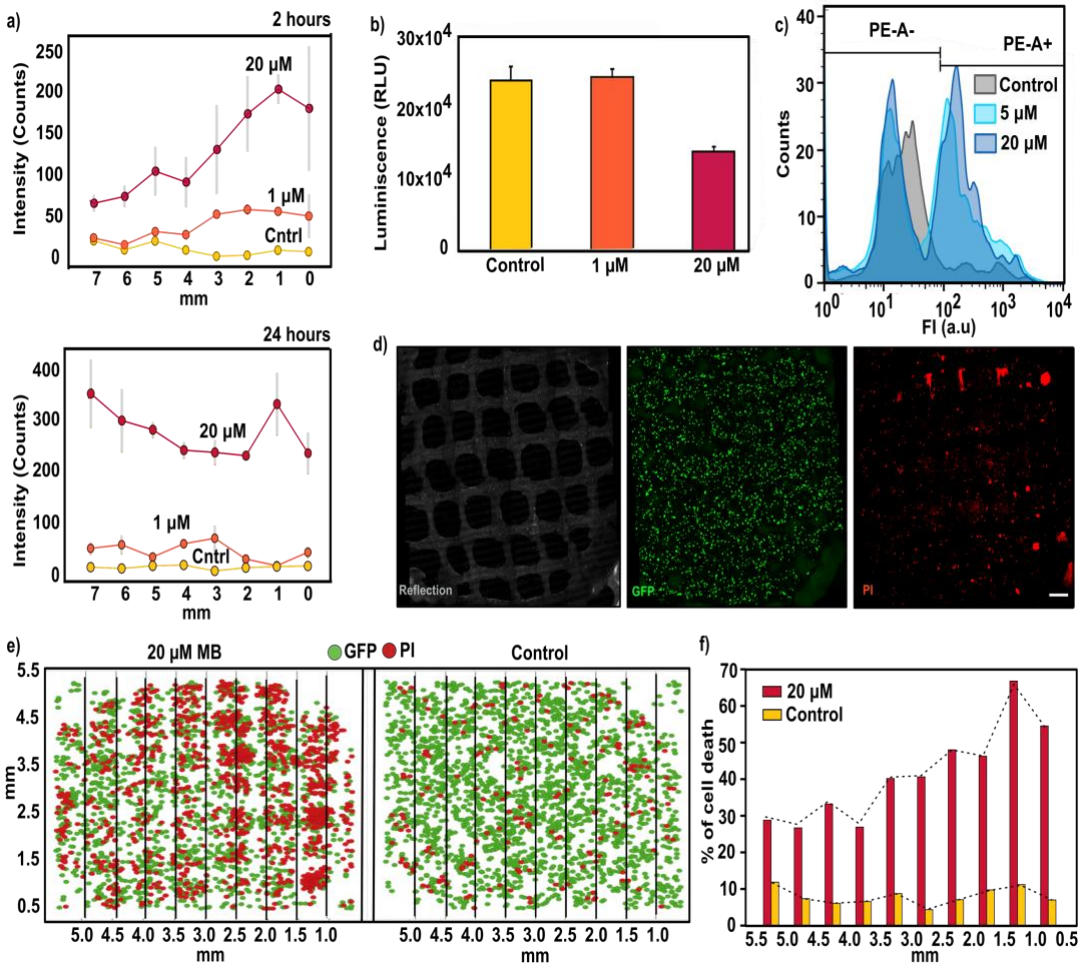

Figure 5.8. a) SERS intensity at increasing doses of MB (control, 1 µM and 20 µM), registered by scaffolds at different points from the reservoir after 2 h (upper panel) and 24 h (lower panel). Gray lines represent the standard deviation from 6 spectra (N=3 samples, n=2). An excitation laser at 785 nm through a 10× objective, with a power of 15.15 mW for 1 s, was used for all measurements. b) Luminescence output 24 h after MB administration monitored with CellTiter-Glo 3D Cell Viability Assay. Error bars indicate the standard derivation of multiple wells measured from the same experiment. c) Flow cytometry analysis representing quantified single cells labeled with PI after treatment with 1 µM and 20 µM MB. The gating indicates the positive and negative cell population after applying a PE emission filter (585/42). d) Maximum intensity projection (XY) images of a representative live confocal image. 3D cells growing in Matrigel and within the nanocomposite scaffold were labeled with PI for visualizing cytotoxic effects 24 h after dispensing 1 µM MB. Images correspond to a 400 µm thick Z-stack. Scale bar: 500 µm. e) Images were acquired after 2 h MB of treatment to visualize the cytotoxicity gradient. Lines indicate columns into which the images were divided to study the distribution of PI (red) and GFP signals (green). f) Automated quantification of cell death percentage for control and 20 µM samples, segmented by columns, dotted line indicates the profile of cell death with the distance.

concentrations of photoactivated MB (**Figure 5.7b**). Specifically, we compared the effects of MB on cell viability when the light photoactivation step occurred before or after drug administration to the cell culture. Non-irradiated MB had a negligible impact on cell viability at this concentration range, showing similar viability to that obtained for control conditions. On the contrary, 20 µM of illuminated MB exhibited an intense cytotoxicity in both photoactivation procedures, owing to the generation of oxidizing species. For assessing the formation of such ROS, we traced the absorbance of a 9,10-Anthracenediyl-bis(methylene)dimalonic acid (ABDA) solution, a dye sensitive to the presence of reactive species (**Figure 5.7c**). Unlike under dark

conditions, a decay in ABDA absorption could be readily recorded upon MB illumination, indicating thereby the consistent formation of ROS species in the solution.

Once we had screened MB photoactivation, we monitored both the distribution of MB and its cytotoxicity by challenging 3D cell cultures with increasing doses of photoactivated MB solution (control, 1 µM and 20 µM). Free MB was illuminated by a red-light lamp prior to administration from the lateral reservoir of the cell culture device. Subsequently, drug diffusion was imaged through the SERS fingerprint of MB at two different time points (2 h and 24 h), followed by evaluation of cell viability at the end of the experiment (24 h). The patterns of MB distribution through the scaffold at the selected times are plotted in **Figure 5.8a**. As expected, the amount of MB was found to dictate both the recorded SERS intensities and the number of dying cells. Whereas no SERS signal was detected upon addition of 1 µM MB at far areas – more than 5 mm – from the lateral reservoir during the first two hours, high SERS intensity could be readily

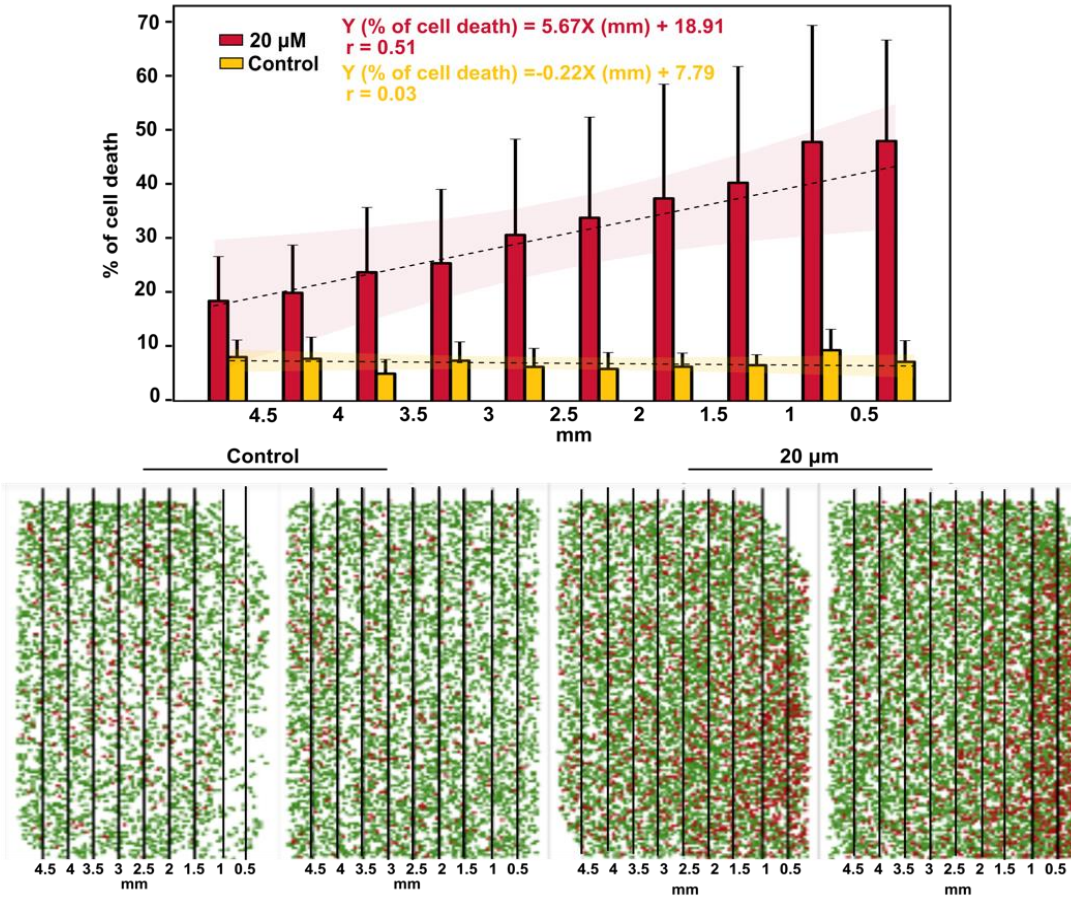

Figure 5.9. Quantification of cell viability (%) under control conditions and with 20 µM of MB delivered by means of the following approach. Cells were challenged with MB, applied at the lateral reservoir for 2 hours. Then cell media containing the diffusing compound was replaced, 3D images from each sample were computationally segmented in columns separated by 0.5 mm. Error bars show the standard deviation of four independent cell assays. The yellow and purple bars are linear fits showing the correlation of cell cytotoxicity (%) with the distance (mm) in control and 20 µM of MB, respectively. Both bars include a regression line (dotted line) and 95% confidence interval. In addition, the corresponding Pearson´s correlation coefficients (r) between the two variables are indicated in the inset. The images in the lower panels display the automated quantification of cell viability percentage from illustrative control and 20 µM.

registered when 20 μM MB was administrated. Quantification of cell viability by CellTiter-Glo test (**Figure 5.8b**) and flow cytometry (**Figure 5.8b**) after recovery of cellular aggregates from Matrigel, demonstrated the dose-dependent cytotoxic effect of MB at both population and single-cell level. Both viability studies revealed extensive cell death when challenging cells with 20 μM of photoactivated MB, registering a decay of luminescence as well as a higher percentage of propidium iodide (PI) positive cell (see section 6.7 for further details). Likewise, live confocal imaging (**Figure 5.8d**) was conducted by following dead cells labelled with PI. Images of the entire culture volume around the scaffold were captured to examine the spatio-temporal location of affected cells and to correlate drug gradients with the distribution of dying cells in 3D. The images obtained by 3D live confocal microscopy were later processed to create two-dimensional representation of the Z-stack projection and automatize the recognition of PI (red) and green fluorescent protein (GFP, green) signals.

Initially, cytotoxic gradients were attempted by fluorescent labeling, 24 hours after the addition of photoactivated MB. However, homogeneous cell death across the 3D culture was observed at this time by confocal microscopy imaging (**Figure 5.7d**). This result is in agreement with SERS results for drug distribution over 24 hours (**Figures 5.6a** and **5.8a**), showing uniform drug distribution throughout the scaffold. Therefore, we developed an alternative approach to enhance the cell death gradient, based on our previous MB transport studies. This strategy consisted of replacing cell media 2 hours after MB administration from the lateral reservoir, thereby rinsing extracellular MB from the 3D culture. By subsequent irradiation with the red lamp, we photoactivated primarily MB that had been uptaken by cells, as well as any remaining MB present in the area closest to the reservoir upon the initial 2 hours of exposition. Finally, automated quantification of fluorescence images after 24 hours (**Figure 5.8e**) revealed a well-defined gradient of dying cells along the X-axis (**Figure 5.8f**) - comparable to the distribution of the MB after 2 hours. For these experiments, confocal images were computationally divided into columns separated by 0.5 mm, to better analyze and represent the cell viability along the measured area. In contrast, the results obtained under control conditions or without extracellular drug removal showed no correlation between proximity to the compound reservoir and cell viability (see **Figure 5.9** for statistical analysis).

5.3 Conclusions

The present study provided compelling evidence supporting the use of plasmonic scaffolds as suitable SERS platforms for drug transport monitoring, potentially fostering a new generation of SERS sensors. As discussed in section 1.5d, the selected alginate-gelatin ink not only acted by creating a 3D polymeric network, but also by enhancing the robustness of the whole sensor over

time. The combination of high stability, through restricted nanoparticle aggregation, along with the high nanoparticle accessibility attained, thanks to the features of high porosity and water-retention, supported the excellent performance of the nanocomposite scaffolds for in situ measurements. Moreover, by integrating 3D-printed composite scaffolds within a customized cell culture device, we could achieve a closer recreation of different compound gradients. Arguably, its specific design effectively assisted in the process of monitoring different parameters of drug diffusion, towards a better understanding of its cytotoxic effect on cell culture model. In particular, the combination of homogenous cell distribution along the scaffold with the selection of MB as a photoactivated drug candidate allowed us to demonstrate that label-free SERS studies can be performed in 3D, under various conditions. Of note, the real-time SERS images acquired clearly evidenced the value of this system to study the extracellular environment in vitro, thereby deciphering the biochemical and biophysical factors involved in drug transport, which might harbor therapeutic relevance.

As already mentioned, a particular benefit offered by this technology is that the plasmonic structure sustaining 3D cell growth can simultaneously function as the SERS sensor, thereby facilitating the acquisition of information in the near vicinity of cells. This approach is foreseen to provide devices where different cell types, or even human explants (e.g. organoids grown from patients' tumor samples) could be monitored over extended periods of time, with high spatial resolution. As a result, the effect of drugs could be tested on these 3D-printed devices, so that SERS analysis would reveal the response of cultured cells against each treatment. Not only that, further improvements in such nanocomposite sensors will be oriented to also monitoring the released secretomes upon specific treatments. Overall, the prospect of combining this technology with the analysis presented in Chapter 4 may laid the foundation to the final expansion of SERS into precision medicine.

In a different direction, additional complexity could be added, by incorporation of AuNPs carrying Raman-active molecules sensitive to different stimuli with well-defined SERS peak shift or intensity changes at each condition, so that environmental changes such as pH or hypoxia can be recorded, again with spatial and temporal resolution. In this scenario, we have recently obtained promising data for the monitoring of local pH in encapsulated cells.[46] In this preliminary step, the polymeric component acted as a microcontainer for the cells, instead of adopting the previous grid architecture. By registering the intensity changes for each protonation state of 4-MBA adsorbed on gold nanostars, we could screen variations in extracellular pH that correlated with the overall state of the embedding cells. We envisage that, in addition to pH, other parameters influencing several cell mechanism and processes could be robustly monitored by the vibrational changes derived from their interaction with pre-tagged Raman reporters (see section 1.5d for

further explanation), or even introducing other types of nanoparticles (such as luminescent nanoparticles based on rare-earth doped materials) to measure small temperature changes at cellular scale.[47]

5.4 References

(1) Barcellos-Hoff, M. H., Lyden, D. & Wang, T. C. The evolution of the cancer niche during multistage carcinogenesis. *Nat. Rev. Cancer* **13**, 511-518 (2013).

(2) Rodrigues, J., Heinrich, M. A., Teixeira, L. M., Prakash, J. 3D in vitro model (R)evolution: unveiling tumor–stroma interactions. *Trends in Cancer* **2021**, *7*, 249–264.

(3) Jordahl, S.; Solorio, L.; Neale, D. B.; McDermott, S.; Jordahl, J. H.; Fox, A.; Dunlay, C.; Xiao, A.; Brown, M.; Wicha, M.; Luker, G. D. & Lahann, J. Engineered fibrillar fibronectin networks as three-dimensional tissue scaffolds. *Adv. Mater.* **31,** e1904580 (2019).

(4) Ntziachristos, V., Pleitez, M. A., Aime, S. & Brindle, K. M. Emerging technologies to image tissue metabolism. *Cell Metab.* **29** , 518–538 (2019).

(5) Vidavsky, N. *et. al.* Mapping and profiling lipid distribution in a 3D model of breast cancer progression. *ACS Cent. Sci.* **5**, 768–780 (2019).

(6) Eggert, S. *et. al.* Automated 3D microphysiometry facilitates high-Content and highly reproducible oxygen measurements within 3D cell culture models. *ACS Sens.* **6**, 1248–1260 (2021).

(7) Cheng, J. X. & Xie, X. S. Vibrational spectroscopic imaging of living systems: An emerging platform for biology and medicine. *Science* **350**, aaa8870 (2015).

(8) Ma, C. *et. al.* W. Leukemia-on-a-chip: Dissecting the chemoresistance mechanisms in B cell acute lymphoblastic leukemia bone marrow niche. *Sci. Adv* **6**, eaba5536 (2020).

(9) Holle, A. W. *et. al.* T. Cell-extracellular matrix mechanobiology: Forceful tools and emerging needs for basic and translational research. *Nano Lett.* **18**, 1–8 (2018).

(10) Carmona-Fontaine, C. *et. al.* Metabolic origins of spatial organization in the tumor microenvironment. *Proc. Natl. Acad. Sci. U. S. A.* **114**, 2934–2939 (2017).

(11) Tucker, L. H. *et. al.* Untargeted metabolite mapping in 3D cell culture models using high spectral resolution FT-ICR mass spectrometry imaging. *Anal. Chem.* **91**, 9522–9529 (2019).

(12) Lyssiotis, C. A. & Kimmelman, A. C. Metabolic interactions in the tumor microenvironment. *Trends Cell Biol.* **27**, 863–875 (2017).

(13) Hanahan, D. & Weinberg, R. A. Hallmarks of cancer: The next generation. *Cell* **144**, 646–674 (2011).

(14) Pampaloni, F. Reynaud, E. G. & Stelzer, E. H. K. The third dimension bridges the gap between cell culture and live tissue. *Nat. Rev. Mol. Cell Biol.* **8**, 839–845 (2007).

(15) Jeong, S. Y., Lee, J. H., Shin, Y., Chung, S. & Kuh, H. J. Co-Culture of tumor spheroids and fibroblasts in a collagen matrix-incorporated microfluidic chip mimics reciprocal activation in solid tumor microenvironment. *PLoS One* **11,** e0159013 (2016).

(16) Yi, H. G. *et. al.* Bioprinted human-glioblastoma-on-a-chip for the identification of patient-specific responses to chemoradiotherapy. *Nat. Biomed. Eng.* ***3***, 509–519 (2019).

(17) Brancato, V., Oliveira, J. M., Correlo, V. M., Reis, R. L. & Kundu, S. C. Could 3D models of cancer enhance drug screening? *Biomaterials* **232**, 119744 (2020).

(18) Pati, F. *et. al*. Printing three-dimensional tissue analogues with decellularized extracellular matrix bioink. *Nat. Commun.* **5***,* 3935 (2014).

(19) Rijal, G. & Li, W. A versatile 3D tissue matrix scaffold system for tumor modeling and drug screening. *Sci. Adv.* **3**, e1700764 (2017).

(20) Luo Gu, D. J. M. biomaterials and emerging anticancer therapeutics: engineering the microenvironment. *Nat. Rev. Cancer* **16**, 56–66 (2016).

(21) Ueno, T.; Nagano, T. Fluorescent probes for sensing and imaging. *Nat. Methods* **8**, 642–645 (2011).

(22) Hong, G., Antaris, A. L. & Dai, H. Near-infrared fluorophores for biomedical imaging. *Nat. Biomed. Eng.* **1**, 0010 (2017).

(23) Kim, N. *et. al*. Surface enhanced Raman scattering artificial nose for high dimensionality fingerprinting. *Nat. Commun.* **11***,* 207 (2019).

(24) Langer, J. *et. al.* Present and future of surface-enhanced Raman scattering. *ACS Nano* **14,** 28–117 (2020).

(25) Plou, J. *et. al.* Multiplex SERS detection of netabolic alterations in tumor extracellular media. *Adv. Funct. Mater.* **30**, 1910335 (2020).

(26) Bodelón, G. *et. al.* Imaging bacterial interspecies chemical interactions by surface-enhanced Raman scattering. *ACS Nano* **11**, 4631–4640 (2017).

(27) García-Astrain, C. *et. al.* 3D-Printed biocompatible scaffolds with built-in nanoplasmonic sensors. *Adv. Funct. Mater.* **30**, 2005407 (2020).

(28) Srichan, C. *et. al.* Highly-sensitive surface-enhanced Raman spectroscopy (SERS)-based chemical sensor using 3D graphene foam decorated with silver nanoparticles as SERS substrate. *Sci. Rep.* **6**, 23733 (2016).

(29) dos Santos, A. F. *et. al.* Methylene Blue photodynamic therapy induces selective and massive cell death in human breast cancer cells. *BMC Cancer* **17**, 194 (2017).

(30) Wu, P. T., *et. al.* Methylene-Blue-encapsulated liposomes as photodynamic therapy nano agents for breast cancer cells. *Nanomaterials* **9***, 14* (2019).

(31) Pastoriza-Santos, I., Kinnear, C., Pérez-Juste, J., Mulvaney, P. & Liz-Marzán, L. M. Plasmonic polymer nanocomposites. *Nat. Rev. Mater.* **3,** 375–391 (2018).

(32) Zhu, K. *et. al*. Gold nanocomposite bioink for printing 3D cardiac constructs. *Adv. Funct. Mater.* **27**, 1605352 (2017).

(33) Erben, A. *et. al.* Precision 3D-printed cell scaffolds mimicking native tissue composition and mechanics. *Adv. Healthc. Mater.* **9**, e2000918 (2020).

(34) Tibbitt, M. W. & Anseth, K. S. Hydrogels as extracellular matrix mimics for 3D cell culture. *Biotechnol. Bioeng.* **103**, 655–663 (2009).

(35) Afewerki, S.; Sheikhi, A.; Kannan, S.; Ahadian, S. & Khademhosseini, A. Gelatin-Polysaccharide composite scaffolds for 3D cell culture and tissue engineering: Towards natural therapeutics. *Bioeng. Transl. Med.* **4**, 96–115 (2019).

(36) Kundu, S. & Nithiyanantham, U. In situ formation of curcumin stabilized shape-selective Ag nanostructures in aqueous solution and their pronounced SERS activity. *RSC. Adv*. **3**, 25278 (2013).

(37) Shin, Y. *et. al.* Facile microfluidic fabrication of 3D hydrogel SERS substrate with high reusability and reproducibility via programmable maskless flow microlithography. *Adv. Opt. Mater.* **8,** 2001586 (2020).

(38) Kim, D. J., Park, S. G., Kim, D. H. & Kim, S. H. SERS-Active-charged microgels for size- and charge-selective molecular analysis of complex biological samples. *Small* **14**, 1802520. (2018)

(39) Lieleg, O., & Ribbeck, K.. Biological hydrogels as selective diffusion barriers. Trends Cell Biol. **2011**, *21*, 543–551.

(40) Dumont, E. *et. al.* Development of a prototype device for near real-time surface-enhanced Raman scattering monitoring of biological samples. *Talanta*, **224**, 121866 (2021).

(41) Orth, K., Beck, G., Genze, F. & Rück, A. Methylene Blue mediated photodynamic therapy in experimental colorectal tumors in mice. *J. Photochem. Photobiol. B Biol.* **57**, 186–192 (2000) .

(42) Vantangoli, M. M. *et al.* MCF-7 human breast cancer cells form differentiated microtissues in scaffold-free hydrogels. *PLoS One* **10,** e0135426 (2015).

(43) Dewhirst, M. W.; Secomb, T. W. Transport of drugs from blood vessels to tumour tissue. *Nat. Rev. Cancer* **17**, 738–750 (2017).

(44) Han, B., Qu, C., Park, K., Konieczny, S. F. & Korc, M. Recapitulation of complex transport and action of drugs at the tumor microenvironment using tumor-microenvironment-on-chip. *Cancer Lett.* **380,** 319–329 (2016).

(45) Klosowski, E. M. *et. al.* The photodynamic and direct actions of Methylene Blue on mitochondrial energy metabolism: A balance of the useful and harmful effects of this photosensitizer. *Free Radic. Biol. Med.* **153**, 34–53 (2020).

(46) Zhang, Y. *et al*. SERS Moniotring of local pH in encapsulated therapeutic cells. *Nanoscale* **13**, 14354-14362 (2021).

(47) M. L. Debasu, *et. al*. All-in-one optical heater-thermometer nanoplatform operative from 300 to 2000 K Based on Er(3+) emission and blackbody radiation. Adv. Mater. **25**, 4868-4874 (2013).

CHAPTER 6

"Experimental Methods"

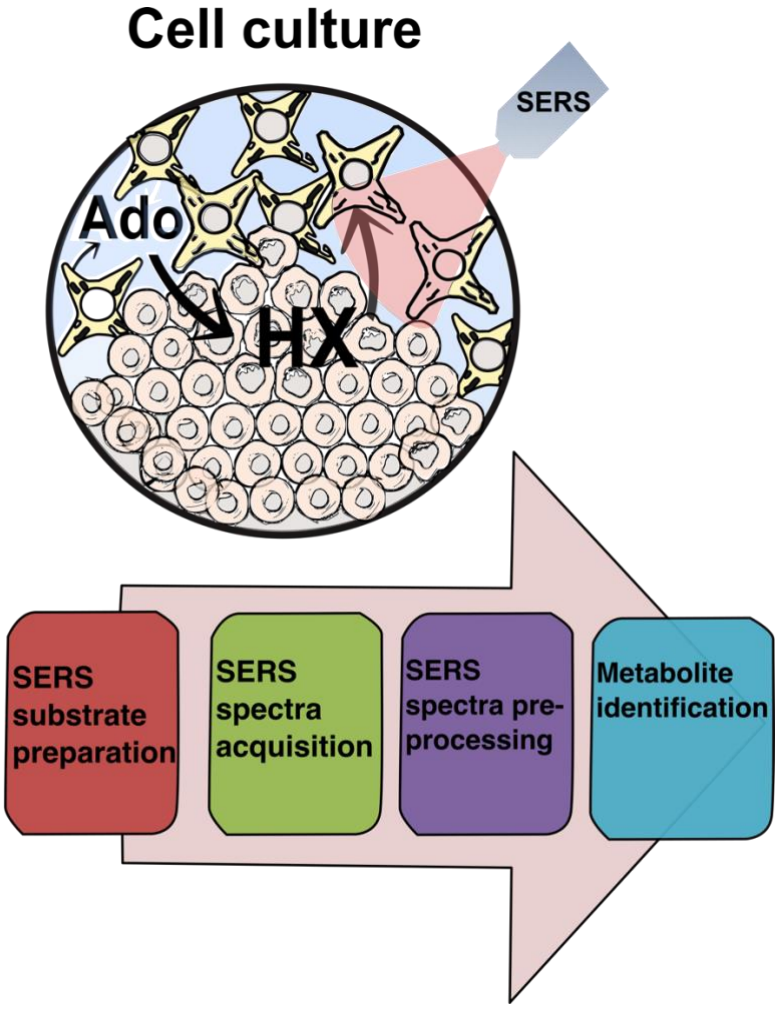

In this chapter, we describe the materials and methods utilized throughout this thesis, ranging from the synthesis of nanoparticles to cell viability tests. To favor readability, we have classified the methods in different sections according to the field of expertise, rather than following the order of the chapters in which they are used. Thus, for instance, the section describing the fabrication of plasmonic substrates includes both substrates on flat glass supports (Chapter 2) and nanocomposite scaffolds (Chapter 5), in which the nanoparticles are embedded within a hydrogel-network.

6.1 Chemicals

The reagents required for AuNPs synthesis and SERS substrates fabrication were purchased as indicated: $HAuCl_4 \cdot 3\ H_2O$ (≥99.9%, trace metal basis) was purchased from Alfa Aesar. Sodium borohydride (ReagentPlus®, ≥99%, $NaBH_4$), L-ascorbic acid (ACS reagents, ≥99%, AA), poly(ethylene glycol) methyl ether thiol average Mn 6000 (PEG-6K), sodium hypochlorite (6-14% active chlorine, Emplura®), cetyltrimethylammonium chloride (≥98%, CTAC), poly(diallyldimethylammonium chloride) (PDDA, average Mw 100 000−200 000), poly(acrylic acid, sodium salt) (PAA, Mw 15 000), hydrogen peroxide (H_2O_2, 28%), sulfuric acid (H_2SO_4, 98%), ethanol (EtOH, 99.8%), 5-bromosalicylic acid (90%, 5-BrSA) were purchased from Sigma-Aldrich. All solutions, except $HAuCl_4$ and CTAB, were prepared immediately before use. Purified Milli-Q water was used in all experiments (Millipore, 18.2 MΩ cm). Glassware (Menzel-Gläser 24x24 #1) was cleaned with aqua regia and rinsed extensively with Milli-Q water before use. Poly-methylmethacrylate (PMMA A2 950) was purchased from EM Resist and used as supplied. Poly lactide co-glycolide 75:25 25000 Mn, acid endcap and poly lactide co-glycolide 95:5 25000 Mn, acid endcap, were purchased from Polysciences.

Commercial metabolites and probe molecules: 4-mercaptobenzoic acid (90%, 4-MBA), 4-nitrothiophenol (80%, 4-NTP), (thiabendazole (> 99% powder, TBZ), Crystal Violet (dye content > 90%) Methylene Blue (> 95%, MB), and nicotinamide (> 98% powder, NAm), were purchased from Sigma-Aldrich. Commercial samples of Kynurenine (25 mg, Kyn), Tryptophan (1g, Trp), Adenosine triphosphate (1g, ATP), adenosine (1g, Ado), adenine (1g, A), hypoxanthine (1g, HX), inosine (1g, Ino), IFN-ϒ, staurosporine (STP), hemin, and erastin drug were supplied by Sigma-Aldrich.

For cell culture, cell media was Gibco Dulbecco's Modified Eagle Medium (DMEM) (Thermo Fisher) with 10% (v/v) of fetal bovine serum (FBS), 1% (v/v) of Penicillin-Streptomycin (PenStrep, 11548876,), 1% Trypsin-EDTA solution were purchased from Thermo Fisher. Biopolymer hydrogels for 3D cell culture: Matrigel from Corning™, and collagen bioink from rat tale type, was purchased from Sigma. Gelatin from porcine skin and sodium alginate from Sigma. Salt (3-(4,5-dimethylthiazol-2-yl)-2,5-diphenyltetrazolium bromide (MTT) from Thermo Fisher, Propidium iodide (PI) and Cytocalcalcein, from Sigma-Aldrich. Cell recovery solution was from Corning, with CellTiter-Glo 3D Cell Viability Assay kit. Polydimethylsiloxane (Sylgard 184) for cancer-on-a-chip devices was bought from Dow Corning.

6.2 Synthesis of Gold Nanoparticles

Citrate-AuNPs (30 nm): Citrate-stabilized Au NPs (30 nm in diameter) were synthesized according to a previously reported seeded growth method.[1] 150 mL of 2.2 mM trisodium citrate water was heated to boiling under vigorous stirring. After 15 min, 1 mL of 25 mM $HAuCl_4$ was injected into the boiling reaction mixture and incubated for 10 min, and then the reaction mixture was cooled to 90 °C. Subsequently, 1 mL of a 25 mM $HAuCl_4$ aqueous solution was injected into the reaction mixture. After 30 min, the addition of $HAuCl_4$ was repeated. After 30 min, the sample was diluted by extracting 55 mL of sample and adding 53 mL of water and 2 mL of aqueous 60 mM sodium citrate solution. This final solution was used again as a seed, and the process (adding 2mL of 25 mM $HAuCl_4$, 1 mL every 30 min and subsequent dilution) was repeated again six times to yield 60 nm Au NPs. To remove the excess of reactants, the colloidal dispersions were centrifuged at 1520g for 20 min and redispersed in the same volume of water

PEG-AuNPs (30 nm): Gold nanospheres were synthesized by seeded growth, as previously described.[2] First, 2 nm seeds were prepared by adding 50 µL of a 0.05 M $HAuCl_4$ solution to 5 mL of a 100 mM CTAC solution. Subsequently, 200 µL of a 0.02 M $NaBH_4$ (0.75 mg/mL) was added under vigorous stirring. After 3 min, the mixture was diluted 10 times with a 100 mM solution of CTAC. The seeds were then overgrown to 10 nm nanospheres. For this purpose, 900 µL of seeds was added to a mixture of 40 µL of a 0.1 M AA solution and 10 mL of a 25 mM CTAC solution. Next, 50 µL of a 0.05 M $HAuCl_4$ solution was added under vigorous stirring. The 10 nm seeds showed a localized surface plasmon resonance (LSPR) at 520 nm. The dispersion was left undisturbed for at least 1 h. Thereafter, the nanospheres were centrifuged at 19300 g and washed at least 3 times with CTAC 25 mM, to obtain a narrower size distribution prior to overgrowth into larger nanospheres. Therefore, 125 µL of 10 nm nanospheres was added to a solution containing 40 µL of a 0.1 M AA solution and 10 mL of a 25 mM CTAC solution. Subsequently, 50 µL of 0.05 M of $HAuCl_4$ was added. The resulting nanoparticles had rough edges, which were removed by oxidative etching. To this end, 10 µL of a dilute solution of sodium hypochlorite (1 to 1.5% of available chlorine), and 10 min later, 5 µL of a 0.05 M solution of $HAuCl_4$ was added under stirring. After 30 min, the nanospheres were centrifuged at 1600 g for 15 min and redispersed in 500 µM CTAC. The particles were then concentrated to 5 mM Au^0 in a 500 µM CTAC solution. PEG functionalization was carried out by addition of 1 mg/mL of PEG6K and stirring overnight at room temperature. Excess of unbound PEG was removed by 4-fold centrifugation at 1600 g for 15 min and redispersion of the sedimented NPs (30 nm) in CTAC 500 µM.

AuNRs (plasmon band at 800 nm): AuNRs were prepared following a well-established procedure.[3] First, seeds were prepared following the standard CTAB/$NaBH_4$ procedure at 30 °C. 25 μL of a 50 × 10^{-3} M $HAuCl_4$ solution was added to 4.7 mL of 0.1 M CTAB solution and the mixture was stirred for 5 min. Then, 300 μL of a freshly prepared 10 ×10^{-3} M $NaBH_4$ solution was injected under vigorous stirring. The seeds were kept for 30 min at room temperature until excess borohydride was consumed. For the preparation of AuNRs, 45 mg of 5-BrSA was added to 25 mL of 0.1 M CTAB. After complete dissolution of 5-BrSA, 480 μL of 0.01 M $AgNO_3$ was added and the solution stirred for 15 min at room temperature. Then, to perform the pre-reduction of Au (III) to Au (I), 500 μL of 50 × 10^{-3} M $HAuCl_4$ solution was added to the mixture. Pre-reduction was monitored by UV–vis spectroscopy until the value of the absorbance at 396 nm was 0.8–0.85, to obtain AuNRs with a longitudinal plasmon band around 800 nm. At this time, 130 μL of 100 × 10^{-3} M AA solution was added and the solution turned colorless within a few seconds. After 30 s, 80 μL of seed solution was added under vigorous stirring. After 30 s, the stirring was stopped, and the mixture was left undisturbed for 4 h. The resulting solution was centrifuged at 8000 rpm for 30 min to purify the AuNRs.

6.3 Fabrication of plasmonic substrates

LBL methodology: The production of randomly deposited AuNP multilayers was based on the well-known layer-by-layer (LBL) assembly methodology (see **Figure 6.1a**).[4] Following this protocol, glass slides were sequentially immersed in polyelectrolyte solutions of PDDA (1 mg/mL, 0.05 M NaCl), PAA (1 mg/mL, 0.05 M NaCl), and PDDA (1 mg/mL, 0.05 M NaCl) for 15 min. AuNP layers were then formed by immersing the polyelectrolyte-coated glass slides in a 0.9 mM citrate-stabilized 30 nm AuNP solution for at least 3 h, followed by rising with water and drying under nitrogen flow. For the deposition of a second and third AuNP layers, the same procedure described above was repeated.

Template assisted self-assembly: a 2 μL droplet of nanoparticle dispersion (50 mM of PEG-AuNPs of 30 nm, calculated from the absorbance at 400 nm, 66% EtOH, 200 μM CTAC) was casted on a nanostructured PDMS stamp. Soft PDMS molds were replicated by pouring a 10:1 mixture of prepolymer and curing agent either onto patterned silicon masters or OrmoStamp® (Microresist Technology) replica thereof (that were kindly provided by Nanopto group, ICMBA).[4] The PDMS stamp featured a square lattice of 270 nm holes, with a center to center spacing of 500 nm or 600 nm (according to the final use and the laser excitation employed for SERS/SERRS). After 40 s, a glass slide (24x24 mm^2 and a thickness of 0.13 mm - 0.16 mm) was placed on top of the droplet, creating a NP dispersion film between the glass substrate and the

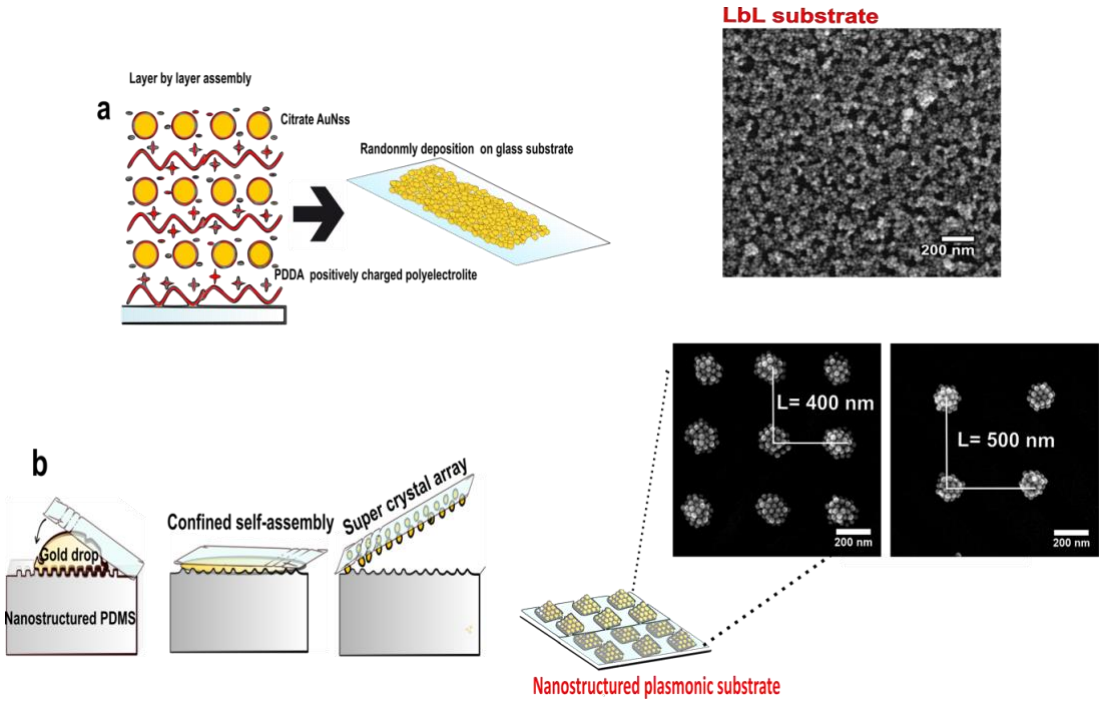

Figure 6.1. a) Schematic view of the methodology followed for LbL assembly of citrate gold nanospheres into random multilayers on glass substrates. b) Graphical representation of the methodology followed for the deposition of ordered 2D superlattices of gold nanospheres, templated by topographically structured PDMS templates. The lattice parameter, i.e. the distance between AuNSs clusters was denoted as "L".

PDMS stamp. After 2 h and complete evaporation of the solvent, the glass slide was carefully lifted off the PDMS template, resulting in transfer of the plasmonic superlattice onto the glass substrate, displaying the inverse shape of the nanostructured mold, as depicted in **Figure 6.1b**. Immobilization and cleaning of the nanoparticle clusters onto a glass slide was achieved by oxygen plasma treatment for 20 s, followed by UV-ozone cleaning (ProCleanerTM chamber) for 5 minutes. The oxygen plasma process was operated using a Diener Electronic nanoplasma cleaner at 100 W and 0.4 mbar oxygen pressure. We observed that these cleaning treatments may alter the final SERS results, so it was crucial to optimize the exposure time and check the absorbance spectra of the substrate before and after cleaning (reported in **Figure 6.2**).

Drop-casting: To fabricate substrates with a random distribution of AuNPs, as a simple strategy to rapidly produce SERS sensors on solid supports, a dispersion of AuNPs (2 mM) in CTAC (500 μM). 50 µL was drop-casted on a glass substrate, pre-cleaned with a dilute solution of Helmanex II, and dried afterwards for 3 hours at room temperature.

Ink preparation for 3D-printed nanocomposite scaffolds: Nanocomposite inks were prepared by mixing 1 mL of a 20 wt%. aqueous solution of gelatin with 40 mg of alginate and 1 mL of aqueous AuNR solution with a concentration of 2 mM in gold. The samples were thoroughly mixed using a Thinky Mixer at 3500 rpm for 1 min. Importantly, AuNRs were washed, by

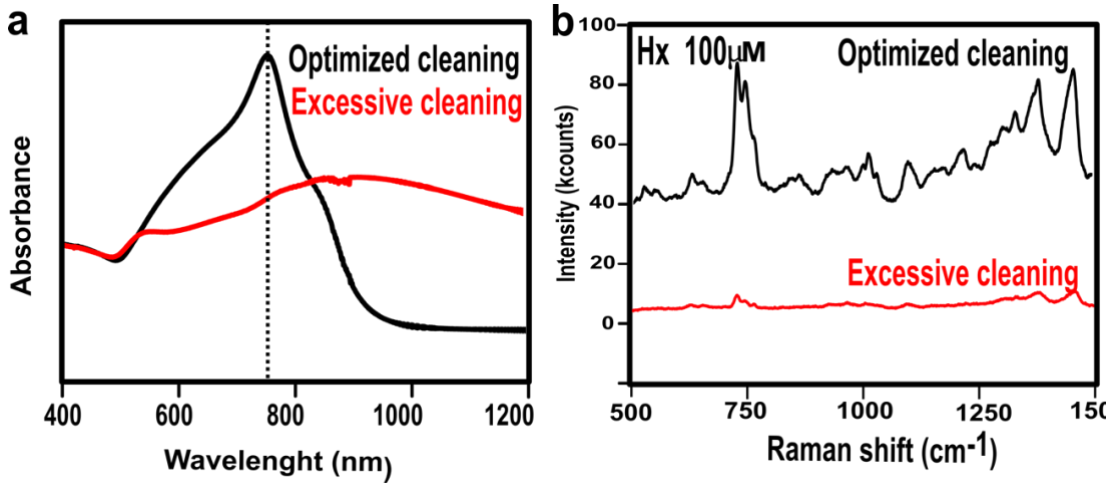

Figure 6.2. Vis-NIR spectra, normalized to 400 nm, of the corresponding plasmonic substrates obtained after different times of cleaning (plasma cleaning, UV-O_3), black spectra correspond to the result obtained after an optimized cleaning procedure (5s plasma cleaning, 5 min UV-O_3), whereas red spectra were measured after longer times, resulting in excessive cleaning and depletion of the plasmonic properties. The observed changes correlate with different SERS enhancing ability of hypoxanthine at 10^{-4} M. SERS measurements were performed with a 50× objective, 20 s of acquisition and a maximum power of the 785 nm laser of 8.50 mW.

centrifugation (8000 rpm) and resuspension in in Mili-Q water, prior to their incorporation to the ink formulation to remove excess CTAB. 3D printed scaffolds were prepared using a RegenHU 3D Discovery Bioprinter at room temperature using a pneumatic pressure-driven cartridge with a 0.2 mm diameter needle, at a pressure of 0.2 MPa. After printing, the scaffolds were immersed in a calcium chloride bath for 5 minutes, to cross-linke the polymers in the alginate, attaching them to each other at many points.

6.4 Fabrication of platforms for cell culture and SERS analysis

Cancer-on-a-chip (silicone chamber): To print the cancer-on-a-chip device, a silicone ink was prepared using an elastomer base (Shin-Etsu Silicone) with curing agent at a 10:1 volume ratio and the mixture was loaded into a 10-mL clear syringe (PSY-E; Musashi Engineering, Ltd.) and printed with a diameter of 2 cm by a multi-headed 3D Discovery bioprinter (RegenHU, Switzerland) on a glass micro slide (26x76 mm) (see **Figure 6.3** for optical image of the device).

Microfluidic chip for flowing analytes: For the microfluidic chip, the channels were etched into PDMS Sylgard® 184, purchased from Sigma-Aldrich. Microdevices were fabricated according to a previously reported protocol.[6] Soft lithography was used to develop positive SU8 240-µm relief patterns with the desired geometry on a silicon wafer. Subsequently, PDMS was mixed at a 10:1 weight ratio of base to curing agent. The mixed solution was poured into the SU8 master and cured in the oven. Finally, the replica-molded layer was trimmed and perforated. The PDMS devices were then exposed to a plasma cleaning treatment (2 min) and subsequently bound to the

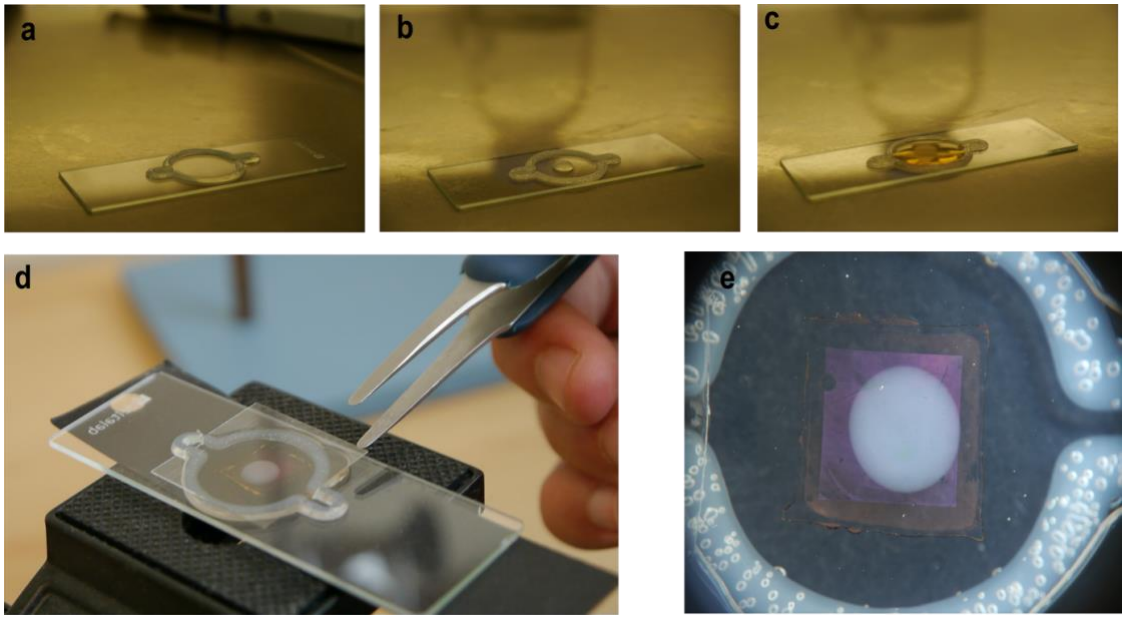

Figure 6.3. a,b,c) Deposition of the HeLa cells, embedded in a collagen bioink at 3mg/mL, inside printed silicone chambers. After collagen polymerization in the incubator chamber, the device was completely filled with cell media. d,e) At the selected time, plasmonic superlattice substrates were combined with the tumor on a chip device, resulting in a direct contact between extracellular milieu and plasmonic structures.

plasmonic substrate by applying a soft pressure on the device with a sterile pair of tweezers, finally presenting a capacity of 10 µL. The flow in the microfluidic channel was generated using a Cetoni Nemesys syringe pump with a low-pressure module. The flow was set at 10 mL/h and the outlet was connected to another syringe pumping at the same flow rate of 10 mL/h.

Diffusion device fabrication to be combined with nanocomposite scaffolds: Custom diffusion devices were designed with Autodesk Inventor Software and fabricated using an Ultimaker 2 printer. The devices were printed with black Polylactic acid (PLA) with 90% filling density, employing a 0.4 mm Print Core AA nozzle (9529, Ultimaker) heated to 210 ºC prior to cell culture, PLA devices were rinsed with distilled water, dried, and sterilized with UV light. Biocompatible adhesive was employed to bind the devices to the cover glass substrate with the scaffold attached. The dimensions of the device can be found in **Figure 6.4**.

6.5 Fabrication of SERS substrates covered by a polymer sheathing layer

Fabrication of polymer films: Commercially available, solid PLGA (75:25 or 95:5) was dissolved in ethyl acetate by mechanical stirring of PLGA granules in the selected solvent for 1 hour. Stock solutions were prepared at 12 wt% in ethyl acetate and kept in the fridge at 8°C, each vial was wrapped with parafilm© to avoid solvent evaporation. PLGA films were created by spin coating (Laurell WS-400B-6NPP LITE) the 12 wt% PLGA/ethyl acetate solution on top of the

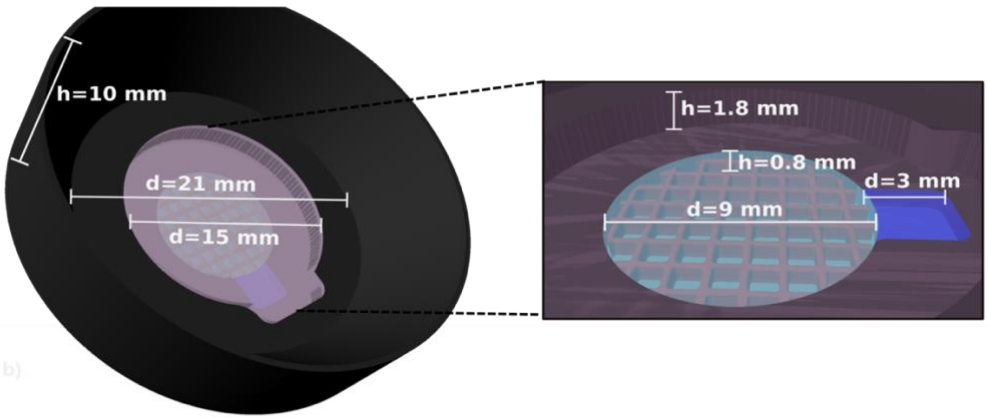

	Scaffold-hydrogel chamber	Compound reservoir	Media well	Immersion well
Area (mm^2)	63.6	9	176.6	346.18
Volume (µL)	50.88	7.2	318	1000

Figure 6.4. Dimensions of the cell culture device. Illustrations of the custom cell culture device designed with AutoCAD software (Illustrator) indicating the main dimensions. Summarized in the table are the area and volumes of the various compartments. The 3D culture had a thickness of 0.8 mm and was nourished with a minimum of 300 µL of media. Additional media could be poured to fill the whole device and perform SERS measurements with immersion objectives. The device also supported the addition of the compound in a controlled compartment to study its diffusion through the 3D culture.

nanoparticle superlattice. To this end, a 300 µL droplet was placed on top of the superlattice, such that it wetted the whole surface of the sample. The spin coating process was then started at a speed of 1500 rpm for 30s. The thickness of the PLGA film was measured to be 1.5 µm by SEM cross section analysis using 5kV acceleration voltage. PMMA coatings were created by spin coating 300 µL of the commercial solution at 1500 rpm for 30 s.

6.6 Equipment for SERS measurements:

Two different Raman microscopes were employed for the different experiments, according to the required spatial resolution.

Standard SERS measurements: SERS spectra were acquired with an InVia Reflex Raman microscope (Renishaw plc) when high spatial resolution was not required (e.g, SERS measurements of cell supernatants in which the scanning step size was above 20 µm in X and Y axes). The Renishaw instrument comprises an optical microscope (Leica) with a XYZ scanning stage coupled to a high-throughput Raman spectrometer equipped with a 1024x512 front-illuminated CCD detector and a grating of 1200 grooves/mm. A line-shaped 785 nm laser excitation source (maximum 119.50 mW) was used, recording in static mode at standard confocality through either 50x or 10x objectives, as indicated for each case, (numerical aperture

NA = 0.5 (50x) and 0,25 (10x)) with integration time ranging from 10s to 0.1s, for large diffusion gradients in Chapter 5, at typically 10% of maximum power was used.

For the experiments performed with collected supernatants (mostly in Chapter 2 and 4), the liquid derived from different assays was typically deposited on a plasmonic substrate circumscribed by the lines created with a hydrophobic pen (sigma), which prevented from liquid spreading. For biological assays, we performed three independent cell assays which were spiked on three independent plasmonic substrates. If the measurements where otherwise performed through the cancer-on-a-chip strategy, the chip was directly assembled with the plasmonic substrate, placing the gold nanoparticle assembly in contact with the extracellular milieu. In these cases (addressed in Chapter 2 and 3), the laser radiation passed through the glass support layer.

Thanks to the XZY scanning stage, control over the Z-axis could be achieved, which enabled focusing the laser on the surface of the plasmonic substrate, whereas XY displacement governed the location of the laser beam over the plasmonic substrate. Once focus is achieved on a specific area of the substrate selected by an optical image, the SERS measurements were carried out, as indicated above. On the other hand, XY scanning allows acquisition of multiple SERS spectra at varying positions. As a common rule, 25 points from different substrate areas were measured every time to sample the plasmonic substrate at different spots. Besides, this procedure was used to generate a SERS map of the scanned area. SERS maps can be processed to detect areas of the substrate which were exposed to the analyte solution and where the characteristic SERS fingerprint of the absorbed molecules can be recorded (revealing in certain cases the structure of the plasmonic sensor, as reported in Chapter 5).

High resolution imaging: To image areas with higher resolution (scanning step size 6 μm or less) and 3D imaging, SERS maps were recorded with a high-resolution confocal Raman microscope alpha 300R (Witec GmbH) comprising an optical microscope (Zeiss) with a motorized XY scanning stage and linked piezo scanner fiber-coupled to an ultra-high-throughput Raman spectrometer (UHTS400-NIR) equipped with a 1024x128 back-illuminated deep depleting CCD detector (DU401 BR-DD, Andor) and a 300 groves/mm grating. As excitation source, a 785 nm laser with tunable output power was used, and spectra were collected through 20x (NA=0.5) or 63x (NA=1) water immersion dip-in objectives, with 10 or 50 ms integration times at 7 mW laser power (if not otherwise stated). The XY scanning stage was used for all confocal SERS mappings except for the high-resolution XZ profile and Z-stack maps for the 3D image, which were acquired using the piezo-scanner. 3D SERS images were created by reconstruction of Z-stack images with ImageJ software.

6.7 Cell culture procedures

Cell culture: All cell lines employed in this thesis **(**HeLa, MCF-7 – with or without GFP transfection-, and HT-1080) were obtained from ATCC. Cells were cultured using DMEM medium supplemented with 10% fetal calf serum and 1% (v/v) of Penicillin-Streptomycin. For the cell passages, adhered cells growing on a T-75 flask were trypsinized with 1% Trypsin-EDTA solution and incubated for 3 minutes after rinsing with PBS solution. Once detached, the cells were diluted 1:3 and resuspended in cell media before planting them in a fresh T-75 flask. For cell counting, 10 µL of cell suspension was mixed with 10 µL of Trypan Blue and dispensed in a Neubauer chamber.

Induction of IDO-1 enzyme expression in HeLa cells: In order to control the activation of IDO-1 in HeLa cells, we harvested HeLa cells in the presence or in the absence of IFN-γ (100ng/mL) for 48 hours. This activation process has been reported to correlate with the expression of large amounts of IDO protein.[7] As soon as the activation process was finished, cell media was exchanged and defined concentrations of diverse metabolites were added. This cell media contained varying concentrations of Trp depending on the cell experiment, 10 µM of Hemin, 2% FCS and 20% of DMEM diluted in HBBS buffer (Hank´s balanced salt solution). After 24 h of cell culture under these conditions, the cell supernatant was collected and measured by SERS.

PCR: With the aim of studying IDO-1 induction by IFN-γ activation, we harvested HeLa cells in the presence or the absence of IFN-γ (100 ng/mL) for 72 hours. RNA was extracted using NucleoSpin® RNA isolation kit from Macherey-Nagel (Ref: 740955.240C). 1 µg of total RNA was used for cDNA synthesis using qScript cDNA Supermix from Quanta (Ref: 95048). Quantitative Real Time PCR (qRTPCR) was performed as previously described.[50] Universal Probe Library (Roche) primers and probes employed are: For: GTGTTTCACCAAATCCACGA, Rv: CTGATAGCTGGGGGTTGC; probe: 20. All qRTPCR data presented were normalized using GAPDH (Hs 02758991_g1 from Applied Biosystems).

3D cell culture: Dissociated 3D cell cultures were prepared from the cell line Hela and MCF7 in Chapters 2 and 5. Once that the cells were detached and resuspended in cell media at the desired concentration, we mixed them 1:1 with Matrigel or collagen (3 mg/mL final concentration) hydrogels. The hydrogel-cell solution mixture was kept in ice and the pipette tips pre-chilled to avoid polymerization. Around 70-80 µL of the hydrogel-cell solution was then dispensed in the central chamber (of the silicone chamber or of the diffusion device) and immediately incubated for 2 h at 37 ºC to promote gelation. After polymerization, plating media was added on top, in the media well, for nourishing the 3D culture.

Stress condition cell assays: We performed different assays that intended to generate stressing environments to the tumor cells. The followed protocols can be classified as a function of the platform where cells were harvested

- **Collected cell supernatants**: For these assays carried out in Chapters 2 and 4, selected cells were harvested in a 12-well plate, at a concentration of 6×10^4 cell/mL and let 24 h for cell attachment. Subsequently, cell media was exchanged to recreate the stress conditions. We added 50 µM of H_2O_2 , 10 µM of Staurosporine, 15 µM of Erastin, to a control cell media containing DMEM (10% FBS) or to a starvation media that do not contain nutrients (we used for these cases a media consisting only a HBBS buffer). After 24 h of cell culture under these conditions, the cell supernatants were collected, centrifuged (3500 rpm, 5 min) and measured by SERS. Within this group of stressing conditions, special considerations were made for the radiotherapy treatment of Chapter 4, as explained below. For the time-course experiments, in section 4.2III, each condition (Control, STP, Erastin) was performed with 4 replicates, one for each time at which the supernatants are collected (30min, 4h, 16h and 24h)

- **Cancer-on-a-chip**: In the experiments with the silicone chamber (cancer-on-a-chip) of Chapter 2, the cell media contained different Staurosporine/Hemin concentrations and were subsequently incubated for 24 hours. The cell device was then assembled with the plasmonic substrate, placing the gold nanoparticle assembly directly in contact with the extracellular milieu.

- **Diffusion device**: On the contrary, for the experiments with the diffusion device hosting nanocomposite scaffolds (Chapter 5), a different protocol was followed. In these assays, Methylene Blue (MB) was used to assess the diffusion of cancer drug in the 3D cell culture model. Final concentrations of MB ranged from 1 µM to 20 µM in cell media. Of note, cells were incubated for 24 h within the 3D Matrigel network prior to the treatment with MB. For XY diffusion assessment, 10x the final concentration of pre-irradiated MB was added to the lateral reservoir, whereas for studying the diffusion in Z, MB was applied on top of the 3D culture, in the media well. As explained in Chapter 5, MB needs a preactivation step by red light irradiation. Irradiation of MB solution was performed for one hour with a light-emitting diode (LED) array, with an emission wavelength of 640 nm and an energy density of 3.5 mW. To visualize the cytotoxicity gradient effect by confocal imaging, MB was applied to the lateral reservoir, incubated at 37 ºC for 2 h, and

rinsed twice with media. Then, the whole media well was filled, and the entire device was irradiated for 1 h. Control experiments with non-exposed MB or without MB were conducted to confirm the specific effect of irradiated MB.

- **Radiotherapy treatment**: MCF-7 were harvested and incubated for 4 days in T75 flasks at an initial cell density determined to achieve 50% confluency at the time of irradiation. One hour prior to irradiation, cells were detached and transferred to 15 mL centrifuge tube (Sigma) filled with fresh media. Cells were then irradiated with a single fraction of 6 MV photons from a Varian 21EX linear accelerator (Varian Medical Systems, Palo Alto, CA, USA) at a dose rate 6 Gy/minute. Single fractions of 0, 5 and 20 Gy were delivered to 3 different cultures.

6.8 Cell viability quantification

Cell viability assays: we implemented different viability assays throughout this thesis, according to the ongoing experiment, which can be divided into two groups (cells attached on cell plates or 3D cell culture within hydrogel-based networks)

- **On cell plates:** Once the cells were challenged under the selected conditions in 12 well plates, the following procedures were carried out:

  - **Quantification of cells attached by Crystal Violet staining**: Cells were seeded at a density of 6×10^4 cell/mL in 12 well plates and let 24 h for cell attachment. Subsequently, cell media was exchanged to recreate stress conditions, varying either Hemin or STP concentrations (Chapter 2). After 24 hours, cells were fixed in formalin (1mL/well) and washed with PBS. We then added 0.5 mL of 0.1% CV (Crystal Violet), which bound to the cells in 20% methanol. The plate was cleaned with DI-water and CV interacting with the cells was resuspended in 10% acetic acid. Finally, this volume was transferred to a spectrophotometer cuvette, to measure the absorbance at 595 nm, which correlates with the number of live cells.

  - **MTT assay**: The MTT assay measures cellular metabolic activity as an indicator of cell viability. For this colorimetric assay, cells cultured on 12 well-plate (under different conditions) were incubated with a yellow tetrazolium salt (3-(4,5-dimethylthiazol-2-yl)-2,5-diphenyltetrazolium bromide or MTT, adding 10µM of 1x solution to 1 mL of cDMEM. Cells were then placed in the incubator for 2 hours, so as to let active cells transform the initial yellow compound into purple formazan crystals. The viable cells

contain NAD(P)H-dependent oxidoreductase enzymes which reduce the MTT to formazan. Subsequently, the 1 mL solution is removed, and the remaining formazan crystals are dissolved using DMSO. Finally the resulting colored solution is quantified by measuring absorbance at 500-600 nanometers using a multi-well spectrophotometer. The darker the solution, the greater the number of viable, metabolically active cells.

- **3D cytotoxic assay**: For those cases in which cancer cells were embedded within polymer matrices (collagen or Matrigel), the previous protocols were not as accurate as in 2D models. Thus, different procedures were implemented, which we classified depending on whether the hydrogel must be depolymerized:

- **Fluorescence microscopy** (no depolymerization required): The media in the device was replaced for complete plating media containing fluorescent probes that selectively label dead cells (1:100 of propidium iodide (PI)), or live cells (1:200 of Cytocalcalcein solution). Both solutions were incubated for 2 h prior to imaging assessment. Images were then acquired with a confocal microscope Zeiss LSM 880, using ZEN software (X, ZEISS). To monitor the spatial cytotoxic effect of drugs, large images of the whole scaffold dimension (5.5x5.5 mm) and approximately 400 μm thickness were acquired with 10x objectives. For a more detailed analysis of cell aggregates, 20x and 40x magnifications were employed. After acquisition, images were processed with ZEN software (ZEN 3.4 (blue edition), ZEISS) and exported by individual channels and Z stacks for precise quantification by CellSENS software (Olympus).

  - **Flow cytometry and CellTiter-Glo (CTG)** (required hydrogel depolymerization): For these cell viability assays, cell aggregates must be first retrieved from the 3D structure. Thus, cell media was rinsed with PBS solution and the media well filled with 300 μL of cell recovery solution. The device with cell recovery solution was incubated for 20 minutes at 4 ºC and complete depolymerization of Matrigel was promoted by pipetting carefully up and down. The solution was then pipetted into an Eppendorf tube and the device rinsed with PBS to recover all remaining cells. Subsequently, recovered cells were counted using a Neubauer cell chamber and divided for flow cytometry analysis and cell viability assay.

    Flow cytometry: Cell viability was monitored using the FACSCanto II flow cytometer and FACSDiva 6.0 software (BD Bioscience). Collected cell solution expressing eGFP and stained with PI was centrifuged (5 min, 3500 rpm and resuspended in 200 μL of

PBS). A minimum of 5000 cells was analyzed. Illumination was performed with a 20-mW 488-nm argon-ion laser. Viable cells labeled with GFP were detected with a 530/30 filter and non-viable cells stained with PI with a 575/26 filter. The cell solution was also measured by flow cytometry for assessment of MB cell uptake, using a 695/40 filter. Posterior analysis was performed with Flow Jo v10.7.

CellTiter-Glo (CTG) 3D Cell Viability Assay kit (354253, Corning). Collected cell culture after hydrogel depolymerization was centrifuged (5 min at 775g), resuspended in PBS, and dispensed in 96 opaque-well plates. Each well containing 50 µL of cell solution was mixed with 50 µL of CellTiter-Glo 3D reagent and incubated at RT for 30 minutes. The solution of each well was vigorously mixed by pipetting up and down and incubated for 30 minutes more. This procedure measures viability by means of the concentration of ATP, which is only present in active cells. The luminesce signal (as a final event of the enzymatic reaction involving ATP as a substrate) generated by this protocol is proportional to the number of active cells. Luminescence was measured with an Orion II LB 965 Microplate Luminometer (Berthold Technologies GmbH), using an integration time of 1 second per well.

6.9 PLGA-SERS strategy

PLGA-SERS method. For the irradiation of plasmonic substrates covered with a PLGA sheathing layer, the laser power was regulated as follows: once the laser spot was focused on the surface of the plasmonic substrate, the 785 nm laser at 0.064 mW/µm^2 was irradiated for 1s, through a 50x objective, so as to create a measurement window in the PLGA layer. Although already at first exposure a SERS signal was detected, exposure time was extended until the intensity of the SERS signal was stabilized. The total irradiation time was *ca.* 5 s, thereby ensuring complete degradation of the PLGA layer over the selected spot. Upon generation of the measurement window, the SERS signal of the analytes was recorded using an irradiance of 0.018 mW/µm^2 with the 785 nm laser for 1 s, in static mode and through a 50x objective (numerical apertures of NA = 0.5, Leica Microsystems, Wetzlar, Germany). In parallel, SERS spectra from control plasmonic substrates (with no PLGA coating) were registered with the same settings: 50x objective with 0.018 mW/µm^2 irradiance for 1s.

Measurement of the PLGA layer permeability: To measure the ability of the covering layer to prevent the analytes in solution from reaching the plasmonic component, a 50 µL drop of the analyte solution (either 100 µM Ado or 100 µM 4-MBA solution) was deposited on a PLGA-coated plasmonic substrate (95:5 lactic/glycolic acid ratio). Fifty SERS spectra were then

randomly acquired from different regions at different times (24h and 48h), with a low laser intensity (0.018 mW/μm^2) at 785 nm through 50x objective, thereby preventing degradation of the PLGA layer. The absence of characteristic SERS signals from the analytes indicated impermeability of the sample to the solution. This strategy allowed for a quick evaluation of the coverage degree of sheathing layers on plasmonic substrates. Thus, it was followed to compare the coverages obtained with different solvents of the PLGA solution: ethyl acetate and acetone.

Multiplex SERS mapping: To confirm the spatial control at different times and analytes, a PLGA-coated plasmonic substrate was sequentially incubated with different molecules at 100 μM concentration. Such analytes were chosen such that their characteristic Raman peaks do not overlap with each other (4-MBA, CV, TBZ, NAm). Once the silicone chamber was stuck onto the plasmonic substrate, 500 μL of the analyte solution was introduced by micropipetting into the inner chamber of the device. Upon addition of the analyte, a laser irradiance of 0.064 mW/μm^2 was applied until SERS intensity stabilization, thus creating a measurement window. The analyte was then removed from the silicone chamber, by aspiration with a micropipette and, after a cleaning step consisting of flowing MiliQ water through the silicone chamber, the following analyte was injected. During this process of sequential incubations, a hole was created at a different spot of the PLGA layer for each analyte. Control of the hole position was achieved using the piezoelectric stage in the Raman microscope. The distribution of holes along the Xaxis was chosen with a step of 20 μm without changing their position in the y-axis (with this step size, no overlap or interference occurred between holes). Once all the different analytes were sequentially incubated and the corresponding PLGA holes created, the whole area was mapped with a laser irradiance of 0.018 mW/μm^2, thereby detecting the analytes retained in the plasmonic layer. Scanning measurements were performed using a 785 nm laser excitation source (maximum 119.50 mW), recorded in static mode using a 50x objective (numerical apertures of NA = 0.5) with 1s integration time, at 0.018 mW/μm^2 or 0.00390 mW/μm^2 laser power. The map of a selected area was acquired with a resolution of 10 μm in X and Y.

Larger areas can be irradiated by reducing to 10x (NA = 0.25) the objective through which the laser beam is focused. Despite considerably decreasing the power of irradiation on the plasmonic surface when illuminating through this lower magnification objective (0.026 mW/μm^2), continuous exposure of the selected area to the laser beam rendered larger measurement windows. For example, a square shape of 200x200 μm^2 was achieved through 40 successive irradiations of 5s over the defined area by 785 nm laser line-scanning. The resolution between two irradiated points was 10 μm in x and y. Finally, when the scanning was completed, a SERS map was acquired in static mode using a 10x with 1 s integration time, at 0.0039 mW/μm^2 laser power.

Cancer-on-a-chip combined with PLGA substrates: HeLa cells ($1x10^6$ cell/mL) were laden inside the silicone chamber and the whole system was then assembled with the plasmonic substrate (obtained as described in previous sections), placing the gold nanoparticles covered with a PLGA layer 95:5 directly in contact with the extracellular milieu. Cells were cultured in 500 µL of Dulbecco's modified Eagle medium (DMEM) with 10% fetal bovine serum (FBS), supplemented with 200 µM of adenosine. SERS measurements were recorded at 0 h and 24 h after Ado supplementation to monitor changes in extracellular concentration over time. For this experiment, irradiation with the 785 nm laser at 0.064 mW/µm^2, for 5 s and through a 50x objective, ensured complete degradation of the sheathing layer at the irradiated spots. Subsequently, SERS spectra were recorded at these positions by irradiating with the same 785 nm laser at 0.018 mW/µm^2 for 10 s.

6.10 SERS data analysis and processing

For data processing, we have generally utilized Renishaw's WiRE software and standard Python Libraries in JupyterNetwork (such as Pandas for data storage or matplotlib for spectra representation).

Once SERS spectra were acquired, each collected spectrum was processed to remove cosmic rays, estimated and subtracted the baseline arising from the substrate and biological fluorescence (following a polynomial curve of 11th order), and normalized to the most intense signal. Then, when so specified, the average spectrum of the collected data was calculated.

Fully processed data sets were typically analyzed by principal component analysis (PCA) and T-Distributed Stochastic Neighbouring Entities (t-SNE) using standard algorithms of Scikit Learn library in Phython. Both are unsupervised algorithms for exploring the data without previous training. PCA is a machine learning tool for reducing the number of dimensions in a dataset while retaining most information. By applying this algorithm (a linear transformation), we retrieved the minimum number of variables that kept the maximum information about how the original data was distributed. Having different cell conditions, PCA analysis provided information on the most significant shift in SERS spectra wavenumbers among such conditions. t-SNE is another tool for reducing data dimensionality that, however, perform a non-linear transformation. t-SNE uses probabilistic methods (Student-t distribution) to compute the similarity between two points in the low-dimensional space, and was used to visualize subset of data with similarities in the spectra.

The input of the CNN for SERS spectra classification is one dimensional and it contains the entire spectrum (600-1500 cm^{-1}). The networks were created in Python (Python Software Foundation.

Python Language Reference, Version 3.6.6. Available at http:// www.python.org) and using Tensorflow (TensorFlow: large-scale machine learning on heterogeneous systems, 2015. Software available from tensorflow.org)

For building our CNN architecture, we trained one-dimensional convolutional kernels across 4 convolutional layers with exponential increase (2^n) in the number of channels. Formally a convolutional layer can be expressed as follows:

$$y = f(b + \sum_i (k * x_i)$$

Where x is input map and the y output map, respectively. k is a convolutional kernel between the maps x and y, and b is the bias parameter.

After each step of convolutional layer, we applied a ReLU nonlinearity defined as:

$$f(x) = \begin{cases} 0, & x < 0 \\ x, & x \geq 0 \end{cases}$$

We applied afterwards Maxpool which calculates the maximum valued for each patch of the feature map, in addition, to avoid overfitting the model to the data, we applied batch normalization after each layer and 50% dropout prior to the fully connected layer.

6.11 Other equipment and procedures

LC-MS:

Adenosine and Hypoxanthine identification and quantification were performed on an Acquity UHPLC chromatograph equipped with a photodiode-array system and coupled to a LCT Premier XE ESI-TOF mass spectrometer (Waters, Milford, MA, USA). Chromatographic separation was carried out using an Acquity BEH C18 (100x2.1mm, 1.7µm) reverse phased column (Waters, Mildford, USA). The elution buffers were 0.1% formic acid in water (A) and acetonitrile (B), and the linear gradient method consisted of 99% A over 1.5 min, 99-1% over 1.5-6 min, 1% for 2 min and 99% for 2 min before next injection. Total run time was 10 min, injection volume was 5 µL and the flow rate was set at 300 µL/min. Both metabolites were detected and quantified after monitoring the UV signal at 254 nm of wavelength.

Kynurenine and tryptophan samples separation was performed in reversed-phase chromatography using an ACQUITY UPLC BEH C18 1.7µm (2.1x100 mm) column (Waters, Manchester, UK)

which was maintained at 30 ºC. The injected sample volume in all cases was 10 µL and the autosampler was set at 4 ºC. For Kyn and Trp, the mobile phase was designed as phase A, consisting of a mixture of 0.1% formic acid-H_2O and phase B, ACN. The method used a gradient at constant flow rate (0.3 mL/min) combining solvent A and solvent B, programmed as follows: 0-0.5 min, linear change from A–B (95:5 v/v) to A–B (1:99 v/v) in 2.5 min and finally returning to 95% A at 3.7 min for column re-equilibration, which was completed at 5 min.. The peaks were characterized by comparing the retention time and UV-vis absorbance at λ = 363 nm for Kynurenine, λ = 277 nm for Tryptophan.

Scanning electron microscopy: images of the nanoparticle distribution on glass-based support were captured using an environmental SEM (FEI Quanta 250). 5-20 kV acceleration voltages were used to take the images.

UV-VIS-NIR spectroscopy: Extinction spectra of colloid dispersions were acquired with a Agilent 8453 UV/vis spectrometer, using polystere cuvettes. Extinction spectra of plasmonic substrates were collected via a Carry 500 UV-vis spectrometer (Agilent)

ROS species generation after MB irradiation: The production of $1O_2$ was measured after irradiation of a 20 µM MB solution, containing the dye 9,10-Anthracenediyl-bis(methylene)dimalonic acid (ABDA). ROS production was followed by a decrease in ABDA absorbance (at 380 nm), which occurred upon reacting the dye with the oxidant species. A stock solution of ABDA in Dymehtyl sulfoxide (~10 mM) was subsequently used in the preparation of 0.4 mM ABDA in PBS. The experiments were carried out in 96 well-plates. ABDA solutions (100 µL) were then mixed with 100 µL of MB (40 µM), to a final concentration of 20 µM, and then irradiated for 60 min with an emission wavelength of 640 nm and an energy density of 3.5 mW for 60 min. The absorbance of ABDA was finally collected, comparing the results with those obtained without MB or without lamp irradiation

Scaffolds characterization: The rheological properties of the inks were characterized using a Physica MCR 302 rheometer (Anton Paar, Spain). All tests were carried out in triplicate at room temperature using a 25 mm parallel plate geometry and a solvent trap to prevent water evaporation. Frequency sweeps were carried out from 0.1 to 500 rad/s at 0.1% strain, determined by previously performed amplitude sweep assays, with a gap of 1 mm. Flow curves were also obtained for shear rates from 0.01 to 1500 s^{-1}. Finally, oscillatory-rotational-oscillatory tests were performed by applying a shear rate of 10 s^{-1} and studying the recovery of the inks at rest. The microstructure of the scaffolds was analyzed using a JEOL JSM-6490LV scanning electron

microscope (SEM), operating at an acceleration voltage of 15 kV and at a working distance of 15 mm.

The stability of the scaffolds in cell culture media (cDMEM) at 37 ºC was assessed after recording the swelling of the material by a general gravimetry method at selected time intervals. The swollen hydrogels were removed, the excess of liquid absorbed with filter paper and the scaffold weighed. The swelling ratio (SR) was calculated using the following equation 1:

$$SR = (Ws-Wd)/Wd \cdot 100$$

where Ws is the weight of the swollen sample and Wd is the weight of the dried hydrogel sample.

6.12 References

1 Bastús, N.G.; Comenge, J & V. Puntes,V. Kinetically controlled seeded growth synthesis of citrate-stabilized gold nanoparticles of up to 200 nm: size focusing versus Ostwald ripening. *Langmuir* **27**, 11098 (2011).

2 Hanske, C.; *et.al.* Large-Scale Plasmonic Pyramidal Supercrystals via Templated Self-Assembly of Monodisperse Gold Nanospheres. *J. Phys. Chem. C* **121**, 10899 (2017).

3 Scarabelli, L.; Sánchez-Iglesias, A.; Pérez-Juste, J. & Liz-Marzán LM. A "Tips and Tricks" Practical Guide to the Synthesis of Gold Nanorods. *J Phys Chem Lett*. **5**, 4270-4279, (2015).

4 Bodelón,G.; Montes-García, V.; Costas,C.; I. Pérez-Juste, I.; Pérez-Juste, J.; I. Pastoriza-Santos,I. & M. Liz-Marzán, L. *ACS Nano* **11**, 4631-4640, (2017).

5 Qin, D.; Xia, Y.; Whitesides, G. M. Soft Lithography for Micro- and Nanoscale Patterning. *Nat. Protoc*. **5**, 491–502. (2010)

6 Shin, Y.; Han, S.; Jeon, J. S.; Yamamoto, K.; Zervantonakis, I. K.; Sudo, R.; Kamm, R. D.; Chung, S. Microfluidic Assay for Simultaneous Culture of Multiple Cell Types on Surfaces or within Hydrogels. *Nat. Protoc.* **7**, 1247−1259, (2012)

7 Jürgens, B.; Hainz, U.; Fuchs, D.; Felzmann, T. & Heitger A. Interferon-gamma-triggered indoleamine 2,3-dioxygenase competence in human monocyte-derived dendritic cells induces regulatory activity in allogeneic T cells. *Blood.* **114**, 3235-43 (2009).

CHAPTER 7

“Conclusion and Outlook”

The detection of cancer biomarkers represents a pivotal stage in the evaluation and diagnosis of cancer patients, so that more precise treatments can be selected according to measured features. Such prognostic biomarkers commonly include proteins and nucleic acids via genomics and proteomics-based analysis. Notwithstanding, the detection of metabolites (metabolomics), produced as the result of altered biochemical processes in tumors, is gaining relevance, owing to the information that can be obtained about the pathophysiology of the disease. To this end, multiple sensing strategies are under development, not only to detect such biomarkers in different biofluids, but also to image their distribution within tissues, including in vivo, ex vivo and in vitro models. Arguably, the advent of improved technologies for biomarkers monitoring will guide the evolution toward a better precision biomedicine, which will eventually drive clinal decision making at different stages of cancer disease.

In this thesis, we set the focus on surface-enhanced Raman spectroscopy, as a promising technology for biomedical monitoring in the context of cancer. This is considered to be a promising application of this Raman spectroscopy modality and has thus fueled recent research on the interplay between biomolecules and plasmonic components. Hence, the experiments performed throughout this thesis sought to demonstrate the suitability of SERS for the screening of extracellular cell environments, including 3D models. We have provided illustrative examples of the use of SERS for monitoring cancer-related biomarkers, with a particular emphasis on identifying those directions that may drive widespread integration into biomedical sensors. Special attention was also paid to those requirements needed for improving in-situ measurements, introducing strategies based on artificial intelligence or responsive materials, thereby creating platforms with a wider versatility to address future exciting opportunities and challenges lying ahead.

In **Chapter 2**, SERS substrates fabricated by two different strategies were compared according to their capacity to enhance the signal of secreted immunomodulatory metabolites, in particular kynurenine, tryptophan and purine derivative metabolites. Although two selected types of SERS substrates (LbL films and 2D superlattices), could accurately screen such biomarkers at the micro-molar concentration range in a buffer solution (PBS), significant discrepancies were noticed when the spectra obtained in the presence of cell media: only the superlattice substrate provided reliable

results for metabolites monitored in this environment. Subsequently, a systematic study was performed to monitor the activity of IDO-1 enzyme (overexpressed in various types of cancer cells) under diverse cell culture conditions (varying activation with interferon-γ, and initial tryptophan concentrations). SERS allowed the multiplex analysis of extracellular fluctuations in both the enzymatic substrate and the product of its enzymatic activity (Trp and Kyn, respectively). Using plasmonic superlattices, we were able to estimate by SERS the Kyn/Trp ratio, as a function of the vibrational bands at 562 cm^{-1} and 760 cm^{-1}. Moreover, we observed that the levels of purine derivative metabolites were directly related to cell death, induced upon challenging the cells with high Hemin concentration. Purine derivatives were thus found to work, in general, as suitable biomarkers of cell death. For this study, we devised a cancer-on-a-chip device that allowed recording the SERS signal while tumor cells were allowed to grow within a 3D collagen matrix. In this implementation, we additionally showed that the plasmonic component of the device could be reconfigured over the course of the experimental protocol, to match on-demand the lattice plasmon resonance of the substrate with the wavelength of the excitation laser light.

Following this line of work, **Chapter 3** abounds in additional improvements for such cancer-on-chip devices, to allow continuous SERS measurements without operator interventions (i.e., using a fresh substrate for each measurement) and without the underlying problems derived from SERS memory effects. We first reported this detrimental effect in a wide range of plasmonic substrates, analytes and concentrations, revealing the widespread impact of such a SERS memory effect. To resolve this extended flaw, we proposed the deposition of a micron-think, thermolabile polymer layer on top of the plasmonic substrates, which would act as a physical barrier against molecular diffusion and adsorption. Subsequently, a laser beam could be focused on the underlying AuNPs and its power modulated to induce a sufficient temperature increase by plasmonic heating. Above a certain temperature threshold, the sheathing layer was degraded and opened a measurement window at the desired time and target location. As soon as a micrometer-sized window was created in the polymer layer, the molecules in solution could reach the plasmonic surface and be subsequently registered by SERS. We additionally demonstrated that this process can be repeated as many times as required for monitoring the event of interest, with no interference from earlier measurements/molecular adsorption, which was finally applied to obtain continuous information about the evolution of tumor extracellular environments.

In Chapter 4, we explored the implementation of artificial intelligence methods to interpret complex spectral signatures. In the literature, machine learning has already shown the potential to identify and classify different SERS profiles. Thus, we intended to evaluate the superiority of this method compared to conventional classification techniques (employed in previous chapters),

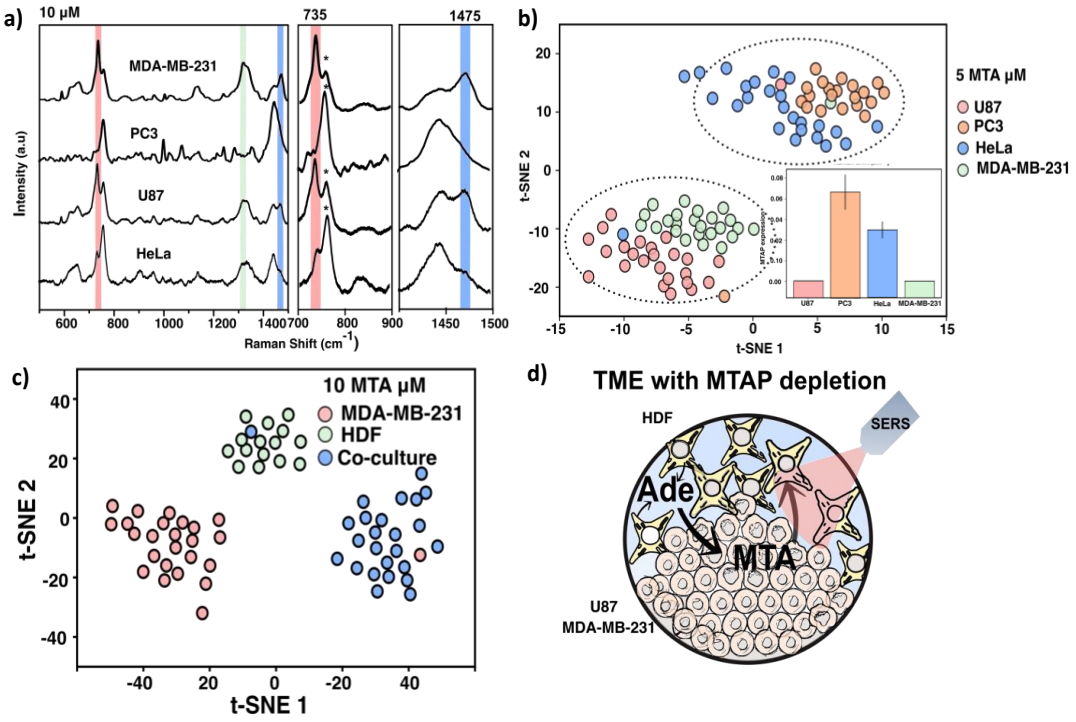

Figure 7.1. a) SERS spectra of HeLa, MDA-MB231, DU145 and U87 cells supernatants after 24 h of incubation with 10 µM of MTA. b) t-SNE analysis of the spectra collected from (a), the inset displays the gene expression of MTAP across such cell lines. c) t-SNE analysis of SERS spectra collected from either monocultures of MDA-MB-231 or human dermal fibroblast (HDF), or co-cultures of both cell lines after 24 hours of incubation with 10 µM MTA. SERS measurements were performed with a 50× objective and 5 s of acquisition time, the maximum power of the 785 nm laser was 295.13 kW cm^{-2}. d) Schematic illustration of the SERS-based system to detect the metabolic interaction between cancers cells and fibroblasts in MTAP depleted tumor environments.

using them to analyze SERS spectra collected from cells exposed to different stress conditions. The choice of a convolutional neural network (CNN) architecture, rather than other types of deep learning methods, was made because of its well-known ability to extract both global and local features, prior to the classification step. Final results showed that the proposed CNN architecture slightly outperformed other conventional classification methods, such as decision trees (DT) and support vector machine (SVM). As a result, the deployed DNN model could perform a classification with sensitivity and specificity of 99% for the different secretomes, which demonstrated the release of different subsets of metabolites under each condition. Additionally, the employed strategies were capable of deciphering time-dependent variations in short (hours) and longer (weeks) time scales. Still, this Chapter can only be considered as a preliminary approximation to this topic, working as a pilot demonstration of the potential integration of SERS monitoring + DNN into the next generation of cell death studies,

Finally, in **Chapter 5**, we introduced the transition from 2D to 3D models by incorporating 3D nanocomposite scaffolds that allowed detailed monitoring of the cell environment and its impact on drug penetration and cell death. The first objective involved the design of suitable alginate-

gelatin scaffolds containing AuNRs, for cellular growth in 3D, which not only allowed the proliferation of tumor cells in a suitable environment (mimicked by a Matrigel© 3D network), but also offered the possibility to create and monitor drug diffusion gradients, over extended periods of time. The final devised structure also provided continued control over nutrients/humidity/etc., thereby maintaining tumor growth and a homogenous cell distribution across the scaffolds. We then proceeded to monitor the dynamics of an anti-cancer drug (methylene blue) upon administration in the manufactured cell device, so that the distribution of the drug within the created tissue can be readily recognized over time, by means of 3D SERS imaging. In particular, the retrieved diffusion profiles provided a wealth of information about both drug distribution and the response of tumor cells to the treatment, correlating parameters of drug diffusion with its cytotoxic effect on cell culture models.

Although still in its infancy, we have explored different strategies toward unraveling the presence of specific biomarkers with spatiotemporal resolution. Sensors integrated with cell culture models have been developed to read extracellular signals, which facilitated the acquisition of additional knowledge about the tumor microenvironment. The landscape of applying nanomaterials to cell cultures seems promising; however, as noted throughout the thesis, limitations exist (such as the SERS memory effect) that deserve close attention. Notwithstanding, by combination of the advances reported in the various Chapters, we have at hand multifaceted SERS sensors for addressing upcoming challenges. We anticipate that the tools and methods presented throughout this thesis will carry over into the future. For instance, by SERS interrogation of supernatants from cells with different mutations in methylthioadenosine phosphorylase (MTAP, see section 1.3), we are currently deciphering novel mechanisms that governs extracellular MTA fluctuations over time (see **Figure 7.1**). We have obtained so far unexpected results in the role of stromal cells (fibroblast, macrophages) towards controlling MTA extracellular concentrations and related derivatives metabolites (such as adenine). This result represents, to the best of our knowledge, the first exploration of metabolic interactions by SERS technology, and enables us to predict that other cell-to-cell communication events can be similarly described by SERS in the future.

APPENDIX

We present herein supplementary experimental data that, albeit significant for accurate characterization, were not performed by the main author of this thesis.

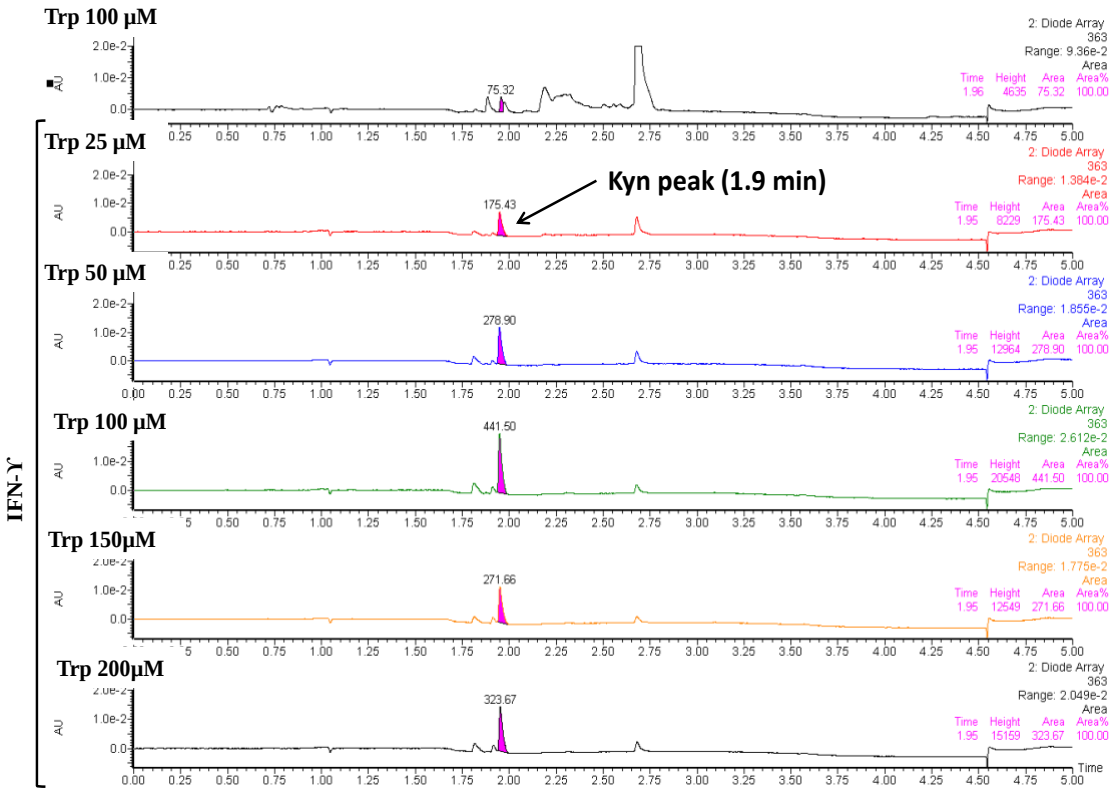

Figure S2.1. HPLC chromatograms of the detection of kynurenine (detection at I363 nm) (see section 6.11 for details) in extracellular media of control HeLa cells or induced HeLa cells treated with IFN-Ɣ (100 µM) and with varying Tryptophan concentration (25, 50, 100, 150 and 200 µM). (HPLC experiments performed by Javier García Calvo, platform manager in CICBiomaGUNE)

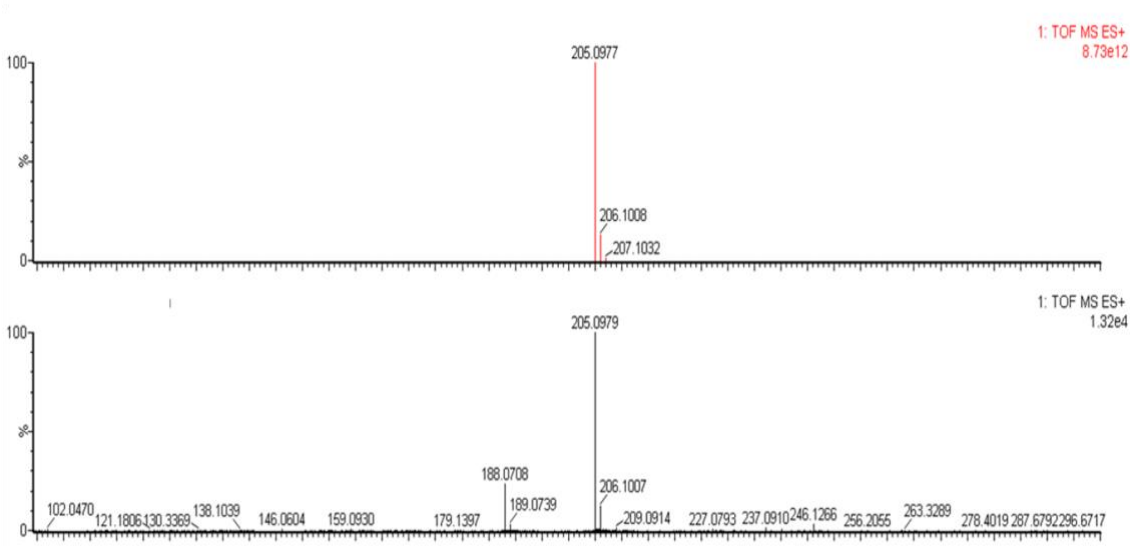

Figure S2.2 LC/ESI-HRMS chromatogram of peak at 1.9 min retention time assigned unequivocally to Kyn; 205.0979 ($[M + H]^+$ calcd 205.0977).

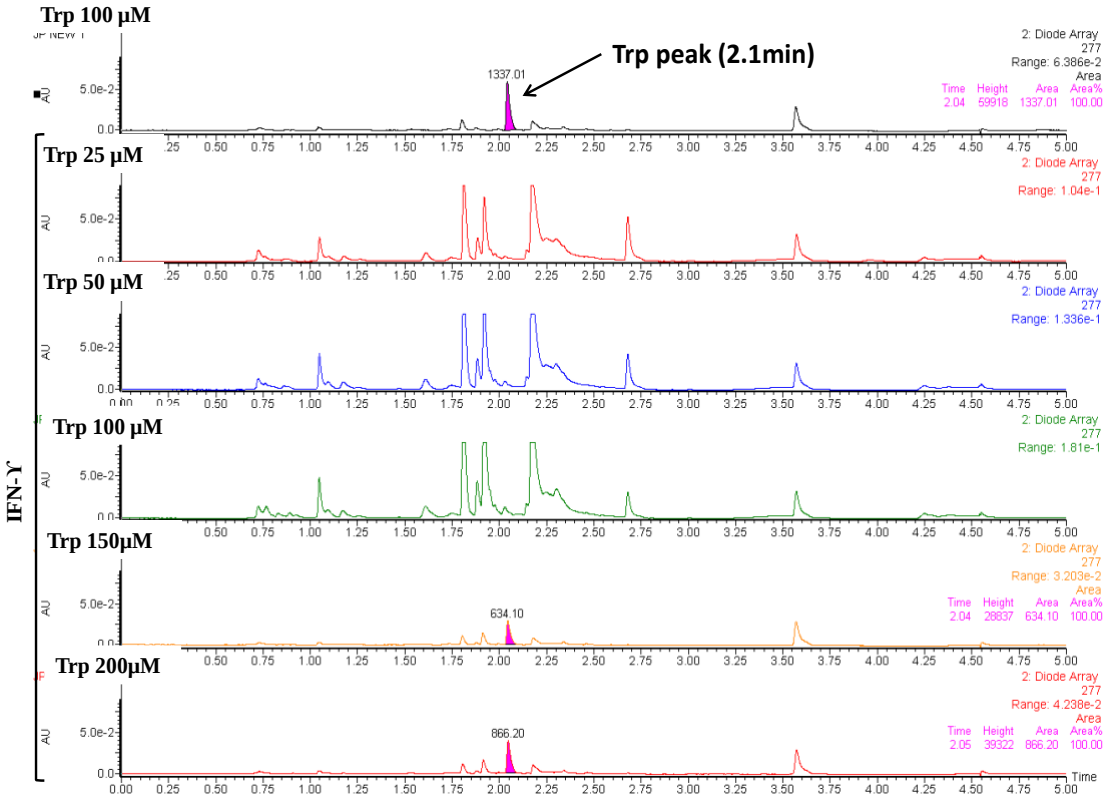

Figure S2.3. HPLC chromatograms of the detection of Tryp metabolite (detection at I363 nm) (see section 6.11 for details) in extracellular media of control HeLa cells or induced HeLa cells treated with IFN-Ɣ (100 µM and with varying Tryptophan concentration (25, 50, 100, 150 and 200 µM).

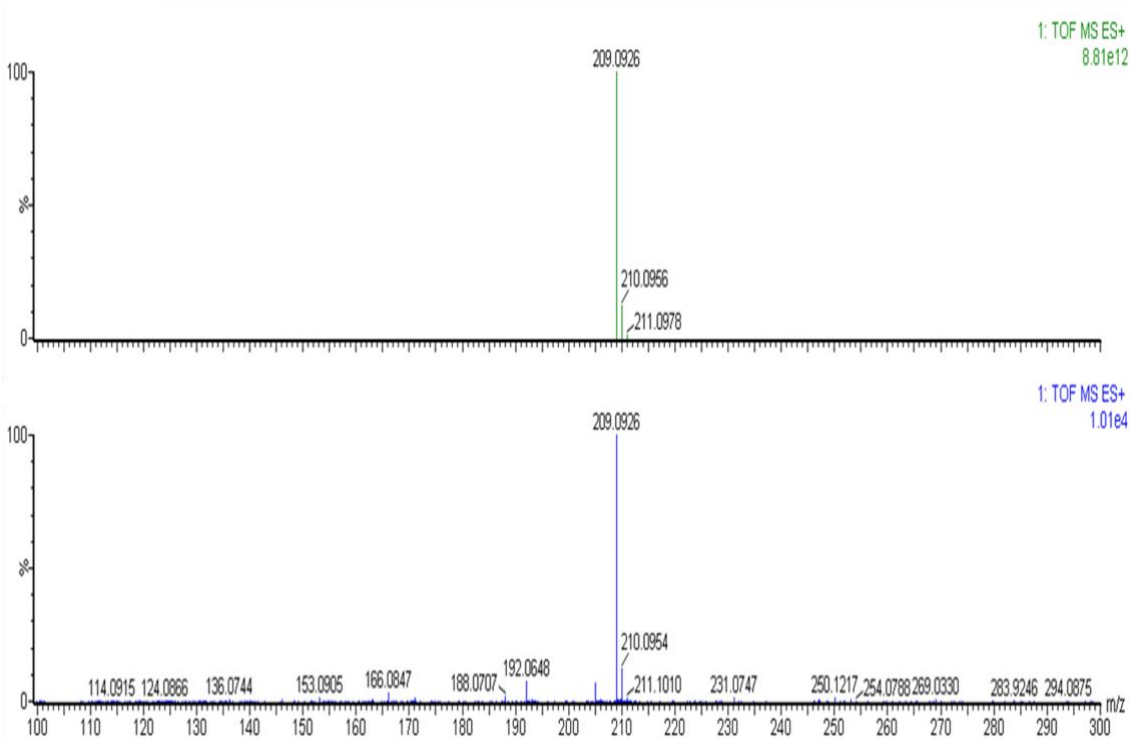

Figure S2.4. LC/ESI-HRMS chromatogram of peak at 2.1 min retention time assigned unequivocally to Trp; 209.0926 ($[M + H]^+$ calcd 205.0926).

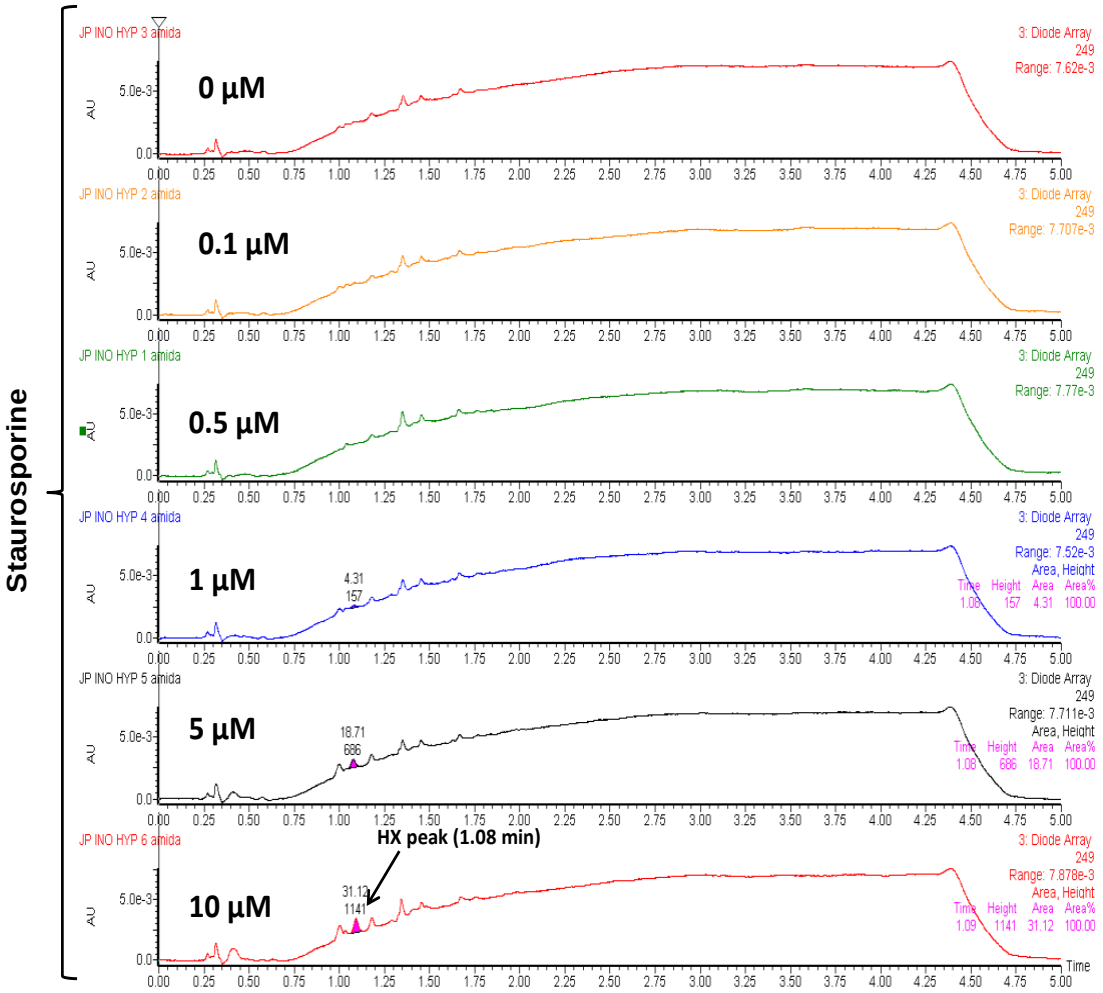

Figure S2.5. HPLC chromatograms of the detection of Hx metabolite (detection at I249 nm) in extracellular media of HeLa cells treated with varying Staurosporine concentrations (0, 0.1, 0.5, 1, 5, 10 µM). Inosine peaks were not detected.

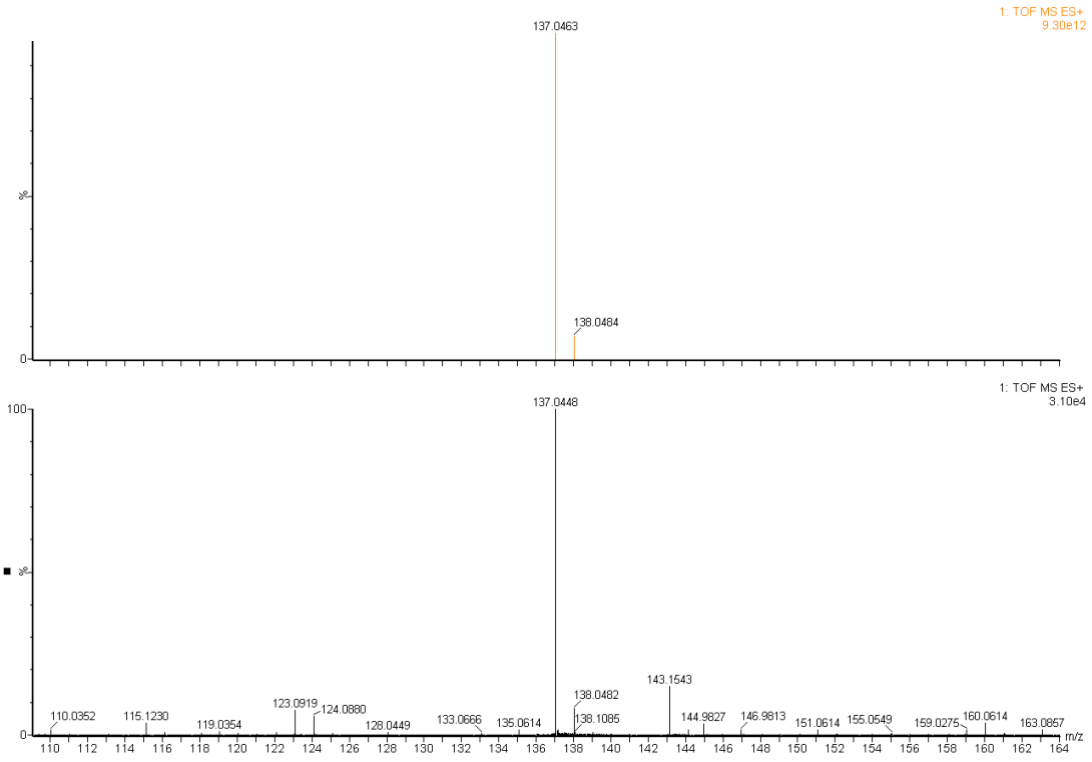

Figure S2.6. LC/ESI-HRMS chromatogram of peak at 1.08 min retention time assigned unequivocally to HX; 137.0448 ($[M + H]^+$ calcd 137.0463).

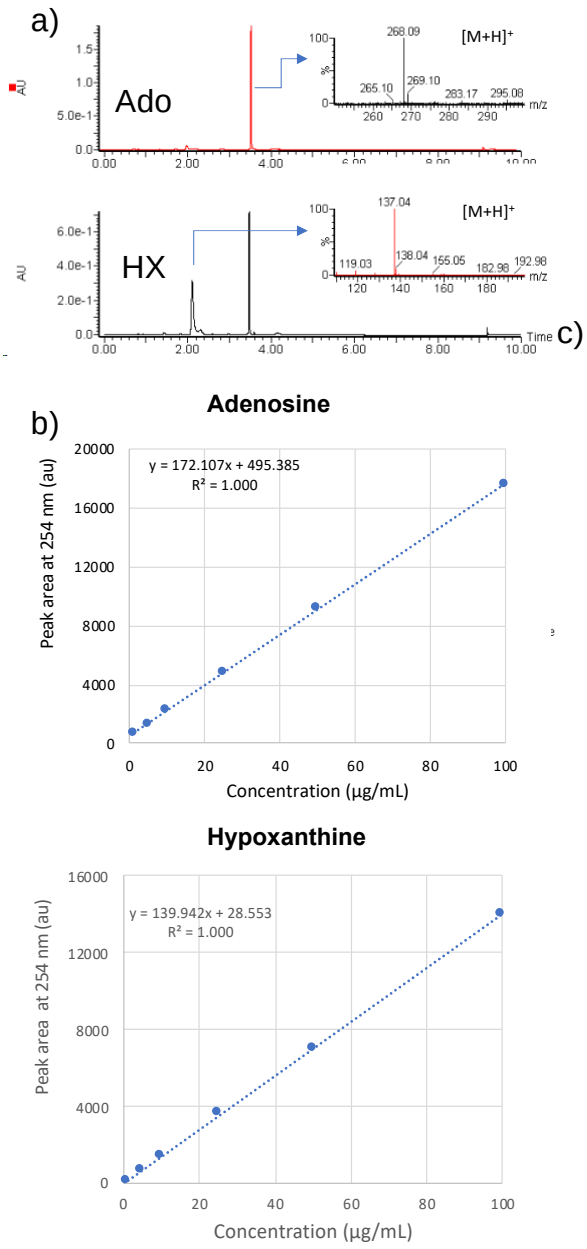

c)

	Sample	Run	Area	Conc. (µM)	Conc. Avr (µM)
Adenosine	0 h Control A	1	ND		
		2	ND		
	0 h Control b	1	ND		
		2	ND		
	24 h Control A	1	380,8	< 1	
		2	353,3	< 1	
	24 Control B	1	363,9	< 1	
		2	377,6	< 1	
	0 h 200 µM Ado A	1	29903,8	170,9	**170,2**
		2	29683,8	169,6	
	0 h 200 µM Ado B	1	29368,1	167,8	**166,3**
		2	28849,8	167,7	
	24 h 200 µM Ado A	1	11273	62,6	**62,2**
		2	11143,1	61,9	
	24 h 200 µM Ado B	1	13543,4	75,8	**76,2**
		2	136685,3	76,6	
Hypoxanthine	0 h Control A	1	ND		
		2	ND		
	0 h Control b	1	ND		
		2	ND		
	24 h Control A	1	303	2,3	**2,4**
		2	330,2	2,5	
	24 Control B	1	54,9	0,6	**0,6**
		2	60,6	0,6	
	0 h 200 µM Ado A	1	2944,7	20,8	**21**
		2	2999,6	21,2	
	0 h 200 µM Ado B	1	3141,3	22,2	**23**
		2	3343,6	23,7	
	24 h 200 µM Ado A	1	17989,3	128,3	**126,6**
		2	175503	124,9	
	24 h 200 µM Ado B	1	15591,1	111,2	**111,8**
		2	15769,1	112,5	

Figure S3.1. a) Representative HPLC chromatograms for the detection of Adenosine (Ado) and Hypoxanthine (HX) in the extracellular media of HeLa cells. The insets show the characteristic LC/ESI-HRMS chromatograms of the peaks located at the retention times indicated for each analyte, which were assigned unequivocally to Ado and HX respectively. b) Calibration curve for determining the Ado and HX concentrations by LCMS. c) The concentrations of Ado and Hx in the extracellular media of bioreactors, measured by LCMS at different times and conditions: control, without prior Ado supplementation or cell media with 200 µM of Ado supplementation.

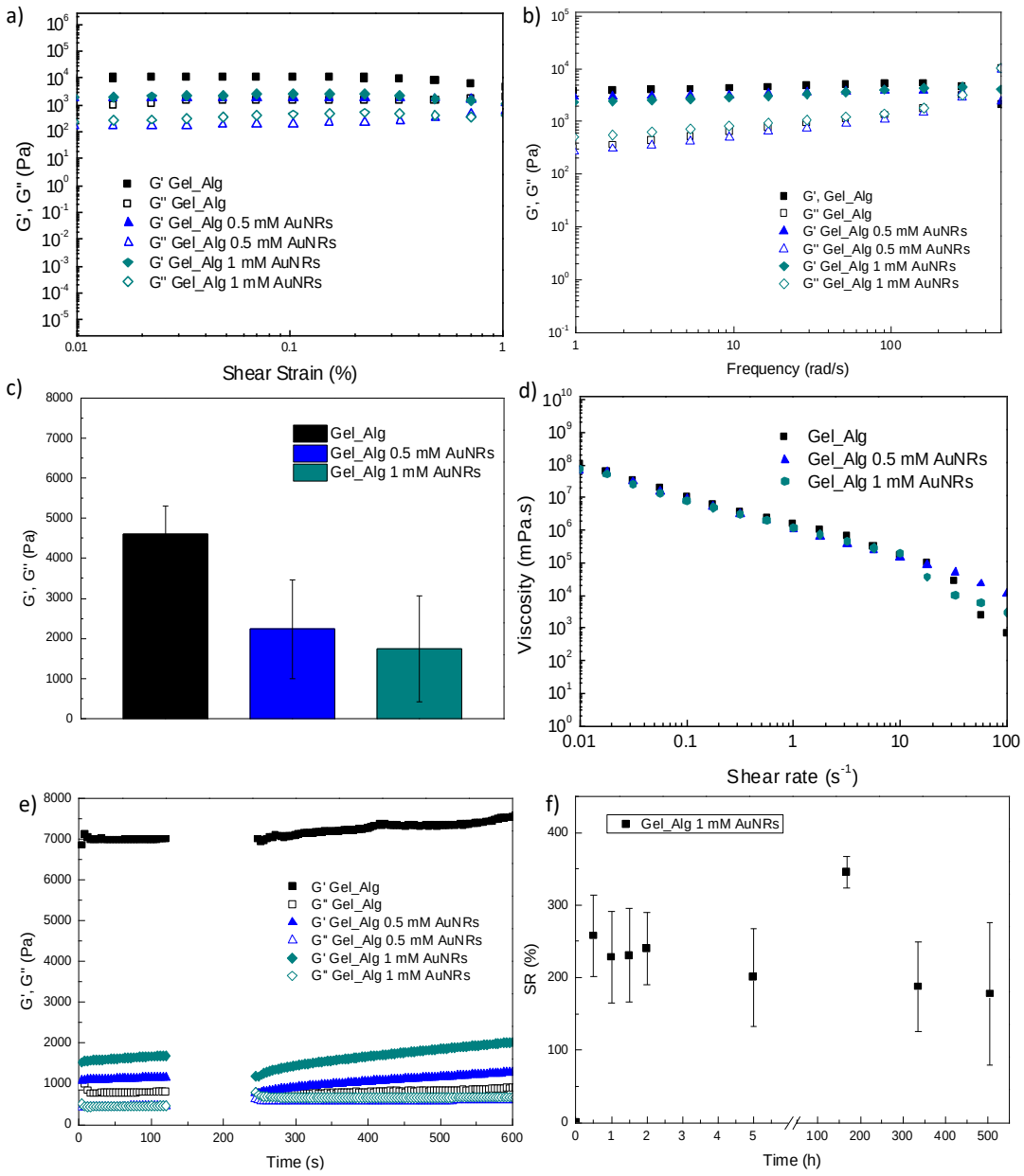

Figure S5.1. Rheological characterization of the hydrogels used as inks for 3D printing (see 6.11 for details). a) Strain sweeps for gelatin (10%) and alginate (2%) with different AuNRs concentrations. b) Frequency sweeps at 0.1% strain. c) Storage moduli values at f = 1 Hz, for gelatin-alginate inks. The storage moduli of the inks were in the range of 2000 Pa and were reduced after addition of AuNRs, indicating that the particles disrupt the gel transition recovery of gelatin chains. d) Flow curves at different AuNRs concentrations, as labeled. e) Thixotropy tests show a quick recovery ability of the viscoelastic properties, thereby ensuring a good printing fidelity of the scaffolds with 75% recovery of the viscosity after a few seconds. f) Swelling studies of printed scaffolds during 20 days of incubation in cDMEM. (Rheological characterization was performed by Clara García-Astrain, Postdoctoral researcher in Bionanaoplasmonics group)